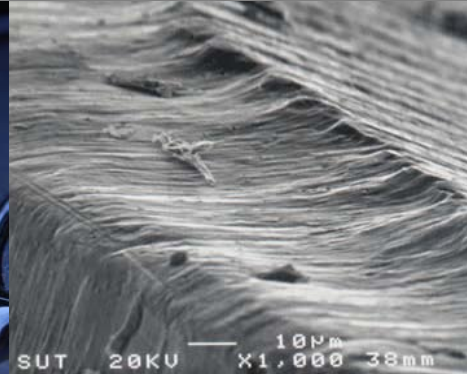
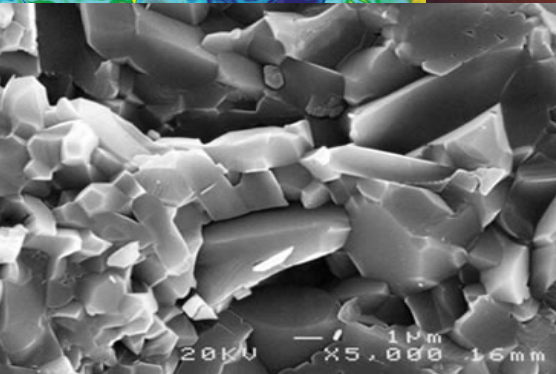
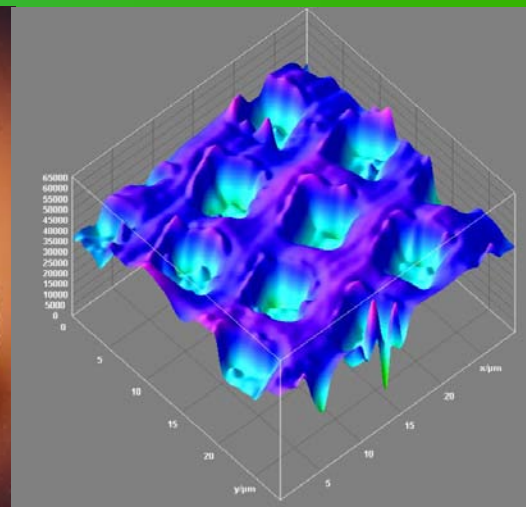
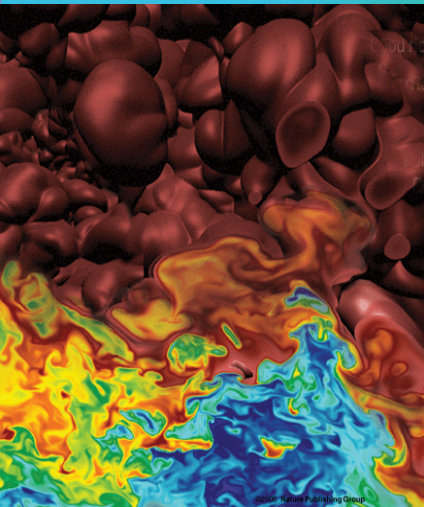


# National Tribology Conference 2009

4 - 5 May 2009, Rimba Ilmu,  
University of Malaya



Organized by

Department of Mechanical Engineering  
University of Malaya, Kuala Lumpur  
and  
Malaysian Tribology Society (MYTRIBOS)



Proceedings of the  
**National Tribology Conference 2009**

(*NTC2009*)

**4-5 MAY 2009**

RIMBA ILMU  
UNIVERSITY OF MALAYA  
KUALA LUMPUR

***Edited By:***

Prof. Dr. Masjuki Hj. Hassan

Prof. Dr. A.S.M.A. Haseeb

Dr. Saidur Rahman

Dr. Mariyam J. Ghazali

Assoc. Prof. Dr. Jahara A. Ghani

*Publisher:* Dept. of Mechanical Engineering, University of Malaya and Mytribos

*Proceedings: National Tribology Conference 2009*

*ISBN: 978-983-42040-1-3*

All rights reserved © 2009. No part of these proceedings shall be reproduced, stored in a retrieval system, or transmitted in any form or by any means, electronic, mechanical, photocopying, recording or otherwise, without prior permission of the copyright holder.

No responsibility is assumed by the publisher for any injury and/or damage to persons or property as a matter of products liability, negligence or otherwise, or from any use or operation of any methods, product, instruction or ideas contained in the material herein.

ISBN 978-983-42040-1-3



# **Organizing Committee**

## ***Advisor***

Prof. Dr. Masjuki Hj. Hassan

## ***Chairperson***

Dr. Saidur Rahman

## ***Secretary***

Husnawan Mutiara

Md. Abdus Sattar

Md. Jayed Hussan

## ***Technical Support***

Dr. Saidur Rahman

Dr. Mariyam J. Ghazali

Assoc. Prof. Dr. Jahara A. Ghani

Md. Hasanuzzaman

Md. Rafiqul Islam

## ***Treasurer***

Assoc. Prof. Dr. Jahara A. Ghani

Assoc. Prof. Dr. Norsani Wan Nik

Muhammad Mahamood Hasan

Jamal Uddin Ahamed

## ***Logistics***

Norhanis Ahmad

Mohammad Abul Fazal

Liaquat Ali Memon

Ashraful Haque

Shamsul Arefin

## **Venue**

Md. Jahirul Islam

## ***Sponsorship, Exhibition & Refreshment***

Saifullah Md. Ghazaly

Md. Abdus Sattar

Md. Arafat Mahmood

## SPONSORS



Hakita Engineering Sdn Bhd  
No.43, Tingkat 1, Jalan Wira2,  
Taman Pewira, 42500,  
Telok Panglima Garang,  
Kuala Langat, Selangor D.E.



Unique Sri Bumi Sdn Bhd  
No. 2-1 Ground Floor  
Jalan Gurney,  
54000 Kuala Lumpur

### **GW OA Sales & Services**

Block H-102, Jasmine Court,  
Bandar Puchong Jaya,  
47100, Puchong Selangor Darul Ehsan

### **Interpadu Sdn Bhd**

9-2A, Jalan Pandan, 3/6,  
Pandan Jaya, 55100,  
Kuala Lumpur



### **Vision Tech Scientific System**

No. 326-2 Jalan Midah Besar  
Taman Midah, Cheras  
56000 Kuala Lumpur  
Malaysia  
Tel: 603-9171 2326 Fax: 603-9171 1326  
Email: vtechss@tm.net.my



No 20-A, Jalan USJ 10/1B, Taipan Town  
Centre, 47620 UEP Subang Jaya Selagor  
Darul Ehsan  
Tel: +603 5637 2536 Fax: +603 5631 4589  
Email: rzecresources@gmail.com



### **SciEDGE Technologies Sdn Bhd**

B-0-1 Megan Phoenix Business Park  
Jalan 2/142A Off jalan Cheras  
56000 Kuala Lumpur  
Tel: +603 9101 2515 Fax: +603 9102 2516  
Email: sales@sciedge.com.my



### **AL-IHSAN ENGINEERING RESOURCES SDN BHD**

No. 37 Jalan 4 Taman Seroja  
Bandar Baru Salak Tinggi, 43900 Sepang,  
Selangor Darul Ehsan  
Tel: +603 8706 2101 Fax: +603 8706 2102



**Advance Altimas Sdn Bhd**  
11 A-3, PJS 8/5 Dataran Mentari  
46150 bandar Sunway  
Selangor Darul Ehsan

# Eranet Technology

**Eranet Technology**  
No. 129 Jalan BK 5/6  
Bandar Kinrara  
47100 Puchong, Selangor Darul Ehsan

MESSAGE FROM  
THE CHAIRMAN  
NATIONAL TRIBOLOGY CONFERENCE (NTC' 09)

The organizing committee is greatly honored for the privilege to organize the 1<sup>st</sup> NTC at Rimba Ilmu, University of Malaya. This event could only have been organized with the full support of the University of Malaya, Faculty of Engineering, Department of Mechanical Engineering, and MYTRIBOS.

Firstly, on behalf of the organizing committee I would like to take this opportunity to sincerely appreciate the NTC keynote speakers, speakers, session chairs, sponsors and attendees whose contributions and efforts made NTC a great success.

Secondly, about 30 abstracts have been received and 25 of them accepted for the conference. Participants will sit in technical sessions over two days, which include exciting keynote lectures delivered by professors and experts from the industry and academia. I am confident that NTC will generate a lot of new ideas and exchange of information among the participants. It will also help promote scientific research, network among the participants and development in the country

Thirdly, on behalf of the International Journal of mechanical and materials Engineering (IJMME) editorial board, I am very pleased to confirm that the selected papers will be published in the December Issue of IJMME, which is a SCOPUS indexed Journal published by the Department of Mechanical Engineering, University of Malaya.

Industry participation is very welcomed, and we hope that the conference will lead to effective and fruitful communication between the researchers, government and industrial communities.

I would like to take this opportunity to thank the Organizing Committee for their hard work in making sure that NTC would be a success. I hope the event will be enjoyable and valuable.

I thank you for your participation and hope to see you again in the next NTC.

**Dr Saidur Rahman**

Chairman

On behalf of organizing committee

NTC'09

## List of Papers

Paper No.	Title of Paper	Corresponding Author & E-mail Address	Pages
NTC-2009-001	THE EFFECT OF NATURAL FREQUENCY OF THE PIN ON DISC SET-UP ON THE FRICTION COEFFICIENT OF MILD STEEL	Md. Liakat Ali <i>E-mail: tusharadd@gmail.com</i>	1 - 6
NTC-2009-002	THE EVALUATION OF FRICTION EFFECT OF RBD PALM STEARIN AS COLD METAL FORMING LUBRICANT	S. Syahrullail <i>E-mail: syahruls@fkm.utm.my</i>	7 - 10
NTC-2009-004	MACHINING AND CUTTING SIMULATION: EFFECT OF RAKE ANGLE AND CLEARANCE ANGLE ON WEAR CUTTING INSERT CARBIDE	Y. Hendri <i>E-mail: hyanda@eng.ukm.my,</i>	11 - 17
NTC-2009-005	INVESTIGATION OF TRIBOLOGICAL PERFORMANCES OF DOMESTIC REFRIGERATORS	J. U. Ahamed <i>E-mail: jamal@cuet.ac.bd,</i>	18 - 25
NTC-2009-006	MACHINABILITY OF FCD 500 DUCTILE CAST IRON USING COATED CARBIDE TOOL IN DRY MACHINING CONDITION	A.G. Jaharah <i>E-mail: jaharah@eng.ukm.my</i>	26 - 31
NTC-2009-007	EFFECT OF ROTOR DIAMETER ON THE QUALITY OF ROTOR SPUN YARN	Ranajit Kumar Nag <i>E-mail: nag.ranajit@yahoo.com</i>	32 - 35
NTC-2009-009	TRIBO-CHEMICAL DEGRADATION OF PHENOLIC RESIN IN AUTOMOTIVE BRAKE PAD DURING DRY SLIDING AGAINST MMC	K.M. Shorowordi <i>E-mail: kmshorowordi@iat.buet.ac.bd</i>	36 - 44
NTC-2009-010	DRY SLIDING WEAR CHARACTERISTICS OF SUGARCANE BAGASSE POLYMER CEMENT COMPOSITES	M.A. Ahmad <i>E-mail: mariyam@vlsi.eng.ukm.my</i>	45 - 51
NTC-2009-011	VARIATION IN FATIGUE CRACK GROWTH DUE TO THE GEOMETRICAL AND LOADING EFFECTS	S. M. Beden <i>E-mail: sabah@eng.ukm.my</i>	52 - 57
NTC-2009-012	THE ASSESSMENT OF RHEOLOGICAL MODEL RELIABILITY IN LUBRICATING BEHAVIOUR OF VEGETABLE OILS	Sunny Goh Eng Giap <i>E-mail: sunnyg@umt.edu.my</i>	58 - 65
NTC-2009-013	EFFECT ON FATIGUE PERFORMANCE OF SURFACE TREATED COMPONENTS: AN INVESTIGATION USING FINITE ELEMENT ANALYSIS	Nawar A. Al-Asady <i>E-mail: Nawar2007@gmail.com</i>	66 - 71
NTC-2009-014	EFFECT OF TEMPERATURE ON THE TRIBOLOGICAL PERFORMANCE OF PALM BIODIESEL	M. A. Fazal <i>E-mail: jewel_mme.buet@yahoo.com</i>	72 - 76
NTC-2009-015	THE EFFECT OF CERIUM ADDITION ON WEAR BEHAVIOUR OF EUTECTIC AND HYPOEUTECTIC Al-Si-Mg ALLOY	A.S.Anasyida <i>E-mail: syida_7853@yahoo.com</i>	77 - 80
NTC-2009-017	TRIBOLOGICAL PROPERTIES OF NANOSTRUCTURED YSZ THERMAL BARRIER COATINGS	R.J. Talib <i>E-mail: talibria@sirim.my</i>	81 - 86
NTC-2009-019	WEAR AND FRICTION CHARACTERISTICS OF WASTE VEGETABLE OIL CONTAMINATED LUBRICANTS	M. A. Kalam <i>E-mail: kalam@um.edu.my</i>	87 - 93
NTC-2009-020	TRENDS TO SUBSTITUTE DIESEL WITH TRIBOLOGICAL PROPERTIES ENHANCED BIODIESEL	M.I. Rafiqul <i>E-mail: rafiqum@yahoo.com</i>	94 - 103
NTC-2009-021	EFFECT OF 12-HYDROXYSTEARIC ACID ON THE TRIBOLOGICAL PROPERTIES OF ENVIRONMENTAL FRIENDLY LUBRICANTS	M. Farooq <i>E-mail: farooq_tribo@yahoo.com</i>	104-108
NTC-2009-022	ADHESION AND WEAR BEHAVIOR OF NANOSTRUCTURED TITANIUM OXIDE THIN FILMS	M.M. Hasan <i>E-mail: mmhasan92@yahoo.com</i>	109-115
NTC-2009-024	IONIC TRANSPORT STUDY OF POLYMETHYLMETHACRYLATE BASED SALICYLIC ACID DOPED PROTON CONDUCTING GEL POLYMER ELECTROLYTES	M.I.N. Isa <i>E-mail: ikmar_isa@umt.edu.my</i>	116-118
NTC-2009-025	NEURO-FUZZY GENETIC ALGORITHM	M. Jalali V. <i>E-mail: jalali@inspem.upm.edu.my</i>	119-124

<b>Paper No.</b>	<b>Title of Paper</b>	<b>Corresponding Authors &amp; E-mail</b>	<b>Page</b>
NTC-2009-026	PARASITIC ENERGY SAVINGS IN ENGINES USING NANOLUBRICANTS	R. Saidur <i>E-mail: saidur@um.edu.my</i>	125-133
NTC-2009-027	DESIGNING MATERIALS AGAINST WEAR FOR ORTHOPEDIC BIOENGINEERING SYSTEMS	Zainul Huda <i>E-mail: drzainulhuda@hotmail.com</i>	134-138
NTC-2009-028	WEAR STUDY OF COATED/ UNCOATED HIGH SPEED STEEL ON NI-RESIST CAST IRON USING THE COMBINATION OF IONIC LIQUID AND VEGETABLE OIL-BASED LUBRICANT	M. Husnawan <i>E-mail: m.husnawan@gmail.com</i>	139-143
NTC-2009-029	INVESTIGATION OF THE SWIRL EFFECT ON CAMPRO 1.6L ENGINE USING GT-SUITE	A.K.M. Mohiuddin <i>E-mail: mohiuddin@iiu.edu.my</i>	144-148
NTC-2009-030	MACHINE CONDITION MONITORING TECHNIQUE IS USED TO DETECT THE FAILURE OF ROLLING ELEMENT BEARING FOR ISMECA MACHINES IN PRODUCTION LINE	Andy S.W. Tan <i>E-mail: tansongwee_20052000@yahoo.com</i>	149-156
NTC-2009-031	TRIBOLOGY IN BIOLOGY: BIOMIMETIC STUDIES ACROSS DIMENSIONS AND ACROSS FIELDS	I.C. Gebeshuber <i>E-mail: ille.gebeshuber@ukm.my</i>	157-164

# THE EFFECT OF NATURAL FREQUENCY OF THE PIN ON DISC SET-UP ON THE FRICTION COEFFICIENT OF MILD STEEL

Mohammad Asaduzzaman Chowdhury<sup>1</sup>, Md. Liakat Ali<sup>2\*</sup>, Syed Md. Ihsanul Karim<sup>3</sup>

<sup>1</sup>Department of Mechanical Engineering, Dhaka University of Engineering and Technology  
Gazipur 1700, Bangladesh

<sup>2</sup>Faculty of Mechanical Engineering, Universiti Teknologi Malaysia, Malaysia

<sup>3</sup>Bangladesh Industrial Technical Assistance Centre (BITAC)  
Ministry of Industries, Tejgoan, Dhaka, Bangladesh

\*Corresponding Author: email: [tusharadd@gmail.com](mailto:tusharadd@gmail.com); Tel: +60167280016

## Abstract

The present paper investigates experimentally the effect of natural frequency of the pin on disc setup on friction property of mild steel. To do so, a pin-on-disc apparatus having facility of vibrating the test samples at different directions, amplitudes and frequencies was designed and fabricated. The natural frequency of the set-up was varied by adding dead loads of the setup from 0 kg to 50 kg. At each added load the friction coefficient has been measured. Results show that both the natural frequency and friction coefficient decrease with the increase of added loads. It has been also observed that the coefficient of friction increases with the increase of natural frequency of the experimental setup. The experimental results are also compared with those available in literature and simple physical explanations are provided.

**Keywords:** Friction coefficient, Natural frequency, Dead load, Mild steel

## 1. Introduction

The coefficient of friction of a material is dependent upon the interface or mating material, surface preparation and operating conditions [1-7]. It is also known that vibration and friction are dependent on each other. Friction generates vibration in various forms, while vibration affects friction in turns [8-18]. The vibration and the natural frequency of a machine have severe effect on its life time and performance. These two factors cause noise in industries. To control noise it is important to determine the natural frequency of the machine. The dynamic body, which is subjected to friction force inherently, changes its static friction property. The general conclusion drawn by W. W. Tworzydło and E. Becker, 1990 [19] is that the ratio of reduction of friction depends very strongly on the characteristics of each experimental set-up, so that these experimental observations could not yield any general law which would estimate the reduction of friction under a wide variety of conditions. Asad and Helali [20-22] observed the reduction of the friction coefficient as a

function of different amplitude and frequency of vibration. However, the frictional behavior of mild steel under natural frequency of the experimental set-up is yet to be investigated.

Therefore, in this study an attempt is made to investigate the frictional behavior of mild steel under natural frequency of the pin on disc set-up. It is expected that the applications of these results will contribute to the improvement of different concerned mechanical systems. In this study vibration is generated artificially in such a way that direction, amplitude and frequency of vibration can be controlled.

## 2. Experimental Details

Fig.1 shows a pin-on-disc machine which contains a pin that can slide on a rotating horizontal surface (disc). A circular mild steel test sample (disc) is to be fixed on a rotating plate (table) having a long vertical shaft welded from the bottom surface of the rotating plate. The shaft passes through three close-fit bush-bearings which are rigidly fixed with three-square plates such that the shaft can move only

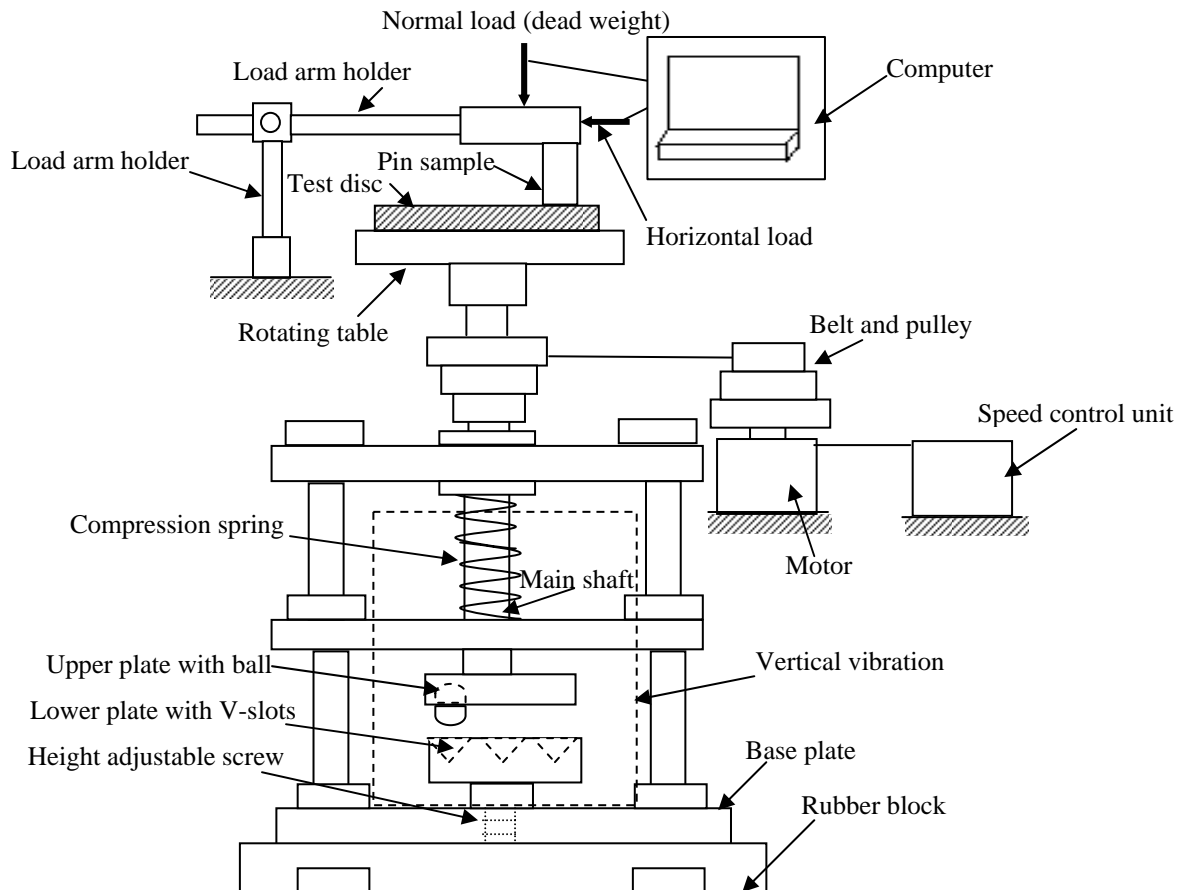


**Fig.1. Block diagram of the experimental setup**

axially and any movement of the rotating shaft is restrained by the bush.

To provide the rigidity to the main structure of this set-up all these three supporting square plates along with a base plate are rigidly fixed with four vertical square bars. The base plate was bolted with the foundation. A 50mm thick neoprene rubber bearing pad was used between the base plate and the foundation. Foundation bolts were passed through this bearing pad to fix base plate with this concrete foundation. Between the top two supporting square plates a compound V-pulley was fixed with the shaft to transmit rotation to the shaft from a motor. A compression spring between the second and the third supporting plates is fitted with the shaft such that any vertical movement of the shaft can be controlled. There are two circular plates near the bottom end of the shaft, one is fixed with the shaft end and another is fixed with the base plate through a height adjusting screw. The circular plate fitted with the shaft has a spherical ball on its lower surface. There are a number of slots on the top surface of the other circular plate. At the time of the rotation of the shaft, the ball of the

upper circular plate will slide on the slotted surface of the lower circular plate and the shaft along with the rotating plate will vibrate due to the spring action. The direction of vibration is vertical i.e perpendicular to the sliding direction of the pin. Due to the cantilever action of the holding arm the pin with the holder has rocking mode of vibration. Considering the small area of contact of the pin and diameter of the rotating disc the sliding velocity can be taken as linear though the sliding surface. Frequency of vibration can be varied (i) by changing the shaft rotation and (ii) the number of slots of the lower circular vibration generating plate. Sliding velocity can be varied by two ways (i) by changing the rotation of the shaft when frequency also changes and (ii) by changing the radius of the point of contact of the sliding pin when frequency does not change. But it can be noted that the change of curvature may affect resisting force measurement. The amplitude of the vibration can be varied by adjusting the height of the slotted plate.

A half-horsepower motor is mounted vertically to rotate the shaft with the table on a

separate base having rubber damper. This separate base was used to reduce the effect of vibration of the motor, which may transmit to the main structure. The speed of the motor is varied as required by using an electronic speed control unit.

Contacting foot of a 6mm diameter cylindrical pin is flat made of mild steel whose carbon content is 0.19-0.20%, fitted on a holder is subsequently fitted with an arm. The arm is pivoted with a separate base in such a way that the arm with the pin holder can rotate vertically and horizontally about the pivot point with very low friction. Pin holder is designed including the facility of putting dead weight on it so that required normal force will act on the test sample through the pin. To avoid the loss of surface material of the pin the contacting surface will remain almost constant and for this the shapes of pin were maintained cylindrical. The natural frequencies of the setup are varied by adding the dead loads of 0 to 50 kg at the upper base plate of the setup. A load cell (TML, Tokyo Sokki Kenkyujo Co. Ltd, CLS-100NA, Serial no. MR2947) was used to measure the vertical force acting on the pin. A data acquisition system was used to measure the force continuously when the system is on and these data are sent directly to the computer. Vibration was measured by using a digital vibration meter (METRIX Instrument Co., Miniature Vibration Meter, Model no. 5500B.). The load cell along with its digital indicator (TML, Tokyo Sokki Kenkyujo Co. Ltd, Model no. TD-93A), calibrated against a standard proving ring was used for measuring loads. Losses of frictional forces at pivot points of the pin holder were determined and incorporated in the results. The total set-up was placed inside a chamber whose relative humidity can be adjusted by supplying requisite amount of moisture. A hygrometer (Wet and Dry Bulb Hygrometer, ZEAL, England) was used to measure the relative humidity of the chamber. A tachometer was used to measure the rpm of the rotating shaft. The surface roughnesses of the test sample were also measured by surface roughness tester (Taylor Hobson Precision Roughness Checker). The average roughnesses of the mild steel before test were maintained 0.20(±5%)  $\mu\text{m}$  (RMS). All experiments were conducted at about 50% relative humidity. During tests each experiment was repeated several times with fresh sample of pin and disc.

### 3. Results and Discussion

Fig. 2 and 3 show the variation of amplitude of vibration with the variation of frequency of vibration. From these figures, it is shown that the natural frequencies of the experimental setup are 60 and 32 Hz for 0 (without added load) and 50 kg dead loads respectively. The method of measurement of the natural frequency of the setup is taken from the book of "Mechanical Measurements" [23]. Variation of natural frequencies with added dead loads of 0, 13.6, 20, 36.1 and 50 kg are presented in Fig. 4. The curve shown in Fig.4 shows that the natural frequency of vibration decreases with the increase of added load. The decrease of natural frequency of vibration with the increase of added load can be explained by the equation:

$$\omega^2 = \frac{k}{m} \quad (1)$$

(where  $\omega$ = natural frequency, k= stiffness of the system and m= mass of the system).

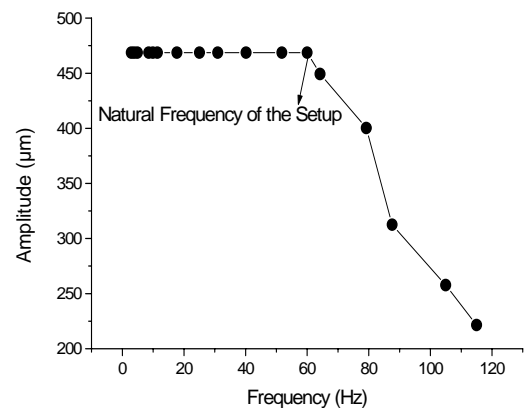


Fig.2: Amplitude vs. frequency curve of the test setup for without added dead load

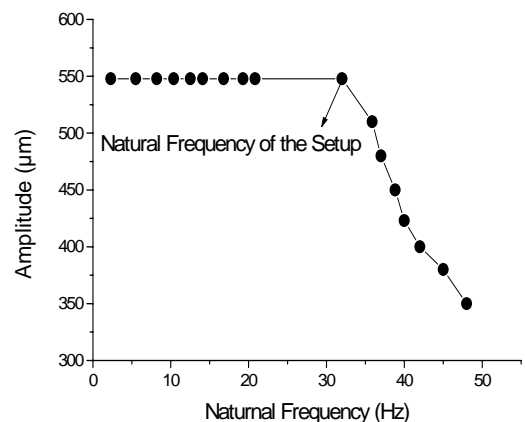
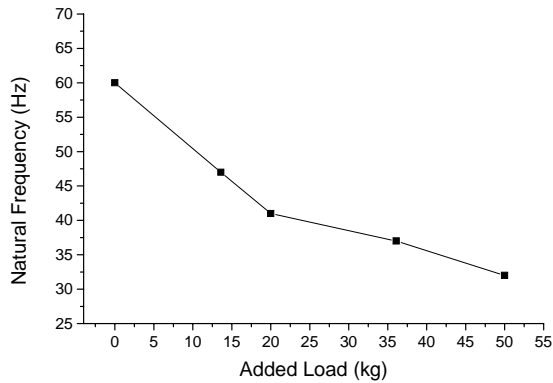


Fig.3: Amplitude vs. frequency curve of the setup for 50 kg added dead load

From equation (1) it is clear that the natural frequency only depends on the stiffness and the mass of the system. Therefore by keeping the stiffness constant if the mass of the system is increased the natural frequency of the system will be decreased.



**Fig.4: Variation of natural frequency with the variation of added dead loads**

Fig. 5 shows the variation of friction coefficient with the duration of rubbing at different natural frequency of vibration for mild steel. Curve 1 of Fig. 5 shows the variation of friction coefficient of mild steel with duration of rubbing at 60 Hz natural frequency of vibration. During the starting, value of friction coefficient is 0.41 which remains constant for few seconds then increases almost linearly up to 0.44 over a

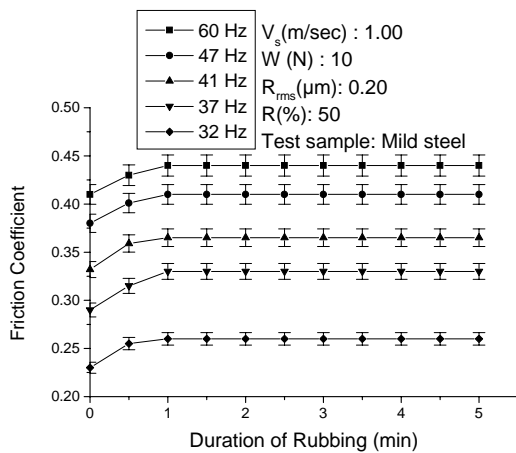


**Fig.5: Variation of friction coefficient with the variation of natural frequency of the experimental setup**

duration of 60 seconds of rubbing and after that it remains constant for the rest of the experimental time. Other curves of this figure show the values of friction coefficient at 47, 41, 37 and 32 Hz natural frequency of vibration. All these curves show similar trend as that of curve-

1 Other parameters such as sliding velocity (1m/sec), normal load (10 N), surface roughness (0.20  $\mu\text{m}$ ) and relative humidity (50%) are identical for these five curves. These findings are in agreement with the findings of Chowdhury for different amplitude of vibration [22]. The friction at the time of starting is low and remains at its initial value for some time and the factors responsible for this low friction are due to the presence of a layer of foreign material. This surface in general comprises of (i) moisture, (ii) oxide of metals, (iii) deposited lubricating material, etc. Mild steel readily oxidizes in air, so that, at initial duration of rubbing, the oxide film easily separates the two material surfaces and there is little or no true metallic contact and also the oxide film has a low shear strength. During initial rubbing, the film (deposited layer) breaks up and clean surfaces come in contact which increase the bonding force between the contacting surfaces. At the same time due to the inclusion of trapped wear particles and roughening the substrate, the friction force increases due to the increase of ploughing effect. Increase of surface temperature, viscous damping of the friction surface, increased adhesion due to microwelding or deformation or hardening of the material might have some role on this increment of friction coefficient as well. After a certain duration of rubbing, the increase of roughness and other parameters may reach to a certain steady state value and hence the values of friction co-efficient remain constant for the rest of the time. In the curves of Fig. 5, it is also seen that the values of friction co-efficient increases with the increase of natural frequency of vibration. These results are presented in Fig. 6.

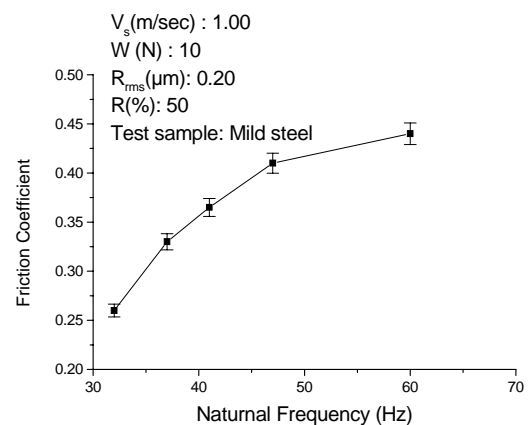


**Fig.6: The variation of friction coefficient with the variation of natural frequency of the experimental setup for mild steel**

If a body (either static or dynamic) is in contact with another moving (either rotation or translation) body, where the second body is vibrating, the contact of those two bodies takes place at some particular points of the second body instead of continuous contact. When the natural frequency of vibration of second body is more, for a constant length of contact, the contact points as well as the area of contact between two bodies will be more (Fig. 7(b)) compared to the situation when the natural frequency of second body is less (Fig. 7(a)). As the area of contact or the points of contact between two bodies are more, they experience more frictional resistance for a constant length of contact. Hence, the friction factor between the two bodies will increase with increased natural frequency.

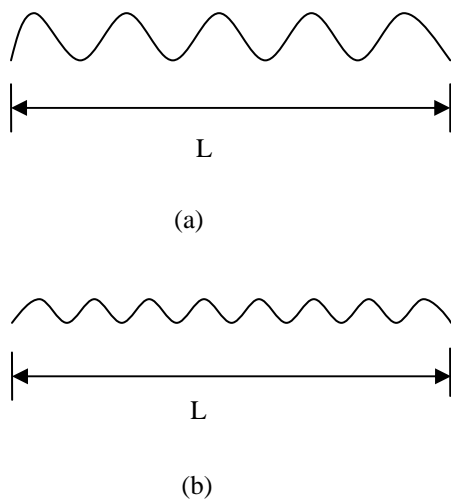


**Fig.7: (a) The points of contact of a body with low natural frequency, (b) The points of contact of a body with high natural frequency for constant length of contact (L).**

#### 4. Conclusions

The presence of natural frequency of vibration indeed affects the friction force considerably. The natural frequency of vibration decreases with the increase of added dead loads to the experimental setup. The values of friction coefficient increase with the increase of natural frequency of vibration of the experimental setup. As the friction coefficient increases with increasing natural frequency of vibration, therefore maintaining appropriate level of natural frequency vibration friction may be kept to some lower value to improve mechanical processes.

#### References

- [1] Archard, J. F., *Wear Theory and Mechanisms*, *Wear Control Handbook*, M. B. Peterson and W.O. Winer, eds., ASME, New York, 1980, NY, pp. 35-80.
- [2] Tabor, D., Friction and Wear—Developments Over the Last 50 Years, Keynote Address, *Proc. International Conf. Tribology—Friction, Lubrication and Wear*, 50 Years On, London, Inst. Mech. Eng., 1987, pp. 157-172.
- [3] Berger, E. J., Krousgrill, C. M., and Sadeghi, F., Stability of Sliding in a System Excited by a Rough Moving Surface, *ASME Journal of Tribology*, October 1997, Vol. 119, pp. 672- 680.
- [4] Bhushan, B., *Principle and Applications of Tribology*, John Wiley & Sons, Inc., New York, 1999, pp. 344-430, Chap. 6.
- [5] Blau, P. J., *Friction Science and Technology*, Marcel Dekker, New York, 1996.
- [6] Bhushan, B., and Gupta, B.K., *Handbook of Tribology-Materials, Coatings, and Surface Treatments*, McGraw-Hill, New York, 1991, Reprinted with corrections, Krieger, Malabar, FL, 1997.
- [7] Blau, P.J., *Scale Effects of Sliding Friction: An Experimental Study*, in *Fundamentals of Friction: Macroscopic and Microscopic Processes* (Singer, I.L., and Pollock, H.M., eds), 1992, vol. E220, pp. 523-534, Kluwer Academic, Dordrecht, Netherlands.
- [8] Lehtovaara, A., Influence of Vibration on the Kinetic Friction between Plastics and Ice, *Wear*, Vol. 115, 1987, pp. 131-138.
- [9] Wertheim, O., and Bucher, I., *On the Influence of Controlled Vibration on Friction*, Research Supported by the ISARELI Academy for Science, 2000, (Grant. No. 030072).
- [10] Lenkiewicz, W., The Sliding Process—Effect of External Vibrations, *Wear*, Vol. 13, 1969, pp. 99-108.
- [11] Aronov, V., D'souza, A. F., Kalpakjian, S., and Shareef, I., Interactions among Friction, Wear, and System Stiffness-Part 1: Effect of Normal Load and System Stiffness, *ASME Journal of Tribology*, Vol. 106, 1984, pp. 54-58.
- [12] Aronov, V., D'souza, A. F., Kalpakjian, S., and Shareef, I., Interactions among Friction, Wear and System Stiffness-Part

- 2: Vibrations Induced by Dry Friction, *ASME Journal of Tribology*, Vol. 106, 1984, pp. 59-64.
- [13] Aronov, V., D'souza, A. F., Kalpakjian, S., and Shareef I., Interactions among Friction, Wear and System Stiffness-Part 3: Wear Model, *ASME Journal of Tribology*, Vol. 106, 1984, pp. 65-69.
- [14] Hess, D. H., and Soom, A., Normal Vibrations and Friction under Harmonic Loads: Part I -Hertzian Contacts, *Journal of Tribology*, Vol. 113, 1991, pp. 80-86.
- [15] Bryant, M. D., and LIN, J. W., Photoelastic Visualization of Contact Phenomena Between Real Tribological Surfaces, With and Without Sliding, *Journal of Wear*, Vol. 170, 1993, pp. 267-279.
- [16] Lin, J. W., and Bryant, M. D., Reductions in Wear Rate of Carbon Samples Sliding Against Wavy Copper Surfaces, *ASME Journal of Tribology*, Vol. 118, 1996, pp. 116-124.
- [17] Budanov, B. V., Kudinov, V. A., and Tolstoi, D. M., Interaction of Friction and Vibration, *Wear*, Vol. 1, 1980, pp. 79-89.
- [18] Skare, T., and Stahl, J., Static and Dynamic Friction Processes Under the Influence of External Vibrations, *Wear*, Vol. 154, 1992, pp. 177-192.
- [19] Tworzydło, W. W., and Becker, E., Influence of forced vibrations on the static coefficient of friction-Numerical Modeling, *Wear*, Vol. 143, 1990, pp. 175-196.
- [20] Chowdhury, M. A., and Helali, M. M., The Effect of Frequency of Vibration and Humidity on the Wear rate, *Wear*, Vol. 262, January 2007, pp. 198-203.
- [21] Chowdhury, M. A., and Helali, M. M., The Effect of Frequency of Vibration and Humidity on the Coefficient of Friction, *Tribology International*, Vol. 39, September 2006, pp. 958-962.
- [22] Chowdhury, M. A., and Helali, M. M., The Effect of Amplitude of Vibration on the Coefficient of Friction, *Tribology International*, Vol. 41, 2008, pp. 307-314.
- [23] Thomas, G., Beckwith, Roy D., Marangoni, John H., Lienhard V., *Mechanical Measurements*, Published by Pearson Education (Singapore) Pte. Ltd., 2001, Fifth Edition, pp. 752-754.

## THE EVALUATION OF FRICTION EFFECT OF RBD PALM STEARIN AS COLD METAL FORMING LUBRICANT

S. Syahrullail, B.M. Zubil, C.S.N. Azwadi, M.J.M. Ridzuan

Faculty of Mechanical Engineering, Universiti Teknologi Malaysia,  
81310 UTM Skudai, Johor, Malaysia

Corresponding Author: email: syahruls@fkm.utm.my

Tel: +607-553-4661, Fax: +607-556-6159

### Abstract

*In this paper, the effect of the frictional constraint from the application of RBD palm stearin as lubricant were investigated by cold work forward plane strain extrusion experiments and viscoplasticity analyses. The experiment used an extrusion apparatus which has taper die and a symmetrical workpiece. The workpiece material is pure aluminum A1100. The extrusion ratio is 2. The results from RBD palm stearin were compared with additive free paraffinic mineral oil. The experimental result shows that the RBD palm stearin could reduce the friction between tool and workpiece by reducing the extrusion load. For RBD palm stearin, thin lubricant layer occur between the taper die and billet surface and produced the low surface roughness surface. There are no obvious different in velocity along on the taper die surface. It is confirmed that RBD palm stearin showed satisfactory lubrication performance, as compared to additive free paraffinic mineral oil.*

**Keywords:** *Extrusion, RBD palm stearin, Velocity*

### 1. Introduction

Ecological aspects are gaining importance in our society. Bearing in mind that our environment is being increasingly contaminated with all kinds of pollutants, any reductions welcome. From an environment point of view and compared to a number of other chemical products, lubricants are not particularly problematic. A large proportion of the lubricants pollute the environment either during or after use [1] stated that of 5 to 10 million tons of petroleum based oleochemicals entering the biosphere every year, about 40% comes from spills, industrial and municipal waste, urban runoff, refinery processes, and condensation from marine engine exhaust. These oleochemical pollutants are derived from food industry, petroleum products, and by products such as lubricating, hydraulic and cutting oils.

The terminology used in connection with environmental compatibility can be split into two criteria, i.e. subjective and objective. The non-measurable or subjective criteria are

environmentally friendly and environmentally compatible. The objective criteria among others include the biodegradability, water solubility, ecological toxicity, efficiency improvements etc. Normally biodegradability of at least 60 percent according to OECD 301 (Organization for Economic Cooperation and Development for European Union) is considered as main objective criteria for bio-lubricants. One of the possible lubricants that can satisfied this need is the vegetable oil, which can offer significant environmental advantages with respect to resources renewability, biodegradability and adequate performance in a variety of application [1].

Natural fatty acid oils such as castor oil, palm oil, rapeseed oil, soybean oil, sunflower oil and tallow oil have been used in lubricant for years. They are so-called triglycerides of more or less unsaturated fatty esters. This type of base is biodegradable and compared to mineral oils, will show excellent tribological qualities such as low friction coefficient and good wear protection. Their range of use is limited by

lower stability against thermal oxidative and hydrolytic stress and partly inferior cold flow properties. These limits can be improved gradually with the addition of an additive.

In Malaysia, palm oil has possibility to be used as industrial lubricating oil. Palm oil is vegetable oil which is biodegradability, and also has high produce rate which could fulfills the demand of vegetable base lubricating oil in the future. One hectare of palm tree could produce almost 10 times more oil compared with other vegetable oils [2].

In this research, the effect of frictional constraint of RBD palm stearin as cold work forward plane strain extrusion process was investigated. The evaluations were focusing on extrusion load, surface roughness and metal flow condition at sliding area. RBD palm stearin could reduce the frictional constraint between tool and billet. The extrusion load for RBD palm stearin is the lowest compared to additive free paraffinic mineral oil VG95 and VG460. Billet surface roughness.

## 2. Experimental Procedure

### 2.1. Experimental apparatus

Fig. 1(a) shows the schematic sketch of plane strain extrusion apparatus used in the experiments. The main components are container wall and taper die, and workpiece (billet). The taper die has 45-degree die half angle. The taper die is made from tool steel SKD11 and necessary heat treatment were done before the experiments. The experimental surface of taper dies (surface which contact the billet) were polished with abrasive paper and have surface roughness  $R_a$  less than  $0.5 \mu\text{m}$ . The lubricant with specified amount was applied on this surface before the experiments. The other surfaces of experimental apparatus were applied with same type of test lubricant.

Fig. 1(b) shows the schematic sketch of billets used in the experiments. The material of billet is pure aluminum A1100. The billets' shape was made by the NC wire cut electric discharge machining device. Two similar billets were stacked and used as one unit of billet. One side of the contact surface of the combined billets was the observation plane of plastic flow in plane strain extrusion. The observation plane is not affected with the frictional constraint by the parallel side walls. A square grid pattern measuring the material flow in extrusion process

was scribed by NC milling machine on the observation plane of billet. The lines were V-shaped grooves with 0.5 mm deep, 0.2 mm wide and 1.0 mm interval length. The billets were annealed before the experiments.

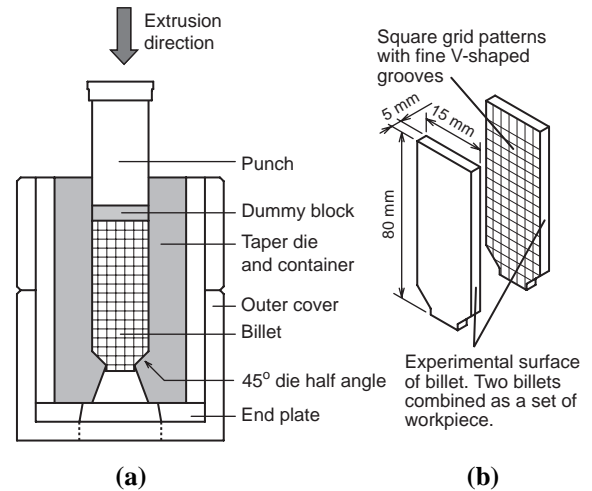


**Fig. 1. (a) The schematic sketch of the plane strain extrusion apparatus and (b) combination of billets**

### 2.2. Testing lubricants

The testing lubricant is RBD palm stearin. RBD is an abbreviation for Refined, Bleached and Deodorized. Palm stearin is the solid fraction obtained by fractionation of palm oil after crystallization at controlled temperature. In this experiments, a standard grade of palm stearin which incorporated in Malaysian Standard MS 815:1991 was used [3]. The results obtained from the experiments used RBD palm stearin were compared with additive free paraffinic mineral oil VG460 (written as paraffin VG460) and VG95 (written as paraffin VG95).

### 2.3. Experimental procedure

The plane strain extrusion apparatus was assemble and placed on the press machine. The forming load and displacement data were recorded by computer. The experiments were carried out at room temperature. Extrusion was stopped at piston stroke of 35 mm. The ram speed is constant to 0.85 mm/s. After the experiment, the partially extruded billets were taken out from the plane strain extrusion apparatus and the combined billets were separated for the surface roughness measurement and metal flow analysis.

### 3. Results and Discussion

#### 3.1. Extrusion load

The extrusion load – piston stroke curves are shown in Fig. 2. The figure shows that the extrusion load in the process reached the steady state condition at the piston stroke 15 mm. From the figure, extrusion load for billet extruded with RBD palm stearin as lubricant is the lowest compared to those using additive free paraffinic mineral oil VG95 and VG460. The extrusion load for paraffin VG95, paraffin VG460 and RBD palm stearin at steady state condition are 65.2 kN, 70.6 kN and 77.1 kN respectively. The condition between the billet and taper die constituted mixed lubrication condition by a thin lubricant layer and adsorption of fatty acids from the palm oil played role of maintaining the lubricant layer [4] and give low extrusion load compared to paraffinic mineral oil. Low friction coefficient of palm oil also influenced this result [5].

#### 3.2. Surface roughness

The distributions of arithmetic mean surface roughness Ra along on the experimental surface of billet (sliding plane) were measured. The experimental surface of billet is surface of billet which contacts the taper die and container. The measure direction is perpendicular to the extrusion direction. The distribution of arithmetic mean surface roughness Ra is shown in Fig. 3. From the figure, the surface roughness Ra for product area of billet which extruded with RBD palm stearin is smaller compare to those extruded with paraffinic mineral oil VG95 and VG460.

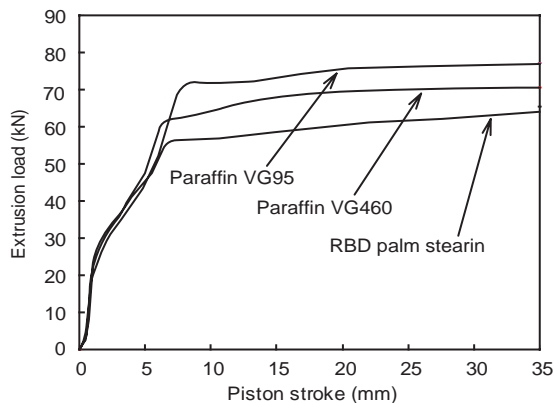


Fig. 2. Extrusion load – piston stroke curves

At taper die are (sliding plane 2 mm - 6 mm), paraffinic mineral oil VG460 shows the lowest value of surface roughness Ra.

The CCD pictures of billet experimental surface at product area (at sliding plane 6 mm) for all experimental condition are shown in Fig. 4. No severe wear were found.

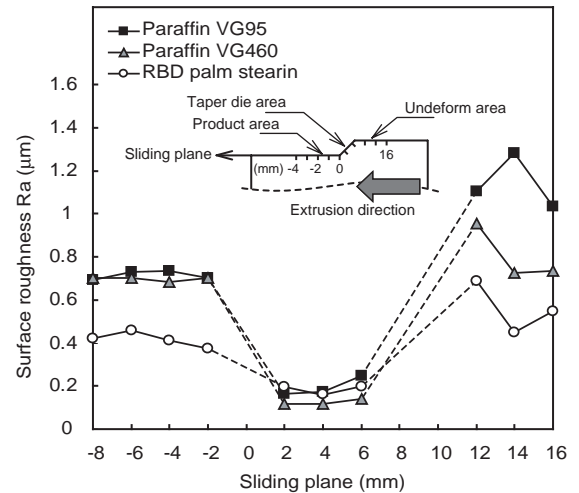


Fig. 3. Surface roughness Ra distribution along on the experimental surface of billet

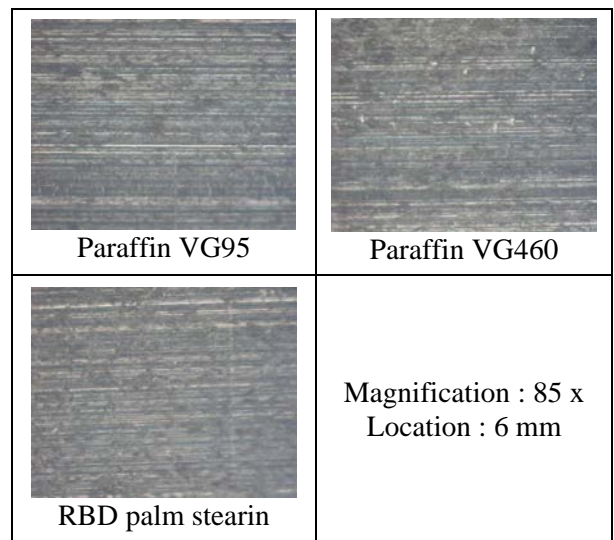


Fig. 4. CCD pictures of experimental surface of billet at product area

#### 3.3. Plasticity flow

The distribution of V-component velocity along on the experimental surface of billet is shown in Fig. 5. All the experimental condition show almost similar pattern of V-component velocity. Billet extruded with paraffinic mineral oil VG460 shows the highest V-component velocity is taper die sliding plane.

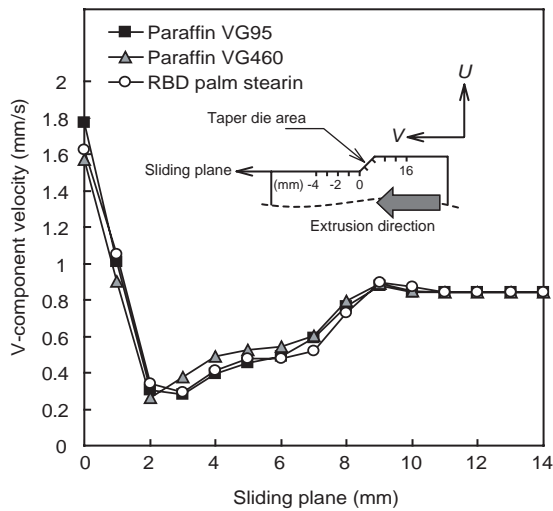


Fig. 5. V-component velocity distribution along on the experimental surface of billet

#### 4. Conclusions

The following conclusions can be deduced from the present research:

1. RBD palm stearin could be applied as cold work forward plane strain extrusion and could reduce the forming load compared to additive free paraffinic mineral oil VG95 and VG460.
2. RBD palm stearin could produce lower surface roughness of billet compared to those extruded with paraffinic mineral oil VG95 and VG460.

3. All the experimental conditions show the similarity on the V-component velocity.

#### Acknowledgements

The author would like to thank Faculty of Mechanical Engineering, Universiti Teknologi Malaysia and IRGS research grant No. RJ012402 for their cooperation on this research.

#### References

- [1] Gawrilow, Palm Oil Usage in Lubricants, *Proceeding of the 3<sup>rd</sup> Global Oils and Fats Business Forum*, United State of Amerika, 2003
- [2] K.K. Ming and D. Chandramohan, Malaysia Palm Oil Industry at Crossroad and its Future Direction, *Oil Palm Industry Economic Journal*, Vol. 2, 2, pp. 10-15, 2002
- [3] *Pocketbook of Palm Oil Uses*, Malaysia Palm Oil Board, Malaysia, U.K., 1980
- [4] F.P. Bowden and D. Tabor, *The Friction and Lubrication of Solids*, Oxford University Press, U.K., 1986
- [5] B.L. Abdulquadir and M.B. Adeyemi, Evaluations of Vegetable Oil-based as Lubricants for Metal-forming Process, *Industrial Lubrication and Tribology, Emerald*, Vol. 65, 5, pp. 242-248, 2008

# MACHINING AND CUTTING SIMULATION: EFFECT OF RAKE ANGLE AND CLEARANCE ANGLE ON WEAR CUTTING INSERT CARBIDE

<sup>1</sup>Hendri. Y., <sup>2</sup>Jaharah A.G., <sup>3</sup>Che Hassan C.H.

Department of Mechanical and Materials Engineering,  
Faculty of Engineering and Built Environment,  
Universiti Kebangsaan Malaysia,  
43600 Bangi, Selangor,  
Malaysia

<sup>1</sup>hyanda@eng.ukm.my, <sup>2</sup>jaharah@eng.ukm.my, <sup>3</sup>chase@eng.ukm.my

## Abstract

High production rates at minimum cost will also be achieved by selecting correct cutting tool geometry for a particular combination of work material and cutting tool. Problem facing in precision turning is how to minimize tool wear in order to obtain good accuracy of geometrical part and surface finish. In this study the effect of changing the insert carbide geometries of rake angle to the wear level was investigated. The tungsten carbide insert type of DNMA 432 was used as cutting tool. FCD 500, a ductile cast iron, was chosen as work material. The seven series of simulations using Deform-3D were carried out using various tool geometries, whilst the cutting speed, feed rate and depth of cut were kept constant at 200 m/s, feed 0.35 mm/rev, and 0.3 mm respectively. Some combination of carbide insert geometries were set up to produce -15, -10, -5 deg (negative rake angle), 0 and +5, +10, +15 deg (positive rake angle) using pre processor of Deform-3D. Changing rake (followed by change of clearance angle) resulted in changes in the cutting forces, therefore causes the change of the wear depth in the tool edge of carbide insert. The simulation results were agreeable with theory, where increase in rake angle, caused conversely decreasing clearance angle and will be bigger area contact between of clearance face and work piece surface, so this caused increase of tool wear.

**Keywords:** tool wear, wear depth, rake angle, stress force, finite element analysis

## 1. Introduction

To increase the efficiency of cutting, carbide tool insert geometries are continually being improved. Thought their cutting distance to life can only be determined by cutting tests under real operating conditions, model wear test are useful for the preselection of tool geometries [1].

Gunay. M et al [2] wrote that the main cutting force was reduced by increasing rake angle in positive and was increased by increasing rake angle in negative value.

The simulation as one of model test is particularly important because cutting test is very expensive and need more rush time. Testing and simulation of this can be done by using Finite Element Analysis.

The aim of the investigations was presented of finding in a one part of ongoing research results in modeling and simulation FEM of

machining processes. In this study, some model wear tests were applied to investigated how the wear depth happened when geometries, especially rake angle ( $\alpha$ ) of DNMA's insert carbide are changed in case of orthogonal turning cutting machining.

During cutting, the rake and flank faces of the cutting tool slide against the surface of the work piece material (Figure 1). In this study, the rake angle was changed in some combination from -15 to +15 deg. The clearance angle was also change in following the change of rake angle Finite Element Analysis (FEA) technique was the first introduced in 1960s and has been widely used to analyze in designing tools and forming processes. Based on the success of FEM simulations for bulk forming processes, many researchers developed their own FEM codes to analyze metal cutting processes during the early 1980s up to now [3], [4], [5], [6] and [7].

Cerenitti et al [3] assumed a rigid sharp tool and elasto-plastic work piece, and defined a node

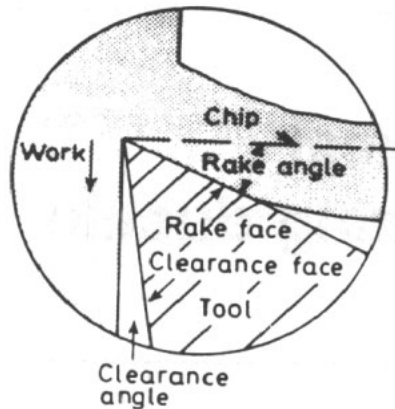


**Fig.1. Terminology of Cutting tool and Workpiece material**

separation criterion based on the geometry of the element approaching the cutting edge. Cerenitti et al. [3] used an early version of a commercial implicit FEM code "DEFORM-2D™". This code uses four-node quadrilateral elements and is based on static Lagrangian formulation. Today, DEFORM-3D™ code is commonly used by researchers and industry in machining simulation [8].

Currently Deform-3D system has Archard's model and Usui's model apart from the user routine support. Especially, Usui's model is used for machining applications to compute insert wear. Archard's model can be used with either isothermal or non-isothermal runs, On the other hand Usui's model can be run only be used with non-isothermal run as it required interface temperature calculations as well [9], [10].

Applications of FEM models for machining can be divided into six groups: 1) tool edge design, 2) tool wear, 3) tool coating, 4) chip flow, 5) burr formation and 6) residual stress and surface integrity. The direct experimental approach to study machining processes is expensive and time consuming. For solving this problem, the finite element methods are most frequently used. Modeling tool wear using FEM has advantages over conventional statistical approach because it requires less experimental effort and it provides useful information such as deformations, stresses, strain and temperature chip and the work piece, as well as the cutting force, tool wear, tool stress and temperature on the tool working under specific cutting parameter [10].

## 2. Methodology

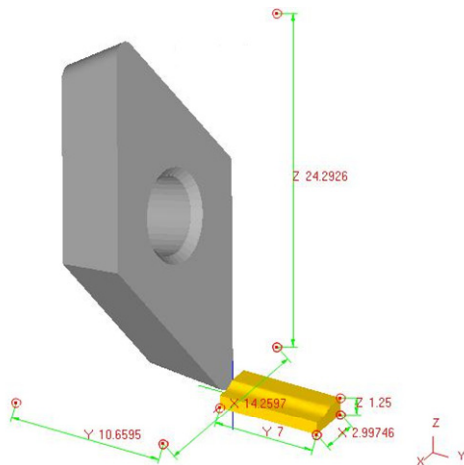
One of the important parameters in the orthogonal metal cutting process is the rake angle between the face of the cutting tool and the plane perpendicular to the cutting direction. The magnitude of tool cutting geometries has significant effects on the performance of the cutting tool and the integrity of the cut surface. The main objective of this research is to apply the finite element method to study the rake angle and clearance angle effects in orthogonal metal cutting of ductile cast iron with continuous chip formation, while the other machining parameters of feed rate and depth of cut were kept constant. Finite element simulation results of the orthogonal metal cutting using seven sets of perfectly sharp cutting tools for DNMA 432 Insert Carbide with rake angles -15, -10, -5, 0 and +5, +10, +15 deg. The commercial software Deform-3D for doing tool wear analysis was used to simulate orthogonal metal cutting process. It is based on an updated Lagrangian formulation and employs an implicit integration scheme.

Figure 2 shows geometry and schematic of orthogonal cutting condition model using DNMA 435 insert carbide and work piece.

The three-dimensional finite element model was generated under a plane strain assumption because the width of cut was larger than the undeformed chip thickness in this orthogonal cutting arrangement. The flow stress behavior of the work material and the contact conditions were used as equation for flow stress  $\sigma$  models,  $\sigma = \sigma_1 \varepsilon^n$  [11]. Physical and thermo-mechanical properties of the work piece and tool materials, and cutting conditions are predefined are shown in Table 1.

The work piece material was FCD 500 (ductile cast iron). This material had been selected as the work piece material in this study because currently, this material was much used in automotive application and had been interesting become the focus of many recent modeling studies. The tool is modeled as a rigid body, so there are no mechanical properties need to be assigned and only thermal properties are needed. The cutting condition to the simulation models and the mechanical properties of carbide cutting tool and work piece are shown in Table 2. The tool was defined to be a rigid body which considers thermal transfer for modeling the cutting temperature field. The model of insert

should be meshed, with appropriate boundary conditions and inter-object relations defined.



**Fig.2. Geometry and schematic of orthogonal cutting condition model**

**Table 1 Input Parameters in the simulation process**

Cutting Speed (m/min)	200 m/min (constant)
Feed Rate	0.35 mm/rev (constant)
Depth of cut	0.3 mm (constant)
Nose Angle (°C)	Kept constant at 55 °C
Rake Angle ( $\alpha$ ), deg	-15 -10 -5 0 +15 +10 +5

**Table 2 Cutting condition to the simulation models and material properties**

Tool Geometry of DNMA 432 (WC as base material, uncoated carbide tool)	
Side Cutting Edge Angle (SCEA)	-3
Back Rake Angle (BR) (deg)	-5
Side Rake Angle (SR) (deg)	-5
Nose Angle (°)	55
Tool properties (uncoated carbide)	
Modulus Young (GPa)	650000
Thermal Expansion	5e-06
Poisson Ratio	0.25
Boundary Condition	
Initial Temperature (°C)	20
Shear friction factor	0,6
Heat transfer coefficient at the interface (N/s mm°C)	45
Work piece geometry	
Depth of cut	0,3
Width of cut (mm)	3,4
Length of workpeace	7
Work piece properties (FCD 500; Poisson's ratio, 0.25)	
Modulus of elasticity (kN/mm <sup>2</sup> )	169
Thermal Conductivity (W/m. °C)	35.2
Thermal expansion Coeff. (10 <sup>-6</sup> °C <sup>-1</sup> )	12.5
Heat capacity (N/mm2 ° C)	3.7
Emissivity	0.95

Deform software had been used to simulate the effect of change in tool cutting geometries (rake angle) when turning ductile cast iron using DNMA 432 uncoated carbide cutting tool (Figure 3). The simulations were performed by changing the rake angle only while the feet rate and depth of cut were kept constant at 0.35 mm/rev and 0.3 mm respectively as shown in Table 1.

The simulation results are in form of cutting force (N), and wear depth (mm), stress in around work piece contact, temperature on tool edge, chip and work piece.



**Fig.3. Some variation of DNMA Cutting Insert Carbide**

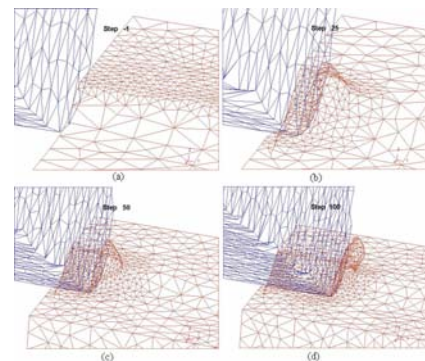


**Fig.4. (a) Initial mesh and tool indentation, (b) Chip formation at step 25, (c) Chip formation at step 50, (d) Developed continues chip at step 100.**

Displacement, shape and surface mesh of tool and work piece at initial mesh in the beginning of the cutting operation until the developed chip formation at step 100 as illustrated in Figure 4.

The work piece and the tool are characterized by non uniform mesh distribution in the simulation. Very small element is required in the contact area between tool and work piece because of very large temperature gradient and stress that will develop in this region during the simulation.

Figure 5 shows an example of simulation result for cutting speed 200 m/min that was found from 200 steps of simulation running.

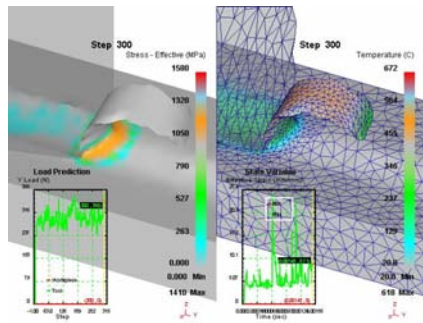


**Fig.5. Example of the simulation result for cutting speed at 200 m/min (300 steps)**

Wear is a constant problem in any process that includes dynamic or static components. Continuous demands for increased productivity and reduced wear cost require constant improvements in design and material properties. Typically, tools with a high hardness are used to prevent wear. But, high hardness (wear resistance) requires a compromise to toughness (impact resistance). For a long time, therefore, steels and cast irons with alloy additives were applied as standard materials. Tungsten carbide (WC), a material known for more than 70 years, opens up new possibilities concerning wear minimization in stone applications through both developments of new materials and targeted analysis of application technology. Tool life varies from customer to customer and from application to application. However, carbide provides tool life that is 10 times longer than steels (Noname, 2001).

### 3. Simulation Results and Discussion

After the simulations were run in seven types of rake angle combinations, the result of wear depth and cutting force read from simulation results were put in Table 3.

**Table 3 Cutting condition to the simulation models and material properties**

No	Rake Angle (deg)	Cutting Force	Wear Depth (mm)	Cutting Force
1	15	203	0.00766	203
2	10	412	0.00633	412
3	5	435	0.00603	435
4	0	451	0.00466	451
5	-5	454	0.00457	454
6	-10	494	0.00449	494
7	-15	522	0.00361	522

#### 3.1. The Effect of Rake Angle Change on Cutting Force.

As can be seen from Figure 6 that the cutting force decreased while the rake angles were increased. Transition from rake angle of -15 to +15 with cutting speed remained constant at 200 m/s, caused decrease of cutting force from 522N to 203N (decreased 61%).

In other meaning, increasing on rake angle on positif section from 0 deg to +15 deg, caused reduce of cutting force from 451N to 203N, and the other hand, increasing of the rake angle on negatif section caused increase the cutting force from 451 N to 522 N.

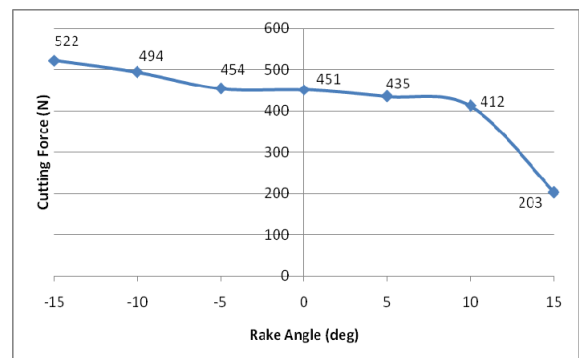


**Fig.6. Effect of increase of rake angle of DNMA to cutting force**

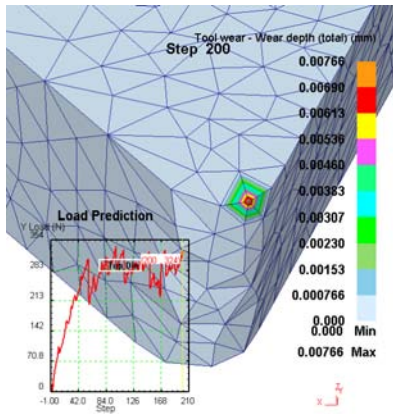
This phenomenon is agreeable with experiment by [2] that the main cutting force was reduced by increasing rake angle in positive and was increased by increasing rake angle in negative value.

#### 3.2. The Effect of Rake Angle Change on Wear Depth.

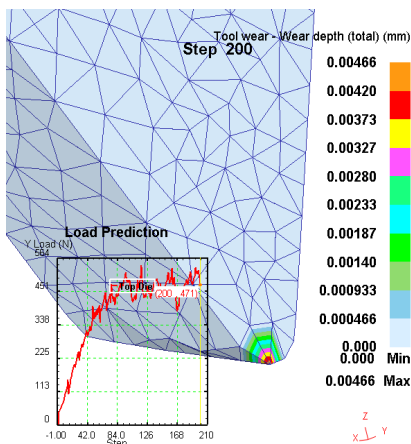
The good result were also get for all of the graph of wear depth where the incrasing of rake angle in negative section will bring the change in cutting force, stress and strain on tool and workpiece, generated temperature on tool and workpiece.

Figure 7 , Figure 8 and Figure 9 show the depth of wear happened after simulation running in 200 steps. Upper step 42 cutting force begin look stabil or just get a bit fluactuation on 283 N. From Figure 7 can be seen that sliding and cutting process during machining process resulted wear depth on nose or cutting edge of carbide insert around 0.00766 mm on depth (+15 of rake angle), then followed by deeper wear were about 0.00307 mm, 0.00230 mm, 0.00153

mm and 0.000766 mm respectively. The same phenomenon occurred for the rake angle 0 and -15, but the maximum wear depth reached for these cases were 0.0046 mm and 0.00361 mm respectively (Figure 8 and Figure 9).



**Fig.7. Wear depth for rake angle +15 maximum wear depth reached 0.00766 mm**



**Fig.8. Wear depth for rake angle 0 maximum wear depth reached 0.00466 mm**

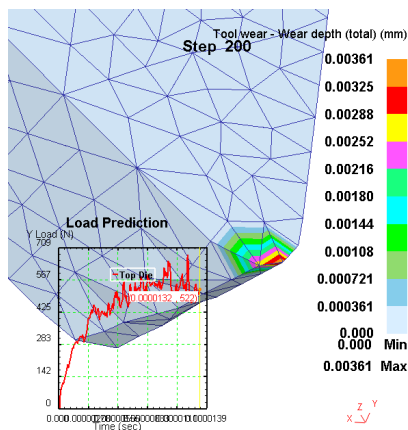


**Fig.9. Wear depth for rake angle -15, the maximum wear depth reached 0.00361 mm**

All of simulation result for every rake angle combination were plotted on graph as can be seen on Figure 8. In this simulation, As the rake angle that was changed, the clearance angle was also changed as the change of rake angle.

As can be seen from Figure 10, the wear depth increased, while the rake angle were increased in positif section and the wear depth decreased while the rake angle were increased in negatif section.

These were agreeable with theory that the when the clearance angle will affect to wear occurred. And, in this study, the simulations were held and just focused for DNMA 430 carbide insert type.

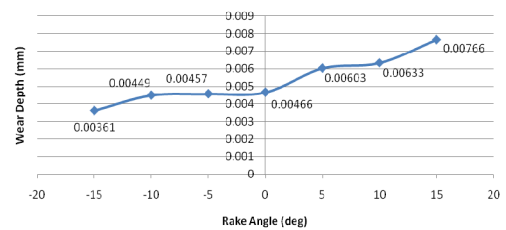


**Fig.10 Effect of increase of rake angle of DNMA to wear depth (decreasing of clearance angle).**

As the rake angle changed, the clearance also changed conversely following as big as rake angle change. When the rake angle was increased in 5 deg, the clearance angle will decreased in 5 deg. For example, the rake angle was increased from +5 to +10 deg, the clearance angle was decreased from from 15 to 10 deg (Figure 11).

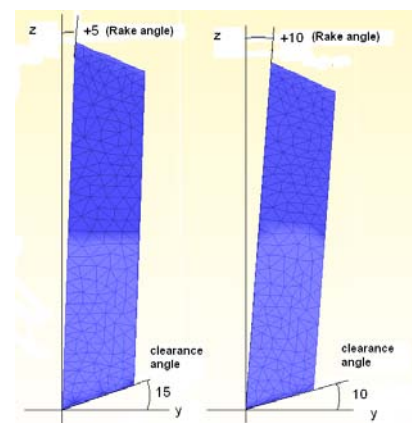


**Fig.11. Change of the rake angle in 5 deg, cause the clearance changed conversely in 5 deg**

Increase of rake angle on positif section means that the clearance angle will be reduced (Figure 11). The reduce of clearance angle means that the area of contact between the clearance face

with material surface increased, so this will bring to increase of wear depth. The wear depth increased by increasing rake angle (reducing clearance angle). This was agreeable with theory that the bigger contact area between clearance face and work piece, so the bigger the wear occurred as denoted by [13].

### 3.3. Analysis of Generated Temperature on Work Piece and Tool.

The generated temperature on chip, material surface and tool edge can be seen on Figure 12.

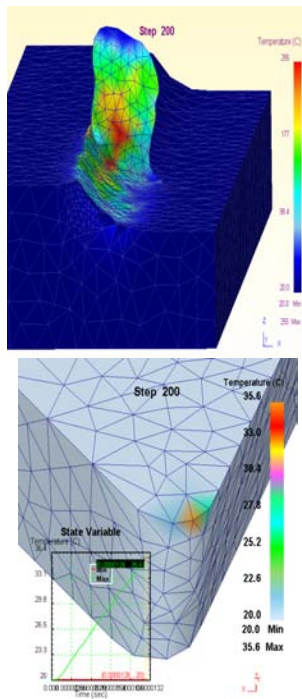


**Fig.12. Generated temperature on chip, work piece and tool edge when set up of rake angle +15**

As can be seen from Figure 13 that the most of heat or generated temperature is carried away by the chip (about 70%), there was maximum of generated temperature on shear zone about 255 °C and only around 35 °C generated on tool (around 10%) and its remain absorbed by work piece.

These are agreeable with the theory denoted by [14] that the maximum heat produced is at shear zone because there is the highest plastic deformation of the metal in this primary shear zone. If it is assumed that all the cutting energy is converted to heat and, so a considerable amount of heat generated at the following three distinct zones are as given Figure 11, those are

1). Shear zone (75%); 2). Chip sliding on the tool face (20%); c). Tool sliding on the

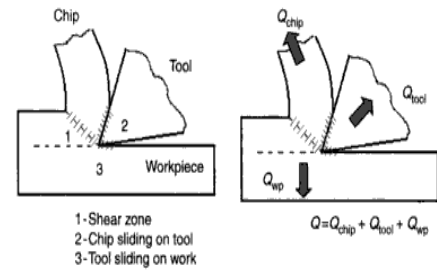


**Fig.13. Heat generated and heat dissipation in metal cutting [14]**

workpiece machined surface (5%) which neglected for perfectly sharp cutting tools.

### 3.4. Analysis of Stress and Shear on chip and Work piece

From Figure 14 can be seen that the highest stress and strain were found on the primary deformation zone, which resulted the stress about 2200 MPa and strain about 4,8 mm/mm.

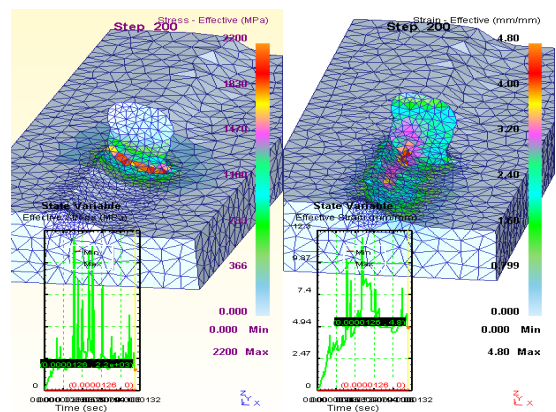


**Fig.14. Stress and strain on chip and material surface when set up of rake angle +15**

This result is agreeable with [15] and [16] where the major deformation during cutting process were concentrated in two region close to the cutting tool edge, and the bigger deformation were occurred in the primary deformation zone, followed by secondary deformation zone, sliding region and sticking region

## 4. Conclusions

The good result were get for all of the graph of wear depth where the increasing of rake angle in

positip section will cause decrease of cutting force, and increase the rake angle in negatif section cause increase of cutting force. Stress and strain on tool and workpiece occurred in primary shear zone because highest defoemation found, the maximum generated temperature was found shear zone then get away by chip, and its remain was in tool and worpiece. The increase of rake angle (the reduce of clearance angle) means that the area of contact between the clearance face with material surface increase, so this will bring to increase of wear depth.

### Acknowledgements

The authors would like to Government of Malaysia and Universiti Kebangsaan Malaysia for their financial support under 03-01-01-SF1214 and UKM-GUP-BTT-07-25-025 Grants.

### References

- [1] Habig, K. H., Kocker, G.M, *Simulation of the the tribological behavior of tools for cutting ductile materials*, Convergence paper, presented at International Convergence of Frontier of Tribology, 15-17 April 1991, IOP Publishing, Ltd, Stratford-upon-Avon, 1992.
- [2] Gunay. M, korkut. I, Seker, U, *Exspermental inverstigation of the effect of cutting tool rake angle on main cutting force*, Journal of Material Processing Technology, 2005, vol 166: 44 – 49.
- [3] Cerenitti A.E, Fallbohmer B.P, W. Wu C.W.T & Altan B.T., *Application of 2D FEM to Chip Formation in Orthogonal Cutting*, Journal of materials Processing Technology, 1996, Volume 59: 169-180.
- [4] Cerenitti.A.E., Lazzaroni.C, Menegardo. L. & Altan. T., *Turning Simulation Using a Three- Dimensional FEM Code*, Journal of materials Processing Technology, 2000, volume 98: 99-103.
- [5] Marusich, T.D. & Ortiz, *Modeling and Simulation of High-Speed Machining*, To appear: International Journal Num. Metallurgy Engineering, 1995.
- [6] Xie. J. Q, Bayoumi. A.E., & Zbib. H. M., *FEA Modelling and Simulation of Shear Localized Chip Formation in Metal Cutting*, Journal of Materials Processing Technology. 1998, Volume 38: 1067-1087.
- [7] Shet, C., *Finite Element Analysis of the Orthogonal Metal Cutting Process*, Journal of Materials Processing Technology, 2000, Volume 105: 95-109
- [8] Columbus, O.H. , *Deform<sup>TM</sup> - 3D Machining (Turning) Lab*, Scientific Forming Technologies Corporation, 2007.
- [9] *Deform<sup>TM</sup>-3D, Deform-3D Tool Wear lab*, Scientific Forming Technologies Corporation, 2007.
- [10] Mackerle. J., *Finite Element Analysis and Simulation of Machining: a Bibliography (1976 – 1996)*, Journal of Materials Processing Technology, 1999, Volume 86: 17-44.
- [11] Oxley, P. L. B., *Mechanics of Machining: An Analytical Approach to Assessing Machinability*, 223–227 (Ellis Horwood, Chichester, West Sussex). 1989.
- [12] Stephenson. A.A, Agapiou, J.S, *Metal Cutting Theory and Practice*, Marcel Dekker. Inc, New York, 1996
- [13] El-Hofy, H. *Fundamentals of Machining Processes: Conventional and Nonconventional Processes*, Published by CRC Press, [http://books.google.com.my/books?id=ZdQEZ5pyCv4C&vq=cutting+speed&dq=effecting,+temperature,+cutting+speed&source=gb\\_s\\_summary\\_s&cad=0](http://books.google.com.my/books?id=ZdQEZ5pyCv4C&vq=cutting+speed&dq=effecting,+temperature,+cutting+speed&source=gb_s_summary_s&cad=0) . Date of download : November, 10<sup>th</sup> 2008
- [14] Kalhori. V., *Modelling and Simulation of Mechanical Cutting*, Doctoral Thesis, Institutionen for Maskinteknik, Sweden. 2001
- [15] Hendri. Y., Jaharah A.G., Che Hassan C.H. *Machining Simulation of AISI 1045 and Carbide Tool Using FEM*, Proceeding Seminar Regional II, AMReG 08, 15 December 2008.

## INVESTIGATION OF TRIBOLOGICAL PERFORMANCES OF DOMESTIC REFRIGERATORS

**J. U. Ahamed and R. Saidur**

*Department of Mechanical Engineering*

*University of Malaya*

*50603 Kuala Lumpur, Malaysia.*

*E-mail: [jamal@cuet.ac.bd](mailto:jamal@cuet.ac.bd), [saidur@um.edu.my](mailto:saidur@um.edu.my)*

### Abstract

*This paper emphasizes on the friction and anti wear behaviors of the lubricants used in the domestic/hermetic refrigerator compressor. Particularly, for long time and better running of the compressor, suitable refrigerant-lubricant mixtures are to be used. As CFC is expected to be phased out due to their ozone depletion potential, so, hydro-fluorocarbon (HFC) has been used as refrigerant. In the point of non- ozone depletion potential (ODP) and non-global warming potential (GWP) and for having better heat transfer coefficient, tetra hydro-fluorocarbon R-134a is becoming a proper replacement of CFCs. Lubrication properties of mineral oils (MO) and poly-ol-ester (POE) are found from the literature. Poly-ol-ester is very miscible with R134a. Though wear rates are greater for POE than that of MO but the friction coefficient is too much lower for POE than that of MO. Oil circulation ratio has a strong effect on heat transfer. It should be kept as minimum as possible. To minimize wear property, it is necessary to mix some additives (Chlorine, Flourine etc) with the lubricant. But the additives must have no chemical affinity with the lubricant. It can help to increase the heat transfer coefficient (HTC) and reduce the wear phenomena in the contact part.*

**Keywords:** *Friction coefficient, Wear; Poly-ol-ester; Mineral oil.*

### 1. Introduction

In the domestic refrigerators until 1990s, CFCs were used as refrigerants with mineral oil as lubricant. The concern caused by the ozone depletion potential (ODP) of the chlorofluoro carbons (CFCs) was at its peak in the 1980s and culminated in the Montreal protocol of 1987, which led to the phase out of CFCs in both developed and developing countries. The developed countries have already phased out the substance, and the developing countries, like India, have to do the same before the end of 2010. Even though many alternative refrigerants are available, none of them could be used in the CFC12 based appliances without making system modifications, that are cumbersome and in some cases, sometimes not economically viable. The energy efficiency of the resultant system is also a major concern.

But due to their ozone depletion potential in the upper atmosphere, the use of these compounds was phased out under the terms of

Montréal protocol [1]. CFCs were replaced initially by hydrofluorocarbons (HFCs) as they have zero ozone depletion potentials (ODP). They have also a problem of global warming potential. But R-134a is used as refrigerant for having zero ODP in the refrigerating system. For this refrigerant mineral oil as lubricant is not miscible and compatible with. So, poly ol ester is used as lubricant for R-134a. But for having some GWP of R-134a it is now becoming as a consideration to replace R-134a by a suitable refrigerant. However, POE is known as to be hygroscopic and hydrolytic, so there are severe problem in refrigeration system using POE oil such as wadding deposition, bulging equipment that chokes the flow and severe friction in the compressor.

Hydrocarbons have high thermal performance as well as very low GWP. The safety precautions to be taken are based on the refrigerant charge quantity and the physical location of the units or the separation of the components where hydrocarbons refrigerants are

contained. Limits are set to ensure that flammable concentration is far from reached if the whole charge is leaked and diffused into the given space. In several standards the use of hydrocarbons are allowed without restrictions if the charge is less than 0.15 kg in hermitically sealed systems. The system is internally safe in design. This assumption gives the possibility to use hydrocarbons in the household refrigerators and freezers.

It is observed that detailed performance studies have been reported with hydrocarbon (HC) as a refrigerant only in small systems. However, HC has not been considered for bigger systems, perhaps due to flammability issues associated with higher charge quantities. This motivated the authors to study the feasibility of making HFC134a work with mineral oil, so that Polyol Ester (POE) oil can be avoided and at the same time larger HC charge quantities in the systems also can be avoided. The work [2] intends to evolve a new refrigerant that could work in the CFC12 systems with better energy efficiency. Already, many research works have been published on the performance of alternatives in refrigeration systems. However, studies on this combination of refrigerant mixture, making HFC134a operate with mineral oil are a pioneering work. R-134a is a good refrigerant that has a higher enthalpy of evaporation and 33% higher heat transfer coefficient than that of CFC12 [3]. The higher polarity of R-134a results in low solubility in nonpolar lubricant such as mineral oil [4], and POE has to be used. Hence, R-134a can not be used in existing CFC12 systems without making changes either in the compressor and/or other components. R-134a/HC 600a (80:20 by weight) has been experimentally investigated [5] in heat pump and a 5% improvement in COP has been reported. Experimental studies on domestic refrigerators with alternative refrigerants showed that the flammability of HCs could be solved by adding  $CF_3I$  however this also reduces the refrigerating capacity [6]. It is also reported that suitable additives could improve the miscibility of HFC134a with mineral oil [7]. In a domestic refrigerator, HFC134a with 9% of the HC blend has yielded 3-12% improvement in COP and 4-6% reduction in energy consumption as compared to CFC12 [8].

In general household refrigerators and freezers all utilize hermetic compressor to continue the refrigeration system. In the hermetic compressors, refrigerant is to be

pressurized and raised its temperature also. So, energy costs increase rapidly. Compressor mechanical losses also increases and attract renewed attention [9]. For the hermetic compressor there are a number of areas where wear can occur. The main friction parts in hermetic compressors are motor-crankshaft bearings, crank pin-connecting rod bearing, piston pin-connecting bearing, and piston-cylinder sliding interface due to the starvation of the lubricating region in the area of these contact points. Various surface treatments are done for the decrease wear and friction in the closed type compressor. Sometimes oil and refrigeration mixtures also cause an effect to change the wear and friction. Though most of the researches are held only on heat transfer performance and to increase the coefficient of performance of the refrigerators. Few researches are done about tribology part in the compressor choosing proper lubricant and additives with this mixture. Some nano particles also help to increase the heat transfer and acts as antiwear materials in the compressor components. Jaekeun et al. [10] found a difference in lubrication properties while using pure oil and nano oil as lubricant. The presence of fullerene nano particles in the lubrication was found to improve the lubrication performance in the friction surfaces by reducing the metal surface contacts. Some additives may be used with the CFC based or HFC based refrigeration system to decrease the wear characteristics. Chlorine may be used in the compressor as antiwear/EP protection purpose. Other additives may be used based on the selection of base fluids.

## 2. Background

Refrigeration and air conditioning systems are very much renowned for their vast uses in the offices as well as houses in the developed countries. All the component parts of the compressor are expected to have a useful life. The useful life is in general around 50,000 hours operation whereas the useful life of a car is about 2500 hours of operation [11]. So, special care about the reliability of the compressor as well as the system should be considered. The ability of the lubricant to provide good lubrication to the internal moving parts in the compressor and be compatible with the refrigerant is necessary for both the system performance and long term durability.

Mineral lubricants have been used for many decades in the refrigeration based industries, indeed since the days of sulphur dioxide, carbon dioxide and CFC's. A great deal of new lubricants has been suggested for the compressor as refrigerants are replaced to HFCs. It is widely accepted that polyol esters are the lubricant of choice for the new refrigerants (HFCs). Refrigerants are changed only the basis of Ozone depletion potential. It is also necessary to choose a refrigerant and lubricant on the basis of energy efficient, more environmental free, and more cost effective. But the widespread introduction of HFCs has presented its problems to the suppliers of the lubricants. At first, HFCs are incompatible with the conventional lubricant mineral oils. So it is necessary to make some developments of synthetic polyol ester based lubricants which are fully compatible and soluble with HFC for the operating temperatures and pressures.

There are three fundamental types of lubricants: mineral, modified mineral and synthetic. Mineral lubricants are selected fraction of crude oil with some components removed for improving performance. Modified mineral oils are hydro-cracked or hydro treated base stocks and produced from selected fractions of the refining process. Synthetic base stocks do not use molecules that were present in the original crude oil. It is synthesized by chemical reaction of a very limited number of well-defined components. For example PAO's are derived from alpha-decene, and POE's are synthesized from acids and alcohols. Its manufacturing is tightly controlled and performance is also maintained. There has been a significant increase in the use of synthetic lubricants in recent decades to their improved performance, longer lifetime and reduced system downtime. Synthetic lubricants are POE, PAO, PAG, PVE and AB. In this group, every lubricant has different viscosity index, solubility in the refrigerant, pour point, surface tension etc. Now we have to choose lubricant according to the refrigerant used in the system.

One of the key criteria for lubrication is the ability to lubricate the compressor. For this lubricant must return to compressor as well. For this purpose nanoparticles and additives can serve this purpose. At high load, lubricant can not support against the critical areas. But some additives/nanoparticles create a film in those parts at high loading condition also. So it needs

to analyze the properties of the refrigerants and effect of lubrication for different cases.

### 3. Properties of Refrigerants

There are three types of refrigerants; synthetic, natural and mixtures. Synthetic refrigerants were used for refrigeration, cold storage and air conditioner. These are: R-11, R-12, R-22 (HCFC 22), R-502 (CFC12+HCFC22) etc. They have to be phased out due to their ODP and replaced by R-134a (HFC-134a) and blends of HFCs. Generally synthetic refrigerants are non-toxic and non-flammable. However, compared to natural refrigerants the synthetic refrigerants offer lower performance and also have higher GWP. As a result synthetic refrigerant faces an uncertain future. The most widely used and oldest natural refrigerant is ammonia. It has good thermodynamic, thermo physical and environmental properties. However, it is toxic and not compatible with some of the common materials of construction such as copper, etc. So, opinions differed on replacements for conventional refrigerants. Natural refrigerants are essentially making comeback, one advantage of using them is that they are familiar in terms of their strengths and weakness. They are also completely environment friendly. It is also possible to use blends of various HFCS with HCs with required properties to suit specific applications. Another thing is that it is important to take precautions from leakage, as this will change the composition of the mixture. Table 1 shows a list of refrigerants being replaced and their replacements.

### 4. Miscibility and Compatibility of the Refrigerants and lubricants

Lubricant is used with the refrigerant only for lubrication in the compressor parts. Lubricant is mixed with the refrigerant and it flows through the entire system. So it is necessary to provide adequate return of the lubricant to the compressor and to prevent fouling in the capillary tube and evaporator. So it should be miscible with refrigerant. To achieve this phenomenon lubricant should be changed and selected according to the refrigerants. For CFC lubricants should be mineral oils, for HFCs polyol ester (POE) synthetic lubricants [12] are preferred while for HCs mineral oils (MO) are favoured although POEs and polyelkaine

glycol (PAG) are also compatible [13]. One of the key criteria of refrigeration is the ability to lubricate the compressor properly. In doing so lubricant should be present physically in the compressor. For that the lubricant that is inevitably lost/remain in the system can efficiently return to the compressor. So we have to use an amount of refrigerant soluble lubricant. POE is more soluble with HFC refrigerant. Now a day hydrocarbons blends are in the research level for replacement of existing refrigerants. There is some researches are going on for using Blend of hydrocarbons with R-134a. It is necessary to have high COP with less flammable, zero ODP and low GWP for the refrigerant-lubricants mixture. Another thing is that wear should be minimized. But if can use the mixture of HCs and R-134a. When we consider fewer amounts of HCs for their flammable charatectr then POE will be the miscible with the mixture. It depends on the amount of HCs used in the mixture.

## 5. Effect of lubricants on Compressor and Refrigeration Performances

For correct working of the compressor oil is necessary. It creates a thin film to allow the mechanical moving parts properly. Mechanical moving parts are pistons, connecting rods and valves. There is wear in those parts. It also reduces the noise of the moving parts. Some times it is also used vas heat transfer medium for cooling the compressor. But oil has some disadvantages. Most often cited one is the reduction of heat transfer coefficients in the two-phase heat exchangers like condenser and evaporator. Pressure of oil also reduces the pressure drops, changes flow configurations, thermodynamic properties and thermodynamic equilibrium. Another problem for lubricant in the compressor is foaming phenomenon due to the mixing of lubricant and refrigerant. For instance, Yanagisawa et al. [14] experimentally investigated the foaming occurring in the hermetic rotary compressor and they noticed that foaming becomes violent at high compressor blade speed. Foam is violent when the pressure is close to saturation pressure on the basis of temperature n the casing.

Oil circulation ratio is also the concern matter. OCR seems to be independent of the operating conditions, at least for R-290/POE oil R-407C/POE oil, but the OCR seems to be slightly higher with POE oils than with mineral

oils [15]. For the calculation of enthalpy, oil circulation ratio and oil presents in the evaporator and condenser are to be considered. We should not take the fluid as a pure refrigerant only. Properties should be taken from the mixture's quantity. Solubility of lubricant into the refrigerant also is a factor. So, the properties of the mixture are to be considered in the different sections. Conde [16] focused on some methods aiming at evaluating the thermo physical properties of oils and their solutions in refrigerants. The wear and friction force within the MO lubricated contact reduces with the introduction of CFC-12 refrigerant but with POE and HFC in actual compressor the wear characteristics increase [17]. Experiment has shown that fluorine with the HFCs create an pressure film to reduce the wear. Nigel P. Garland and Mark Hadfield [18] investigated the tribological effect of hydrocarbon refrigerant applied to the hermetic compressor. He performance of refrigerant/lubricant combinations are evaluated within the pressurized environment. The best performance was shown for additised MO sample compared to additised POE samples on the basis of wear. In the case of additised POE initial wear rate was higher but after a long time it became lower shown in the Table 2 and Table 3. But the friction coefficients were lower for additised POE compared to that of additised MO.

## 6. Effect of Nanoparticles

To improve the heat transfer performance of the refrigerator and air conditioner and save energy nanoparticles are to be introduced with the lubricant. Many researches have been started. Choi et al. [19] first proposed creating nanoparticles by suspending high thermal conductivity nanoscale (0-100nm) metallic or nonmetallic particles in the base fluids (lubricants). These nano particles have a superior heat transfer capabilities and have popular research topic in heat transfer. More recently, some investigations showed that nanoparticles enhance the heat transfer efficiency as well as refrigerator reliability [20]. TiO<sub>2</sub> as a nanoparticles increase the solubility of mineral oil in the HFC refrigerant. Refrigerant system using a mixture of R-134a amd MO with TiO<sub>2</sub> nanoparticles appear to give better better performance to return more lubricant oil to the compressor. Jaekeun et al. [10] investigated and found a difference in lubrication properties

while using pure oil and nano oil as lubricant. The presence of fullerene nanoparticles in the lubrication was found to improve the lubrication performance in the friction surfaces by reducing the metal surface contacts. In the recent year the lubricant industry is dealing with an intense research activity in the field of nanotechnologies with the aim of improving the tribological performance of lubricants [21]. The results achieved in the industrial applications are extremely encouraging showing very good performances when adding carbon nanotubes or nanoparticles of copper oxides. Nevertheless several aspects have still to be investigated before making this technology ready for large industrial application.

Only recently few Far East companies have started to experimentally investigate the possibility of using the “nanolubricants” in refrigeration compressors in particular for the compressor typologies, like scroll ones, which efficiency is more affected by the lubricant performance. Lee et al. [22] investigated the behavior of the thrust slide-bearing of a scroll compressor with R22 and mineral oil with carbon nano particles added. The Authors found out experimentally that the nanoparticles (0.1 mass percentages in oil) increase up to 225% the breaking pressure of the oil film. The cooling performance of the contact surfaces was shown to be by far more efficient than the pure oil. The friction coefficient with pure oil was found to be higher than the one with oil+nano-particles. As an outcome, the wear of the surfaces in contact after several working hours was measured to be lower with the “nanolubricant”. Furthermore, the addition of carbon or copper oxides or aluminum oxides or titanium oxides nano - particles to liquids is recognized to improve significantly the single-phase HTC in several applications (the behavior in two-phase applications is still a much debated question). The very “intriguing” hypothesis is then: since the addition of nanoparticles is expected to improve significantly the lubricant performance in terms of compressor reliability and efficiency, should we expect also that the nanoparticles induce in the lubricant also an improvement in the heat transfer performance, as it happens when adding the same particles to liquids? If this should occur, the circulating oil could be an opportunity for increasing refrigerating machines efficiency, rather than a source of concerns for the engineers.

## 7. Conclusion/Summary

Concerning the above literature survey and analysis it can be concluded that for household refrigerators, wear and thermodynamic performance can be improved using R-134a and hydrocarbons mixture with suitable proportion and nanoparticle like TiO<sub>2</sub>, carbon nanotubes, CuO etc can be added with a small percentage. The lubricant should be mineral oil. Where flammable issue is not a prime factor then replacing R134a, a blend of R600a and R-290a can be used with mineral oil. Some additives Chlorine for mineral oil and fluorine for POE can be used. But for time operation additised POE is better for reduction of wear and friction in the compressor. It is necessary to check whether the mixture miscible or not for different proportions. Further research is necessary to investigate to justify the compressor run with performance with the different condition for long time.

## Acknowledgment

We would like to acknowledge gratefully the financial support by the Ministry of Science Technology and Innovation (MOSTI), Malaysia.

## References

- [1] UNEP. Montreal Protocol on Substances that Deplete the Ozone layer. New York: United Nations; 1987.
- [2] S. Joseph Sekhar, K. Senthil Kumar, D. Mohan Lal. Ozone friendly HFC134a/HC mixture compatible with mineral oil in refrigeration system improves energy efficiency of a walk in cooler. *Energy Conversion and Management* 45(2004) 1175-1186.
- [3] Eckels SJ, Pate MB. An experimental comparison of evaporation and condensation heat transfer coefficient condensation heat transfer coefficient for HFC134a and CFC12. *Int J Refrig* 1991;4:70–6.
- [4] Devotta S, Gopichand S. Comparative assessment of HFC134a and some refrigerants as alternatives to CFC12. *Int J Refrig* 1992;15:112–8.
- [5] Kim MS, Mulroy WJ, Didion DA. Performance evaluation of two azeotropic refrigerant mixtures of HFC-134a with R-

- 290 (propane) and R-600a (isobutene). *Trans ASME* 1994; 116: 148–54.
- [6] Baskin E. Synopsis of residential refrigerator/freezer alternative refrigerants evaluation. *ASHRAE Trans* 1998; 3: 266–73.
- [7] Sunami M. Physical and chemical properties of refrigeration lubricants. *ASHRAE Trans* 1999;14(2):983–94.
- [8] Sekhar SJ, Lal DM, Renganarayanan S. Eco-friendly and energy efficient refrigerant mixture as drop-in substitute for CFC12. In: Proc. *Int. Conf. on New Millennium—Alternative Solutions for Sustainable Development. Coimbatore India: PSG Tech*; 2003. pp. 538–43.
- [9] Kemal Sariibrahimoglu, Huseyin Kizil, Mahmut F. Aksit, Ihsan Efeoglu and Husnu Kerpici, Tribological Behavior of Sintered Steel Under Straved Lubrication in R600a environment. *2<sup>n</sup> d International Conference on Advanced tribology*, 3-5 December 2008, Singapore. Paper No. iCAT 169.
- [10] Jaekeun Lee, Sanwon Cho, Yuji Hwang, Han-Jong Cho, Changgun Lee, Youngmin Choi, Bon- Chul Ku, Hyeongkook Lee, Donghan Kim, Soo H. Kim. 2009, Application of fullerene –added nano-oil for lubrication enhancement in friction surfaces. *Tribology International*. 42, 440-447.
- [11] Technological Innovations in Refrigeration, in Air Conditioning and in the Food Industry. Development of Lubricants for Industrial Refrigeration, *Politecnico Di Milano*, 27-28 June, 2003.
- [12] Na BC, Chun KJ, Han D-C. A tribological study of refrigeration oils under HFC -134a environment. *Tribol. Intl.* 1998; 30(9): 707-16.
- [13] Granryd, E. Hydrocarbons as Refrigerants. *Int. J. Refrig* 2000; 24: 15-24.
- [14] Yanagisawa, T., Shimizu, T., Fukuta, M., 1991. Foaming characteristics of an oil-refrigerant mixture. *International J. refrigeration* 14(3), 132-136.
- [15] Navarro, E., Urchueguia, J., Gonzalez, J., Corberan, J. M., 1998. Comparative experimental investigation of oil behavior in a hermetic piston compressor using propane (R290) as refrigerant. In. *Proceedings of the 6<sup>th</sup> IIR-Gustav Lorentzen conference, Oslo, Norway*.
- [16] Conde, M. R., 1996. Estimation of thermophysical properties of lubricating oils and their solutions with refrigerants. An appraisal of existing methods. *Applied Therm. Eng.* 16, 51-61.
- [17] Mizuhara K, Akei M, Matsuzaki T. The friction and wear behavior in controlled alternative refrigerant atmosphere. *STLE Tribo Trans* 1994; 37(1): 120-8.
- [18] Nigel P. Garland and Mark Hadfield, Tribological analysis of hydrocarbon refrigerants applied to the hermetic compressor. *Tribology International* 2005; 38: 732-739.
- [19] S.U.S. Choi, Enhancing thermal conductivity of fluids with nanoparticles, *ASME FED* 231 (66) (1995) 99-103.
- [20] S. S. Bi, L. Shi and L. L. Zhang, Application of nanoparticles in domestic refrigerators, *Applied Thermal Engineering* 28 (2008) 1834-1843.
- [21] Liu G., Li X., Fan R., 2004, Enhancing AW/EP property of lubricant oil by adding nano Al/Sn particles, *Tribology letters*, 18(1): 85-90.
- [22] Lee J. K., Kim H. S., Lee B. C., Park J. S., 2006, Performance evaluation of nanolubricants at thrust slide-bearing of scroll compressors, *11th Int. Refr. Air-Conditioning Conf.*, C023: 1-8.

**Table 1: Refrigerants, their applications and substitutes (Lesson 26 Refrigerants, Version 1 ME, IIT Kharagpur, India)**

Refrigerant	Application	Substitute suggested Retrofit (R)/New(N)
R-11(CFC) NBP=23.7 <sup>0</sup> C, T <sub>cr</sub> = 197.98 <sup>0</sup> C h <sub>fg</sub> at NBP = 182.5 kJ/kg C <sub>p</sub> /C <sub>v</sub> = 1.13, ODP = 1.0 GWP = 3500	Large in air conditioning systems, industrial heat pumps as foam blowing agent	R-123(R,N), R-141b(N), R-245fa (N), n-pentane(R,N)
R-12(CFC) NBP=-29.8 <sup>0</sup> C, T <sub>cr</sub> = 112.04 <sup>0</sup> C h <sub>fg</sub> at NBP = 165.8 kJ/kg C <sub>p</sub> /C <sub>v</sub> = 1.126, ODP = 1.0 GWP = 7300	Small air conditioning, domestic refrigerators, Water coolers and small cold storages.	R-22 (R,N), R-134ab (R,N), R-227ea (N), R-401A and R-401B (R,N), R-411A and R-411B (R,N), R-717(N).
R-22(HCFC) NBP=-40.8 <sup>0</sup> C, T <sub>cr</sub> = 96.02 <sup>0</sup> C h <sub>fg</sub> at NBP = 233.2 kJ/kg C <sub>p</sub> /C <sub>v</sub> = 1.166, ODP = 0.05 GWP = 1500	Air conditioning systems Cold storages.	R-417A(R,N), R-407C(R,N), R-404A (R,N),R-507 and R-507A (R,N), R-410A and R-410B (N), R-717(N).
R-134a (HFC) NBP=-26.15 <sup>0</sup> C, T <sub>cr</sub> = 101.06 <sup>0</sup> C h <sub>fg</sub> at NBP = 222.05 kJ/kg C <sub>p</sub> /C <sub>v</sub> = 1.102, ODP = 1.0 GWP = 1200	Used as replacement for R-12 in domestic refrigerators, Water coolers and automobiles A/Cs etc..	No replacement required * Immiscible in mineral oils * Highly hygroscopic.
R-717 (NH <sub>3</sub> ) NBP=-33.35 <sup>0</sup> C, T <sub>cr</sub> = 133.0 <sup>0</sup> C h <sub>fg</sub> at NBP = 1368.9 kJ/kg C <sub>p</sub> /C <sub>v</sub> = 1.31, ODP = 0 GWP = 0	Food processing, Frozen food cabinets, Ice plants and cold storages.	No replacement required * Toxic and flammable * Incompatible with copper * Highly efficient * Inexpensive and available.
R-744(CO <sub>2</sub> ) NBP=-78.4C, T <sub>cr</sub> = 31.1 <sup>0</sup> C h <sub>fg</sub> at NBP = 321.3 kJ/kg C <sub>p</sub> /C <sub>v</sub> = 1.3, ODP = 0 GWP = 1.0	Air conditioning systems, Simultaneous cooling and heating and Cold storages.	No replacement required * Very low critical temperature * Eco-friendly * Inexpensive and available.
R-718(H <sub>2</sub> O) NBP100.0 <sup>0</sup> C, T <sub>cr</sub> = 374.15 <sup>0</sup> C h <sub>fg</sub> at NBP = 2257.9 kJ/kg C <sub>p</sub> /C <sub>v</sub> = 1.33, ODP =0 GWP = 1.0	Absorption system Steam jet systems.	No replacement required * High NBP and freezing point * large specific volume * Eco friendly * Inexpensive and available

Refrigerant	Application	Substitute suggested Retrofit (R)/New(N)
R-600(iso-butane) NBP=-11.73 <sup>0</sup> C, T <sub>cr</sub> = 135.0 <sup>0</sup> C h <sub>fg</sub> at NBP = 367.7 kJ/kg C <sub>p</sub> /C <sub>v</sub> = 1.086, ODP = 0 GWP = 3	Replacement for R-12 Domestic refrigerators, Water coolers	No replacement required * Flammable * Eco- friendly.

**Table 2 Average friction and wear coefficients [19]**

Test No.	Charge Conditions		Friction Coefficient	Wear Coefficient
	Temp. (°C)	Charge		
1	5	R600a MO	0.120	5.1x 10 <sup>-7</sup>
2	25	R600a MO	0.116	8.7x 10 <sup>-8</sup>
3	57	R600a MO	0.107	2.0x 10 <sup>-7</sup>
4	110	R600a MO	0.108	1.8x 10 <sup>-7</sup>
5	5	R600a MO+	0.124	7.8x 10 <sup>-7</sup>
6	25	R600a MO+	0.118	2.0x 10 <sup>-6</sup>
7	57	R600a MO+	0.127	7.3x 10 <sup>-6</sup>
8	110	R600a MO+	0.111	3.6x 10 <sup>-7</sup>
9	5	R600a POE+	0.118	5.8x 10 <sup>-7</sup>
10	25	R600a POE+	0.114	2.2x 10 <sup>-5</sup>
11	57	R600a POE+	0.119	1.8x 10 <sup>-5</sup>
12	110	R600a POE+	0.110	5.0x 10 <sup>-6</sup>
13	5	R134a POE+	0.135	8.6x 10 <sup>-8</sup>
14	25	R134a POE+	0.123	1.7x 10 <sup>-7</sup>
15	57	R134a POE+	0.111	5.1x 10 <sup>-6</sup>
16	110	R134a POE+	0.101	1.0x 10 <sup>-5</sup>

**Table 3 Friction and wear coefficients, extending tests [19]**

Test No.	Charge Conditions		Friction Coefficient	Wear Coefficient
	Duration	Charge		
17	14,400	R600a MO	0.118	3.7x 10 <sup>-9</sup>
18	86,400	R600a MO	0.118	2.7x 10 <sup>-9</sup>
19	14,400	R600a MO+	0.127	6.1x 10 <sup>-8</sup>
20	86,400	R600a MO+	0.103	2.1x 10 <sup>-7</sup>
21	14,400	R600a POE+	0.109	9.5x 10 <sup>-6</sup>
22	86,400	R600a POE+	0.064	2.3x 10 <sup>-6</sup>
23	14,400	R134a POE+	0.083	5.1x 10 <sup>-6</sup>
24	86,400	R134a POE+	0.079	1.2x 10 <sup>-6</sup>
25	86,400	R600a MO	0.104	7.08x 10 <sup>-9</sup>
26	237,600	R600a MO	0.090	1.54x 10 <sup>-8</sup>
27	86,400	R134a POE+	0.071	2.14x 10 <sup>-6</sup>
28	237,600	R134a POE+	0.037	7.87x 10 <sup>-7</sup>

# MACHINABILITY OF FCD 500 DUCTILE CAST IRON USING COATED CARBIDE TOOL IN DRY MACHINING CONDITION

Jaharah A.G., Abdul Rahman A., Mohd Nor Azmi, and Che Hassan C.H.

Department of Mechanical and Material Engineering,  
Faculty of Engineering and Built Environment,  
Universiti Kebangsaan Malaysia  
Email: [jaharah@eng.ukm.my](mailto:jaharah@eng.ukm.my)

## Abstract

*Machining is the most important manufacturing process in these modern industries especially for producing automotive component. In this study, ductile cast iron grade FCD 500 was machined using carbide cutting tool in dry end milling condition. The end milling parameters used were cutting speed of 180 m/min, 210 m/min dan 260 m/min. The feed rate of 0.10 mm/tooth, 0.25 mm/ tooth and 0.40 mm/ tooth, and the depth of cut of 0.30 mm, 0.60 mm dan 0.90 mm. Orthogonal  $L_9$  array in Taguchi method was employed in to carry out experimental work. The results were analyzed using Analysis of Variance (ANOVA) to determine the effect of end milling parameters on the tool life, cutting force and surface roughness measured. From the analysis it was found that the depth of cut and feed rate are the most important parameter influencing the tool life. The optimal tool life was found at cutting speed of 180 m/min, feed rate of 0.10 mm/tooth and depth of cut of 0.30 mm. A good surface finish was obtained at cutting speed of 260 m/min, feed of 0.10 mm/ tooth and depth of cut of 0.90 mm. Whereas, at cutting speed of 210 m/min, feed of 0.10 mm/ tooth and depth of cut of 0.30 mm, the lowest cutting force was measured. Wear mechanism at the tool surface such as crater wear, cracking and chipping were observed. These optimum parameters obtained will help automotive industry to have a competitive machining operation from the economical and manufacturing perspective.*

**Keywords:** FDC500 ductile cast iron, carbide tool, Taguchi Method, Wear mechanism, machining performance.

## 1. Introduction

Cast iron usually refers to grey cast iron, but identifies a large group of ferrous alloys, which solidify with a eutectic [1]. Casting of gray cast iron has relatively few shrinkage cavities and little porosity [2]. Generally, white cast iron is hard and brittle, which is difficult to machined [3]. In addition, the casting process is never perfect especially when dealing with large components [3]. Instead of scrapping the defective castings parts, repaired can be also done by welding. Very high carbon concentration in the typical cast iron causes difficulties due to the brittle martensite in the heat-affected zone of the weld. In order to avoid cracking, it is therefore necessary to preheat the cast iron to the temperature of about 450°C followed by slow cooling after welding [4].

Goodrich [4] discussed that the machining problems of cast iron is not necessarily foundry-

related. Machining problems associated with cast iron were drilling, milling, turning and other machining processes. Most of the problems were due to the microstructure formation/changes during the machining process itself. As an example, during the high pressure drilling operation, the matrix structure of the cast iron was actually being changed due to stress transformation of the high carbon-retained austenite in the matrix into martensite [5]. This transformation produces a much greater wear, and machining-resistant matrix-martensite. Hence, the drilling nearly stops and soon the drill was "fried." The solution suggested to overcome the problems were to increase the feed rate and reduce the turning rate so that any material that was transformed will be removed as the transformation was occurring. Thus, a hardened layer would not be developed under

the tool [4]. Cast iron is comparatively brittle material; therefore it is not suitable for product where a sharp edge or flexibility is required. It also has a property which is strong under compression but not under tension [3].

FCD 500 is widely used in automotive industry such as for fuel pump and oil pump, engine cylinder and cranks shaft. This material has a great potential due to good mechanical property, easy to cast and cheap. Carbide tool is important in machining application due to availability and cheap as compared to other cutting tool material such as CBN, even though it is preferred in machining cast iron.

Dry machining is becoming important due to the awareness towards the environment and worker's health [6]. Cutting fluid also add another 16-20% of manufacturing cost [6], therefore optimum use of cutting fluid is a must. According to Komanduri [7], associated cost with the cutting fluid, sometimes exceed the cost of labour and tooling.

This paper will presents the machining factors that affecting the machinability of FCD500 in terms of cutting force, surface roughness and tool life. The wear mechanism of the carbide tool also will be discussed in detailed.

## 2. Experimental Work

The machining trials were carried out on a Cincinnati Milacron, model Sabre 750 / TNC 415 Control in dry condition. The FC 500 (JIS) grade cast iron with eutectic graphite and ferrite was prepared in 180mm x 100mm x 50mm block. The hardness and tensile strength are in the range of 75 - 95 HRB and 250 – 350 N/mm<sup>2</sup> respectively. Table 1 shows the composition of cast iron grade FCD500 used in the experiment.

The T150M grade coated Al<sub>2</sub>O<sub>3</sub> carbide cutting insert was used in these experiments. The technique of CVD coating applied for the insert is suitable for machining ductile gray cast iron material. Table 2 show the mechanical properties of the coated carbide insert T150M.

**Table 1 The composition of cast iron grade FC500 [8]**

Element percentage (%)										
C	Si	S	P	Mn	Ni	Cr	Cu	Mg	Al	Co
2.77	1.26	0.11	0.036	1.24	0.26	0.27	0.18	0.127	0.063	0.073

**Table 2 The mechanical properties of coated carbide insert T150M**

Nose radius $r_e$	Rake angle $\alpha$	Main coating material
0.4	24°	Al <sub>2</sub> O <sub>3</sub> + Ti (C,N)

**Table 3 Experimental details of the machining trials**

Experiment no.	Cutting speed, $V$ (m/min)	Feed rate, $f$ (mm/tooth)	Depth of cut (mm)
1	180	0.1	0.3
2	180	0.25	0.6
3	180	0.40	0.9
4	210	0.1	0.6
5	210	0.25	0.9
6	210	0.40	0.3
7	260	0.1	0.9
8	260	0.25	0.1
9	260	0.40	0.6

Taguchi's design of experiment with a standard  $L_9$  ( $3^4$ ) orthogonal array was utilised [9].

The orthogonal array was chosen because of its minimum number of required experimental trials. The nine machining conditions are shown in Table 3.

The tool wear on the flank face was measured after the first path using a tool maker's microscope equipped with graduated scale in mm. The wear measurement requirement would then depend on the rate of wear growth. The measured parameter to represent the progress of wear was the maximum tool wear  $VB_{max}$ . The machining would be stopped when  $VB_{max}$  reached 0.3 mm. The cutting forces in X, Y, and Z directions were measured online during the milling operation using Kistler dynamometer model 9275B. The surface roughness of the workpiece was measured at several locations along the length of the cut using a portable Mitutoyo surface roughness tester.

### 3.0 Results and Discussions

#### 3.1 Experimental Results and ANOVA

Table 4 shows the tool life of T150M grade carbide tools in minutes when machining cast iron in dry cutting condition. The longest tool life of 41.34 minutes was achieved in trial 1 at cutting speed of 180m/min, feed rate of 0.1 mm/tooth and depth of cut of 0.3 mm. ANOVA analysis in Table 5 shows that the effect of cutting speed is almost negligible as compared to feed rate and depth of cut of 30% and 70% respectively on the tool life. Generally, at the combination of low cutting speed, feed rate and depth of cut resulted in better tool life; Ghani et al. [10] obtained similar results when machining hardened steels. The lowest tool life of 0.26 minutes was obtained with trial 3, at the biggest feed rate (0.4 mm/tooth) and the biggest depth of cut (0.9 mm). However, increase of cutting speed while keeping the feed rate at high value would further shorten the tool life as in Test 9. This was due to the feed rate which strongly influenced the range of chip thickness from tooth entry to exit [11] and chip area on the end mill [12].

Generally, low values of cutting force and surface roughness were obtained at low combination of feed rates and depth of cut as shown in Table 4 for trial 1, 4, 6 and 8. ANOVA analysis in Table 6 shows that the feed rate and

depth of cut will greatly influence the generated cutting force. These parameters contribute about 98% to the generated cutting force. The combination of feed rate and depth of cut determines the undeformed chip section and hence the amount of energy required to remove a specified volume of material. The required force to form the chips is dependent on the shear yield strength of the work material under cutting conditions and on the area of the chip section and the shear zone. The feed per tooth and the depth of cut determine this area. The low value of cutting force is desired to cut an unsupported beam or thin sections as well as to preserve material properties against residual stress and change in micro hardness at the subsurface.

ANOVA analysis in Table 7 shows that the feed rate is significantly affecting the  $R_a$  produced, followed by the cutting speed and depth of cut. The contribution of feed rate, cutting speed and depth of cut are 45%, 32%, and 23% respectively. The surface roughness produced in milling operation depends on feed rate [13], and the tool angular position depends on the depth of cut and radius of the cutter [14]. The influence of the cutting speed on the work-piece surface roughness is complex and it is quite dependent on the material properties of the cutting tools. For the tools with higher hardness and fracture toughness, the work-piece surface roughness decreases as the cutting speed increases. Tools with lower hardness and fracture toughness, the work-piece surface roughness increases as the cutting speed increases [15].

#### 3.2 Wear Mechanisms

Wear rate is defined as the volume or mass material removed per unit time or per unit sliding distance and is a complex function of time [16]. The initial period during which wear rate changes is known as the 'run-in' or 'break-in' period. Figure 1 shows the wear mechanism on the flank face when machining at cutting speed of 180 m/min, feed rate of 0.1 mm/tooth and depth of cut of 0.3 mm. At this cutting condition, the longest tool life of 41.34 minutes was obtained. Examination under the SEM shows that the wear on the flank face was uniformed and the coating material of  $Al_2O_3$  was removed from the cutting edge. It is said so due to the presence of two layers of material observed on the cutting edge. This phenomenon was believed to occur due to the stress concent-

**Table 4 The tool life of T150M coated carbide tool when machining cast iron in dry condition**

Experiment no	Cutting speed $V_c$ (m/min)	Feed rate $f$ (mm/gigi)	Depth of cut $d$ (mm)	Tool life (min)	Surface roughness, $R_a$ ( $\mu\text{m}$ )	Cutting force, $F_c$ (N)
1	180	0.10	0.30	41.34	1,357	290.92
2	180	0.25	0.60	10.39	1,793	845.9
3	180	0.40	0.90	0.26	1,845	1654.08
4	210	0.10	0.60	10.38	0.580	579.11
5	210	0.25	0.90	0.73	2,370	922.38
6	210	0.40	0.30	9.16	1,814	642
7	260	0.10	0.90	3.70	0.732	870.93
8	260	0.25	0.30	6.41	0.814	540.43
9	260	0.40	0.60	2.90	2,507	1067.48

**Table 5 ANOVA for tool life**

	Factors and contribution			Net total
	A	B	C	
Sum at factor level	Cutting speed, $V_c$	Feed rate, $f$	Depth of cut, $d$	
0	40.9592	64.0154	67.7025	172.6771
1	36.8283	33.7359	49.9042	120.4685
2	36.7492	16.7853	-3.0700	50.4645
Sum of squares (S)	34.7948	3434.8465	8131.8000	11601.44
Percentage contribution (%)	0.3	29.6	70.1	100.0

**Table 6 ANOVA for cutting force**

	Factors and contribution			Net total
	A	B	C	
Sum at factor level	Cutting speed, $V_c$	Feed rate, $f$	Depth of cut, $d$	
0	-172.1930	-163.3304	-160.0810	-495.6043
1	-170.7041	-172.4994	-174.3688	-517.5723
2	-174.0216	-181.0890	-182.4690	-537.5797
Sum of squares (S)	16.5667	473.2232	770.9794	1260.7694
Percentage contribution (%)	1.3	37.5	61.2	100.0

**Table 7 ANOVA for surface roughness**

	Factors and contribution			Net total
	A	B	C	
Sum at factor level	Cutting speed, $V_c$	Feed rate, $f$	Depth of cut, $d$	
0	-133.0431	-55.2104	-126.0368	-314.2903
1	-127.9363	-130.7791	-128.3233	-387.0386
2	-63.4858	-138.4758	-70.1051	-272.0667
Sum of squares (S)	9018.1665	12702.988	6522.9358	28244.091
Percentage contribution (%)	31.9	45.0	23.1	100.0

ration which led to the cohesive failure on the flank cutting wedge as found by Lin and Khrais [17]. Sharif and Rahim [18] found that the flank wear land increases gradually at low cutting speed. At low cutting speed wear mechanism is due to abrasion [19], and micro-attrition [20] as shown in Figures 1-3.

Catastrophic failure of cutting edge is found when used high depth of cut and feed rate of 0.9 mm and 0.4 mm/tooth respectively as shown in Figure 2. Grooving and chipping are clearly observed on the cutting edge as similarly found by Ghani et al. [20]. Failure may probably due to sudden of sharpness loss at the cutting edge [1]. Finding from Sharif and Rahim [18] also show that feed rate and depth of cut play an important role in determining the tool life.

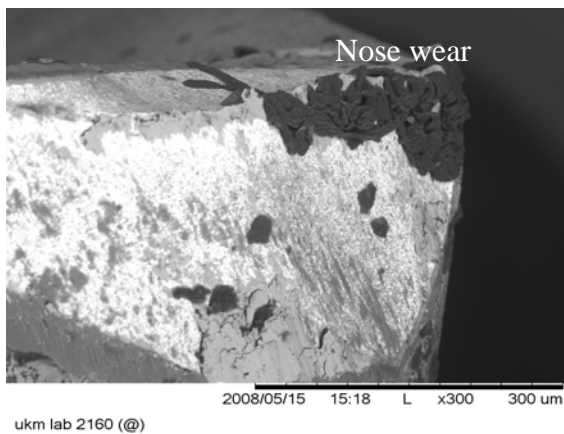


**Fig. 1. Wear on the flank face when machining at cutting speed of 180 m/min, feed rate of 0.1 mm/tooth and depth of cut of 0.3 mm**

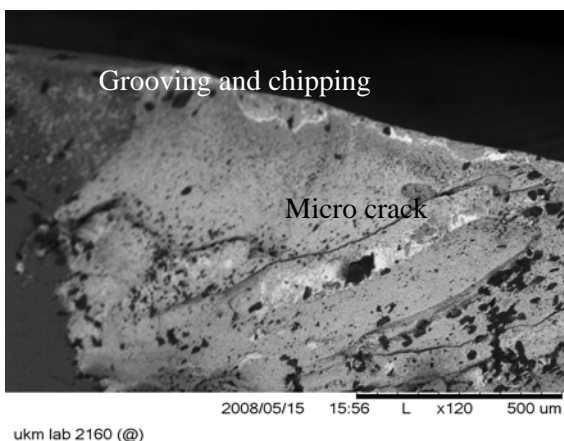


**Fig. 2. Chipping and grooving on the flank face when machining at cutting speed of 180 m/min, feed rate of 0.4 mm/tooth and depth of cut of 0.9 mm**

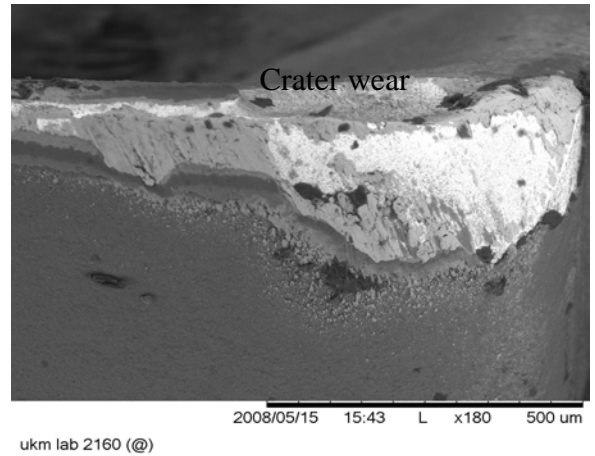


**Fig. 3. Crater wear on the rake face when machining at cutting speed of 210 m/min, feed rate of 0.4 mm/tooth and depth of cut of 0.3 mm**

#### 4. Conclusions

The effect of cutting speed is almost negligible as compared to feed rate and depth of cut on the tool life of the carbide cutting tool. The effect of rate and depth of cut are 30% and 70% respectively on the tool life. Low values of cutting force and surface roughness are obtained at low combination of feed rates and depth of cut. ANOVA analysis shows that the feed rate and depth of cut will greatly influence the generated cutting force which contributed about 98% to the generated cutting force. Feed rate is significantly affecting the  $R_a$  produced, followed by the cutting speed and depth of cut. The contribution of feed rate, cutting speed and depth of cut are 45%, 32%, and 23% respectively. The experimental results revealed that the major contribution to wear mechanism were feed rate and depth of cut, for this range of cutting speed, feed rate and depth of cut. The wear mechanism is predominantly controlled by the flank wear on the flank face at all ranges of cutting speed, and crater wear at high cutting speed. Moreover, catastrophic failure such as chipping and grooving were observed on the cutting edge at high cutting speed of 210 m/min, feed rate of 0.4 mm/tooth and depth of cut of 0.3 mm, which then limit the tool life only up to 0.29 min. Other wear mechanism observed was nose wear at low cutting speed of 180 m/min, feed rate of 0.1 mm/tooth and depth of cut of 0.3 mm.

## Acknowledgements

The authors would like to thank to the Government of Malaysia/Universiti Kebangsaan Malaysia for financial support under 03-01-02-SF0214 grant.

## References

- [1] Trent, E. M. 1981. *Metal Cutting*. 3<sup>rd</sup> Edition. Butterworth-Heinamman (Oxford) Ltd.
- [2] Kalpakjian, S., Schmid, S.R. 2001. *Manufacturing Processes for Engineering Materials*, 4th ed., Pearson Education Inc.
- [3] Gonzalez M.A.Y. and Bhadeshia H.K.D.H., 2007, Cast Iron, <http://msm.cam.ac.uk/phase-trans/2001/adi/cast.iron.html>, on line 08/08/2007
- [4] Goodrich, G. M., 2007, Case histories of cast iron machinability problems, <http://www.allbusiness.com/manufacturing/fabricated-metal-product-manufacturing/630735-1.html> on line 08/08/2007
- [5] Griffin, R.D., Li, H.J., Eleftheriou, E., Bates, C.E. 2001. Machinability of Gray Cast Iron, University of Alabama, Birmingham, Alabama.
- [6] Gundlach, R. B, Janowak J. 1985. Metal Progress. *International Journal of Machine Tools & Manufacture* 41 1003–1014
- [7] Komanduri, R., J. Desai, 1983. Tool Mater. *Encyclopaedia Chem. Technology*. 23 455-642
- [8] SIRIM (National Centre for Machinery & Tooling Technology) 2008
- [9] S.H. Park, *Robust Design and Analysis for Quality Engineering*, Chapman and Hall, 1996
- [10] Ghani, J.A., Choudhury, I.A., Masjuki, H.H. 2004. Wear mechanism of TiN coated carbide and uncoated cermets tools at high cutting speed applications. *Journal of Materials Processing Technology*. 153-154 (2004) 1067-1073: Elsevier Science Ltd.
- [11] S.N. Melkote, W.J. Endres, The importance of including size effect when modeling slot milling, *Transactions of ASME*, Feb 1998, Vol. 120, pp. 68-75.
- [12] J.W. Sutherland, R.E. Devor, An improved method for cutting force and surface error prediction in flexible end milling systems, *Journal of Engineering for Industry*, Nov 1986, Vol. 108, pp. 269-279
- [13] M.E. Martellotti, *An Analysis of the Milling Process*, Transactions of the ASME, 1941, pp. 677-695.
- [14] C.H. Borneman, *Chip Thickness in Milling*, American Machinist Reference Book Sheet, Vol.82, pp. 189-190, 1938.
- [15] Li X.S., and Low I.M., *Evaluation of advanced alumina-based ceramic tool inserts when machining high-tensile steel*, *Journal of Material Science*, 29 (1994) pp. 3121-3123.
- [16] B. Bhushan, *Principles and Applications of Tribology*, John Wiley & Sons, Inc. 1999.
- [17] Lin, Y.J., Khrais, S.K. 2007. Wear mechanisms and tool performance of TiAlN PVD coated inserts during machining of AISI 4140 steel. *Wear*. 262 (2007) 64-69: Elsevier Science Ltd.
- [18] Sharif S., E.A. Rahim. 2007. Performance of coated- and uncoated-carbide tools when Drilling titanium alloy Ti-6Al4V. *Journal of Materials Processing Technology* 185.
- [19] Arsecularatne, J.A., Zhang L.C, Montross, C. 2006. Wear and tool life of tungsten carbide, PCBN and PCD cutting tools. *International Journal of Machine Tools & Manufacture*. 46, 482-491: Elsevier Science Ltd.
- [20] Ghani, J.A., Choudhury, I.A., Masjuki, H.H. 2004. Wear mechanism of TiN coated carbide and uncoated cermets tools at high cutting speed applications. *Journal of Materials Processing Technology*. 153-154 (2004) 1067-1073: Elsevier Science Ltd.

## EFFECT OF ROTOR DIAMETER ON THE QUALITY OF ROTOR SPUN YARN

Ranajit Kumar Nag<sup>1</sup>, Farid Ahmed<sup>2</sup>, Abul Kalam Azad<sup>3</sup>

<sup>1</sup>Associate Professor, Ahsanullah University of Science and Technology  
Dhaka, Bangladesh, e-mail: nag.ranajit@yahoo.com

<sup>2</sup>Professor, Jahangir Nagar University, Savar  
Dhaka, Bangladesh, e-mail: fahmed\_ju@yahoo.com

<sup>3</sup>Principal Scientific Officer, Bangladesh Jute Research Institute  
Manik Mia Avenue, Dhaka, Bangladesh.

### Abstract

The quality of yarn depends on raw material selection, machineries used and various process parameters. Spinners set these process parameters on the basis of their experience to optimise the cost and quality of the yarn to be produced. To produce open end rotor spun yarn, rotor diameter is a vital parameter to enhance the production, to minimise the production cost and to achieve better quality of the yarn. In this research work researcher produced yarn of same fineness by using three different diameter rotor which were available at the time performing experimental work. Here same sliver was used for the whole experimental work. Also rotor rotational speed and opening roller speed were same. The raw material was cotton and cotton waste. After production, yarns were tested for quality aspects. The results show that bigger diameter rotor produces better quality yarn for almost all important yarn quality parameters.

**Key Words:** Rotor, Yarn, U%, CV%, Neps, Thin Places, Thick Places, Hairiness, Tenacity.

### 1. Introduction

To optimise the quality of rotor spun yarn various research works [1], [2], [3], [4], [5], [6], [7], have been done. They tried to optimize different process parameters; like linear density of the intermediate materials, setting of the rollers, amount of draft, drafting zone pressure, opening roller speed, rotor diameter, rotor speed etc to observe their effect of yarn quality. In this research work rotor diameter was taken as variable to observe its effect on the yarn quality parameters. Rotor is the chief element to produce yarn in rotor spinning frame. So that rotor form, material, finishes, design, diameter, groove angle etc will certainly contribute on the quality of the yarn. Considering the importance of rotor on yarn quality the rotor diameter has been taken as variable to observe its impact on yarn quality.

### 2. Raw Material Information

To produce 12 Ne yarn raw material was as follows:

Virgin Cotton 40%  
Waste 60%  
( Dropping I : 35%, Noil : 20%, Pneumafil: 5%)

### 3. Sample Preparation

To produce carded rotor spun yarn the following flow chart was followed:

Blow Room → Carding → Draw Frame I → Draw Frame II → Rotor Spinning Frame. The rotor spinning machine is an excellent recycling machine and from the raw material information we can see that maximum portion of raw material was waste cotton rather virgin cotton. But rotor spinning machine needs very clean feed stock for producing yarn. So that intensive cleaning of feed material without damaging the fibres is very vital. For that reason selection of machineries plays very important role on yarn quality as well as rotor life. Here we selected the following machineries for this research work. In blow room, the machineries were, Bale Plucker (Manufacturer: Rieter, Switzerland, Model A11, Year: 2001), Uniclean (Manufacturer: Rieter, Switzerland, Model: A11, Year: 2001), Unimix (Manufacturer:

Rieter, Switzerland, Model B70, Year: 2001), Uniflex (Manufacturer: Rieter, Switzerland, Model B60, Year: 2001). Carding machine was from Rieter, Switzerland, Model C51, Year 2001. Breaker Draw Frame was from Rieter, Switzerland, Model SB-D10, Year 2001, Finisher Frame was from Rieter, Switzerland, Model RSB-D30, Year 2001 and The Rotor Spinning Frame was from Oerlikon Schlafhorst, Germany, Model SE11, Year 2005.

#### 4. Results

After producing yarn the following test results were noted.

##### 4.1. Experimental Results

**Table 1**

Quality Parameters	Rotor Diameter		
	43 mm	54 mm	66 mm
Unevenness, U%	13.73	11.78	10.59
Coefficient of Variation, CV% (mass)	17.45	14.85	13.42
Thin Places -50%	22.5	7.5	0
Thick Places +50%	262.5	115	25
Neps + 280%	122.5	70	32.5
Imperfection Index, IPI	407	192.5	57.5
Hairiness	6.34	6.83	7.87
Tenacity (cN/tex)	6.63	9.88	10.88

##### 4.2. Graphical Representation of Results

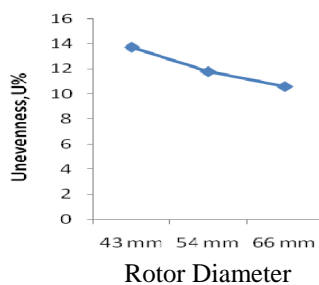


**Fig: 1** Effect of rotor diameter on U%

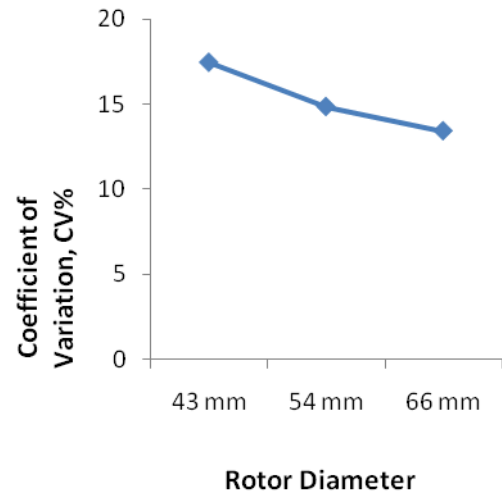


**Fig: 2** Effect of rotor diameter on CV%(m)

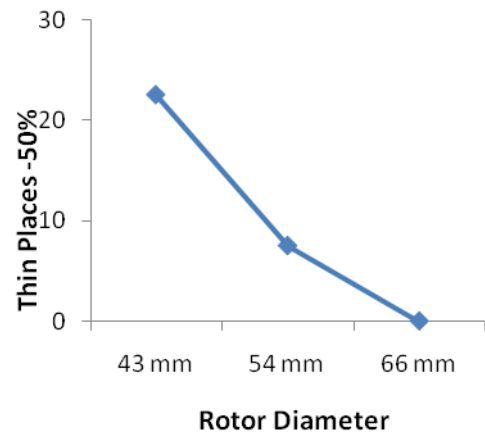


**Fig: 3** Effect of rotor diameter on Thin Places - 50%

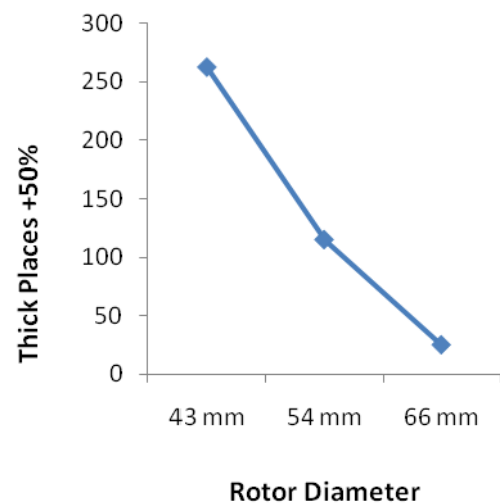


**Fig: 4** Effect of rotor diameter on Thick Places +50%

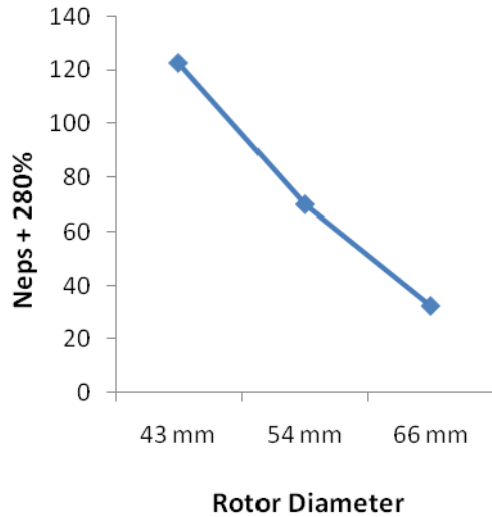


**Fig: 5 Effect of rotor diameter on Neps +280%**

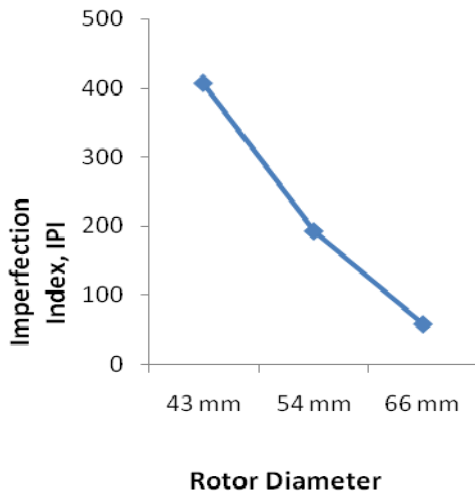


**Fig: 6 Effect of rotor diameter on IPI**

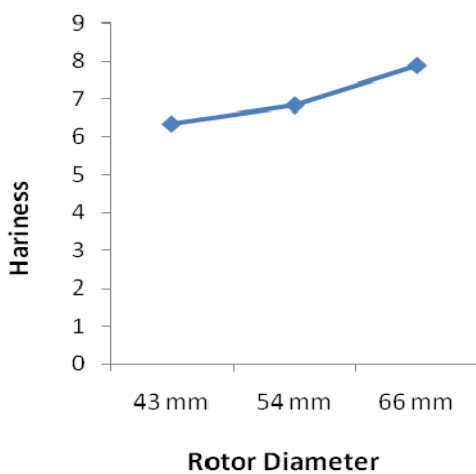


**Fig: 7 Effect of rotor diameter on Hairiness**

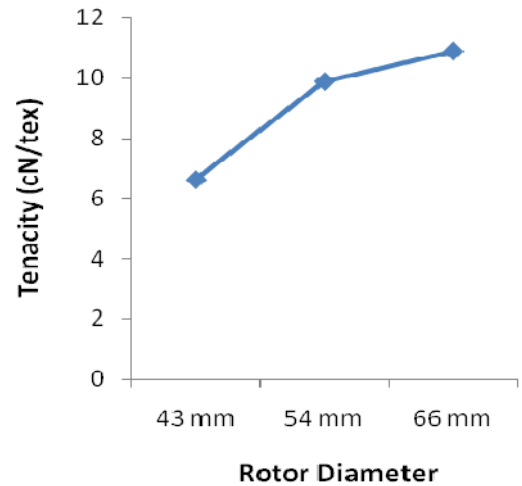


**Fig: 8 Effect of rotor diameter on Tenacity**

## 5. Discussion

If we throw light on the results of different yarn parameters it is easily visible that the highest diameter rotor gives better yarn quality yarn except hairiness point of view. It is possibly due to better orientation and possibility of higher back doubling or cyclic doubling for higher diameter rotor. As rotor diameter increases, there is a chance of better fibre orientation inside the rotor groove, which gives better evenness of yarn as well as less mass CV%, less thick and thin places and obviously high yarn tenacity. Higher diameter rotor also leads higher number of back doubling [8]. This phenomena again improves the quality of yarn. Reverse result is noted for yarn hairiness. It is may be due to the possibility of less number of wrapper fibre for higher diameter rotor. It is because for higher diameter rotor withdrawl point passes the feed tube less frequently than that of less diameter rotor. Higher the number of wrapper fibre, higher the possibility of embedding fibre ends by sheath fibres. This may be the cause of higher hairiness for higher diameter rotor and vice-versa.

## 6. Conclusion

From this research work it can be observed that higher diameter rotor gives better quality yarn. But in practical cases always we try to go for small to smaller diameter rotor. It is mainly due to intention of increasing production. If we think only for quality yarn we may go for higher diameter rotor. At the same time we have to bear

in mind that larger the diameter less that speed can be obtained due to various technical reasons.

## References

- [1] Azad A.K.Md. Influence of Blend Ratio on the Properties of Rotor Spun Yarn, *Ph.D. thesis* pp 54-55, 2006.
- [2] J.S. Manohar, A.K. Rakshit , N. Balasubramanian, Influence of Rotor Speed, Rotor Diameter, and Carding Conditions on Yarn Quality in Open-End Spinning, *Textile Research Journal*, Vol. 53, No. 8, 497-503 (1983).
- [3] A. Barella; J. M. Tura; J. P. Vigo, Aa Application of Mini-Computers to the Optimization of the Open-End-Spinning Process. Part III: The Effect of the Rotor Diameter on the Properties of Open-End-Spun Yarns, *Journal of the Textile Institute*, Volume 67, Issue 12 December 1976 , pp 421 – 425.
- [4] A. Barella; A. M. Manich; Patricia N. Marino; J. Garófalo, Factorial Studies in Rotor-Spinning Part I: Cotton Yarns, *Journal of the Textile Institute*, Volume 74, Issue 6, November 1983 , pp 329 – 339.
- [5] Sh. Muhammad Nawaz, Nisar Ahmad Jamil, Muhammad Iftikhar, Bilal Farooqi, Spinning Performance of Open-End Yarn as Effected by some Processing Variables, *International Journal of Agriculture and Biology*, 1560–8530/2002/04–2–252–255, <http://www.ijab.org>.
- [6] Sh. Muhammad Nawaz, Nisar Ahmad Jamil, Muhammad Iftikhar, Bilal Farooqi, Effect of Multiple Open-End Processing Variables Upon Yarn Quality, *International Journal of Agriculture and Biology*, 1560–8530/2002/04–2–256–258 <http://www.ijab.org>
- [7] P. Grosberg, Rotor Spinning-State of the Art, 1981, *Seminar on Rotor Spinning*, September 1981, pp 1-12,
- [8] W. Klein, *Manual of Textile Technology, New Spinning Systems*, The Textile Institute, U.K., Vol-V, p 34, 1993.

# TRIBO-CHEMICAL DEGRADATION OF PHENOLIC RESIN IN AUTOMOTIVE BRAKE PAD DURING DRY SLIDING AGAINST MMC

K.M. Shorowordi<sup>1\*</sup>, A.S.M.A. Haseeb<sup>2</sup> J.P. Celis<sup>3</sup>

<sup>1</sup>Institute of Appropriate Technology, Bangladesh University of Technology (BUET)  
Dhaka 1000, Bangladesh

<sup>2</sup>Department of Mechanical Engineering, University of Malaya  
50603 Kuala Lumpur, Malaysia

<sup>3</sup>Department of Metallurgy and Materials Engineering, Catholic University of Leuven  
de Croylaan 2, Heverlee B 3001, Belgium.

\*Corresponding Author: E-mail: kshorowordi@iat.buet.ac.bd, Fax+880 2 9662365

## Abstract

*Degradation of phenolic based automotive brake pad material during friction against two aluminium matrix composites (MMC) viz. Al-SiC and Al-B<sub>4</sub>C was studied. Wear tests were carried out in a pin-on-disk type friction testing apparatus at a linear sliding speed of 1.62 m s<sup>-1</sup> under a contact pressure 3.00 MPa for an hour in ambient air. Morphology, thermal degradation and structural changes of phenolic resin in the debris during friction process were investigated by stereomicroscope, infrared spectroscopy (IR) and thermogravimetry analysis (TGA). It is revealed from stereomicroscopic investigation that the debris mainly consists of dark fluffy powdery material. IR study of debris shows that carbonyl and carboxylic acids are present in phenolic resin in debris, while phenolic resin in the as-received pad material does not show these groups. This indicates that thermal degradation occurs through oxidation in the present sliding conditions. Cross linking of phenolic resin also occurs along with oxidation during friction process which enhances the oxidation of phenolic resin in debris materials. TGA study shows higher weight loss of debris material as compared to as-received pad material.*

**Keywords:** Phenolic resin - Friction material – Degradation - Infrared spectroscopy

## 1. Introduction

The brake systems of automobile consist of brake pads and rotor. During braking operation, the brake pad, usually made of phenolic based composites, is pressed against a cast iron rotor which is attached to the wheel. Nowadays cast iron rotor are being replaced by aluminium metal matrix composites (MMC) which has the advantage of having lower density offering opportunities for fuel saving in automobiles.

Commercial brake pads are proprietary item and their composition is usually not disclosed. It is however generally known that commercial organic type brake pad material basically consists of a) phenol formaldehyde binder; b) fiber reinforcement, such as mineral based fiber like asbestos, synthetic fiber like

glass fibre, carbon fibre etc.; c) filler like barium sulfate, mainly for cost reduction; and d) friction modifier such as brass, iron chips [1, 2].

During braking operation, the brake pad undergoes friction and wear which lead to frictional heating and mechanical damage. Normal braking operations in passenger cars can increase the bulk temperature at the friction interface to about 150-250°C [1]. But during severe braking operations the temperature may reach about 370°C or even higher [3-4]. The input of both thermal and mechanical energy can trigger different tribochemical reactions at the friction interface. Such tribochemical reactions may degrade the organic compounds like phenol formaldehyde binder in the brake pad and affect its properties. The inorganic compounds in brake pad have been found to be ground and

pulverized without much change in chemical composition and physical structure under the combined action of wear and friction [5]. Although a good number of studies have been done on the thermal degradation of phenol formaldehyde in ambient air as well as in inert atmosphere, not much information is available on the tribochemical degradation of phenol formaldehyde particularly sliding against Al MMC.

Early studies of Conley and coworkers [6-9] suggested that the primary degradation pathway for phenolic resins is oxidative in nature even in an inert atmosphere, and that thermal processes only start to compete at higher temperatures. Recent studies [10-18] have revealed that the prime route of the thermal degradation of phenolic resin in inert atmosphere is the cleavage of phenol-methylene bonds and subsequent abstraction of hydrogen. As a result, phenols and methylene-substituted phenols as volatile products were formed. The cleavage of the methylene bridge occurs due to the decrease in strength of the O-H bond at increased temperature [16]. Hydrogen abstraction is kinetically favoured over the scission of benzyl phenol bond [18]. It was also found that H<sub>2</sub>O, CO<sub>2</sub> and CH<sub>3</sub>OH are evolved in the degradation of phenolic resins in N<sub>2</sub> atmosphere at temperature as low as 250°C [19]. This means the polymer undergoes fragmentation and dehydration reactions and is subsequently oxidized by OH radicals, carbonyls and carboxylic acids. In the presence of air the oxidation reaction takes place via the formation of peroxides caused by oxygen. In this case, the polymer is oxidized at relatively lower temperature and to a higher extent than when heated in nitrogen.

Kristkova et al. [13] studied the influence of metal particles (Cu, Fe, Cu-Zn) on the degradation process of phenolic based friction materials. They found that a concentration (~20-25 vol.%) of Cu or Fe, in the friction materials has a catalysis effect on the degradation of phenol formaldehyde. The main step in the phenolic resin degradation process involves the elimination of formaldehyde, as an important curing agent, caused by metal and metal oxide catalysis. Brass was not found to act as catalyst in the degradation process. Sallite et al. [20] while investigating the frictional and wear behaviour of brake pad against aluminium matrix composites could not identify any degradation of phenol formaldehyde by FTIR.

The present study intends to investigate the tribochemical degradation of phenolic resin in commercial brake pad sliding against two metal matrix composites viz. Al-SiC and Al-B<sub>4</sub>C. For this purpose optical microscopy, infrared spectroscopy (IR) and thermogravimetric analysis (TGA) were employed to characterize the debris that was generated from the pad during the sliding friction test.

## 2. Materials and Experimental

### 2.1. Materials

A commercial brake pad was used in this study. Since its composition is not disclosed by the manufacturer, composition was therefore investigated before the friction study. Phenol formaldehyde resin was identified as a binder in friction composite by IR. X-ray fluorescence spectroscopy revealed that the brake pad contains elements like O, Mg, Si, S, Ca, Mn, Fe, Cu, Zn, Ba and C. C belongs to resin; Mg, Si and O belong to asbestos fiber which was used as reinforcement; Ba, S and O belong to BaSO<sub>4</sub> which acts as filler; Fe, Cu, Zn etc. belong to metallic chips acting as friction modifier. Wet chemical analysis also revealed that the friction material used in the present used in this study contains 34% phenolic resin, 42% asbestos fiber, 3.7% Cu, 2.1 % Zn, 3.2% iron (along with other constituents). As counterpart in friction couple, two aluminium metal matrix composite (MMC) were used. One contains 13% volume percent SiC particles in pure aluminium matrix and the other contains 13% volume percent B<sub>4</sub>C. The average size of the particle in both cases was 40 μm.

### 2.2. Friction tests

Friction tests were performed in a unidirectional pin-on-disc apparatus in which a disc shape (dia: 80 mm, thickness: 10) piece cut from the brake pad rotates in a horizontal plane. Al MMC pin specimen (dia: 5 mm, length: 12 mm) was pressed against the rotating disc by applying a normal load of 58.86 N, which resulted in a contact stress of 3.00 MPa. At the contact position the linear speed of the disc was 1.62 m s<sup>-1</sup>. Friction force was recorded during the friction tests using a load cell and the coefficient of friction was calculated by dividing friction force by normal applied. The temperature generated during friction test due to friction, was

measured by inserting a thermocouple (chromel-alumel) in the pin at position 2 mm above from the contact surface. The temperature ( $^{\circ}\text{C}$ ) was plotted against sliding distance (m). During friction tests, wear debris was collected on an aluminium foil placed below pin-disc assembly. After the test, debris was preserved in a desiccator for optical macroscopy, IR analysis and TGA.

### 2.3. Stereomicroscopic study

After the friction tests the wear track on the brake pad and the collected debris were examined under a stereomicroscope.

### 2.4 Infrared spectroscopy (IR)

Sample of as-received brake pad material and debris from brake pad/Al-SiC and debris from brake pad/Al-B<sub>4</sub>C was pulverized to less than 2.0  $\mu\text{m}$  with KBr using an agate mortar. The KBr mixed powdered sample was pressed into pellet under 8 tons load. The pellet was subjected to the test by using a Shimadzu infrared spectrometer Model-460 at a scanning speed of 360  $\text{cm}^{-1} \text{min}^{-1}$  in the range of 400-4000  $\text{cm}^{-1}$ . The spectra were analyzed and the possible functional groups for the recorded absorption peaks in the spectra were identified by comparing with standard spectrum.

### 2.5 Thermogravimetric analysis (TGA)

Thermogravimetric analysis of as-received brake pad material and debris from Al-SiC/brake pad system and debris from Al-B<sub>4</sub>C/brake pad system was done by Thermo-Gravimetric analyzer CAHN TG 171-09 between a temperature range of 25 $^{\circ}\text{C}$  and 600 $^{\circ}\text{C}$ . The sample of about 30 mg was heated in an oxygen atmosphere at a heating rate of 10 $^{\circ}\text{C}/\text{min}$ .

## 3. Results and Discussions

### 3.1. Stereomicroscopic examination of friction track and debris

Photographs of wear track on brake pad and debris generated during friction test against Al-SiC MMC taken under a stereomicroscope are shown in Fig. 1. These photographs are typical and represent both friction couples studied i.e. brake pad/Al-SiC and brake pad/Al-B<sub>4</sub>C. The wear track (Fig. 1a) is seen to consist of abrasive

sliding marks. This is likely to be caused by the abrasive action of hard ceramic particles viz SiC or B<sub>4</sub>C present in the MMC. At places some pits or spalling of material from the pad is seen. These are thought to be the result of removal of different constituents like reinforcement, friction modifier etc. from the pad. Materials dislodged from the brake pad undergoes mechanical interactions at the sliding interface and the interface temperature rises as a result of frictional heating. In the course of the friction test, a part of the debris is ejected out of the wear track which was collected. The collected debris as shown in Fig. 1b mainly consists of dark fluffy, powdery material. The debris also contains some dark compacted flakes. These are mainly generated from the phenolic brake pad. In addition, the debris also contains some aluminium particles dislodged from Al-MMC. The collected debris was sorted under the stereomicroscope in order to separate out the metallic particles, fibers and other constituents from the fluffy polymeric constituents. The fluffy polymeric constituents, presumably phenolic resin from the pad and its degradation products, were further examined by IR spectroscopy and TGA.

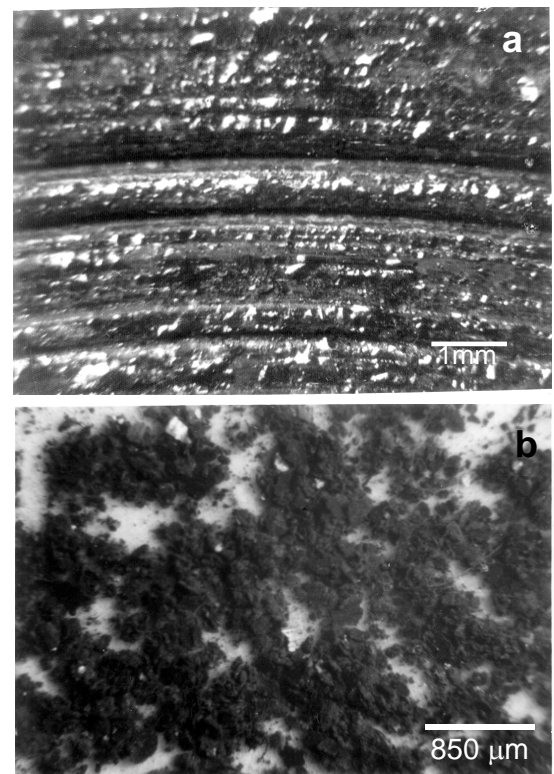


**Fig. 1. Photograph of (a) A wear track formed on brake pad and (b) Debris generated during sliding of Al-SiC MMC against brake pad.**

### 3.2 Coefficient of friction (COF) and frictional temperature rise

The coefficient of friction (COF) of brake pad/Al-SiC and brake pad/Al-B<sub>4</sub>C composites recorded during friction test is shown in Fig. 2a. It is seen that the COF quickly reaches a peak then falls to a steady state value as the sliding distance increases. Brake pad-Al-SiC and brake pad-Al-B<sub>4</sub>C couple have a steady state COF value of 0.38 and 0.35 respectively. The slightly lower value of COF for brake pad/Al-B<sub>4</sub>C couple was attributed to the formation of oxides of boron at the interface [21,22]. Frictional temperature developed during the test are shown in Fig. 2b as a function of sliding distance. It is observed that temperature increases fairly rapidly at the beginning and reaches a steady value after sliding of about 1000 m. The steady state frictional temperature is about 182°C for both friction couples. However a slightly lower friction temperature is developed for the brake pad-Al-B<sub>4</sub>C couple. This is consistent with the fact that this couple also has a lower COF value.

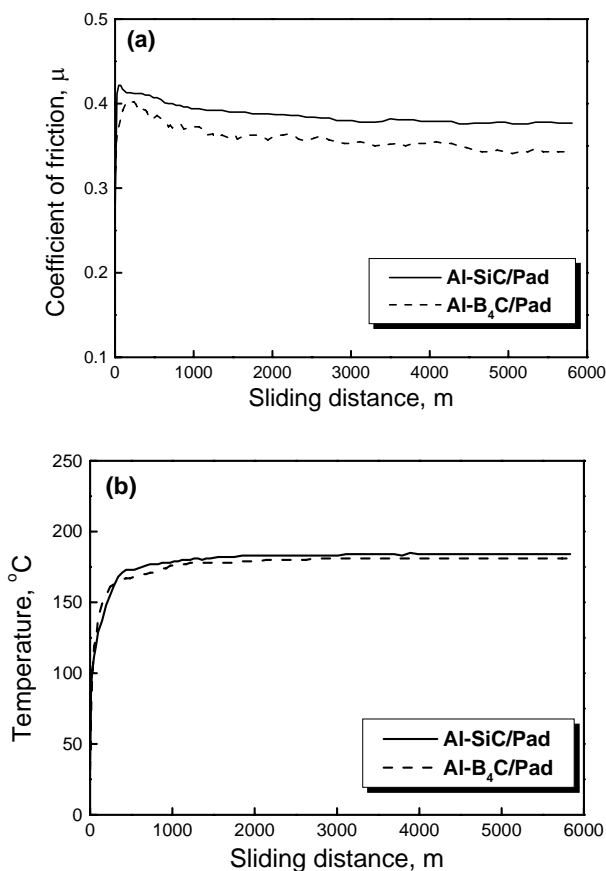


Fig. 2 (a) Coefficient of friction and (b) temperature versus sliding distance of Al-SiC and Al-B<sub>4</sub>C composites sliding against pad friction material at 1.62 m s<sup>-1</sup> under 3.00 MPa.

### 3.3 Infrared spectroscopy (IR)

The IR spectra of as-received friction material and debris generated during wear of Al-SiC/pad and Al-B<sub>4</sub>C/pad are shown in Fig. 3. The absorption peaks and their corresponding functional groups are listed in Table 1. As reference, absorption peaks for the degradation of phenolic resin studied by others [10,11,13] are also included in Table 1. The OH stretching bands at 3670 cm<sup>-1</sup> and 3415 cm<sup>-1</sup> of as-received phenolic pad are shifted respectively towards the lower wave number and towards higher wave number for the debris of both composites. The intensity of OH band at 3670 cm<sup>-1</sup> decreases after the friction test. The changes of position and intensity decrease indicate that the changes in the H bonding and decrease in the amount of OH groups occurs [10]. These change may take place due to the condensation process according to reactions 1 and 2 [23, 24] and reaction 3 (cross-linking) [11]. As a consequence of condensation, ethers are formed and evidence of this is found in the growing bands at 1260 cm<sup>-1</sup> which is not found in the original pad friction materials.

The absorption peaks of 2800-3100 cm<sup>-1</sup> are attributed to the stretching of C-H bands. The absorption peak at 2910 cm<sup>-1</sup> observed in original pad material, shift to the higher wave number and intensity become low in the debris materials. This indicates that during wear process aliphatic bands are disappeared.

A new weak absorption appears at 1646 cm<sup>-1</sup> and 1650 cm<sup>-1</sup> for the debris samples of pad/Al-SiC and pad/Al-B<sub>4</sub>C couple. These absorption peaks are thought to be due to the presence of carbonyl group in the debris sample that are formed after oxidation of methylene bridge (reaction 4) [25]. This peak was absent in the original pad material.

More evidence for oxidation is given by the peak at 1730 cm<sup>-1</sup> (Fig. 3). This peak reveals the presence of carboxylic acids in the resin (reaction 5) [10]. The presence of carboxylic acids in the spectra of the debris confirms the thermal degradation of the pad through oxidation in air atmosphere. Cross-linking and branching occur with oxidation and provide higher substitution as can be seen from the changing intensity of the peak at 1610 cm<sup>-1</sup> in debris material. Moreover, peak at 1539 cm<sup>-1</sup> for ring stretching in the debris occurs due to cross linking during friction process, while this peak is absent in pad material. Besides that the

increased intensity at  $870\text{ cm}^{-1}$  and changing appearance of peaks in the  $800\text{-}700\text{ cm}^{-1}$  region also confirm that higher substitution has taken place during wear process in phenolic resin [11].

Absorption peak at  $1455\text{ cm}^{-1}$  is attributed

to bending of the C-H bands of an aliphatic bridge. The change of intensity observed in Fig. 3 occurs due to the changes in the nature of the aliphatic bridges.

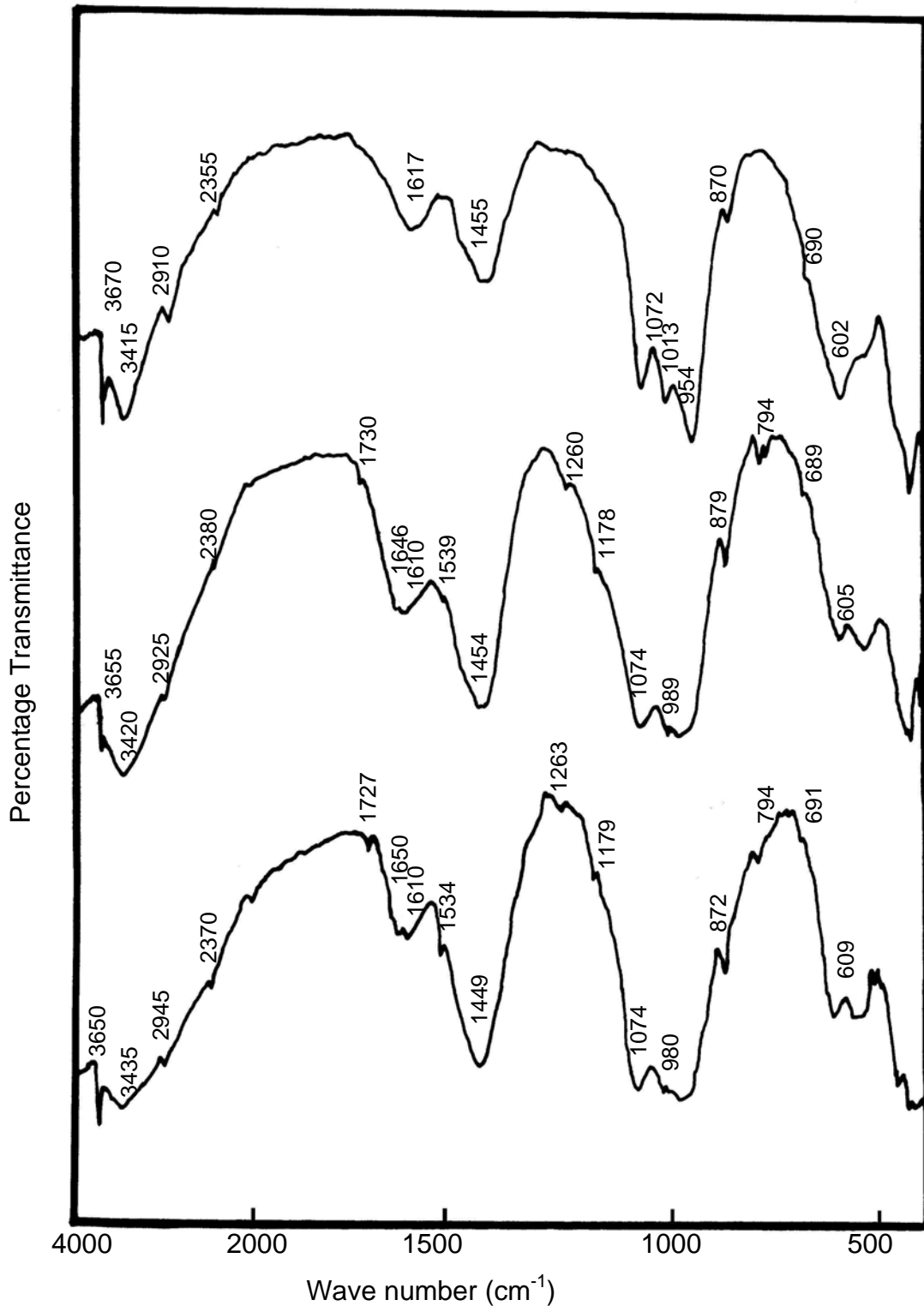
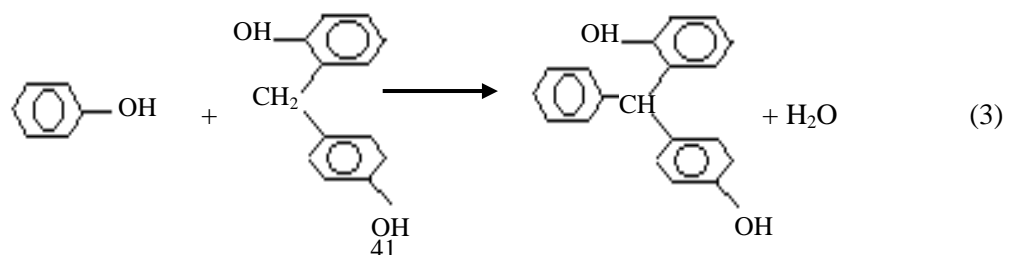
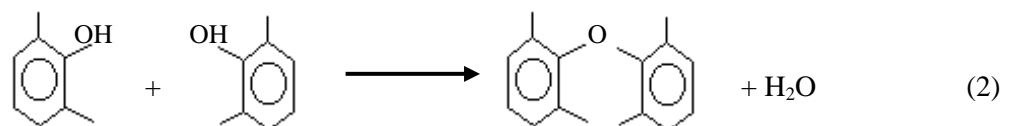
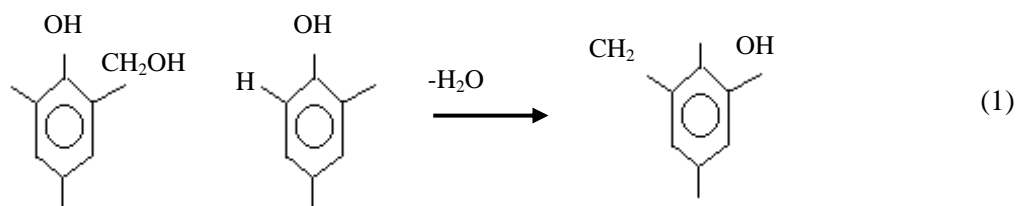


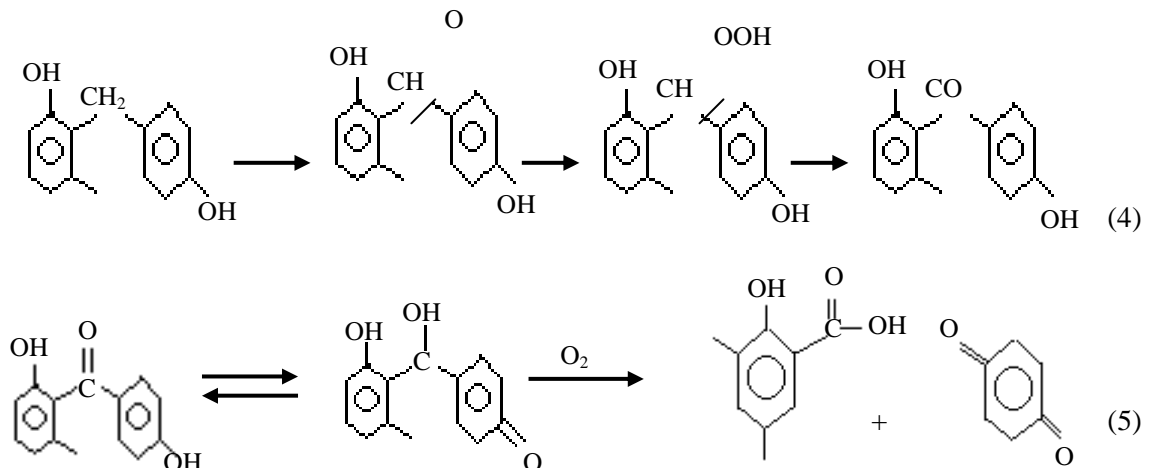
Fig. 3 Infrared spectra of (a) original pad friction materials, (b) debris of Al-SiC and (c) debris of Al-B<sub>4</sub>C

Table 1 Infrared bands and assignments (band position in cm<sup>-1</sup>) of pad friction material, debris from Al-SiC/pad friction material and Al-B<sub>4</sub>C/pad friction material and other studies from literatures (w= weak, m= medium, s=strong, vs=very strong, br s= broad strong).

Brake pad (as-received)	Debris from Al-SiC/pad	Debris from Al-B <sub>4</sub> C/pad	Kristkova et al., 2004[13]	Costa et al., 1997[10]	Trick and Saliva, 1995[11]	Functional groups
3670 (s)	3655 (w)	3650 (m)	-	-	-	Phenolic OH Str.
3415 (br. s)	3420 (br. s)	3435 (s)	-	3350	3500	Phenolic OH Str./Arom. CH Str.
-	-	-	3016	3016	3100-3000	Aromatic CH Str.
2910 (m)	2925 (w)	2945 (m)	2927	2920	3000-2800	Aliphatic OH asymmetric
-	-	-	2837	2840	-	Aliphatic CH Str. sym.
2355 (w)	2380 (vw)	2370 (vw)	-	-	-	-
-	1730 (vw)	1727 (vw)	1720-1740	1740	1735	Carboxylic group
-	1646 (br vs)	1650 (br vs)	1650	-	1658	C=O of Carbonyl Struct.
1617 (br s)	1610	1610	1610	1610	1607	C=C Aromatic ring str. (1,2,4)
-	-	-	1595	1590	-	C=C Aromatic ring str. (1,2,4)
-	1539 (w)	1534 (w)	1510	1501	-	Semi circle ring str. (1,2,4)
-	-	-	1476	1475	1475	Tetra substituted ring
1455 (br s)	1454 (br vs)	1449 (br vs)	1455	-	-	Semi circle ring str. (1,2,4)
-	-	-	1440	-	-	Aliphatic CH <sub>2</sub> Scisbend
-	-	-	1371	1360	-	Phenolic OH in plane deform.
-	-	-	1134	1340	-	Phenolic OH in plane deform.
-	1260 (br m)	1263 (br m)	1250	1270	1264	Alkyl phenol C-O str.
-	-	-	1236	1226	1200	Alkyl phenol C-O str.
-	1178 (w)	1179 (w)	1171	1170	-	2/and/or 4-substituted ring
-	-	-	1101	1100	-	CH inplane ring deform. (1,2,4)
1072 (vs)	1074 (br s)	1076 (s)	-	-	-	Aromatic C-H inplane deform/C-O str. of phenol.
1013 (vs)	989 (br s)	980 (br s)	-	-	-	CH <sub>3</sub> attached to the arom. ring
945	-	-	912	911	-	Aliphatic CH <sub>2</sub> wagging
870 (m)	879 (s)	872 (s)	881	-	880	Tetra subst. benzene ring(1,2,4)
-	794	794	816	816	-	Out of plane ring deform. (1,2,4)
-	-	-	756	756	756	Out of plane ring deform. (1,2,6)
690 (vw)	689 (w)	691 (w)	691	-	-	Mono subst. benzene ring
602 (vs)	605 (s)	609 (s)	-	-	-	Mono subst. benzene ring

MMC collected during the sliding at 1.62 m s<sup>-1</sup> and 3.00 MPa.





In the present case, the bulk temperature is around 182°C during the friction test from where debris is collected. The presence of carbonyl group and carboxylic acids in the debris confirms the thermal degradation of the pad through oxidation in air atmosphere during the wear process even at such low temperature.

### 3.4 Thermogravimetry analysis (TGA)

The TGA curve for as-received brake pad shows slight weight loss at temperature below 100°C (Fig. 4). This can be attributed to the loss of water. After this the weight changes little until about 265°C. Above this a major weight loss occurs which accounts for a decrease of about 24%. In the case of debris, in addition to initial weight loss due to dehydration, a significant weight loss accounting for about 10% of original weight occurs between 50 and 175°C. After this, the weight of debris changes little until about 300°C. Above this temperature, major loss in weight occurs which corresponds to 22% and 21% respectively in debris from pad/Al-SiC and pad/Al-B<sub>4</sub>C couples. The temperature range and percentage reduction in weight at the major weight loss event for as-received brake pad and debris are compared in Table 2.

The reason for the weight loss of debris samples between 50 and 175°C is thought to be due to occurrence of cross linking in phenolic resin of brake pad during friction. The IR spectroscopic result as discussed earlier also revealed the occurrence of cross linking in phenolic resin in debris. The cross linked resins are less stable in air atmosphere and oxidised at low temperature [10]. Thus more oxidation of

debris is expected which provide higher weight loss of debris as compared to the as-received brake pad.

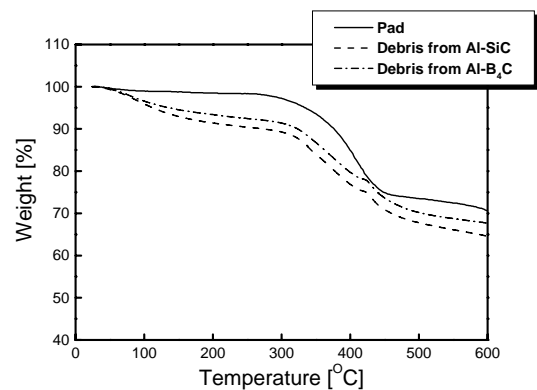


Fig. 4. TG thermogram of pad and debris from the Al-SiC and Al-B<sub>4</sub>C.

One interesting feature of TGA curves of both debris sample is that small peak occurs at around 420°C indicating a slight weight gain. Such feature is absent in the TGA curve of as-received brake pad. It may be noted that some aluminium particles originating in Al-MMC were also present in the debris. Although these particles were separated from the debris under the stereomicroscope, it is possible that a very few fine aluminium particles not resolved under the microscope could still remain in the debris. Such aluminium particles are likely to get oxidized at about 410°C leading to a weight gain [26-27].

The major weight loss events for all the samples are due to the oxidation of phenolic resin. Ingo et al. found from combined study of DTA-TG a wide exothermic peak at 350-370°C due to oxidation of organic constituents in brake pad [5]. Besides, the evidence of presence of

carboxylic and carbonyl groups in debris material in IR spectra also indicates that the oxidation occurs during friction in present sliding condition

where bulk temperature at interacting surface is 182°C.

**Table 2 Characteristics of major weight loss event.**

Sample	As-received brake pad		Debris from Pad/Al-SiC		Debris from pad/Al-B <sub>4</sub> C	
Degradation temperature	Starting temperature	Finishing temperature	Starting temperature	Finishing temperature	Starting temperature	Finishing temperature
	265°C	475°C	300°C	510°C	300°C	500°C
Weight loss	24%		22%		21%	

#### 4. Conclusions

Thermal degradation of phenolic brake pad sliding against Al MMC in a pin on disc wear type wear testing machine has been studied. Stereomicroscopic investigation revealed that the collected debris mainly consists of dark fluffy powdery material. The debris also contains some dark compacted flakes. These are mainly generated from the phenolic brake pad. IR and TGA analysis of as-received pad material and debris of Al-SiC/friction material and Al-B<sub>4</sub>C/friction material were carried out to study the thermal degradation of phenolic resin in pad friction materials during friction process. IR analysis reveals that carbonyl group and carboxylic are present in the debris while these are not found in as-received pad material. This indicates that the thermal degradation of pad material occurs through oxidation in air atmosphere during friction process at the present sliding condition. Cross linking is also found to occur with oxidation in phenolic resin. Since the more cross linked resins are less stable in air at temperature, TGA analysis shows more weight loss of debris as compared to as-received pad material.

#### References

- [1] Jacko, M.G., Rhee, S.K., in M. Grayso (ed), *Encyclopedia of Composites Materials and Components*, 1983, pp. 144-154.
- [2] Briscoe, B.J., Ramirez, I., Tweedle, P.J., *Int. conf. on disk brakes for commercial vehicles; Institute of mechanical engineers, London*, 1998, pp. 15-29.
- [3] M.G., Jacko, Sopurgeon, N.M., Rusnak, R.M., Catalano, S.B., *SAE Q. trans.* Paper 680417, 1968.
- [4] Laden, K., Guerin, J.D., Watremez, M., Bricout, J.P., Frictional characteristics of Al-SiC composite brake discs, *Tribology Letters*, Vol. 8, pp. 237-247, 2000.
- [5] Ingo, G.M., Uffizi, M.D., Falso, G., Bultrini, G., Padeletti, G., Thermal and microchemical investigation of automotive brake pad wear residues, *Thermochemica Acta*, Vol. 418, pp. 61-68, 2004.
- [6] Conley, R.T., in *Thermal stability of polymers John Wiley*, New York, p. 457, 1970.
- [7] Conley, R.T., Bieron, J.F.J., A study of the oxidative degradation of phenol-formaldehyde polycondensates using infrared spectroscopy. *Appl. Polymer Sci.*, Vol. 7, pp. 103-117, 1963.
- [8] Conley, R.T., Bieron, J.F., A kinetic study of the oxidative degradation of phenol-formaldehyde polycondensates using infrared spectroscopy, *J. Appl. Polymer Sci.*, Vol. 7, pp. 171-180, 1963.
- [9] Conley, R.T., Oxidative degradation of phenol-formaldehyde polycondensation initial degradation reactions, *J. Appl. Polymer Sci.*, Vol. 9, pp. 1117-1126, 1965.
- [10] Costa, L., Rossi di Montelera, I., Camino, G., Weil, E.D., Pearce, E.M.: Structure-charring relationship in phenol-formaldehyde type resins, *Polymer Degradation and Stability*, Vol. 56, pp. 23-35, 1997.
- [11] Trick, K.A., Saliba, T.E., Mechanisms of the pyrolysis of phenolic resin in a carbon/phenolic composite, *Carbon*, Vol. 33;11, pp. 1509-1515, 1995.

- [12] Hetper, J., Sobera, M., Thermal degradation of novolac resins by pyrolysis-gas chromatography with a movable reaction zone, *Journal of Chromatography*, Vol. A. 833;2, pp. 7-281, 1999.
- [13] Kristkova, M., Filip, P., Weiss, Z., Peter, R., Influence of metals on the phenol-formaldehyde resin degradation in friction composites, *Polymer Degradation and Stability*, Vol. 84, pp. 49-60, 2004.
- [14] Liu, Y., Gao, J., Zhang, R., Thermal properties and stability of boron-containing phenol-formaldehyde resin formed from paraformaldehyde. *Polymer Degradation and Stability*, Vol. 77, pp. 495-501, 2002.
- [15] Reghunadhan Nair, C.P., Bindu, R.L., Ninan, K.N., *Thermal characteristics of addition-cure phenolic resins. Polymer Degradation and Stability*, Vol. 73, pp. 251-257, 2001.
- [16] Lin, J., Ma. C.M., Thermal degradation of phenolic resin/silica hybrid ceramers, *Polymer Degradation and Stability*, Vol. 69, pp. 229-235, 2000.
- [17] Rao, M.P.R., Rao, B.S.M., Rajan, C.R., Chadage, R.S., Thermal degradation kinetics of phenol-crotonaldehyde resins, *Polymer Degradation and Stability*, Vol. 61;2, pp. 283-288, 1998.
- [18] Prokai, L., *Journal of Analytical and Applied Pyrolysis*, Vol. 12;3-4, pp. 265-273 1987.
- [19] Nyden, M.R., Brown, J.E., Lomakin, S.M.: in *Fire and polymers II, Materials and test for hazard prevention*, *American Chemical Society, ACS symposium series 599*, Aug. 21-26, Washinton D.C, 1994.
- [20] Sallite, I., Richard, C., Adam, R., Valloir, F.R., Characterization Methodology of a Tribological Couple Metal Matrix Composite/Brake Pads, *Materials characterization*. Vol. 40, pp. 169-188, 1998.
- [21] Shorowordi, K.M., Haseeb, A.S.M.A., Celis. J.P., Velocity Effects on the Wear, Friction and Tribochemistry of Aluminium MMC Sliding Against Phenolic Brake Pad, *Wear*, Vol. 256, pp. 1176-1181, 2004.
- [22] Gogotsi, Y.G., Chonko, A.M.K., Kossko. I.A., Tribochemical interactions of boron carbides against steel, *Wear*, Vol. 154, pp. 133-144, 1992.
- [23] Morterra, C., Low, M.J.D., IR studies of carbons-VII. The pyrolysis of a phenol-formaldehyde resin, *Carbon*, Vol. 23, pp. 525-530, 1985.
- [24] Serio, M.A., Charpenay, S., Bassilakis, R., Solomon, P.R., *ACS Div. Fuel Chem. Prepr*, Vol. 36, p. 66, 1991.
- [25] Camino, M., Luda, P., Costa, L., Trssarelli, L., in *Thermal analysis, Proc. VIIth nt. Conf G. on thermal analysis*, Vol.11, ed. B. Miller. Wiley, New York, p. 1137, 1982.
- [26] Claussen, N., Wu, S., Holz, D., *J. Eur. Ceram. Soc.*, Vol. 14, pp. 97-109, 1994.
- [27] Wu, S., Holz, D., Claussen, N., Mechanisms and Kinetics of Reaction-Bonded aluminum Oxide Ceramics, *J. Am. Ceram. Soc.*, Vol. 76, pp. 970-980, 1993.

## DRY SLIDING WEAR CHARACTERISTICS OF SUGARCANE BAGASSE POLYMER CEMENT COMPOSITES

C.J. Kee, M.J. Ghazali, M.A. Ahmad\*, N.I.I. Mansur  
A.E.A. Ruslan & C.H. Azhari

Department of Mechanical and Materials Engineering  
Universiti Kebangsaan Malaysia  
43600 Bangi, Selangor, Malaysia

\*Corresponding Author: E-mai: mariyam@vlsi.eng.ukm.my

### Abstract

*This study is to investigate the wear behaviour of several bagasse-polymer-cement composites with different ratios of styrene butadiene latex (SBR) content; 3%, 6% and 12%. The main precursor; sugar cane were chopped into 5mm in length and randomly dispersed within the matrices bagasse-polymer-cement composites with 6% of SBR content was found to gain the highest value of hardness. They were selected to irradiate to dose of 10kGy and 20kGy of electron beam irradiations, in order to modify the microstructure of bagasse-cement composites. It was noted that tensile strength was greatly improved with greater irradiations dose. The sliding wear test was conducted in a dry sliding condition against hardened carbon steel of +60 HRC of 1 m/s. Under a pin-on disk configuration, the tests were carried out at 10N and 50N of load range in a room temperature (~25 °C). It was found that composites with 6% of SBR content which exposed at 20kGy irradiation showed the best wear resistance with  $463-5.2 \times 10^{-4}$  Mm<sup>3</sup>/Nm, at both low and high load. Observation by the scanning electron microscopy on the microstructure of the irradiated composites indicated that the voids within the matrices were greatly reduced, which therefore increase the mechanical properties, as a whole, than there of unirradiated areas. Finally, the predominant wear mechanism on this case were mostly plastic deformation, ploughing, fragmentation of were debris on the matrix, excessive determination of fibre surface followed by delimitation and fiber removal.*

### 1. Introduction

In the old days, most agriculture side-products, i.e; sisal, coir, bamboo, sugarcane bagasse or paddy chaff, will be destroyed via burning or being used as burning materials despite of its low calories compared to coals. However, today, interestingly, several types of natural fibres which are still in abundance, have proved to be a good and effective reinforcement in both thermoset and thermoplastic matrices (Jacob et al., 2004, Joseph et al., 2002, Pothana et al., 2003 and Tong et al., 2005). Due to its low cost and high specific mechanical properties, natural fibres have emerged as a potential candidate for renewable and biodegradable alternative to most synthetic reinforcement like glass fibres (Corbierre-Nicollier et al., 2001). In fact, fibres like sisal, jute, coir and flax straw have proved to be good and effective reinforcement in both

thermoset and thermoplastic matrices. However, little information concerning the tribological performance of natural fibres reinforced composites has been reported (Yousif et al, 2005, Tong et al., 2005, El-Sayed et al., 1995), particularly literatures on the tribological behaviour of sugarcane bagasse as reinforcement in cement composites. As reported by El-Tayeb (2008) the sugarcane fibres have a promising potential as a reinforcement agent especially in adhesive sliding contacts. However, some researchers claimed that the fibres need to be treated chemically to improve the mechanical properties of the composites. Thus, in order to study the real tribological role of the fibers in the polymer cement composites, untreated and both irradiated/unirradiated is carried out in this

study. For composition use, samples with 6% of SBR content were selected in this world due to its great and significant hardness. Due to this characteristic, only those with 6% of SBR were carried out for irradiation treatment.

## 2. Background

In general, cellulose is one of the main components in natural fibres. The macromolecule based unit for cellulose is anhydrous-d-glucose which contains 3 hydroxyl alcohols (-OH). This hydroxyl group forms the hydrogen bond in between its own macromolecule with other cellulose macromolecules. Thus, all natural fibres are natural hydrophilic where its moisture can achieve up to 8 up to 12.6%. One of the main characteristic for natural fibre is the degree of its polymerisation. The degrees of polymerisation are different for different fibres. The fibril which own by cellulose macromolecule will form a spiral along the axis. Normally, toughness and stiffness for hemp, ramie, and jute, for example are connected between axis angle and fibril fibres. The mechanical properties of this composite will increase when the angle becomes smaller.

## 3. Experiment Procedures

### 3.1 Sample preparation

The main precursor; sugarcane bagasse is obtained by crushing the cane stalks using the RLL-3 Portable Crusher before being washed under running water. The crushed bagasse was then dried at 105°C for 24 hours and grind. After grinding, the fibers were sieved; yielding fibers

with < 5 mm in length and diameter that ranged between 300–500  $\mu\text{m}$ . Blended cement composites were prepared by mixing the Portland cement with bagasse fibers (30% of the composite) and water. The mixing process was carried out by using the Winkworth mixer machine with water to cement ratio (W/C) of 0.25. The water was added gradually to the fiber-cement mixture for 5 minutes. Polymer emulsions were added to the mixture of fiber-cement composites after a complete addition of water, for a period of 10 minutes, with different weight percentages of 3, 6 and 12% to the weight of the mixture, respectively. The homogenous mixture was then hot-pressed into a mould of 10 mm diameter and 3.5 mm thick at 130°C with 50 tons load for 30 minutes. The samples were finally cooled at room temperature and kept for mechanical testing.

### 3.2 Wear test

Prior to the wear test, the hardness value of each sample was carried out. It was noted that samples with 6% of SBR exhibited the greatest hardness. This was followed by irradiation process at 10kGy and 20kGy of electron beam. The wear test was carried out by using a pin-on-disc configuration in dry condition at room temperature. The dry sliding was kept at a fixed speed of  $\sim 1\text{m/s}$  under 10N and 50N of applied load. Morphologies of run samples were then examined by the Scanning Electron Microscope (SEM) with the aid of the energy disperse X-ray (EDX) spectrum.

## 4. Result and Discussion

Table 1 Specific wear rate for bagasse polymer-cement composite sample

Composite sample	F, Load (N)	V, Volume loss ( $\text{mm}^3$ )	t, Time (s)	v, Velocity (m/s)	s, (= v·t) (m)	Specific wear rate, $K'$ (= V/F·s), ( $\text{mm}^3/\text{Nm}$ )
6% SBR	10	14.29	1200	1	1200	1.19E-03
	50	35.71	1200	1	1200	5.95E-04
6% SBR, (10kGy)	10	8.93	1200	1	1200	7.44E-04
	50	33.93	1200	1	1200	5.66E-04
6% SBR, (20kGy)	10	5.56	1200	1	1200	4.63E-04
	50	31.48	1200	1	1200	5.25E-04

Table 1 shows the data between the specific wear rate ( $K'$ ) as a function of applied load for both unirradiated and irradiated samples. Based on the result in Figure 1, specific wear rate for 6% SBR decreased with increasing load for each composite. Meanwhile for 6% SBR, 10kGy and 6% SBR, 20kGy composite sample, load did not influence its specific wear rate. Hence, percentage of SBR latex composition could influence specific wear rate on each sample composites. Specific wear rate,  $K'$  was a suitable parameter in reporting wear rate in tribology. It was a logical parameter because it was closely related to total wear (wear volume) to input as mechanical energy to contact (load and sliding distance) (Kenneth Holmberg 2005). The lower the value of  $K'$ , the better wear resistance (Ghazali et al. 2007). Hence, 6% SBR (20kGy) composite sample showed the best wear resistance property.

Table 2 showed average coefficient of friction for all studied samples. Graph of coefficient of friction versus time (second) for 6% SBR with 10N and 50N load was shown in Figure 2. Based on the result obtained, the value of average coefficient of friction decreased with increasing load. From observation, all the three loads experienced ploughing. Figure 3 showed graph of coefficient of friction versus time (second) for 6% SBR (10kGy) composite sample with 10N and 50N loads. The result obtained showed that the coefficient of friction decreased with increasing load. The sample experienced ploughing on these two loads. (Bharat Bhushan 1999). Figure 4 showed graph of coefficient of friction versus time (second) for 6% SBR (20kGy) composite sample with 10N and 50N loads. Based on the result obtained, the value of coefficient of friction

decreased with increasing load. Sample with 10N load showed increment in its coefficient of friction to a certain limit before declining. This was because plastic deformation occurred on the composite sample (Bharat Bhushan 1999). Based on all the results, 6% SBR, 6% SBR (10kGy), and 6% SBR (20kGy) composite sample yielded the same result which was their coefficient of friction decreased with increasing load.

**Table 2 Average coefficient of friction for bagasse polymer-cement composite sample.**

Composite Sample	Load (N)	Coefficient of friction, $\mu$
6% SBR	10	0.953
	50	0.557
6% SBR (10kGy)	10	0.408
	50	0.404
6% SBR (20kGy)	10	0.532
	50	0.429

Figure 5 (a) to Figure 5 (c) showed SEM micrograph for surface wear of the composite sample with 10N load. Meanwhile Figure 6 (a) to Figure 6 (c) showed SEM micrograph for surface wear of the composite sample with 50N load. Based on Figure 5 and Figure 6, generally crack on all samples would increase with increasing load. However, the value of  $K'$  for 6% SBR, and 6% SBR (10kGy) composite sample showed decrement with increasing load. The crack in 6% SBR (20kGy) composite sample showed piece crushed shape on composite sample and showed the best wear property among all.

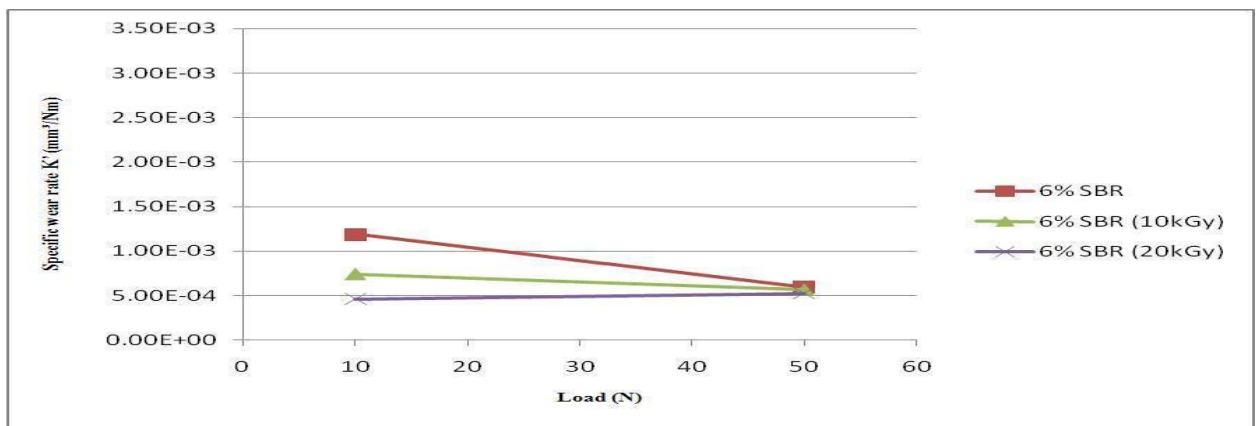


**Fig. 1. Specific wear rate  $K'$  vs Load**

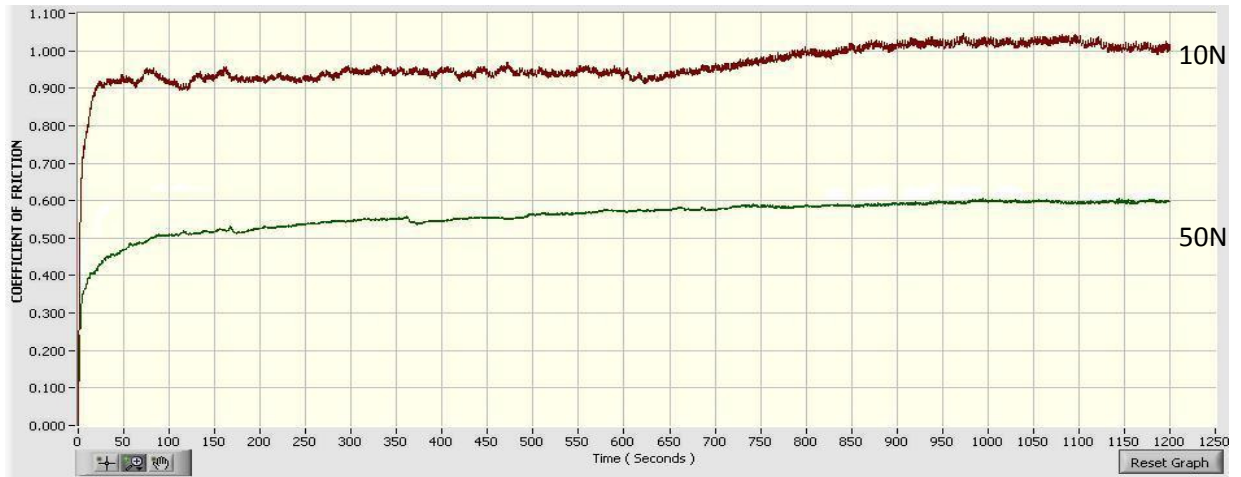


**Fig. 2. Graph of coefficient of fraction vs time for composite sample 6% of SBR with load of 10N and 50N**

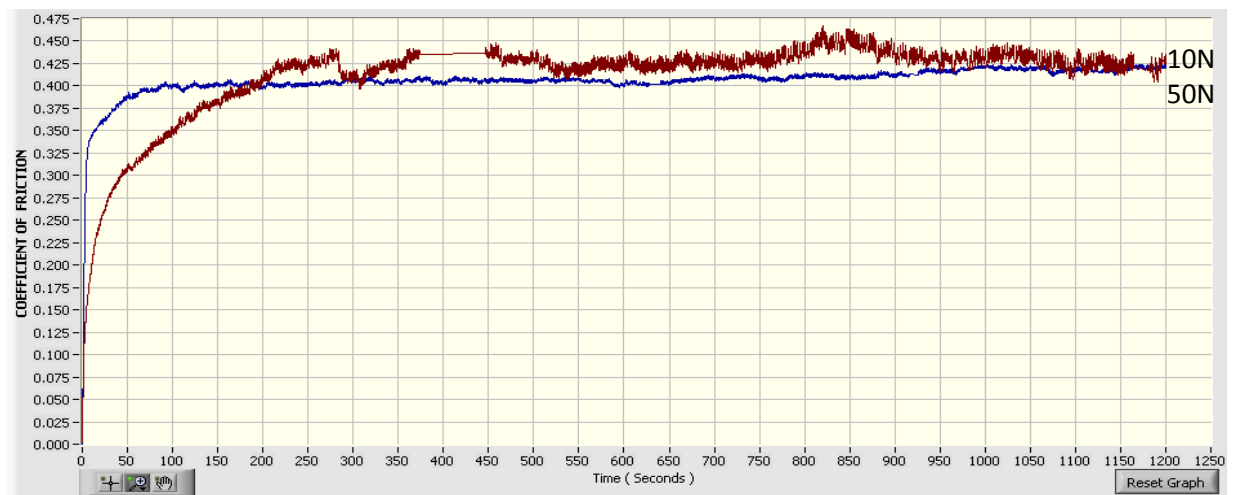


**Fig. 3. Graph of coefficient of fraction vs time for composite sample 6% of SBR (10kGy) with load of 10N and 50N**



**Fig. 4. Graph of coefficient of fraction vs time for composite sample 6% of SBR (20kGy) with load of 10N and 50N**

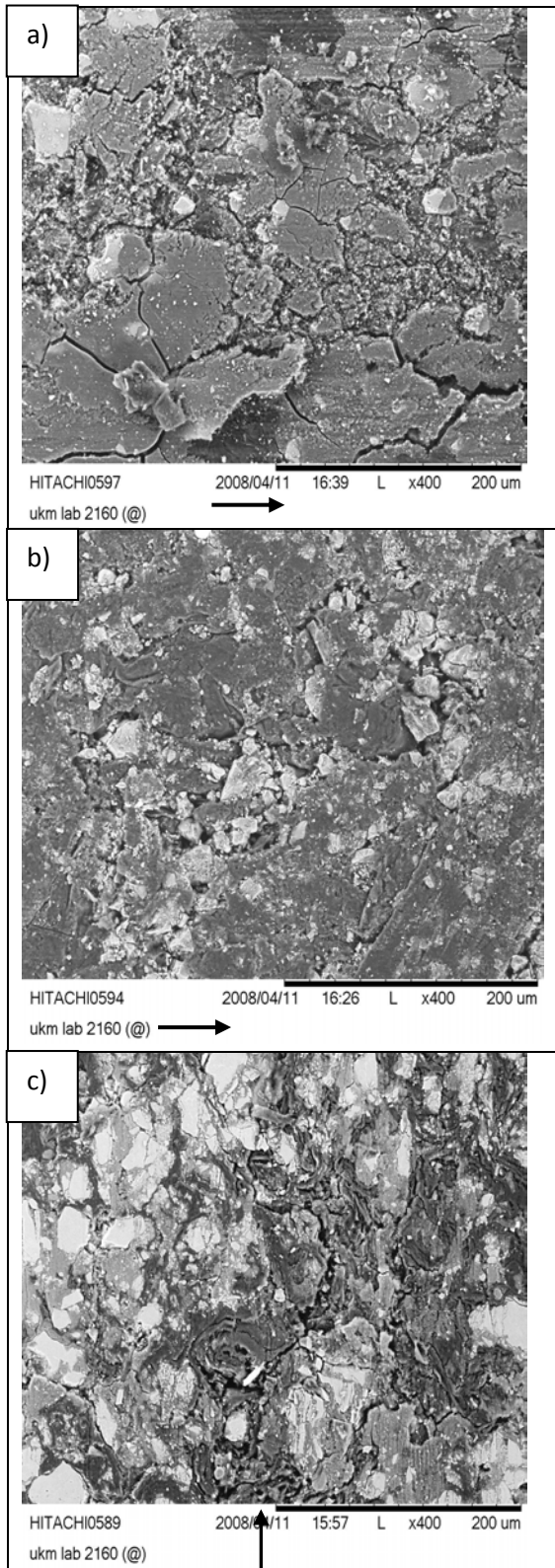


**Fig. 5. SEM Micrograph for surface wear of composite sample with 10N load a) 6% SBR, b) 6% SBR (10kGy), c) 6% SBR (20 kGy). The arrow showed the direction of sliding.**

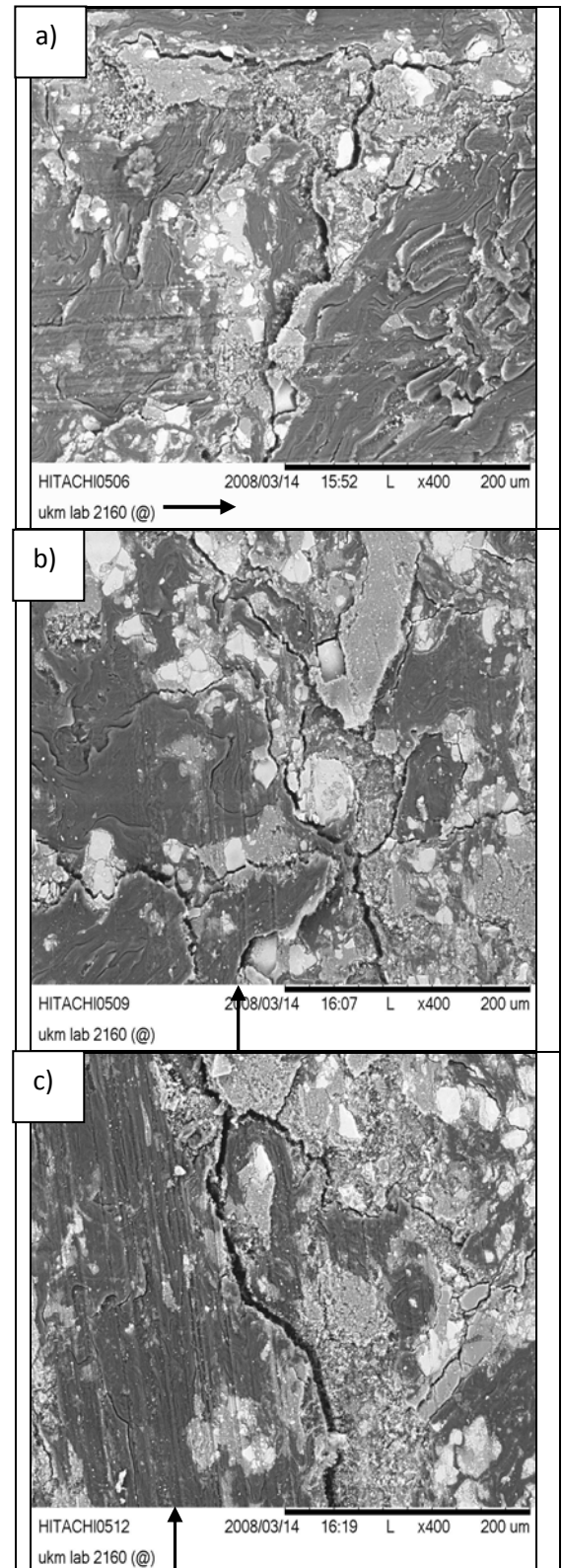


**Fig. 6. SEM Micrograph for surface wear of composite sample with 50N load a) 6% SBR, b) 6% SBR (10kGy), c) 6% SBR (20 kGy). The arrow showed the direction of sliding.**

## 5. Conclusion

As a conclusion, the objectives achieved. Couples of results obtained after several test were conducted. The results for the wear tests shows that the 6% SBR composite with 20kGy electron stream have the most optimum wear attribute. The sample shows the lowest lost of mass and volume. The 6% SBR (20 kGy) composite sample shows the lowest K' value. While the 6% SBR composite sample shows the worst wear attribute among the entire composite sample studied. This matter is supported by the total of mass lost and the highest K' value. The K' value for the 6% SBR (20kGy) shows an increment with an added force, adhesive wear occurs, and the composite sample may stick to the disc.

## References

- [1] Aggarwal, L. K. 1995. Bagasse-reinforced cement composites. *Cement & Concrete Composites* **17**:107-112.
- [2] Ashby & Jones, 1986. *Engineering Materials 2: An Introduction to Microstructures, Processing and Design*. Great Britain. Pergamon Press.
- [3] Bilba, K., Arsene, M-A. & Quensanga, A. 2002. Sugar cane bagasse fibre reinforced cement composites. Part I. Influence of the botanical composites of bagasse on the setting of bagasse/cement composite. *Cement & Concrete Composites* **25**: 91-96.
- [4] Bledzki, A.K., Reihmane, S., Gassan, J.-1996. Properties and modification method for vegetable fibers for natural fiber composites. *J. of Appl. Polym. Sci.* **59**: 1329-1336.
- [5] Callister, W.D. 2000. *Materials Science and Engineering : An Introduction*. 5th Ed. New York. John Wiley and Son.
- [6] Drayman, M., Zakaria, S. & Murshidi, J. A. 2001. Estimation of Crystallinity and Crystalline Size of Cellulose in Benzylated Fibres of Oil Palm Empty Fruit Bunches by X-Ray Diffraction. *Jpn. J. App. Phys. Pt. 1.* **40**: 3311-3314.
- [7] Hassan, M.L., El-Wakil, N.A. & Sefain, M.Z. 2001. Thermoplastization of Bagasse by Cyanoethylation. *J. App. Polym. Sci.* **79**: 1965-1978.
- [8] Hassan, M.L., Rowell, R.M., Fadi, N.A., Yakoub, S.F. & Christainsen, A.W.. 2000. *J. App. Polym. Sci.* **76**: 561.
- [9] Hollaway, L. 1993. *Polymer Composites For Civil and Structural Engineering*. Blakie Academic and Professional.
- [10] Ismail, M.R, Youssef, H.A. Magdy.A.M.Ali A.H.Zahran and Afifi, M.S.. 2005. Utilization of emulsion polymer for preparing bagasse fibers polymer-cement composites. *Journal of Applied Polymer Science. Research Article*.
- [11] Jones, R.M. 1993. *Mekanik Bahan Rencam*. Terj. Daud Abd Rahman. Skudai; Unit Penerbitan Akademik Universiti Teknologi Malaysia.
- [12] Kuzminskii, A., Nikitian, T.S., Zhuravskaya, E.V., Oksentievich, L.A., Sumita, L., and Vituskhin, T.S., 1958, *Proceedings of Inter. Conf. of Peaceful uses of atomic energy*, Geneva, Switzerland, vol. (99), p.258.
- [13] Mantegazza, G., Penna, A.M., and Tattoni, S.. 1994. Modification of cement mortars by polymeric latexes and their use for repairing concrete. *ACI Special Publication*, vol. (148).
- [14] Marshall Cleland, Richard Galloway, Frederic Genin, & Mikael Lindholm. 2002. The use of dose and charge distributions in electron beam processing. *Radiation Physics and Chemistry* **63**: 729-733.
- [15] M. Madani & M. M. Badawy. 2004. Influence of Elektron Beam Irradiation and Step-Crosslinking Process on Solvent Penetration and Thermal Properties of Natural Rubber Vulcanizates. *Egypt. J. Solids*, Vol. 27, No.2.
- [16] Paiva, J.M.F. & Frollini, E. 2002. Sugarcane Bagasse Reinforced Phenolic and Lignophenolic Composites. *J. App. Polym. Sci.* **83**: 880-888.
- [17] Radwan Q. M. Dweiri. 2003. Property-morphology relationship of sugarcane bagasse fibre-filled polyamide 6 composites. Tesis Sarjana. Universiti Kebangsaan Malaysia.
- [18] Rozli, 2006. *Nota Kuliah Komposit*. Bangi: JKMB Fakulti Kejuruteraan Universiti Kebangsaan Malaysia.

- [19] Rowell, J. S. & Han, J.S. 1996. *Chemical Composition of Fibers: Paper and Composites From Agro-Based Resources*. hlm. 95-91. Boca Raton, FL: CRC Lewis Publishers.
- [20] Salyer, I. O., Ball III, G. L., Usmani, A. M. & Werkmeister, D. W. 1975. Development of Low Cost Roofing from Indigenous Materials of Developing Nations. AID/US. Pp. 31,32, 109, 199.
- [21] Vazquez, A., Dominguez, V.A. & Kenny, J.M. 1999. Bagasse Fibre-Polypropylene Based Composites. J. Thermoplast. Compos. Mater. 12: 477-497.

## VARIATION IN FATIGUE CRACK GROWTH DUE TO THE GEOMETRICAL AND LOADING EFFECTS

S. M. Beden\*, S. Abdullah, A. K. Ariffin and N. A. Al-Asady

Department of Mechanical and Materials Engineering

Universiti Kebangsaan Malaysia

43600 Bangi, Selangor

Malaysia

\*Corresponding Author: E-mail: [sabah@eng.ukm.my](mailto:sabah@eng.ukm.my)

### Abstract

*The problem of crack growth is a major issue in the prediction and maintenance of aerospace structures, as well as other structural elements in mechanical engineering. Fatigue crack growth as consequence of service loads depends on many different contributing factors. Due to the number and complexity of the mechanisms involved in the fatigue crack growth problem, no universal solution exists yet and there is no general agreement among researchers for any of the available models. Most of the results reported are dealing with geometry with some factors separately. This paper simulates the factors affecting the fatigue crack growth of metallic materials under cyclic loading. For the simulation purpose, three points bend (TPB) with span to width ratio 8:1 and compact tension (CT) specimen geometries were used. There are many factors affecting the fatigue crack growth in structures, such as initial crack length, stress ratio, aspect ratio and type of geometry. The behavior of such cases is shown using Forman model. The fatigue crack growth obtained from the two geometries was compared. Different values of these factors showed different effects on the fatigue crack growth. For further study need to validate the modelling procedure with experimental work as well as take into account the other factors such as; other types of geometries with fatigue crack models and environmental effects.*

**Keywords:** Cyclic loading, factors; fatigue crack growth model; geometry; simulation

### 1. Introduction

The fracture mechanics scientists and engineers have made tremendous advances, from the basic practical approach dominated by Paris–Erdogan law [1] to more and more sophisticated crack growth models. Mathematical and metallurgical models, experimental analysis of simple models and testing of complex structures have resulted in thousands of publications, dozens of models for crack growth and life prediction. In some cases the difficulty of machining a full-size specimen has made investigators to design sub-size specimens [2-5]. There are many factors affecting the fatigue crack growth in structures, such as; stress ratio, thickness of the specimen or aspect ratio, types of specimen geometries,

fatigue crack growth model etc [6, 7]. A major concern of fracture mechanics is the influence of the load ratio on the behaviour of cracks. This is expressed in the stress ratio ( $R$ ), which is classically defined as: the ratio of minimum to maximum applied stresses [8].

Many semi-empirical and empirical models for fatigue crack growth have been proposed in the literature to account for the stress ratio dependence of FCG curves [9-12]. It was argued that the reason for this influence is the crack closure effect which introduced first by Elber [13, 14]

From the previous literature papers, which studied on the effect of thickness on fatigue crack growth rate (FCGR) three different responses have been reported as; FCGR is not affected by thickness [15], FCGR decreased by decreasing thickness [16,

17] and FCGR accelerated by decreasing thickness [18]. Thus results reported by various investigators do not yield a general explanation for the thickness effect on FCGR.

Most of the results reported are dealing with geometry with some factors separately. Due to the number and complexity of the mechanisms involved in the fatigue crack growth problem, no universal solution exists yet and there is also no general agreement among researchers for any of the available models. In the present investigation, for the purpose of standardizing the fatigue crack studies for different geometries as well as the factors on metallic materials under cyclic loading, two types of specimen geometries were examined; three points bend (TPB 8:1) and compact tension shape (CT). This study mainly focuses on the evaluating of the fatigue crack growth with application of the factors such as; initial crack length, stress ratio, aspect ratio and the capability of geometries to show their effects. The results from these different geometries are compared with application of these factors. The behaviour of such cases is shown using Forman model. The comparison shows different effects on FCG for these specimen geometries.

## 2. Theoretical Background

A simple and well-known method for predicting fatigue crack propagation is a power law described by Paris and Erdogan [1], and it is also known as the Paris Law. The equation represents the first application of fracture mechanics to fatigue and is given by the following relationship:

$$\frac{da}{dN} = C_p (\Delta K)^{mp} \quad (1)$$

where  $C_p$  is the intercept and  $mp$  is the slope on the log-log plot of  $da/dN$  versus  $\Delta K$ . Equation 1 represents a straight line on the log-log plot of  $da/dN$  versus  $\Delta K$  and thus describes region II of the fatigue rate curve.

Although, Walker [10] improved the Paris model by taking account of the stress ratio, neither model could account for the

instability of the crack growth when the stress intensity factor approaches its critical value. Forman [19] improved the Walker model by suggesting a new model, which is capable of describing region III of the fatigue rate curve and includes the stress ratio effect. The Forman law is given by this mathematical relationship:

$$\frac{da}{dN} = \frac{C_F (\Delta K)^{m_y}}{(1-R)K_c - \Delta K} = \frac{C_F (\Delta K)^{m_y}}{(1-R)(K_c - K_{max})} \quad (2)$$

where  $K_c$  is the fracture toughness for the material and thickness of interest. Equation 2 indicates that as  $K_{max}$  approaches  $K_c$ , then  $da/dN$  tends to infinity. Therefore, the Forman equation is capable of representing stable intermediate growth (region II) and the accelerated growth rates (region III).

## 3. Methodology

In this application three points bend (TPB 8:1) and compact tension (CT) specimen geometries (Figure 2) are used [20,21]. For these geometries the stress intensity factors were calculated using different equations depending mainly on the function  $f(\alpha)$ , where  $\alpha=a/w$  [22]. The equations for each geometry are shown in Table 1. Experience shows that the great majority of crack results from the opening (tensile) mode, while the other two modes (II and III) are rare and occur in a combined fashion only. It appears that the majority of such combinations are converted to mode I by nature itself, unless there is a preferred direction of crack growth in a particular material.

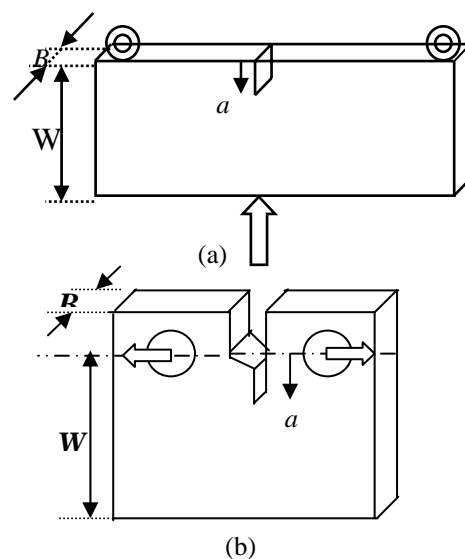


Fig. 2. Specimen geometries (a) Three Point Bend (TPB), (b) Compact Tension (CT)

**Table 1 Relations of aspect ratio for different geometries**

<u>Three Point Bend</u>	
$f(\alpha)=$	$\frac{1.99 - \alpha(1 - \alpha)(2.15 - 3.39\alpha + 2.7\alpha^2)}{(1 + 2\alpha)(1 - \alpha)^{3/2}}$
<u>Compact Tension</u>	
$f(\alpha)=$	$\frac{(2 + \alpha)(0.886 + 4.64\alpha - 13.32\alpha^2 + 14.72\alpha^3 - 5.6\alpha^4)}{(1 - \alpha)^{3/2}}$

Many pipes and pressure vessels are subjected to complex cyclic loading spectrums ranging from small vibrations to large load excursions. To conduct structural reliability analyses of these applications, fatigue crack growth properties are crucial material data input parameters. Moreover, an understanding of the fatigue crack growth characteristics of the required pipes and pressure vessels grade materials is essential to evaluate useful life. A most common steel material used is ASTM A533 for these purposes with the specification of the mechanical and fatigue properties shown in Table 2.

**Table 2: Mechanical and fatigue properties of the material**

Yield Stress (MPa) $Y_S$	485
Ultimate Tensile Strength (MPa) $UTS$	602
Plane Strain Fracture Toughness (MPa $\sqrt{m}$ ) $K_{IC}$	121
Plane Stress Fracture Toughness (MPa $\sqrt{m}$ ) $K_{ID}$	242
Paris Law Coefficient (m/MPa $\sqrt{m}$ ) <sup>n</sup> $C$	3e-12
Paris law Exponent	3
Delta K threshold at $R=0$ (MPa $\sqrt{m}$ ) $D_o$	5.252
Delta K threshold at $R>0$ (MPa $\sqrt{m}$ ) $D_I$	1.952
Fatigue strength coefficient (MPa) $S_f$	1005
Fatigue strength exponent $b$	-0.095
Fatigue ductility coefficient $E_f$	0.35

Components and structures are subjected to quite diverse load histories; their histories may be rather repetitive with

different values. Cyclic load history as a constant amplitude loading was used with this analysis. To account load ranges and mean of the load history, rainflow counting method was used. The two specimen geometries were analyzed under the cyclic loads with different initial crack ratio (6 to 14 mm), different aspect ratio (0.26 to 0.11). Most mean stress effects on crack growth have been obtained for only positive stress ratio, i.e.,  $R \geq 0$ . In the present analysis, to show the effects of different stress ratio from negative to positive are shown in Table 3. The Forman model was examined and the modelling and simulation analyzed based on the Glyphwork software package [23].

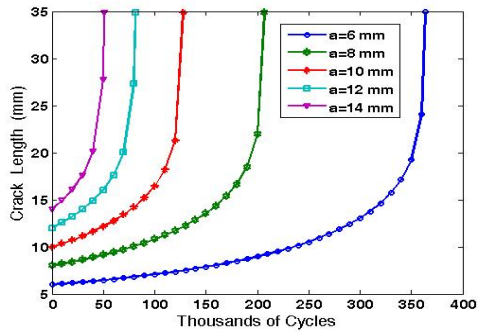
**Table 3 Fatigue loading of load histories with stress ratios**

Stress Ratio ( $R$ )	Max. Load (kN)	Min. Load (kN)
0.3	146	- 44
- 0.15	165	-24
0	190	0.2
0.3	275	84
0.5	385	195

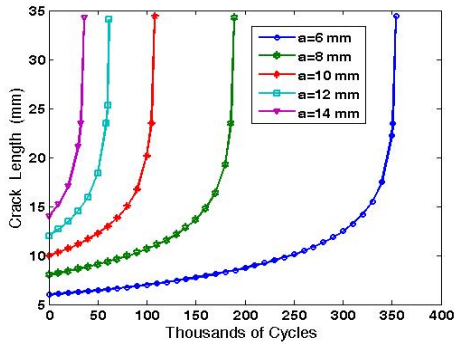
#### 4. Results and Discussion

For given stress range, the number of cycles required for crack growth depends on the initial crack length. Local stress range ahead of the crack tip will be higher for a deeper crack than for shallow crack because the stress intensity factor is higher for deeper crack. This explains why the number of cycles required for crack growth in structures having a long crack would be less in comparison to the structures having a small crack, this shown clearly in Figures 3 (a and b). The highest number of cycles is given by TPB geometry (Figure 3a). The differences between the numbers of cycles for the two specimen geometries in average are about 20%.

The effects of stress ratio ( $R$ ) ranging from  $-0.3$  to  $0.5$  on crack growth are shown in Figures 4 (a and b). The findings show that higher stresses ratio lead to the less number of cycles for fatigue crack growth, when it compared to the low stress ratio for the geometries. In the present results, although, the curves show the same behaviour, but the average differences are about 16% for negative to positive values. The results also indicate a good agreement with the finding in previous work performed by Maymon [24] and Huang et al. [25,26]. Generally, the TPB geometry gave the maximum number of cycles, while the CT geometry gave the minimum cycles for the same values of stress ratio.

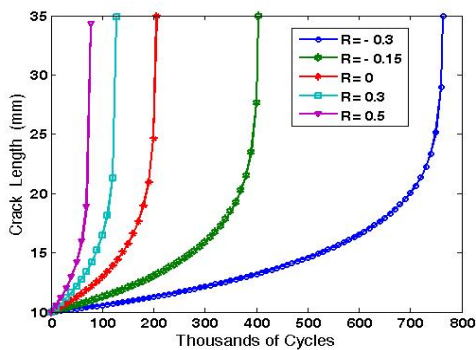


(a)

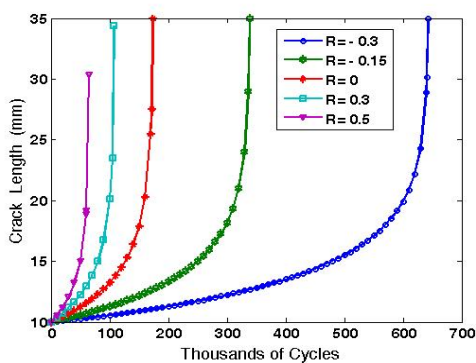


(b)

**Fig. 3. Effects of initial crack length on FCG for the following specimen geometries. (a) TPB and (b) CT**



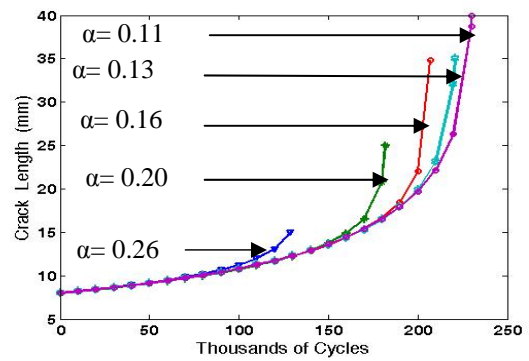
(a)



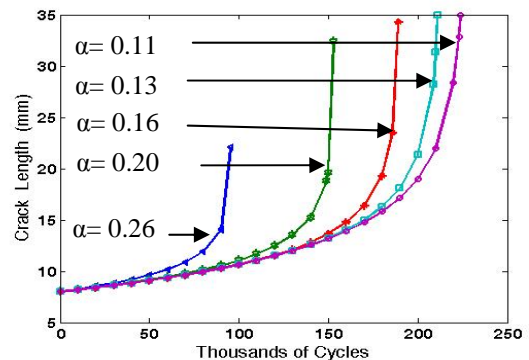
(b)

**Fig. 4. Effects of stress ratio on FCG for specimen geometries (a) TPB, (b) CT**

Among the factors affecting the crack growth is the aspect ratio ( $\alpha$ ), which represents the ratio of the crack length ( $a$ ) to the width of the specimen geometry ( $w$ ). This factor was simulated and shown in Figures 5 (a and b) for the two geometries. These figures showed the increasing of the aspect ratio (reducing the width with constant initial crack length) gave less number of cycles and vice versa, which means the width has much effect on the life of different geometries. The difference in the number of cycles for the two geometries is about 20% in average and the number of cycles calculated for TPB is higher than for CT.



(a)



(b)

**Fig. 5. Effects of different aspect ratios on FCG for specimen geometries. (a) TPB, (b) CT**

## 5. Conclusion

In order to simulate the fatigue crack on metallic materials under cyclic loading, two types of specimen geometries (TPB and CT) were examined. This study mainly focuses on the evaluating of the fatigue crack growth for these geometries related to different factors. The results are compared with application of initial crack length, stress ratio and aspect ratio to show their effects. The number of cycles required for crack growth in structures has a long crack would be less in comparison to that with a small crack at the

same stress ratio. Local stress range ahead of the crack tip will be higher for a deeper crack than for shallow crack. The observation shows that geometry with higher stress ratio require less cycles for crack growth towards failure compared to that with lower stress ratio for all geometries.

Observation shows that high stress ratio leads to less number of cycles for fatigue crack growth compared to that with low stress ratio for the all geometries. As a general the geometry TPB gave the maximum number of cycles for the same values of stress ratio. For different aspect ratio the differences in the number of cycles for the two geometries is about 20% in average. Increasing the aspect ratio gives less number of cycles.

Finally, there are a large number of factors affecting the FCG, so it is difficult to judge which one can be used as the standard one relating to such factors. For further study, need to take into account other factors such as; other type of geometries, FCG models as well as the aspect ratio, initial crack length and stress ratio.

## References

- [1] Paris, PC., Erdogan, F. A Critical Analysis of Crack Propagation Laws. *Journal of Basic Engineering*; Transaction, American Society of Mechanical Engineers, Series D, Vol. 85, pp. 528-534,1963.
- [2] Jeelani, S., Natarajan, R., Reddy, GR. A subsize fatigue specimen. *International Journal of Fatigue*, Vol. 8, pp.159-164, 1986.
- [3] Molent, L., Jones, R., Barter, S. Pitt, S. Recent developments in fatigue crack growth assessment. *International Journal of Fatigue*; 28:1759-1768, 2006.
- [4] Tianwen Zhao, Jixi Zhang, Yanyao Jiang, A study of fatigue crack growth of 7075-T651 aluminum alloy. *International Journal of Fatigue*, Vol. 30, pp. 1169-1180, 2008.
- [5] Lee, EU., Glinka, G., Vasudevan, AK., Iyyer, N., Phan, ND. Fatigue of 7075-T651 aluminum alloy under constant and variable amplitude loadings. *International Journal of Fatigue*, 2009 (under press).
- [6] Christopher, D., Stephens, R. Fatigue crack growth and life predictions under variable amplitude loading for a cast and wrought aluminum alloy. *International Journal of Fatigue*. Vol. 28, pp.53-60, 2006.
- [7] Richard, H., Sander, M. Fulland, M. Kullmer, G. Development of fatigue crack growth in real structures. *Engineering Fracture Mechanics*, Vol. 75, pp. 331-340, 2008.
- [8] Ellyn, F.; Li, H.P. Fatigue crack growth in large specimens with various stress ratios. *Journal of Pressure Vessel Technology*, Vol. 106, pp. 255-260, 1984.
- [9] Forman, RG., Kearney, VE., Engle, RM. Numerical analysis of crack propagation in cyclic-loaded structures. *Journal of Basic Engineering*, Vol. 89, pp. 459-464, 1967.
- [10] Walker, EK. The effect of stress ratio during cracks propagation and fatigue for 2024-T3 and 7076-T6 aluminum. In: Effect of environment and complex load history on fatigue life, ASTM STP 462. Philadelphia: *American Society for Testing and Materials*, pp. 1-14, 1970.
- [11] Newman, Jr JC. A crack closure model for predicting fatigue crack growth under aircraft spectrum loading. *ASTM/STP,748*, pp. 53-84, 1981.
- [12] Schijve, J., Skorupa, M., Skorupa, A., Machniewicz, T., Gruszczynski, P. Fatigue crack growth in the aluminium alloy D16 under constant and variable amplitude loading. *International Journal of Fatigue*, BVol. 26, pp. 1-15, 2004.
- [13] Elber, W. Fatigue crack closure under cyclic tension. *Engineering Fracture Mechanics*, Vol. 2(1), pp. 37-44, 1970.
- [14] Elber, W. The significance of fatigue crack closure. In: *Damage Tolerance in Aircraft Structures*, ASTM-STP 486, ASTM PA; pp. 230-242, 1971.
- [15] Sullivan, AM., Crooker. TW. The effects of specimen thickness and stress relief on fatigue crack growth rate in Ni-Cr-Mo-V steel. *Journal of Testing and Evaluation*, Vol. 5, pp. 96-101, 1977.
- [16] Fujitiani, K., Sakai, T., Nakagawa, A., Tanaka, K. Effect of specimen thickness on fatigue crack propagation in high strength steels. *Bulletin Japan Society of Mechanical Engineers*, Vol. 25, pp. 1195-1201, 1982.
- [17] Heung-Bae, P., Kyung-Mo, K., Byong-Whi, L. Plastic zone size in fatigue cracking.

- International Journal of Pressure Vessel and Piping, Vol. 68, pp. 279-285, 1966.
- [18] Tesch, A., Pippan, R., Doker, H. New testing procedure to determine  $da/dN$ - $dK$  curves at different, constant R-values using one single specimen. International Journal of Fatigue, Vol. 29, pp.1220-1228, 2007.
- [19] Forman, RG. Study of fatigue crack initiation from flaws using fracture mechanics theory. Engineering Fracture Mechanics, Vol. 4(2), pp. 333-345, 1972.
- [20] ASTM Standard E399-90. Standard test method for plane strain fracture toughness of metallic materials. Annual book of ASTM Standards, vol. 03.01. ASTM International; 2002.
- [21] ASTM Standard E647-00. Standard test method for measurement of fatigue crack growth rates. Annual book of ASTM Standards, vol. 03.01. ASTM International; 2002.
- [22] Mohanty, J. R., Verma, B. B., Ray, P. K. Prediction of fatigue crack growth and residual life using an exponential model: Part II (mode-I overload induced retardation). International Journal of Fatigue, Vol. 31, pp. 425-432, 2009.
- [23] nCode User guide manual. ICE-FLOW cracks growth. V2.0. 2003.
- [24] Maymon, G. A 'unified' and a  $(\Delta K.K_{max})^{1/2}$  crack growth models for aluminum 2024-T351. International Journal of Fatigue, Vol. 27, pp. 629-638, 2005.
- [25] Huang, Xi and Moan, T. Improved modeling of the effect of R-ratio on crack growth rate. International Journal of Fatigue, Vol. 29, pp. 591-602, 2007.
- [26] Huang Xi., Moan, T., Cui W. An Engineering model of fatigue crack growth under variable amplitude loading. International Journal of Fatigue, Vol. 30, pp. 2-10, 2008.

## THE ASSESSMENT OF RHEOLOGICAL MODEL RELIABILITY IN LUBRICATING BEHAVIOUR OF VEGETABLE OILS

Sunny Goh Eng Giap<sup>1\*</sup>, Wan Mohd Norsani Wan Nik<sup>2</sup>  
Mohammad Fadhli Ahmad<sup>2</sup>, Azira Amran<sup>1</sup>

<sup>1</sup>Department of Engineering Science, Faculty of Science and Technology, Universiti Malaysia Terengganu, Mengabang Telipot, 21030 Kuala Terengganu, Terengganu, Malaysia

<sup>2</sup>Department of Maritime Technology, Faculty of Maritime Studies and Marine Science, Universiti Malaysia Terengganu, Mengabang Telipot, 21030 Kuala Terengganu, Terengganu, Malaysia

\*Corresponding Author: [sunnyg@umt.edu.my](mailto:sunnyg@umt.edu.my); Tel: +609-668 3622; Fax: +609-669 4660

### Abstract

Viscosity as a function of shear rate and temperature can be modelled with a number of equations. Among them are power-law, Carreau, Cross, Arrhenius, etc. Each model has its own limitation, for which, under certain circumstance the models failed to provide an adequate observation of the fluid behaviours. The objectives of the current study are to evaluate the viscosity changes of vegetable oils, model viscosity with well-known rheological equations, and also to identify model limitation through graphical and numerical observations. Few food grade vegetable oils were subjected to viscometer measurements of viscosity at shear rate and temperature ranged from 3 to 100 rpm, and 40 to 100 degree Celsius, respectively. Results have shown that vegetable oils behaved as pseudoplastic. Although none of these of models provide a complete representation of oils behaviour, some models' constants could be used to explain the characteristic of the oils.

**Keywords:** viscosity; rheology; vegetable oils

### 1. Introduction

Viscosity study has been widely studied by scientists and engineers on various purposes. These include polymer science, heat transfer phenomena, petroleum reservoir development, coatings, scale modelling of magmatic intrusion, oil degradation, lubrication, etc. [1-5]. Viscosity is influenced by different factors, such as, additive, catalyst, temperature, shear rate, time, molecular weight, moisture, pressure, concentration, etc. Among these, temperature and shear rate are the most studied parameters.

In general, viscosity is defined as the ratio of shear stress (force over cross section area) to the rate of deformation (the difference of velocity over a sheared distance), and is presented by:

$$\eta = \tau / \left( \frac{\partial u}{\partial x} \right) \quad (1)$$

where:  $\eta$ , dynamic viscosity (Pa.s);  $\tau$ , shear stress (N/m<sup>2</sup>); and  $\partial u / \partial x = \gamma$ , rate of deformation or velocity gradient or better known as shear rate (1/s). This relation will give constant viscosity, if shear stress is proportionally changed with velocity gradient. Fluid that follows this behaviour is termed as Newtonian fluid.

However, in the measurement of viscosity, an increase in shear stress leads to a greater portion increase in shear rate, and therefore, reducing viscosity value as indicated by viscometer. This phenomenon is known as shear-thinning behaviour. For inverse observation, it exhibits shear-thickening. In this study, the authors limit the following literature reviews to shear-thinning, which is the topic of the current study.

Thus, in nature, Eq. 1 has failed to provide a good representation of real phenomena for all fluids. It indicates the presence of scientific gap for which new equation is needed. There were

numerous researchers responded to propose alternative equation. Among those equations are power-law, Cross, Carreau, Bingham, Herschel-Bulkley, Casson, Sisko, etc. These equations are presented in sequence as followings [6, 7]:

$$\eta = K_p \dot{\gamma}^{n_p-1} \quad (2)$$

$$\eta = \eta_{\infty, \dot{\gamma}} + \frac{\eta_{o, \dot{\gamma}} - \eta_{\infty, \dot{\gamma}}}{1 + (\alpha_c \dot{\gamma})^m} \quad (3)$$

$$\eta = \eta_{\infty, \dot{\gamma}} + \frac{\eta_{o, \dot{\gamma}} - \eta_{\infty, \dot{\gamma}}}{[1 + (\lambda_c \dot{\gamma})^2]^N} \quad (4)$$

$$\eta = \eta_o + \eta' \quad (5)$$

$$\eta = K_H \dot{\gamma}^{n_H-1} + \eta_{\infty, \dot{\gamma}} \quad (6)$$

$$\sqrt{\eta} = \frac{K_C}{\sqrt{\dot{\gamma}}} + \sqrt{\eta_{\infty, \dot{\gamma}}} \quad (7)$$

where:  $K_p$  and  $K_H$ , consistency index (Pa.s<sup>n</sup>);  $K_C$ , consistency index (Pa<sup>1/2</sup>.s);  $n_p$  and  $n_H$ , flow behaviour index (dimensionless);  $\eta_{\infty, \dot{\gamma}}$ , viscosity at infinite-shear rate (Pa.s);  $\eta_{o, \dot{\gamma}}$ , viscosity at zero-shear rate (Pa.s);  $m$  and  $N$ , constant (dimensionless);  $\lambda_c$  and  $\alpha_c$ , characteristic relaxation time (s);  $\eta_o$ , yield stress-viscosity at initial flow condition (Pa.s); and  $\eta'$ , Bingham plastic viscosity (Pa.s).

From the many equations which relate viscosity as a function of shear rate, power-law, Cross, Carreau, and Herschel-Bulkley are the most commonly appeared in literatures. Particularly on power-law model, it is perhaps the most widely applied equation to many fields of research, which can be a result of its simple form of equation providing reasonable fitting, and also, a reasonable representation of equation constants in terms of degree of viscous and fluid flow behaviour.

Apart from the effect of shear rate, viscosity is also highly influenced by the changes of fluid body temperature. Fluid viscosity as a function of temperature is normally found to have a good correlation between natural logarithmic of viscosity, and the reciprocal of absolute temperature. Thus, its relation is well represented by Arrhenius-type relationship [8], which has the following form of equation:

$$\eta = \eta_{\infty, T} e^{E_a / RT} \quad (8)$$

where:  $\eta_{\infty, T}$ , viscosity at infinite-temperature (Pa.s);  $E_a$ , activation energy (N.m.mol<sup>-1</sup>);  $R$ , universal gas constant (N.m.K<sup>-1</sup>.mol<sup>-1</sup>); and  $T$ , absolute temperature (K).

In addition to Arrhenius-type relationship, there are Fulcher and William-Landel-Ferry equations [9], as follows:

$$\log \eta = A' + \frac{B'}{T - T_{\infty}} \quad (9)$$

$$\log \left( \frac{\eta}{\rho T} / \frac{\eta_o}{\rho_o T_o} \right) = - \frac{c_1^0 (T - T_o)}{c_2^0 + (T - T_o)} \quad (10)$$

where:  $A'$  and  $B'$ , constant (dimensionless and K, respectively);  $T_{\infty}$ , constant (K);  $\rho$ , density of fluid (kg/m<sup>3</sup>);  $\rho_o$ , fluid density at reference temperature (kg/m<sup>3</sup>);  $T_o$ , reference temperature (K);  $\eta_o$ , viscosity at reference temperature (Pa.s);  $c_1^0$ , constant (dimensionless); and  $c_2^0$ , constant (K).

The influence of either temperature or shear rate on viscosity is only the two of the many parameters involved. In the literature, there are numerous equations addressing either or a combination of parameters on viscosity, such as, shear-time, composition, moisture, pressure, oil degradation, molecular weight, density, etc [10-18]. Since a complete understanding on these parameters is not part of the objective of this study, the current work is only limited to the effect of shear rate and temperature as an individual factor rather than a combination of both or other related parameters.

Thus, the objectives of the current study are: (1) to evaluate the changes of viscosity on vegetable oils as a function of temperature and shear rate; (2) to model the vegetable viscosity data through some well-known rheological equations; and (3) to evaluate the viscosity properties of oils through the comparison of numerical data and graphical observation. Also, the validity of models' constant will be justified of its usefulness as reliable indication on oils flow behaviour.

## 2. Materials and Methods

The food grade vegetable oils of coconut, olive, rice bran, and sesame used in this study were purchased from local market.

A Brookfield (Viscometer model DV-I+) rotational-type viscometer was used to measure the viscosity of oil samples. Before use, the viscometer (accuracy,  $\pm 1\%$  full-scale range; repeatability, 0.2% full-scale range) was calibrated with 4.7 cP Brookfield silicone viscosity standard. The viscosity of the oils was measured in triplicate at ten different shear rates. SP-18 spindle was operated at different speeds between 3 and 100 rpm. A temperature controller (temperature accuracy of  $\pm 1\%$ ) was used to increase the temperature of the oil samples from 40 up to 100 °C with an increment of 10 °C. For each increment of 10 °C, the oil samples were left 15 minutes until steady-state heat transfer was achieved.

Viscosity measurement begins by setting 40 °C at temperature controller before assigning discrete rotational speed at viscometer meter, which was from the highest speed 100 rpm to the lowest 3 rpm. After viscosity measurement at ten discrete rotational speeds, an increase to 50 °C was set and then, repeated steps of viscosity measurement at discrete rotational speeds from 100 to 3 rpm were followed. A similar step was repeated for other temperatures until 100 °C.

The viscosity value from viscometer was based on the built-in calculation as part of the physical rotational torque sensor. Shear stress and shear rate was calculated base on the respective equations [19]:

$$\tau = \frac{M}{2\pi R_b^2 h} \quad (11)$$

$$\gamma = 1.318 \times N \quad (12)$$

where:  $M$ , torque (N.m);  $R_b$ , radius of the spindle (m);  $h$ , height of the spindle (m); and  $N$ , rotational frequency of spindle (rpm).

The shear rate dependence of vegetable oils was modelled with power-law, Cross, Carreau, and Herschel-Bulkley which is represented by Eqs. 2, 3, 4, and 6, respectively. Bingham equation was not used due to the nature of its equation unable to model shear-thinning behaviour. Sisko equation was more or less equivalent to Herschel-Bulkley and it has one constant less than Herschel-Bulkley. For this reason, it was not used in the modelling.

The temperature dependence of oils was investigated with Arrhenius-type relationship, as presented in Eq. 8. Fulcher and William-Landel-

Ferry equations were not implemented due to unexplainable constant properties, and unavailable experimental data as require in the equation.

The data analysis was completed with Microsoft Excel for simple calculation and graphical preparation, and Mathematica for equation modelling. Based on limited timeframe, the equation fitting on experimental data was carried out at 50 and 90 °C for shear rate dependence equation, and 5 and 60 rpm for temperature dependence equation.

### 3. Results and Discussion

#### 3.1. Shear rate dependence of oil viscosity

Result shows a decreasing viscosity of all four oils as the shear rate increases. This flow behaviour is known as shear-thinning or better known as pseudoplastic. The reduction of viscosity is more apparent at the region of low shear rate, and followed by lesser influence of shear rate as the shear rate continue to increase to the high shear rate region. It is also noticed larger difference between oils viscosity at low shear rate region, and a convergent of their values was observed at high shear rate region, except for coconut oil. The convergent was observed greater at higher temperature (Figs. 1 and 2). Among the four oils, olive was observed as the most viscous oil, in relative comparison to the other three oils. This was then followed by sesame, rice bran, and coconut oils. Moreover, the oils did not exhibit time dependence behaviour under the condition of experiment.

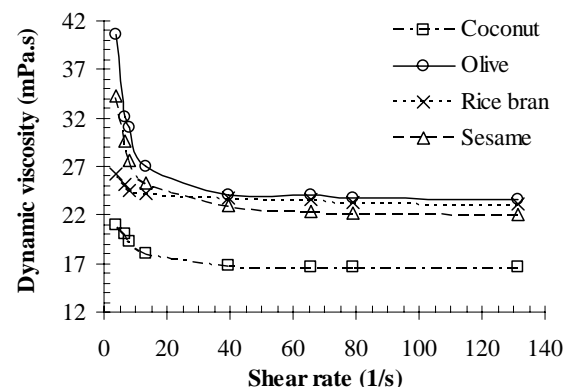
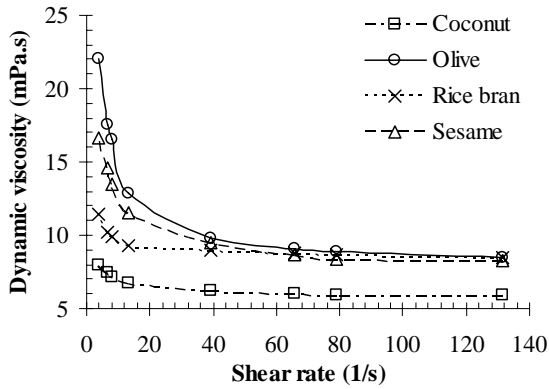


Fig. 1. Viscosity decreases with increasing shear rate at 50 degree Celsius



**Fig. 2. Viscosity decreases with increasing shear rate at 90 degree Celsius**

### 3.2. Shear rate dependence of rheological models

The rheological model as for power-law, Cross, Carreau, and Herschel-Bulkley, their usage are not limited to the summarization on viscosity measurement data. These equation constants in nature summarized the fluid flow properties, which can provide a good observation on existing behaviour within the range of experimental conduct, or even to provide an estimation/projection of unavailable/unreachable flow condition. Hence, this section is to address the usage of shear rate dependence equation constants to explain the oil properties. Comparison was carried between different rheological models, and reliability of the equation constants was validated with experimental results.

From the models, viscous level of oils can be based on the consistency index from power-law ( $K_p$ ) and Herschel-Bulkley ( $K_H$ ). From Table 1, the  $K_p$  values were in the following sequence:  $(K_p)_{Olive} > (K_p)_{Sesame} > (K_p)_{Rice\_Bran} > (K_p)_{Coconut}$ . This applies to temperatures at 50 and 90 °C, and is in consistent observation with graphical presentation in Figs. 1 and 2. However, no reliable trend can be retrieved from  $K_H$  at both temperatures.

For non-Newtonian level of fluid, it can be investigated through the flow behaviour index from power-law ( $n_p$ ) and Herschel-Bulkley ( $n_H$ ). Table 1 shows the  $n_p$  values in the following sequence:  $(n_p)_{Rice\_Bran} > (n_p)_{Coconut} > (n_p)_{Sesame} > (n_p)_{Olive}$ , at both temperatures. This result shows rice bran is the most Newtonian oil

in comparison to the other three, and also, olive is relatively the most pseudoplastic oil. This trend is in consistent observation with the difference of viscosity value between 3 and 60 rpm, except at 90 °C, which coconut was calculated as more Newtonian than rice bran. At 90 °C,  $|\eta_{3rpm} - \eta_{60rpm}|$  was found as 2.1, 3.0, 8.4, and 13.6 mPa.s on coconut, rice bran, sesame, and olive, respectively. Again, no reliable trend can be observed from Herschel-Bulkley, in the case  $n_H$  values. The  $m$  and  $N$  values, respectively, from Cross and Carreau were solely as exponential constant rather than any useful indication on Newtonian behaviour of fluid.

**Table 1 Estimated power-law, Herschel-Bulkley, Cross, and Carreau equations constants at selected temperatures (50 and 90 °C)**

T (°C)		A*	B*	C*	D*
<b>Power-law</b>					
50	$K_p$	0.022	0.045	0.027	0.038
	$n_p$	0.93	0.85	0.97	0.87
	$R^2$	0.92	0.84	0.87	0.89
90	$K_p$	0.0087	0.031	0.012	0.022
	$n_p$	0.91	0.70	0.92	0.78
	$R^2$	0.96	0.97	0.87	0.97
<b>Herschel-Bulkley</b>					
50	$K_H$	0.023	-44	-383	-70
	$n_H$	0.93	1.0	1.0	1.0
	$\eta_{\infty,\gamma}$	-0.00076	44	383	70
	$R^2$	0.92	0.79	0.86	0.85
90	$K_H$	-372	-144	-383	-112
	$n_H$	1.0	1.0	1.0	1.0
	$\eta_{\infty,\gamma}$	372	144	383	112
	$R^2$	0.94	0.91	0.85	0.94
<b>Cross</b>					
50	$\eta_{\infty,\gamma}$	0.017	0.023	0.023	0.022
	$\eta_{o,\gamma}$	0.022	0.15	28	0.070
	$\alpha_c$	0.11	0.97	3487	0.59
	$m$	2.3	1.4	0.96	1.2
	$R^2$	1.00	1.00	0.98	1.00
90	$\eta_{\infty,\gamma}$	0.0057	0.0081	0.0086	0.0079
	$\eta_{o,\gamma}$	0.017	0.12	39	0.024
	$\alpha_c$	1.5	-0.71	2185	0.22
	$m$	0.75	0.93	1.1	1.1

	R <sup>2</sup>	1.00	NA	0.99	1.00
Carreau					
50	$\eta_{\infty,\gamma}$	0.017	0.023	0.023	0.022
	$\eta_{0,\gamma}$	0.022	0.094	1.3	0.050
	$\lambda_c$	0.11	0.71	138	0.44
	$N$	1.2	0.66	0.48	0.60
	R <sup>2</sup>	1.00	1.00	0.98	1.00
90	$\eta_{\infty,\gamma}$	0.0056	0.0082	0.0086	0.0077
	$\eta_{0,\gamma}$	0.025	0.029	2.6	0.020
	$\lambda_c$	-7.8	0.26	166	0.25
	$N$	0.30	0.56	0.53	0.45
	R <sup>2</sup>	1.00	1.00	0.99	1.00

\* A – coconut oil, B – olive oil, C – rice bran oil, D – sesame oil.

Viscosity at infinite shear rate is represented by  $\eta_{\infty,\gamma}$  values from Herschel-Bulkley, Cross, and Carreau. It was found that this value was approximately similar between Cross and Carreau. The average percentage of difference of  $\eta_{\infty,\gamma}$  value (50 and 90 °C) between Cross and Carreau was 0.88, 0.46, 0.00022, and 0.96 % of Cross  $\eta_{\infty,\gamma}$  value (50 °C) for coconut, olive, rice bran, and sesame, respectively. However,  $\eta_{\infty,\gamma}$  value from Herschel-Bulkley was largely deviated from Cross and Carreau estimations. Without any experimental data at infinite shear rate region, hence, the best way to evaluate is to calculate the percentage of difference between the  $\eta_{\infty,\gamma}$  value that estimated from the model and the viscosity data that recorded at the highest shear rate (100 rpm) from the experiment. Result shows that all the  $\eta_{\infty,\gamma}$  values from Cross and Carreau deviate less than 6.4 % from experimental data, whereas for Herschel-Bulkley it deviates at least 100 % with 7 out of 8  $\eta_{\infty,\gamma}$  values greater than respective viscosity at 100 rpm. Hence, it is justifiable that the estimated  $\eta_{\infty,\gamma}$  value from Herschel-Bulkley is not reliable. Furthermore, the current study could also conclude that the  $\eta_{\infty,\gamma}$  values estimated from Cross and Carreau equations are comparable and having a similar trend of those experimental viscosity value at 100 rpm for both 50 °C (olive > rice bran > sesame > coconut) and 90 °C (rice bran > olive > sesame > coconut), however, the reliability of estimation could not

be justified due to the required extrapolation of viscosity value that is not within the experimental range.

For oil that behaves as pseudoplastic fluid, at a very low shear rate region, viscosity always gives the highest value. This is the condition that is to determine whether or not the existence of yield stress. Zero-shear rate viscosity ( $\eta_{0,\gamma}$ ) is indeed can be estimated from the equation of Cross and Carreau. However,  $\eta_{0,\gamma}$  value varies from as low as 1 % to over 100 % for the percentage of difference between  $(\eta_{0,\gamma})_{\text{Cross}}$  and  $(\eta_{0,\gamma})_{\text{Carreau}}$ , of Carreau estimation at zero-shear rate viscosity. Moreover, as showed in Fig. 3, alternatively, the zero-shear rate viscosity could further increase rather than levelling off before crossing y-axis as shear rate approaching zero value. Base on a limited available of experimental data at this very low region of shear rate, it is to say that the  $\eta_{0,\gamma}$  values estimated by Cross and Carreau could not be justified due to insufficient data to justify the start of levelling off region (Newtonian region). For this reason, Cross and Carreau models are not suitable in modelling oil viscosity at very low shear rate region which does not possess a relaxation time characteristic ( $\alpha_c$  and  $\lambda_c$ ). Relaxation time is the time-lag before the fluid exhibiting shear-thinning behaviour, as shear rate continues to increase.

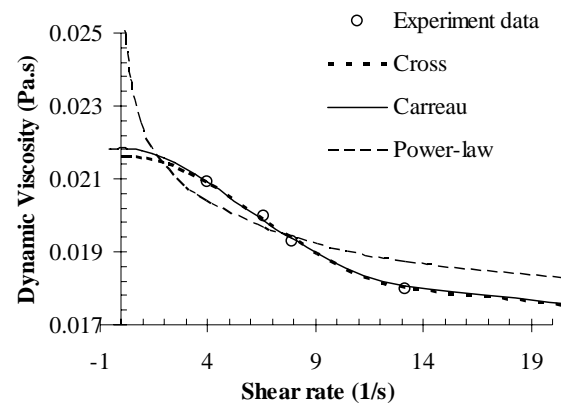


Fig. 3. Viscosity data of coconut oil at 50 °C modelled data with Cross, Carreau, and power-law model

### 3.3. Temperature dependence of oil viscosity

As shown in Figs. 4 and 5, the viscosity of oil decreases with increasing temperature. Similar

to the observation of shear rate, viscosity decreased at a greater rate in the region of lower temperature. The viscosity rate of reduction

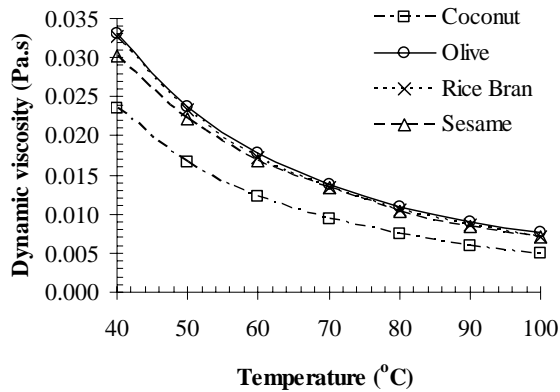


Fig. 4. Viscosity decreases with increasing temperature at 60 rpm

gradually reduces to a smaller rate as the temperature continues to increase towards the high temperature region. Again, similar to that of shear rate observation, oils viscosity tends to converge as the temperature continue to increase, but not as apparent as that observe on shear rate dependence. The viscosity of oil was observed as most viscous on olive oil and then, followed by rice bran, sesame, and coconut oils, at 60 rpm. At 3 rpm, the sequence of relative comparison of viscous oil was similar to that of shear rate observation.

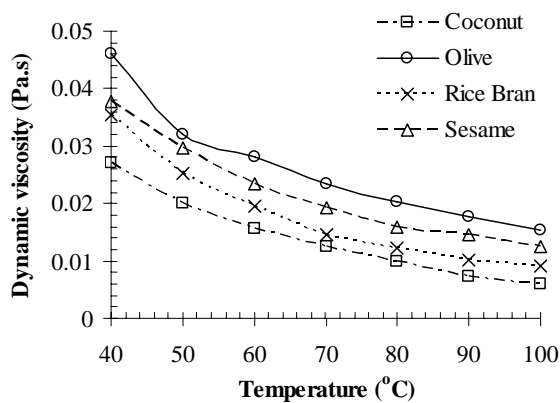


Fig. 5. Viscosity decreases with increasing temperature at 5 rpm

### 3.4. Temperature dependence of rheological model

In shear rate dependence study, shear-thinning behaviour was investigated from  $n_p$  and  $n_H$  of power-law and Herschel-Bulkley, respectively.

Similarly, for temperature dependence study, viscosity-temperature behaviour can be assessed from activation energy ( $E_a$ ). In a relative comparison, oil with the lowest  $E_a$  value is the least affected by the changes of temperature. At 5 rpm, the  $E_a$  value for oils is in the following sequence:  $(E_a)_{Coconut} > (E_a)_{Rice\_Bran} > (E_a)_{Sesame} > (E_a)_{Olive}$ , whereas at 60 rpm, the  $E_a$  value is:  $(E_a)_{Coconut} > (E_a)_{Rice\_Bran} > (E_a)_{Olive} > (E_a)_{Sesame}$  (Table 2). In order to validate this observation, the difference of viscosity between viscosity at 50 and 100 °C ( $\eta_{50-100^\circ C}$ ) was calculated for both 5 and 60 rpm. At 5 rpm, the following sequence was found:  $(\eta_{50-100^\circ C})_{Sesame} > (\eta_{50-100^\circ C})_{Olive} > (\eta_{50-100^\circ C})_{Rice\_Bran} > (\eta_{50-100^\circ C})_{Coconut}$ , whereas at 60 rpm,  $(\eta_{50-100^\circ C})_{Olive} > (\eta_{50-100^\circ C})_{Rice\_Bran} > (\eta_{50-100^\circ C})_{Sesame} > (\eta_{50-100^\circ C})_{Coconut}$ . The experimental result indicates coconut oil viscosity is the least affected by temperature at both shear rates, in addition to an opposite behaviour for sesame and olive oils at respective 5 and 60 rpm. This result shows an inconsistency from the trend of  $E_a$  value and therefore, Arrhenius-type relationship is unable to provide a reliable observation on the sensitivity of oil viscosity on temperature changes, in the relative comparison of the different oils.

Similar to Cross, Carreau, and Herschel-Bulkley, Arrhenius-type relationship is also able to estimate viscosity at infinite condition, as in this case it is at infinite temperature. The estimated  $\eta_{\infty,T}$  value at 5 rpm is in this sequence:  $(\eta_{\infty,T})_{Olive} > (\eta_{\infty,T})_{Sesame} > (\eta_{\infty,T})_{Rice\_Bran} > (\eta_{\infty,T})_{Coconut}$ , whereas at 60 rpm, the sequence is as follows:  $(\eta_{\infty,T})_{Sesame} > (\eta_{\infty,T})_{Olive} > (\eta_{\infty,T})_{Rice\_Bran} > (\eta_{\infty,T})_{Coconut}$ . This trend is identical to that of experimental viscosity data at 100 °C for both 5 and 60 rpm. With the viscosity data that is limited to the highest at 100 °C, the current study is unable to justify the reliability of viscosity at infinite temperature due to the required extrapolation of viscosity value that is not within the experimental range.

**Table 2 Estimated Arrhenius-type relationship equation constants at selected rotational speeds (5 and 60 rpm)**

Oil type	Speed (rpm)	$E_a$	$\eta_{\infty,T}$	$R^2$
Coconut	5	24251	2.45E-06	1.00
	60	25267	1.38E-06	1.00
Olive	5	16825	6.61E-05	0.98
	60	23970	3.19E-06	1.00
Rice	5	22357	6.21E-06	0.99
Bran	60	24483	2.58E-06	1.00
Sesame	5	17765	3.95E-05	0.99
	60	23520	3.51E-06	1.00

#### 4. Conclusions

For all the investigated oils, it was found that temperature has a greater influence on the reduction of viscosity than shear rate. The vegetable oils exhibit non-Newtonian behaviour by showing a shear-thinning relationship between viscosity and shear rate, which is better known as pseudoplastic behaviour. The shear rate dependence and temperature dependence of rheological models gave a good fitting on experimental data with R-squared value range from 0.84 to 1.00.

The estimated value from the model constants were further categorized into those of reliable, unreliable, and those of unjustifiable validity of the model constant value. Reliable means the model constant that was validated with observed experimental data. The unjustifiable validity means insufficient of experimental data to make any justification, due to model that estimating extreme condition such as those at infinite-shear rate, zero-shear rate or infinite-temperature viscosity. Table 3 indicates the final conclusion of the assessment.

This assessment is strictly based on the following conditions:

- four vegetable oils that were coconut, olive, rice bran, and sesame oils;
- a Brookfield viscometer model DV-I+;
- rotational spindle SP-18;
- temperature range 40-100 °C with an increment of 10 °C for each step size;
- shear rate range 3.9-131.6 s<sup>-1</sup> (3, 5, 6, 10, 30, 50, 60, and 100 rpm);
- shear rate dependence modelled at 50 and 90 °C; and
- temperature dependence modelled at 5 and 60 rpm.

**Table 3 Rheological model constant reliability**

Constants	Reliable	Unreliable	Unjustifiable
Power-law			
$K_p$	X		
$n_p$		X	
Herschel-Bulkley			
$K_H$		X	
$n_H$		X	
$\eta_{\infty,\gamma}$		X	
Cross			
$\eta_{\infty,\gamma}$			X
$\eta_{o,\gamma}$			X
$\alpha_c$			X
$m$		X	
Carreau			
$\eta_{\infty,\gamma}$			X
$\eta_{o,\gamma}$			X
$\lambda_c$			X
$N$		X	
Arrhenius-type relationship			
$E_a$		X	
$\eta_{\infty,T}$			X

“X” indicates the assessed result based on the current experiment constraints.

#### Acknowledgements

The authors greatly acknowledge the assistance of science officer, Mr. Mahmood Sulaiman, and the laboratory technicians, Mr. Rozimi, and Mrs. Siti Zalaikhar for their indirect contribution in completing the experimentation.

#### References

- [1]. Isayev, A.I., S.P. Yushanov, J. Chen, Ultrasonic devulcanization of rubber vulcanizates. I. Process model, *Journal of Applied Polymer Science*, Vol. 59:5, pp. 803-813, 1996.
- [2]. Nagano, Y., C. Kim, Two-equation model for heat transport in wall turbulent shear flows, *Journal of Heat Transfer*, Vol. 110:3, pp. 583-589, 1988.

- [3]. Quinones-Cisneros, S.E., K.A.G. Schmidt, J. Creek, U.K. Deiters, Friction theory modeling of the non-Newtonian viscosity of crude oils, *Energy & Fuels*, Vol. 22, pp. 799-804, 2008.
- [4]. Xu, J., K.W. Koelling, Temperature dependence of rheological behavior of a metallic automotive waterborne basecoat, *Progress in Organic Coatings*, Vol. 53;3, pp. 169-176, 2005.
- [5]. Høglund, E., Influence of lubricant properties on elastohydrodynamic lubrication, *Wear*, Vol. 232, pp. 176-184, 1999.
- [6]. Wan Nik, W.B., F.N. Ani, H.H. Masjuki, S.G. Eng Giap, Rheology of bio-edible oils according to several rheological models and its potential as hydraulic fluid, *Industrial Crops and Products*, Vol. 22, pp. 249-255, 2005.
- [7]. Natarajan, V.P., G.J. Suppes, Rheological studies on a slurry biofuel to aid in evaluating its suitability as a fuel, *Fuel*, Vol. 76;14-15, pp. 1527-1535, 1997.
- [8]. Fasina, O.O., H. Hallman, M. Craig-Schmidt, C. Clements, Predicting temperature-dependence viscosity of vegetable oils from fatty acid composition, *Journal of the American Oil Chemists' Society*, Vol. 83;10, pp. 899-903, 2006.
- [9]. Rao, M.A., *Rheology of fluid and semisolid foods: Principles and Applications*, Aspen Publishers, Inc., Gaithersburg, Maryland, 1999.
- [10]. Hae Ryu, C., Y. Chan Bae, S. Hwan Lee, S. Yi, Y.H. Park, Rheological properties of hollow sphere loaded polymer melts, *Polymer*, Vol. 39;25, pp. 6293-6299, 1998.
- [11]. Armelin, E., M. Marti, E. Rude, J. Labanda, J. Llorens, C. Aleman, A simple model to describe the thixotropic behavior of paints, *Progress in organic coatings*, Vol. 57, pp. 229-235, 2006.
- [12]. Al-Zahrani, S.M., T.F. Al-Fariss, A general model for the viscosity of waxy oils, *Chemical Engineering and Processing: Process Intensification*, Vol. 37;5, pp. 433-437, 1998.
- [13]. Akdogan, H., T.H. McHugh, Twin screw extrusion of peach puree: Rheological properties and product characteristics, *Journal of Food Processing and Preservation*, Vol. 23;4, pp. 285-305, 1999.
- [14]. Novak, L.T., Entity-based Eyring - NRTL viscosity model for mixtures containing oils and bitumens, *Industrial and Engineering Chemistry Research*, Vol. 45;21, pp. 7329-7335, 2006.
- [15]. Benedito, J., J.V. García-Pérez, M. Carmen Dobarganes, A. Mulet, Rapid evaluation of frying oil degradation using ultrasonic technology, *Food Research International*, Vol. 40;3, pp. 406-414, 2007.
- [16]. Akinoso, R., J.C. Igbeka, Modelling of oil expression from sesame seed, *Journal of Food Science and Technology*, Vol. 43;6, pp. 612-614, 2006.
- [17]. Ceriani, R., C.B. Gonçalves, J. Rabelo, M. Caruso, A.C.C. Cunha, F.W. Cavaleri, E.A.C. Batista, A.J.A. Meirelles, Group contribution model for predicting viscosity of fatty compounds, *Journal of Chemical and Engineering Data*, Vol. 52;3, pp. 965-972, 2007.
- [18]. Ceriani, R., F.R. Paiva, C.B. Gonçalves, E.A.C. Batista, A.J.A. Meirelles, Densities and viscosities of vegetable oils of nutritional value, *Journal of Chemical and Engineering Data*, Vol. 53;8, pp. 1846-1853, 2008.
- [19]. Brookfield Engineering Laboratories, *More solution to sticky problems: a guide to getting more from your Brookfield viscometer*, Brookfield Engineering Laboratories, Inc., Middlebore, USA, 2005.

# EFFECT ON FATIGUE PERFORMANCE OF SURFACE TREATED COMPONENTS: AN INVESTIGATION USING FINITE ELEMENT ANALYSIS

Nawar A. Al-Asady<sup>1</sup>, S. Abdullah<sup>2</sup>, A. K. Arrifin<sup>3</sup> and S.M.Beden<sup>4</sup>

<sup>1</sup>Department of Mechanical and Materials Engineering  
Universiti Kebangsaan Malaysia,  
43600 UKM Bangi, Selangor, Malaysia  
[Nawar2007@gmail.com](mailto:Nawar2007@gmail.com); Tel: 0389216012

## Abstract

*The effects of nitriding, cold rolled and shot peening on fatigue life of an automotive lower suspension arm component which fabricated of SAE1045 steel were investigated. The finite element modeling and analysis have been performed using finite element analysis software Package MSC.PATRAN/ MSC.NASTRAN and the fatigue life prediction was carried out using MSC.FATIGUE software. The finite element analysis results indicate a great effect for all surface finish parameters on fatigue life. It shows that nitriding increased the fatigue life of the component better than shot peening, while cold rolled effect was between them. In a nut shell, nitriding can be considered as the best surface treatment to improve the fatigue life of the automotive lower suspension arm which fabricated of SAE1045 steel.*

**Keywords:** fatigue; finite element analysis; lower suspension arm; SAE1045 steel; Surface treatment.

## 1. Introduction

Due to market pressures for improvements in productivity, reliability, ductility, and wear resistance as well as the durability of mechanical systems, manufacturers are placing increasing demands on available materials [1]. Moreover, fatigue is an important parameter to be considered in the behaviour of components subjected to constant and variable amplitude loading [2]. Fatigue is of great concern for components subject to cyclic stresses, particularly where safety is paramount, for examples automotive components. It has long been recognized that fatigue cracks generally initiate from free surfaces and that performance is therefore reliant on the surface topology/integrity produced by surface finishing. Whilst it is known that fatigue life is heavily influenced by residual stresses, the metallurgical condition of the materials and the presence of notch-like surface irregularities induced by machining play a key role [3]. The surface treatments have been the most effective and widely used method of introducing compressive residual stresses into the surface of

metals to improve fatigue performance [4]. Surface treatments such as nitriding, shot peening, cold rolling are often performed on high strength aluminum, titanium alloys and steel to improve fatigue performance [3].

There are many factors affecting the fatigue behaviour; stress or strain range, mean stress, surface finish and quality, surface treatments, and sequence effects. The surface treatment can be applied to improve the fatigue resistance of a component. There are several methods for improving the surface condition of components. These include mechanical and thermo-chemical methods. These processes aim to increase hardness, wear resistance and/or fatigue strength and load-bearing capacity of material by creating a hard layer with high compressive residual stresses on or near the surface of tools [5]. These usually work by inducing a residual compressive stress at the surface. Under low amplitude cycles the stresses at the surface are significantly lower or even remain compressive. Therefore the fatigue life is greatly improved. There are several methods used to cold work the surface of a component to produce a residual compressive stress. The two most important are

cold rolled and shot peening. Along with producing compressive residual stresses, these methods also work-harden the surface material. The great improvement in fatigue life is due primarily to the residual compressive stresses. In shot peening process, the surface of the component undergoes plastic deformation due to the hit of many hard shots. The fatigue life of the component is improved due to the development of compressive residual stresses and the increase of hardness near the surface.

Nitriding, one of the most widely used thermo-chemical methods, produces a strong and shallow case with high compressive residual stresses on the surface of steel components such as gears, crankshafts, dies and tools. Nitriding is a process for hardening the surface by diffusing nitrogen into the surface. Nitriding processes are performed at temperatures between 500 and 550 °C where the structure is still ferritic [6-7].

Cold rolling is a method of cold working a metal. When a metal is cold worked, microscopic defects are nucleated throughout the deformed area. These defects can be either point defects (a vacancy on the crystal lattice) or a line defect (an extra half plane of atoms jammed in a crystal). As defects accumulate through deformation, it becomes increasingly more difficult for slip, or the movement of defects, to occur. This results in a hardening of the metal.

Shot peening is a mechanical surface treatment that is known to improve the fatigue strength of many materials by producing a beneficial near-surface compressive residual stress [9,10]. The improvement in fatigue life stems from a combination of work hardening of the surface and an increased dislocation density, and the introduction of a near-surface compressive residual stress. Compressive surface residual stresses helps to improve the life of engineering components by retarding fatigue crack initiation and growth [11,12].

Despite the benefits of surface treatment on the fatigue life of metals are widely known, the modelling and simulation of this kind of treatment on the components under load service were recently performed [12-14]. Farrahi and Ghadbeigi [10] investigate the effects of gas nitriding, nitrocarburizing and shot peening on fatigue life of a cold tool steel. Gas nitriding and nitrocarburizing have been used in improving wear resistance of this steel. Yazdania et al. [11] applied shot peening to improve the durability life of cyclically loaded components. They

experimentally studied the effect of tempering temperature and shot peening on fatigue behavior. The experimental results showed that, fatigue strength increases with decrease of tempering temperature and shot peening treatment and the last only has an effect on crack initiation stage. Mahagaonkar et al. [4] used a technique to examine the effect of process parameters such as pressure, shot size, nozzle distance and the exposure time on the fatigue performance of AISI 1045 and 316L material. After going through confirmation test the analysis reveals the right combination of the parameters for better process control. Expressions correlating fatigue life and the process parameters for both materials were developed, which are useful in predicting fatigue life. This technique could prove beneficial in industries for reduction of performance variation and cost and to increase productivity.

The objectives of this paper is to predict the fatigue life of the automotive lower suspension arm using two of strain life approaches and also investigate the effect of Mechanical surface treatments on the component fatigue life. To investigate the effect of treatment methods on the structure, the linear finite element analysis under service loading was used. However, these investigations are essential in order to understand the involved microstructural mechanisms of hardening or softening in the wake of service load. Numerical investigations are performed to characterize completely the different induced effects before and after surface treatments. The numerical results were discussed and analysed.

## **2. Fatigue Strain Life Models**

Many practical problems in engineering are either extremely difficult or impossible to solve by conventional analytical methods. Such methods involve finding mathematical equation which define the required variables. For example, the distribution of stresses and strain in a solid component. One of the main attractions of finite element methods is the ease with which they can be applied to problems involving geometrically complicated systems [18].

Fatigue life prediction represents one of the applications for finite element. Among the plastic strain models, the Morrow and Smith Watson-Topper (SWT) models are widely used. In this paper, these two models have been used

The first strain-life model is based on the proposal by Morrow (1965) [19], the relation of the total strain amplitude ( $\varepsilon_a$ ) and the fatigue life in reversals to failure ( $2N_f$ ) can be expressed as

$$\varepsilon_a = \frac{\sigma'_f}{E} \left( 1 - \frac{\sigma_m}{\sigma'_f} \right) (2N_f)^b + \varepsilon'_f (2N_f)^c \quad (2)$$

where E is the material modulus of elasticity,  $\varepsilon_a$  is a true strain amplitude,  $2N_f$  is the number of reversals to failure,  $\sigma'_f$  is a fatigue strength coefficient,  $b$  is a fatigue strength exponent,  $\varepsilon'_f$  is a fatigue ductility coefficient and  $c$  is a fatigue ductility exponent.

Another strain-life mean stress correction model was suggested by Smith et al. [20], or often called the SWT parameter. This relationship was based on strain-life test data which was obtained at various mean stresses. Thus, the SWT expression is mathematically defined as

$$\sigma_{max} \varepsilon_a E = (\sigma'_f)^2 (2N_f)^{2b} + \sigma'_f \varepsilon'_f E (2N_f)^{b+c} \quad (3)$$

where  $\sigma_{max}$  is the maximum tensile stress for the particular cycle. This equation is based on the assumption that for different combinations of strain amplitude,  $\varepsilon_a$ , and mean stress,  $\sigma_m$ , the product remains constant for a given life.

### 3. Methodology

#### 3.1. Material specification

In order to classify the lower suspension arm material specification, analyzing the chemical composition of the steel sample is done. Based on table 1, the steel can be classified as medium carbon steel, since both AISI and SAE classified steel whose carbon content ranges between 0.3-0.6%, manganese content ranges between 0.60-0.9% to be medium carbon steel [21] which represents the fabricated material for the 2000 cc Sedan lower suspension arm. The measured values have been get using INCA Energy system. Three samples were cut from the lower suspension arm using a cutter. The samples were subsequently ground with successive SiC papers (grit 200-1200) and then polished with polishing cloth and Alomina solution of grain size 6 $\mu$ m then 1 $\mu$ m.

**Table 1 Chemical composition of the steel**

Element	C	Mg	Si	V	Cr	Ni	Mn	Fe
Measured value wt%	0.33	0.13	0.29	0.04	0.14	0.49	0.9	Bal.

#### 3.2. Geometrical and finite element model

A geometric model of a lower suspension arm for a 2 Liter engine Sedan car is considered in this study, and this component is presented in Fig. 1. The finite element approach is used for modeling and simulating. Three-dimensional lower suspension arm model geometry is drawn using CATIA software, as shown in Fig. 2.



**Fig. 1. A geometric model of a lower suspension arm**

The auto tetrahedral meshing approach is a highly automated technique for meshing solid regions of the geometry. It creates a mesh of tetrahedral elements for any closed solid including boundary representation solid. Tetrahedral meshing produces high quality meshing for boundary representation solids model imported from the most CAD systems. The TET10 mesh can give more accurate solution since the 10 nodes tetrahedral (TET10) element is used for the analysis with the adoption of a quadratic order interpolation function. There are three main parts in the lower suspension arm which their behaviour has been considered in the FE boundary conditions, ball joint, pivot 1 and pivot 2. The FEM (Fig.2) has boundary conditions as followed:

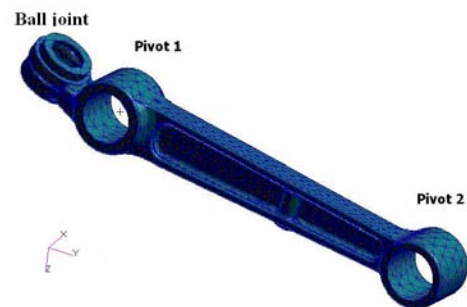


**Fig. 2. Finite element model of the lower suspension arm**

distributed load has been applied on the inner surface of pivot 1. Pivot 2 considers as a rigid section with a rotation around  $x$ -axis from the side of the vehicle body. In the same time, rigid has been considered on the ball joint with translations in  $x$  and  $y$  direction while rotation around  $x$ ,  $y$ , and  $z$ -axis to represent the braking and cornering loads. There are no acceleration loads as inputs, due to collecting data during driving of the car at constant velocity.

### 3.3. Loading information

The load history which has been used for this analysis was obtained from the real automotive lower suspension arm, which was driven over country road. The frequency sampling,  $f_s$  for this case is 500 Hz. This  $f_s$  value was chosen in order to collect a wide range of road data [22,23]. The data was measured using a fatigue data acquisition system (Fig. 3) at car velocity of 25 km/h, and, recorded data in a form of strain time histories.



Fig. 3. The setup of fatigue data acquisition system data collection.

A strain gauge was fixed in an exact position on the lower suspension arm as shown in figure 4. Finite element analysis was performed in order to classify the critical areas in order to get clear idea to choose the positions area for fixing strain gauge during the experimental test to get the strain history data, as shown in Fig. 5.

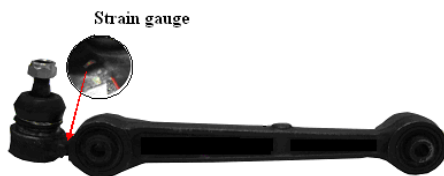


Fig. 4. Strain gauge location on the lower suspension arm

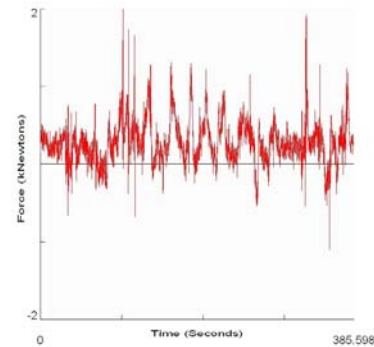


Fig. 5. Experimental loading history for the lower suspension arm.

## 4. Results and Discussion

The linear static finite element analysis was performed using MSC.PATRAN-NASTRAN finite element software. The finite element analysis has been performed using SAE1045 steel due to use this kind of steel material in fabricate the automobile lower suspension arm. Fig. 6. shows the equivalent maximum principal strain contour of the lower suspension arm. The strain value from the analytical simulation was within the range of the collected data during driving of the car on the road. This was due to accurate boundary conditions and static load in the pre-processing stage. The value of the collected strain load history in the second critical area of the lower suspension arm between the ball joint and Pivot1 was  $4.3 \times 10^{-4}$  microstrain while the value from the finite element analysis was  $2.7 \times 10^{-4}$ .



Fig. 6. The equivalent maximum principal strain contour of the lower suspension arm

The equivalent maximum principal stress contour is presented in Fig 7. From the stress contour result, the state of stress can be obtained and consequently used for life predictions. Linear elastic analysis was used, since the lower suspension arm is designed for long life. The maximum stress of 264 MPa at node 14449 was obtained. This value is less than the ultimate stress for the material. For that reason, linear analysis can be used. All the results presented in this paper are based on the fine mesh in the most critical area of the arm model.



**Fig. 7. The equivalent maximum principal stress contour**

Fig 8 shows the fatigue life plot and critical location on the lower suspension arm using crack initiation method. The maximum damaged area was in the ball joint while the second damaged area was between the ball joint and PivotI area. A two mean stress correction methods are considered i.e. Smith-Watson-Topper (SWT) and Morrow. The contributions of surface treatments on the lower suspension arm fatigue life at critical location are summarized in Table 2. It shows the fatigue component life results using Morrow and SWT strain-life methods for three kinds of surface treatment, nitriding, cold rolled, and shot peening, in addition to the untreated case. Mechanical surface treatments are often utilized after surface finishing in order enhancing fatigue performance. For the purpose of finite element analysis simulation, the polished surface finish has been used.

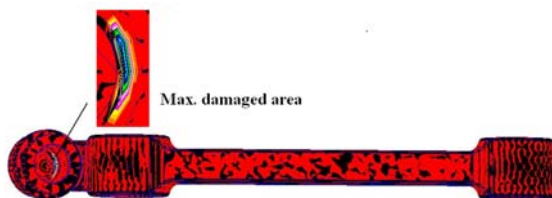


**Fig. 8. The fatigue life plot and critical location on the lower suspension arm**

From the Morrow and SWT model results of Table 2, longer life can be obtained for SWT model for all the three kinds of surface treatments. It is difficult to categorically select one procedure in preference to the other. However, for loading sequences which are predominantly tensile in nature the Smith Watson Topper approach is more conservative and is, therefore, recommended. In the case where the loading is predominantly compressive, particularly for wholly compressive cycles, the Morrow correction can be used to provide more realistic life estimates.

The effect of the surface treatment results for the polished lower suspension arm which tabulated in Table 2, shows that nitriding surface treatment gave better enhancement for fatigue life while shot peening surface treatment gave less enhancement, but cold rolled surface treatment effect was between them. This is may be due to produce different amount of compressive residual stresses on Surface treatments (nitriding, cold rolled, and shot peening).

**Table 2 The effect of surface treatment on lower suspension arm fatigue life**

Strain life method	Life per Cycle for treatment status			
	Untreated	Nitrided	Cold Rolled	Shot Peened
Morrow	8.21E5	7.11E8	5.43E7	7.18E6
SWT	9.98E5	8.51E9	9.25E8	9.54E7

## 5. Conclusions

The effect of surface treatments on fatigue life of the SAE1045 steel were studied under variable amplitude loading conditions at most critical location of the automotive lower suspension arm. According to the results, all surface treatment processes can be applied to increase the fatigue life of the steel components. It can also be concluded that the nitriding has been found as the process that can give highest life for the lower arm. Mechanical surface treatments can be beneficial in improving components fatigue performance. Therefore it can be used an efficient and reliable means for the sign-off of durability of a prototype components with actual service environments in the early-developing stage.

## References

- [1]. B. Podgornik, J. Vižintin, O. Wänstrand, M. Larsson, S. Hogmark, H. Ronkainen, and K. Holmberg, *Tribological properties of plasma nitrided and hard coated AISI 4140 steel*, *Wear*, Vol. 249; pp. 254-259, 2001.
- [2]. M. Torres, and H. Voorwald, An evaluation of shot peening, residual stress and stress relaxation on the fatigue life of AISI 4340 steel, *International Journal of Fatigue*, Vol. 24; pp. 877-886, 2002.

- [3]. D. Novovic, R. Dewes, D. Aspinwall, W. Voice, and P. Bowen, The effect of machined topology and integrity on fatigue life, *International Journal of machine Tools & Manufacture*, Vol. 44; pp. 125-134, 2004.
- [4]. S. Mahagaonkar, P. Brahmankar, and C. Seemikeri, Effect on fatigue performance of shot peened components: An analysis using DOE technique, *International Journal of Fatigue*, Vol. 31; pp. 693-702, 2009.
- [5]. T.Bell, *ASM Handbook*, vol. 4, Heat Treating, ASM International, Ohio, pp. 425-436, 1997.
- [6]. *ASM Metals Handbook*, vol. 4, Heat Treating, ninth ed., American Society for Metals, Metals Park, OH, 1991.
- [7]. D. Pye, Practical Nitriding and Ferritic Nitrocarburizing, *ASM International*, 2003.
- [8]. William L. Roberts, *Cold Rolling of Steel*, CRC Press, US, 1978.
- [9]. K.J.e. Marsh, *Shot Peening: Techniques and Applications*, Chamelion Press Ltd, 1993.
- [10]. A. Ezeilo, in: M.E. Fitzpatrick, A. Lodini (Eds.), *Analysis of Residual Stress by Diffraction using Neutron and Synchrotron Radiation*, Taylor and Francis, London, pp. 251-262, 2003.
- [11]. G.A. Webster, A.N. Ezeilo, Residual stress and their influence on fatigue lifetimes, *International Journal of Fatigue*, Vol. 23; pp. S375- S383, 2001.
- [12]. G.A.Webster, A.N. Ezeilo, *Physica B* 234 (1997) 949-955.
- [13]. G. H. Farrahi, H. Ghadbeigi, An investigation into the effect of various surface treatments on fatigue life of a tool steel, *Journal of Materials Processing Technology*, Vol. 174, pp. 318-324, 2006.
- [14]. Yazdania, S., Yoozbashi, N., Ebrahimi, A. Enhancement of Fatigue Strength of SAE 1045 Steel by Tempering Treatment and Shot Peening, Trans tech Publications, Switzerland. 2007.
- [15]. Shen S., Z. Han, C. Herrera, and S. Atluri. *Assessment, development and validation of computational fracture mechanics methodologies and tools for shot-peened materials used in rotorcraft principal structural elements* ,National technical information service (NTIS), US, 2004.
- [16]. Lillamand I et al. Cyclic modelling of the mechanical state produced by shotpeening. *Fatigue Fract Eng Mater Struct*, Vol. 24; pp. 93-104, 2001.
- [17]. Guechichi H, Castex L. Fatigue limits prediction of surface treated materials. *J Mater Proc Technol*;172:381-7, 2006.
- [18]. T.F. Roger, *Finite Element Methods for Engineers*, Imperical College Press, 1997.
- [19]. J. Morrow, *Fatigue Design Handbook*, Advances in Engineering, Society of Automotive Engineers, Warrendale, Pa., Vol.4, 1968, pp. 3-36.
- [20]. K.N., Smith, P. Watson and T. H.Topper, A stress-strain function for the fatigue of metals, *Journal of Materials*, Vol.4, No.5, pp. 767-778, 1970.
- [21]. Lindberg. R.A. *Processes and Materials of Manufacture*, 2<sup>nd</sup> ed. Allyn and Bacon, Boston, MD, USA. 1977.
- [22]. C. Oh, Application of wavelet transform in fatigue history editing, *International Journal of fatigue*, Vol. 23; No.3, pp. 241-250, 2001.
- [23]. R.I Stephens, P.M. Dindinger and J.E. Gunger, Fatigue damage editing for accelerated durability testing using strain range and SWT parameter criteria. *International Journal of fatigue*, Vol. 19; No.8, pp. 599-606, 1997.

## EFFECT OF TEMPERATURE ON THE TRIBOLOGICAL PERFORMANCE OF PALM BIODIESEL

<sup>1</sup>Shang Yuen Sia, <sup>2</sup>A. S. M. A. Haseeb, <sup>3</sup>M. A. Fazal, <sup>4</sup>M. I. Jahirul, <sup>5</sup>H. H. Masjuki

<sup>1-5</sup>Department of Mechanical Engineering, University of Malaya, 50603 Kuala Lumpur, Malaysia.

Corresponding Author: email: jewel\_mme.buet@yahoo.com. Tel/Fax: +0379674448

### Abstract

*Biodiesel, as an alternative fuel is steadily gaining attention and significance to replace diesel fuel partially or completely. The tribological performance of biodiesel is crucial for its application in automobiles. In the present study, effect of temperature on the tribological performance of palm biodiesel was investigated by using four ball wear machine. Tests were conducted at temperature 30, 45, 60 and 75°C, under a normal load of 40 kg for 1 h at speed 1200 rpm. For each temperature, the tribological properties of diesel (B0) and three biodiesel blends like B10, B20, B50 were investigated and compared. During the wear test, frictional torque was recorded on line. Wear scar of the used ball was investigated by optical microscopy. Results showed that friction and wear were increased with increasing temperature.*

**Keywords:** Wear, Friction, Four ball, Biodiesel, Ddiesel.

### 1. Introduction

Biodiesel, as an alternative fuel derived from vegetable oils or animal fats, has a number of technical advantages over conventional diesel fuel. These include reduction of most exhaust emissions and biodegradability, higher flash point, reduced toxicity, derivation from a renewable feedstock, and domestic origin [1-3]. It can be used in diesel engine with little or no modification [4]. Although these attributes of biodiesel have drawn attention as an alternative fuel, there exist some significant drawbacks which have limited its commercial applications. These include viscosity and oxidation instability as a consequence of changing temperature as well as exposure to air, lower volatility, reactivity of unsaturated hydrocarbon chains [5-6]. These characteristics of biodiesel are more prone to influence the lubrication parameters, wear of various engine components and so on. The impact of these issues can also be varied for different concentration of biodiesel in diesel blends. Besides, the adaptation of a selected alternative fuel to suit diesel engine is considered more economically attractive in using it as blend with diesel fuel than in its pure form [7-8]. It was reported that neat biodiesel

possesses inherently greater lubricity than conventional diesel fuel [5]. Such effectiveness was also reported for even lower (<1%) blend levels [9-11] or higher (10-20%) levels [12-13]. Masjuki and Maleque, [14] found that above 5% palm oil methyl ester (POME) in lubricant causes oxidation and corrosion. According to Maleque et al. [15], for 5% POME in lubricant, the total acid number (TAN) increases after a certain temperature (80°C). They found that at higher temperature, oxidation of the lubricants caused increased wear. These results seem to imply that different temperature have different impact on lubricity for different blended fuels.

The present study aims to investigate the effect of temperature on the lubricity for different biodiesel blends.

### 2. Experimental

The tribological performance of palm oil methyl ester was investigated by four ball wear machine, IP 239/85. The ball test material was chrome alloy steel (E-52100 with grade 25 extra polish) containing (0.95-1.10)% carbon and (1.3-1.6)% chromium. Palm oil methyl ester used in this study meets EN14214 specifications (Table 1).

**Table 1. Composition of biodiesel.**

Test parameters	EN 14214 Limits
Ester content (%mass)	96.5 min
Monoglyceride (%mass)	0.8 max
Diglyceride (%mass)	0.2 max
Triglyceride (%mass)	0.2 max
Free glycerol (%mass)	0.02 max
Acid value (mg KOH/g)	0.5 max
Water content (mg/Kg)	500 max
Methanol content (%mass)	0.2 max
Na + K content (mg/Kg)	5 max
Ca + Mg content (mg/Kg)	5 max

The wear and friction characteristics of biodiesel blends were investigated at four different temperature viz, 30, 45, 60 and 75°C, under a normal load of 40 kg for 1 h at speed 1200 rpm. The blends like B10, B20, B50 were made on volume basis and stored in glass bottles at room temperature. The balls had a diameter of 12.7 mm. Among the four balls, the lower three were held in fixed position against each other in a steel cup by means of a clamping ring. Another ball into the upper chuck was rotating one. Testing fuel was poured in sufficient amount (approx 10 ml) to cover the balls to a depth of at least 3 mm. During each test, friction torque was recorded in order to calculate the friction coefficient. The wear scar diameters were measured before removing the balls from the cup. The results reported here are mean wear scar diameter of three balls. Fuel degradation was analyzed by FTIR. The surfaces of worn balls were investigated by using optical microscopy.

### 3. Results

At the very beginning of each test, friction torque recorded on line was unstable with time and few minutes later it came to a stable condition. Steady state friction coefficient for the last 1000s was calculated from the recorded torque. Figure 1 shows that steady state friction coefficient for different fuel increases with increasing temperature. On the other hand, it decreases with increasing the concentration of biodiesel.

It is seen from Figure 2 that the wear scar diameter increases with increasing temperature. For each temperature, it decreases as a consequence of increasing biodiesel concentration [Figure 2]. However, effect of

temperature in changing wear scar diameter is very less.

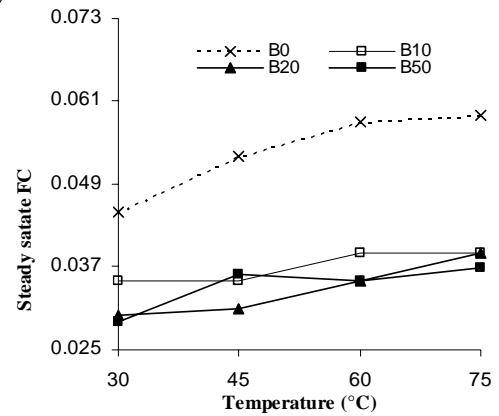


**Fig. 1. Variation of steady state friction coefficient (FC) of last 1000s for each test with temperature for different concentration of biodiesel.**

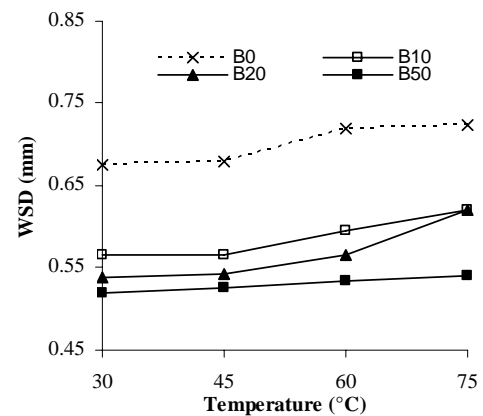


**Fig. 2. Variation of wear scar diameter with temperature for different concentration of biodiesel.**

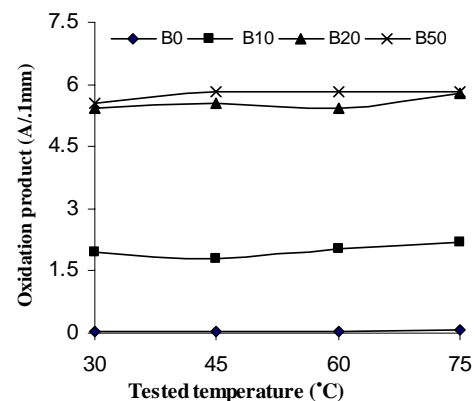


**Fig. 3. Oxidation product rate of the fuels obtained after conducting the four ball test at different temperature.**

Figure 3 shows that the increasing of oxidation product with temperature is lesser than that with increasing the concentration of biodiesel in blends [Figure 3].

It is seen in Figure 4 that with increasing temperature, free water content of the tested fuel

increases. But, no free water was found for as received both diesel and biodiesel.

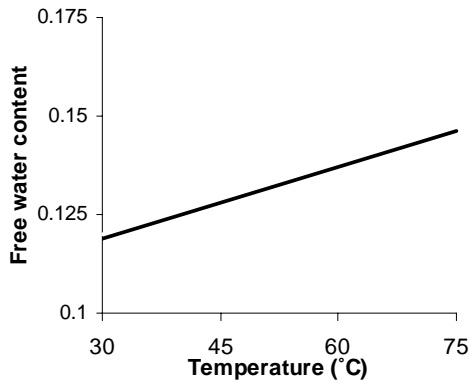


**Fig. 4. Water percentage for the fuel B50 obtained after conducting the four ball test at different temperature.**

Figure 5 shows that the deformation of the surface decreases with increasing the concentration of biodiesel. The worn surfaces at 75°C are comparatively blacker than those at 30°C.

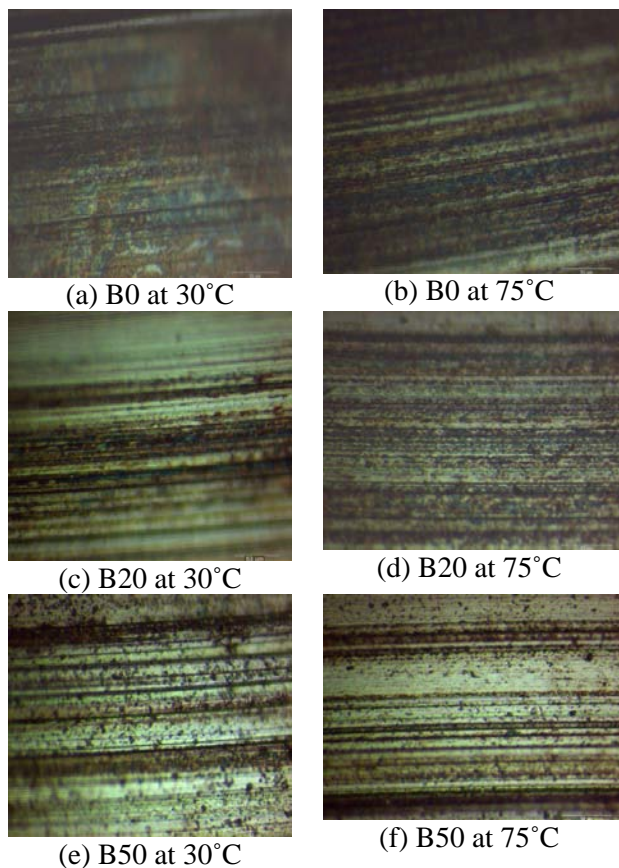


**Fig. 5. Photograph (500X) by optical microscope showing the appearance of the wear scar from wear for B0 at (a) 30°C, (b) 75°C; B20 at (c) 30°C (d) 75°C; B50 (e) 30°C, (f) 75°C.**

#### 4. Discussion

This study shows that friction and wear are increased with increasing temperature. This may be attributed to decreasing of viscosity with increasing temperature. According to Clark et al. [2], viscosity of the fuel decreases with increasing of temperature. Another possible interpretation given by Masjuki et al. [16] is that the lower boundary effect and/or breakdown of boundary lubrication is due to the lower viscosity. According to Brajendra et al. [17] the ester ends of the fatty acid chain are adsorbed to metal surfaces, thus permitting monolayer film formation with the hydrocarbon end of fatty acids oriented away from the metal surface. The fatty acid chain thus offers a sliding surface that prevents the direct metal-to-metal contact. The stability of these films depend on operating conditions such as load, temperature, speed as well as fluid viscosity and composition [15]. This suggests that at higher temperature, these films seem to be less stable and is thereby cause comparatively higher wear and friction.

It is found that the lubricity in terms of friction and wear increases with increasing the concentration of biodiesel. According to Wain et al. [18] biodiesel containing more oxygen can reduce friction and wear as compared to diesel fuel. This can also be attributed to the presence of aliphatic fatty acid of general formula  $C_nH_{2n+1}COOH$ , such as stearic acid in POME which can enhance lubrication property by controlling friction and wear between contact surfaces through developing of lubrication films [19]. The protective films can reduce thermal energy in sliding contact and thereby improve lubricity [20]. These lubricity enhancing films are most likely carboxylic acid moiety based [21]. In an another explanation, trace components found in biodiesel fuels including free fatty acids, monoglycerides, diglycerides are reported to improve the lubricity of biodiesel [22]. Oxygenated moieties, degree of unsaturation, chain length of molecules in biodiesel also play an important role in increasing lubricity.

From the obtained results it is found that oxidation rate increases with increasing the concentration of biodiesel. During oxidation, with increasing temperature, water content is increased while no water was found for as-received biodiesel. According to Tsuchiya et al. 2006, the oxidation process produces water and free fatty acids like formic acid, acetic acid,

propionic acid, caproic acid etc. [23]. They also added that these acids are strongly corrosive and corrode metals in vehicle fuel system. The causes of oxidation may be attributed to the exposure of biodiesel to air at higher temperature. Apparently, in short term test, by increasing viscosity through oxidation process can provide better lubricity but in case of long term application, it causes degradation of fuel and is therefore results in reduced lubricity [23], enhanced corrosion and degradation of materials [24]. So, it is assumed that effect of oxidation on lubricity is crucial. This possible mechanism will be explored in future studies.

Surface morphology shows that layers of debris from the surfaces have been extruded sideways, while flakes of debris are extruded out from the contact interface in the sliding direction of the rotating ball. Removal of small particles (<20 $\mu\text{m}$ ) with a few surface features results abrasive wear [25]. Deformation of surface decreases with increasing biodiesel concentration. This implies that biodiesel blends provided better lubricity even at higher temperature.

## 5. Conclusions

The following conclusions are drawn from this study:

1. Lubricity in terms of friction and wear rate is decreased with increasing temperature.
2. Lubricity at each temperature increases as a consequence of increasing biodiesel concentration.
3. Deformation of the worn surface increases with increasing temperature. On the other hand, it decreases with increasing biodiesel concentration.
4. At higher temperature, biodiesel become oxidized and free water content also increases.

## References:

- [1] Knothe G. Analysis of oxidized biodiesel by  $^1\text{H-NMR}$  and effect of contact area with air. *Eur J Lipid Sci Technol* 2006;108:493–500.
- [2] Clark SJ, Wagner L, Schrock MD, Piennaar PG. Methyl and ethyl soybean esters as renewable fuels for diesel engines. *J Am Oil Chem Soc* 1984;61:1632–8.
- [3] Masjuki HH, Zaki AM, Sapuan SM. Methyl ester of palm oil as an alternative diesel fuel. In: *Fuels for automotive and industrial diesel engines: Proceedings of the second Institute of Mechanical Engineering seminar, Institute of Mechanical Engineering, London; 1993. p.129–37.*
- [4] Lebedevas, S.; Vaicekauskas, A. Research into the application of biodiesel in the transport sector of Lithuania, *Transport XXI* (2) (2006), pp. 80–87.
- [5] Rashid, U.; Anwar, F.; Moser, B. R. Gerhard Knothe. Moringa oleifera oil: A possible source of Biodiesel. *Bioresource Technology* (2008), doi.10.1016/j.biortech.2008.03.066.
- [6] Holser R. A.; Harry-O’Kuru, R. Transesterified milkweed (*Asclepias*) seed oil as a biodiesel fuel, *Fuel* 85 (2006) 2106–2110.
- [7] Fraer R., Dinh H., Proc K., McCormick R.L., Chandler K., Buchholz B. “Operating Experience and Teardown Analysis for Engines Operated on Biodiesel Blends (B20).” SAE Technical Paper No. 2005-01-3641, 2005.
- [8] Kenneth Proc, Robb Barnitt, R. Robert Hayes, Mathew Ratcliff, Robert L. McCormick, Lou Ha, Howard L. Fang. 100,000 – Mile Evaluation of Transit Buses Operated on Biodiesel Blends (B20) NREL/CP-540-40128, 2006 SAE International.
- [9] Karonis, D.; Anostopoulos, G.; Lois, E.; Stournas, S.; Zannikos, F.; Serdari, A. Assessment of the Lubricity of Greek Road Diesel and the Effect of the Addition of Specific Types of Biodiesel. SAE Tech. Pap. Ser. 1999, 1999-01-1471.
- [10] Anostopoulos, G.; Lois, E.; Serdari, A.; Zannikos, F.; Stornas, S.; Kalligeros, S. Lubrication Properties of Low-Sulfur Diesel Fuels in the Presence of Specific Types of Fatty Acid Derivatives. *Energy Fuels* 2001, 15, 106–112.
- [11] Anostopoulos, G.; Lois, E.; Karonis, D.; Kalligeros, S.; Zannikos, F. Impact of Oxygen and Nitrogen Compounds on the Lubrication Properties of Low Sulfur Diesel Fuels. *Energy* 2005, 30, 415–426.

- [12] Lacey, P. I.; Gunsell, S.; De La Cruz, J.; Whalen, M. V. Effects of High Temperature and Pressure on Fuel Lubricated Wear. SAE Tech. Pap. Ser. 2001, 2001-01-3523.
- [13] Hughes, J. M.; Mushrush, G. W.; Hardy, D. R. Lubricity Enhancing Properties of SoyOil When Used as a Blending Stock for Middle Distillate Fuels. *Ind. Eng. Chem.* 2002, 41, 1386-1388.
- [14] Masjuki, H.H.; Maleque, M.A. Investigation of the anti-wear characteristics of palm oil methyl ester using a four ball-ball tribotester test, *Wear* 206 (1997) 179-186.
- [15] Maleque, M. A., Masjuki, H. H., Haseeb, A. S. M. A. Effect of Mechanical factors on tribological properties of palm oil methyl ester blended lubricant, *wear* 239 (2000) 117-125.
- [16] Masjuki, H.H.; Maleque, M.A.; Kubo, A.; Nonaka, T. Palm oil and mineral oil based lubricants – their tribological and emission performance, *Tribology International* 32 (1999) 304-314.
- [17] Brajendra K. Sharma, Kenneth M. Doll, Sevim Z. Erhan, Ester hydroxy derivatives of methyl oleate: Tribological, oxidation and low temperature properties, *Bioresource Technology* 99 (2008) 7333–7340.
- [18] Wain, K. S.; Perez, J. M.; Chapman, E.; Boehman, A. L. Alternative and low sulfur fuel options: boundary lubrication performance and potential problems. *Tribology International* 38 (2005) 319.
- [19] Masjuki, H. H., Maleque, M. A. The effect of palm oil diesel fuel contaminated lubricant on sliding wear of cast irons against mild steel, *Wear* 198 (1996) 293-299.
- [20] Knothe, G.; Steidley, K.R. Kinematic viscosity of biodiesel fuel components and related compounds. Influence of compound structure and comparison to petrodiesel fuel components. *Fuel* 84 (2005) 1059-1065.
- [21] Knothe, G., Steidley, K.R. Lubricity of Components of Biodiesel and Petrodiesel. The origin of Biodiesel Lubricity. *Energy & Fuels* 2005, 19, 1192-1200.
- [22] Hu J., Du Z, Li C, Min E. “Study on the lubrication properties of biodiesel as fuel lubricity enhancers.” *Fuel* 2005;84(12&13):1601-6.
- [23] Tsuchiya, T.; Shiotani, H.; Goto, S.; Sugiyama, G.; Maeda, A. Japanese Standards for Diesel Fuel Containing 5% FAME blended diesel fuels and its Impact on Corrosion, Copyright©2006SAE International. 2006-01-3303.
- [24] Agarwal AK, Bijwe J, Das LM. Wear assessment in biodiesel fuelled compression ignition engine. *J Eng Gas Turbine Power (ASME J)* 2003;125(3):820–6.
- [25] Sperring, T.P.; Nowell, T.J. SYCLOPS—a qualitative debris classification system developed for RAF early failure detection centres. *Tribology International* 38 (2005) 898–903.

# THE EFFECT OF CERIUM ADDITION ON WEAR BEHAVIOUR OF EUTECTIC AND HYPOEUTECTIC Al-Si-Mg ALLOY

A.S.Anasyida<sup>1</sup>, A.R.Daud<sup>2</sup>, M.J.Ghazali<sup>3</sup>

<sup>1,2</sup>School of Applied Physics, Faculty of Science and Technology,  
Universiti Kebangsaan Malaysia, 43600 Bangi, Selangor

<sup>3</sup>Department of Mechanical and Materials Engineering  
Universiti Kebangsaan Malaysia, 43600 Bangi, Selangor

Corresponding Author: email: syida\_7853@yahoo.com; Tel/Fax: 03-89213806/03-89213777

## Abstract

*Wear behaviour of as-cast eutectic and hypoeutectic Al-Si-Mg alloys with cerium addition was studied. The Al-12Si-4Mg and Al-4Si-4Mg alloys were prepared using casting process by varied cerium addition in the alloy from 1 to 5 wt%. Dry sliding wear tests were performed against a hardened carbon steel (Fe-2.3%Cr-0.9%C) using a pin-on-disc configuration with fixed sliding speed of 1 m/s and load 50 N at room temperature of ~25°C. Morphologies of both worn surfaces and collected debris were characterised by a scanning electron microscope (SEM) equipped with an energy dispersive X-ray spectrometer (EDS). It was revealed that the by addition of cerium, intermetallic Al-Ce needle-like structure was present in both alloys whereas Al-Si-Ce blocky phase only presence in the hypoeutectic alloys. The increase in cerium content up to 2 wt% led to higher wear resistance behaviour for both as-cast alloys. Formation of craters and localised plastic deformation were observed on the worn surface of both as-cast alloys, resulting fine particulate and sheet-like wear debris. The wear resistance was found higher for hypoeutectic alloy compared to the hypoeutectic alloy.*

**Keywords:** wear resistance, cerium, friction, aluminium alloy; microhardness

## 1. Introduction

Aluminium alloy was used widely in transportation engineering applications because of their high strength-to-weight ratios [1]. However, the relatively low wear resistance of the aluminium alloys is one of the major factors that restricts the further replacement of several automotive engine components and brake rotors made of cast iron by these energy efficient materials. Recent advances in the processing technologies have provided new means of producing for tribological applications. One approach has been to incorporate minor alloying element into cast aluminum alloys. Savaskan and coworkers [2] found that the wear loss of a monotectoid-based zinc-aluminium alloy was decreased by the addition of 2 wt% Cu. The addition of Na and Sr result in modification of siliocon morphology of silicon from angular platelets to fine fibrous leading to additional improvement in the mechanical properties [3]. Lead content from 2 to 10 wt% in Al-Si-Pb

alloys has been found to decrease the wear rate of the alloys [4]. This work carried out to determine the the effect of cerium (Ce) on wear behaviour of the eutectic and hypoeutectic alloys under 50 N applied load and various sliding distances.

## 2. Experimental

A cast Al-12%Si-4%Mg and Al-4%Si-4%Mg alloy was processed by conventional casting processes. Experimental alloys were prepared by controlled melting of high-purity aluminium (99.9%), magnesium (99.9%) and silicon (99.9%) and varied cerium (99.9%) from 1 to 5 wt% in a graphite crucible using an electric furnace under an argon gas atmosphere. The molten metal of the alloys were poured into steel mould at 850 °C to produce castings 12 mm in diameter and 80 mm in length. The specimens was polished using standard metallographic procedure consisting grinding, polishing and etching (Keller's reagent).

The microstructure of the castings was studied under optical microscope (Axiotech 1000HD). The scanning electron microscopy (1450 LEO SEM) of wear surfaces was carried out to study the mode of wear. Wear behaviour of both eutectic and hypoeutectic alloys were conducted on standard pin-on-disc machine. Each alloy was sectioned to 10 mm in diameter and 15 mm in length. The alloys (pin) then clamped against a counter surface hardened carbon steel EN-31 (Fe-2.3%Cr-0.9%C) with hardness of 60 HRC. Length of travel on wear path was 100 mm under a constant load of 50 N. Volume loss was used as a measure of wear. Wear rate was calculated as weight loss per unit of sliding distance ( $\text{mm}^3/\text{m}$ ). Both pins and counterface were cleaned with acetone before and after each wear test.

### 3. Results and Discussion

#### 3.1 Microstructure

Optical micrographs in Fig. 1(a,b) show the eutectic and hypoeutectic of as-cast alloy without Ce added comprising primary  $\alpha$ -aluminium dendritic network, Al-Si eutectic mixture in the interdendritic and  $\text{Mg}_2\text{Si}$  phase. The addition of Ce led to the precipitation of Al-

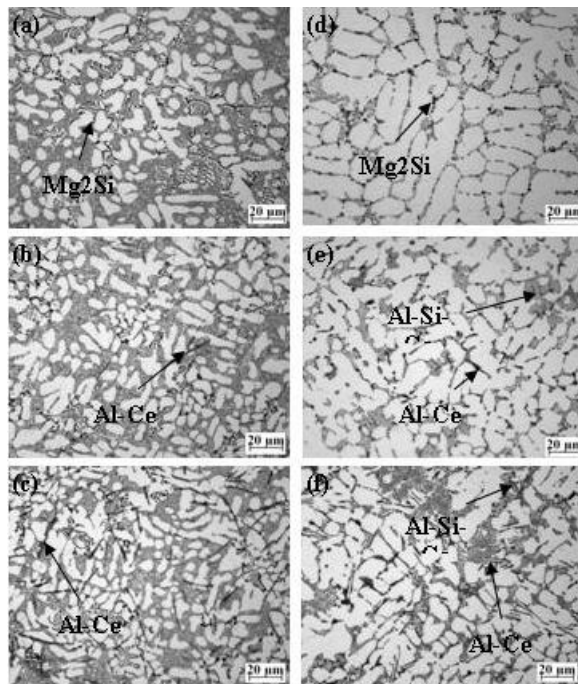
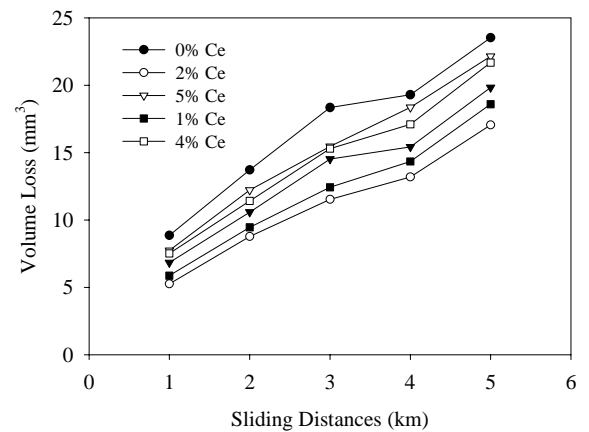


Fig. 1 (a) 0% Ce, eutectic (b) 2 wt% Ce, eutectic (c) 5 wt% Ce, eutectic (d) 0 wt% hypoeutectic (e) 2wt% Ce, hypoeutectic and (f) 5 wt% Ce, hypoeutectic.

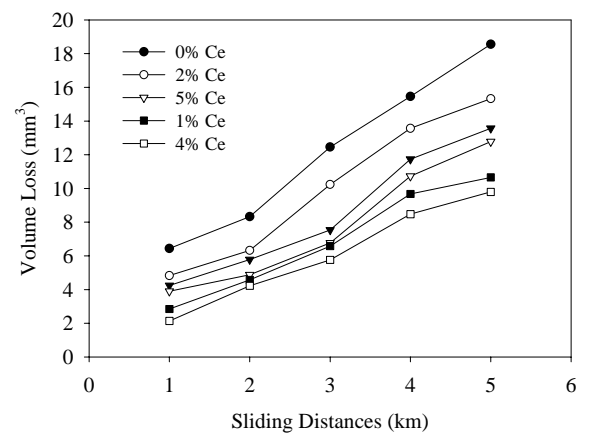
Ce intermetallic phases in both alloy which exhibited a needle-like structure [5] as shown in Fig. 1 (c,e). A blocky shape Al-Si-Ce intermetallic phases was detected only in hypoeutectic alloy (Fig. 1e,f). Further increase of Ce content up to 5 wt%, the needle-like Al-Ce phase was increased and coarsened. These intermetallic phases help to improve hardness [6] and wear resistance of the as-cast alloy.

#### 3.2 Wear response

Fig. 2 shows the wear test results, which represent the volume loss as a function of the sliding distances for both as-cast alloys. Clearly, the volume loss of both as-cast alloys increases with increasing sliding distances. It is observed that the volume loss of eutectic as-cast alloys initially decreases with Ce content up to 2 wt.% and increases dramatically with cerium addition



(a)



(b)

Fig. 2 Volume loss as a function of sliding distances (a) Eutectic alloys (b) Hypoeutectic alloys.

of 3 to 5 wt.%. In fact, the wear resistance behaviour of eutectic alloy containing up to 2 wt% Ce was found to be lower than the Al-Si-Mg without any Ce addition. For hypoeutectic alloys, the volume loss was found to be decreased with increasing Ce content.

Decrease in volume loss may be attributed to an increase in the microhardness as a result of the increase in amount of Al-Ce and Al-Si-Ce intermetallic phases. The strong bonds between intermetallic phases and matrix will help to protect the surface from severe wear mechanism [7]. Fig. 3 shows the wear rate as a function of Ce content. Generally, wear rate of the hypoeutectic alloys is lower compared to the eutectic alloy. The lower wear rate in hypoeutectic alloys may be attributed to the presence of Al-Ce and Al-Si-Ce which improved the hardness and bonding between the Al matrix.

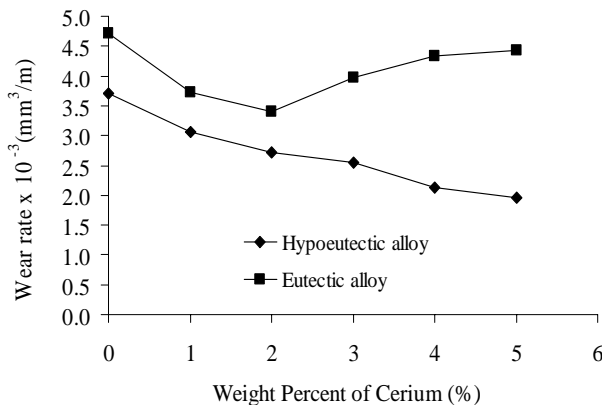
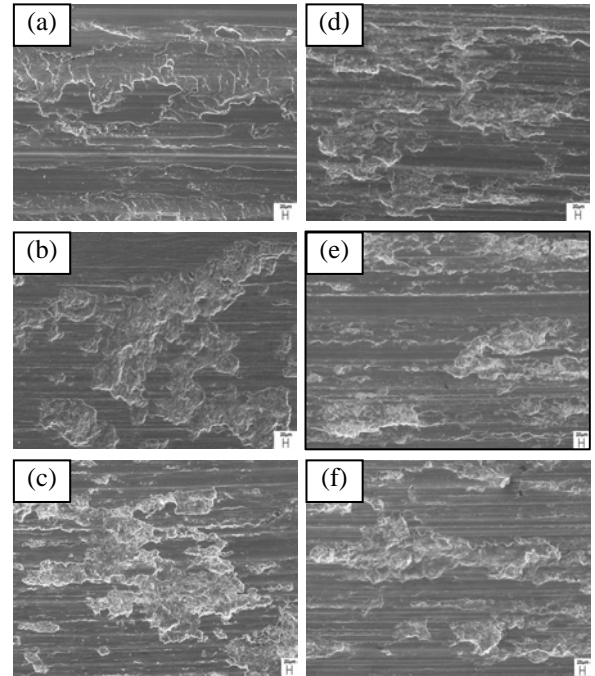


**Fig. 3** Wear rate as a function of Ce content (a) Eutectic alloys (b) Hypoeutectic alloys.

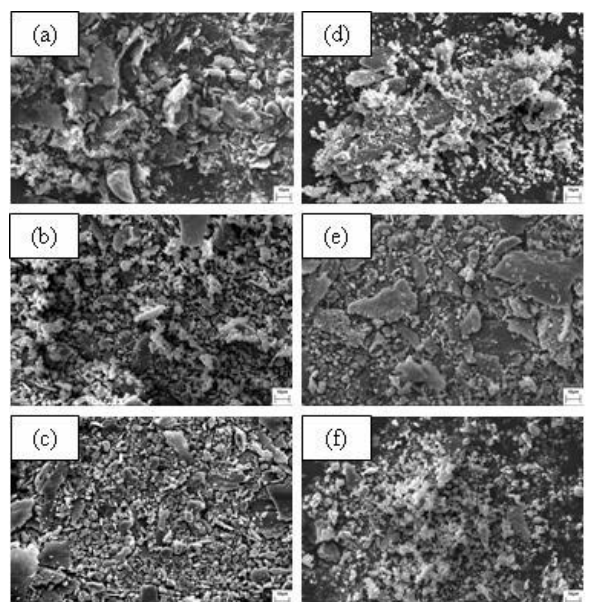
### 3.3 Worn surface and wear debris

Fig. 4 showed the worn surface of both eutectic and hypoeutectic alloy containing 0 wt%, 2 wt% and 5 wt% Ce at 5 km sliding distance. Both alloys display surface damages like micro-grooves, craters and abrasive scoring marks. The worn surface of eutectic alloy without Ce addition showed truncated grooves, delamination and shallow grooves was observed in alloy containing 2 wt% Ce. In addition, alloy containing 5 wt% Ce showed delamination. In hypoeutectic alloys, severity of worn surfaces decreases with increasing Ce content. The worn surface of the hypoeutectic alloys has a rather smooth appearance as a result of homogeneous wear; it indicates that wear process mainly took place by plastic deformation [8]. Fig. 5 shows SEM micrographs of the wear debris; the wear

debris was present as a mixture of large irregular-shaped platelets and a small amount of particles. A number of the platelets were compact and appeared in some plastic deformation.



**Fig. 4** SEM morphologies of worn surfaces with (a) 0% Ce, eutectic, (b) 2% Ce, eutectic (c) 5% Ce, eutectic, (d) 0% Ce, hypoeutectic, (e) 2% Ce, hypoeutectic (f) 5% Ce, hypoeutectic



**Fig. 5.** SEM micrographs of wear debris with (a) 0% Ce, eutectic, (b) 2% Ce, eutectic (c) 5% Ce, eutectic, (d) 0% Ce, hypoeutectic, (e) 2% Ce, hypoeutectic (f) 5% Ce, hypoeutectic

#### 4. Conclusions

The addition of Ce in both alloys led to precipitation of Al-Ce intermetallic phase exhibited needle-like structure. Intermetallic phase Al-Si-Ce only presence in the hypoeutectic alloys. Wear mechanism is combination of abrasive delamination. Wear behaviour of hypoeutectic alloys show higher wear resistance compared to eutectic alloys

#### References

- [1] Basavakumar, K.G, Mukunda, P.G. and Chakraborty, M., Influence of melt treatments on sliding wear behavior of Al-7Si and Al-7Si-2.5Cu cast alloys, *Journal of Material Science* Vol. 42, pp. 7882-7893, 2007.
- [2] Savaşkan, T., Hekimoğlu, A.P. and Pürçek, G., Effect of copper content on the mechanical and sliding wear properties of monotectoid-based zinc-aluminium-copper alloys, *Tribology International* Vol. 37, pp. 45-50, 2004.
- [3] Kori, S.A., Murty, B.S. and Chakraborty, M., Development of an efficient grain refiner for Al-7Si alloy and its modification with strontium, *Materials Science and Engineering A* Vol. 283, pp.94-104, 2000.
- [4] Torabian, H., Pathak, J.P.S. and Tiwari, N., On wear characteristics of leaded aluminium-silicon alloys, *Wear* Vol. 177, pp. 47-54, 1994.
- [5] Fan, Y., Wu, G. and Zhai, C., The microstructure of as-melt spun Al-7%Si-0.3%Mg alloy and its variation in continuous heat treatment, *Material Science Engineering A* Vol. 433, pp. 208-215, 2006.
- [6] Wu, A., Xia, C. And Wang, S., Effects of cerium on the microstructure and mechanical properties of AZ31 alloy, *Rare Metals* Vol. 25, pp 371-376, 2006.
- [7] Sawla, S. and Das, S., Combined effect of reinforcement and heat treatment on the two body abrasive wear of aluminum alloy and aluminum particle composites, *Wear*, Vol. 257, pp.555-561, 2004.
- [8] Wang, F., Zhang, Z., Ma, Y. and Jin, Y., Effect of Fe and Mn additions on microstructure and wear properties of spray-deposited Al-20Si alloy, *Material Letter*, Vol. 58, pp. 2442- 2446, 2004.

## TRIBOLOGICAL PROPERTIES OF NANOSTRUCTURED YSZ THERMAL BARRIER COATINGS

**R.J. Talib, S. Istikamah, N.Roslani, M.S. Mariam, M.F. Fazira**

Advanced Material Research Center (AMREC) SIRIM Berhad,  
Lot 34, Jalan Hi-Tech 2/3, Kulim Hi-Tech Park,  
09000 Kulim, Kedah, Malaysia  
E-mail address: [talibria@sirim.my](mailto:talibria@sirim.my) tel 044017166

### Abstract

*Thermal barrier coatings (TBCs) have been widely used to reduce the temperature imposed on hot section of the metallic components (vaness, blades, shrouds) which are subjected to high temperature such as gas turbines and diesel engines. Zirconia is used as thermal barrier coating due to its low thermal conductivity, high melting point, excellent thermal shock resistance, high resistance to oxidation and high hardness. In this work, the nanostructured yttria stabilized zirconia (YSZ) powders were deposited on stainless steel substrates using atmospheric plasma spray system. The steel substrates were plasma-sprayed with three different plasma powers while the other significant parameters such as plasma gas pressure, powder flow rate, standing distance, and spray speed were kept constant. Each sample was then subjected to tribological test using pin-on-disc CSEM Tribometer, hardness test and surface roughness measurement. Scanning electron microscope is used to observe the morphology of the nanostructured coatings and wear track after tribological tests. Based on the test results, the following phenomena on the plasma-sprayed nanostructured YSZ coating could be concluded; (i) lower friction coefficient, (ii) higher wear resistance, (iii) higher hardness, (iv) smoother surface. It is shown that the optimum mechanical and tribological characteristics were obtained under the plasma power of 32kW.*

**Keywords:** TBC, nanostructured YSZ, tribology, hardness, roughness

### 1. Introduction

Thermal barrier coatings (TBCs), consisting of an yttria stabilized zirconia as top coat sprayed on superalloys precoated with a metallic bond coat deposited on metal alloy substrate using atmospheric plasma spraying [1, 2]. Zirconia coatings have excellent thermal shock resistance and low thermal conductivity, high melting point, high resistance to oxidation and high hardness were used as thermal barrier coating. The thermomechanical properties between YSZ top coat and a metal alloy substrate are different, and thus an intermediate layer between the two is required. The intermediate layer of metallic alloy bond coat such as NiAl, NiCrAlY, CoNiCrAlY, FeNiCr is used to reduce the mismatches of the thermal expansion between top coat and the substrate. This bond coat is also used to improve the adhesion of the coating.

The friction coefficients of the coatings sprayed using the nanostructured powder were

almost the same as those of the coatings sprayed using the conventional powder [3]. However, the plasma-sprayed nanostructured zirconia coating possessed better wear resistance than that of traditional zirconia coating [4]. The higher wear resistance of the plasma-sprayed nanostructured zirconia coating is attributed to its enhanced cohesion, improved microhardness and homogenous microstructure [5].

The objective of this work was to study the tribological properties of nanostructured zirconia coatings against alumina under dry friction conditions. The effect of the plasma power on the tribological properties will be also discussed.

### 2. Method

A commercial stainless steel disk with a diameter of 20 mm and thickness of 5 mm and possesses the following composition (wt. %): C, 0.07; P, 0.03; S, 0.05; Mn, 1.38; Cr, 15.48; Mo, 1.79; V, 0.09; Si, 0.39; Ni, 9.68; Fe, balance was used as a substrate in this study. Nanostructured

ZrO<sub>2</sub>-7wt.%Y<sub>2</sub>O<sub>3</sub> (Nanox S4007, Inframat) was deposited on stainless steel substrate using Praxair 100-kW, standard SG100 plasma torch (Praxair, USA.) atmospheric plasma spraying system. Fig. 1 shows the plasma spraying system layout. Prior to the spraying process, the samples were first grid blasted with alumina particles (40 mesh) and then ultrasonically cleaned in acetone. The nanostructured YSZ powder was sprayed under three different plasma powers, whereas other significant spraying parameters were kept constant as depicted in Table 1. High purity argon and helium were used as plasma and secondary gases, respectively. During spraying, compressed air was applied to stainless steel substrates for cooling purpose.

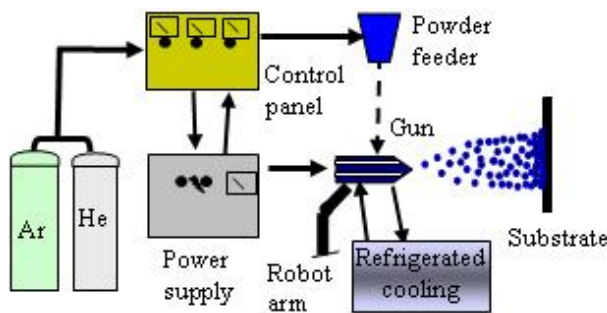


Fig.1. Schematic diagram of Plasma spraying system

The hardness was conducted under the load of 500 g on as-sprayed surface of the sample using Vickers hardness tester (ZHV Germany). All of the reported values of microhardness of the coatings are the mean of 10 indentations. The information on the tribological properties were gathered from the experiment conducted on a pin-on-disc CSEM tribometer (CSEM, Switzerland) using a 6 mm diameter alumina ball at sliding speed of 5.0 cm/s and radius of 6mm for a distance of 750 m under a load of 5N. Surface microstructures of the powder and the as-sprayed coatings were examined by a field emission scanning electron microscope (FESEM, LEO1525, Germany) equipped with energy dispersive X-ray analysis (EDX, Oxford Oxford Inca Wave). The surface roughness of each sample was measured with a surface rougher tester (Mitutoyo Surftest SJ-301) complying with Japanese Standard JIS B 0601 [6]. All measurements were performed under ambient conditions at 25 °C and 50% RH.

Table 1 Spraying parameters

Spraying Parameters	A	B	C
Power (kW)	24	28	32
Argon primary gas (psi)	40	40	40
Argon carrier gas (psi)	30	30	30
He secondary gas (psi)	30	30	30
Powder flow rate (gm/min)	10	10	10
Standing distance (mm)	100	100	100
Spray speed (%)	40	40	40

### 3. Results and Discussion

#### 3.1 Characterisation of Nanostructured Powders

In the plasma spray process, the individual nanoparticles cannot be thermally sprayed because of their low mass and inability to be carried in a moving gas stream thus could not be deposited on the substrate [7]. In order to make the nanoparticles sprayable, the nanosized particles were agglomerated through spray drying to form micrometer-sized powders. Subsequently the powders were subjected to a heat treatment. Fig. 2 shows the SEM-EDX

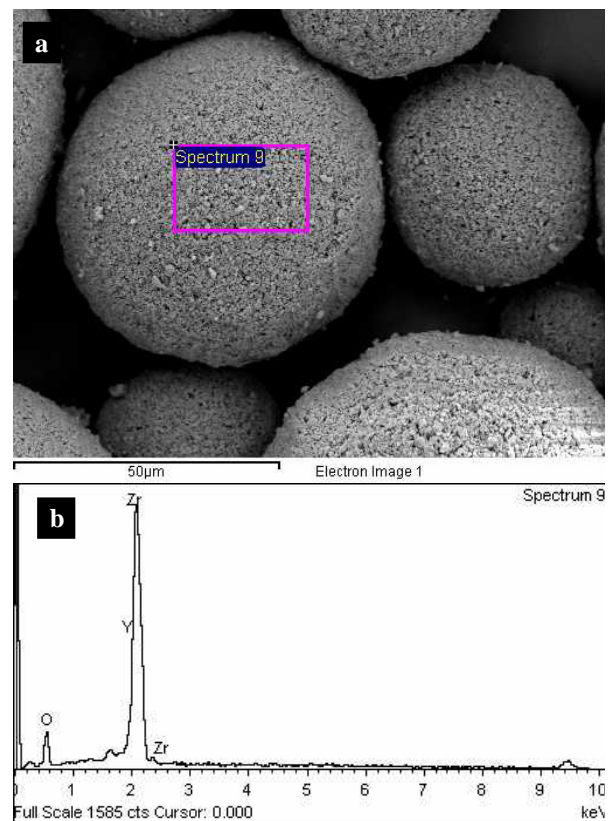


Fig. 2. SEM-EDX analysis (a) Morphology of the agglomerated powders, (b) EDX spectrum

analysis on the nanostructured  $ZrO_2$  7wt.%  $Y_2O_3$  YSZ powders used in this study. The agglomerated YSZ powders having size range of 15 - 150  $\mu m$  are spherical in shape and dense, which improves the flowability and increases the

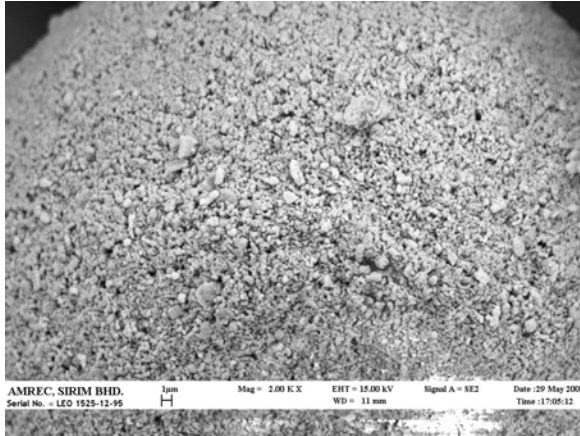


Fig. 3. Microstructure of the agglomerated powders

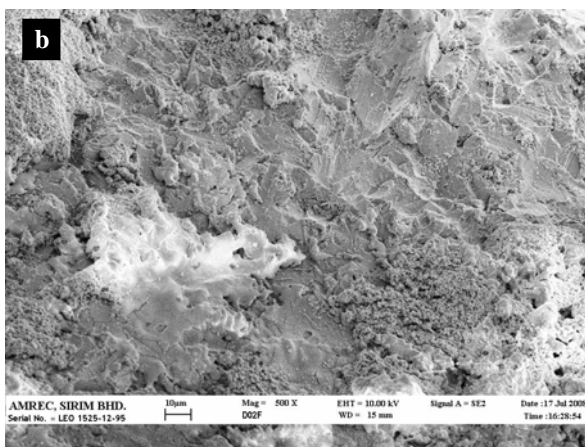
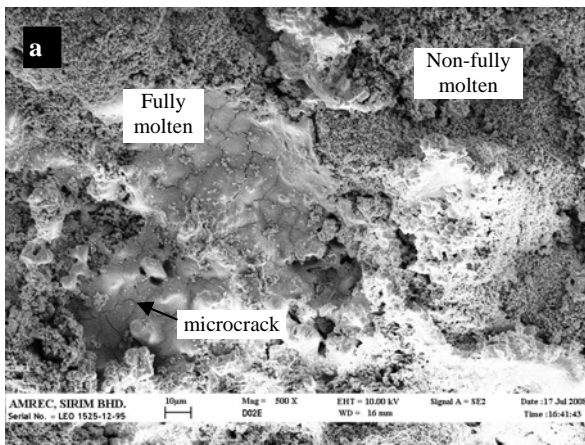


Fig.4. Surface morphology of as-sprayed nanostructured YSZ coating; (a) 24 kW, sample A, (b) 32 kW, sample C

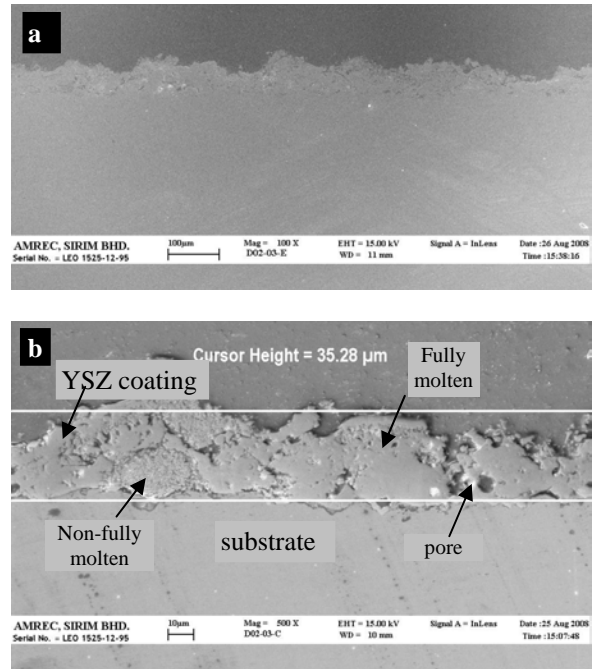


Fig. 5. Cross-section microstructure of as-sprayed YSZ coating: (a) Peak and valley on the as-sprayed surface (b) close-up view showing morphology consists of fully molten, non-fully molten and non-homogeneous structures

mass (Fig. 2a). EDX spectrum on the nanostructured powder indicated that this powder composed of zirconia and yttria. The SEM surface morphology indicated that nanostructured YSZ powders were composed of a large number of nanoparticles as shown in Fig. 3 and these agglomerated powders are also known as nanostructured powders.

Figure 5 presents the cross-section microstructure of the nanostructured YSZ coating. Fig. 5a shows that the coating surface is rough on microscopic level and has peaks and valleys. In this nanostructured coating, the splats that are typical for conventional YSZ coatings were not observed. A splat is in the shape of pancake-like, single impacted particle. Racek and Berndt (2007) also observed the same phenomena [8]. It was observed that the thickness this nanostructured coating is 35.28  $\mu m$  (Fig. 5b) which is not thick enough for TBC application. Generally, the thickness for TBC application is 300  $\mu m$ . This is a preliminary work, further studies will be carried out by increasing the powder feed rate, spraying passes and spraying speed parameters in achieving the desired thickness of coatings and other TBC optimum characteristics.

### 3.2 Roughness and Hardness

Fig. 6 and 7 show the surface roughness and hardness test results respectively. As expected, the coating hardness slightly increases and the surface roughness decreases with increasing plasma power. Increasing plasma power increases temperature and velocity isocontours of the in flight particles, thus enhanced melting and lowering particle viscosity [9]. High velocity with lower viscosity may increase the spreading of the in flight particle, subsequently highly flattened and more molten particles deposited on the surface which will form a coating layer with a low surface roughness (Fig. 4b and Fig. 6).

Lower roughness shows that the coatings are well packed and this may be the reason why the hardness increased with increasing plasma power (Figure 4b and Fig. 7). Lower plasma power resulted increase number of non-molten particle (Fig. 4a) and this will increase the roughness and lower the hardness due to low particle cohesion of the coating.

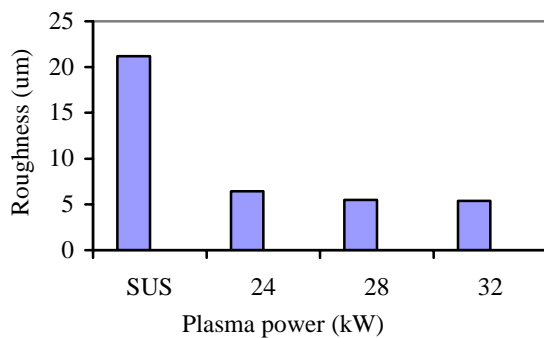


Fig. 6. Surface roughness the as-sprayed TBC

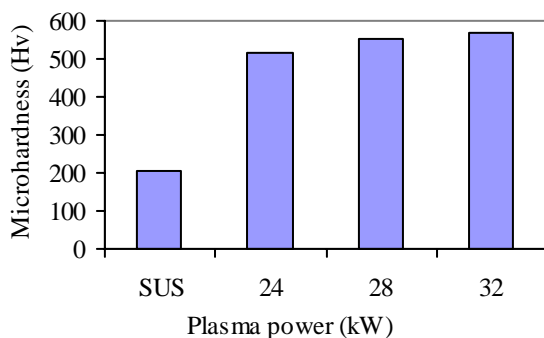


Fig. 7. Hardness of the as-sprayed TBC

### 3.3 Friction Coefficient

Fig. 8 presents the variation of friction coefficients with sliding distance under a load of

5 N against alumina at room temperature. It can be seen that the friction coefficient of as-sprayed nanostructured Zirconia coating is lower than that of the stainless steel substrate. The friction coefficient increase gradually with increasing sliding distance after the run-in period. This increase is attributed to the increase of actual contact area of the friction couples as the sliding distance increased. The nanostructured YSZ coating of all samples still intact even after a sliding distance of 750 meters. Once the coating layer has been exposed, the friction is between the alumina ball and stainless steel substrate where friction coefficient will be reaching is 0.8 which is the friction coefficient of substrate material.

The friction coefficients of the nanostructured zirconia coating against alumina ball increased lineally with increasing sliding distance depending on plasma powers applied. The curves show that the sample deposited with higher plasma power recorded the lowest friction coefficient. This sample C was sprayed under high plasma power which may produce coating layer with less porous as a result of in flight particles have more velocity and subjected to high temperature. High temperature resulting more molten particles, while high velocity resulting high impact energy and subsequently improve the as-sprayed coating surface characteristics. This sample is less porous and much smoother than other samples (Fig. 6) which may result higher contact area but the sliding resistance is less. Rougher and more porous structure have a higher sliding resistance as a result of more peaks and valleys on the surface as shown in Fig.5.

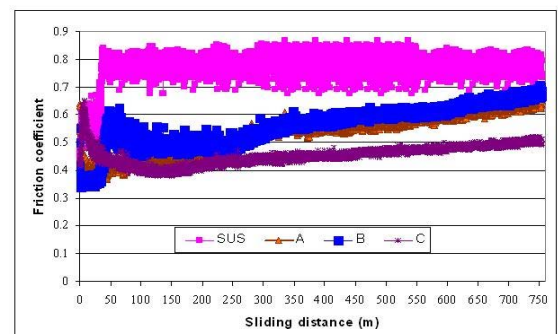


Fig. 8. The variation of friction coefficients of stainless steel substrate and nanostructured zirconia coatings with sliding distance

### 3.4 Wear track

Test results show that the wear track width of as-sprayed coatings decreased with increasing of

plasma power as depicted in Table 2 and Figure 9. It was observed that sample C has the shortest wear track width as compared with other samples in the same testing conditions. This show that sample C is superior in terms of wear resistance and this can be attributed to high surface hardness and low friction coefficient. The improved wear resistance is also attributed to the optimization of microstructure and the enhancement of mechanical property, which improved the ability of plastic deformation [4].

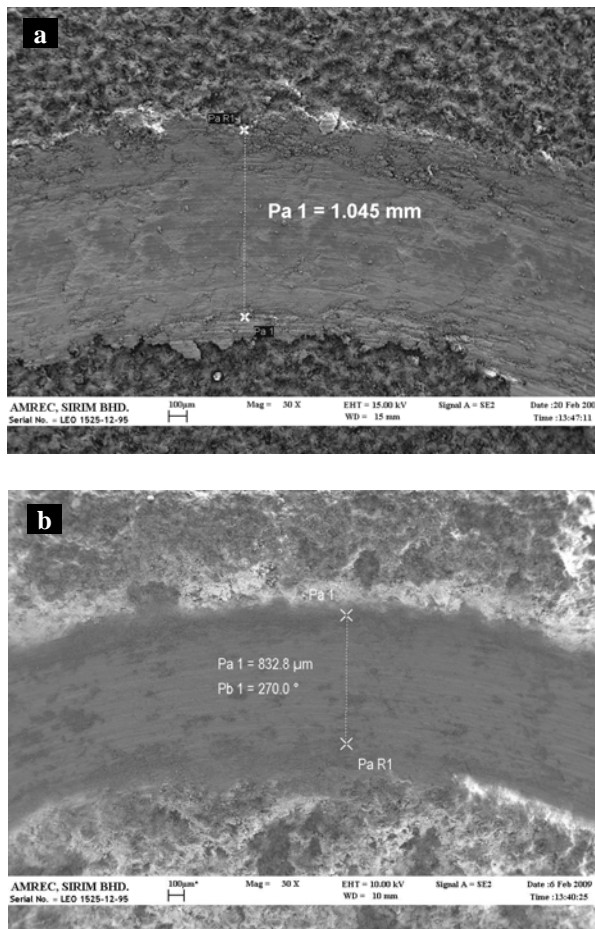


Fig. 9. SEM micrograph showing the wear track width; (a) sample A, (b) sample C

Table 2. Wear track width

Bil.	Sample	Track width (mm)
1.	Substrate	1.440
2.	Sample A	1.045
3.	Sample B	0.944
4.	Sample C	0.832

Fig. 10 shows the SEM micrograph of wear track on sample C. EDX analysis carried out on the surface of layers exposed during wear tests shows that there are no elements composed in

the stainless substrate was found (Fig. 9b and 9c). This proved that the nanostructured YSZ coating still intact and the adhesion between the coating and substrate are in good condition even after a sliding distance of 750m. All samples show the same phenomena. If the coating layer has been exposed, the elements that composed in the stainless substrate such Fe, Cr, V, Mo, Mn and Ni will be detected by EDX analysis.

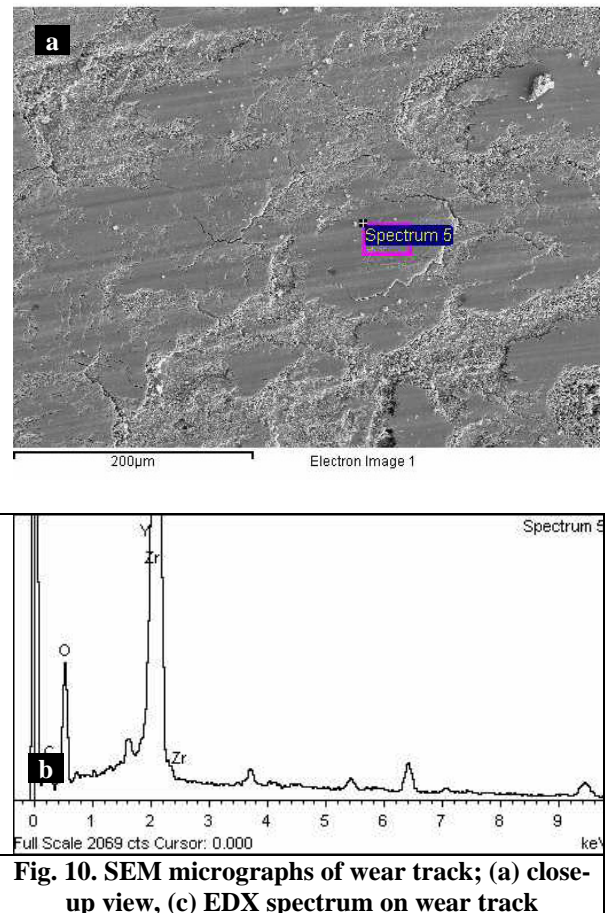


Fig. 10. SEM micrographs of wear track; (a) close-up view, (c) EDX spectrum on wear track

#### 4. Conclusions

In this work, nanostructured zirconia coatings were successfully deposited by atmospheric plasma spraying by varying the plasma powers. It is shown that the best plasma power applied in this investigation was at 32kW. This postulation is based on the optimum mechanical and tribological characteristics produced under this plasma power applied. Nanostructured YSZ coating have improved the following characteristics; (i) reduce friction coefficient, (ii) higher wear resistance, (iii) higher hardness, (iv) smoother surface, as compared with uncoated substrate. These improvements will definitely

improve the life span of the components which will be subjected to high temperature and corrosive atmosphere.

### Acknowledgements

The authors are grateful to the Government of Malaysia for funding this research project through Science Fund grant (003-03-02-SF0080) and SIRIM Berhad for providing research facilities. The authors would also like to thank Mr. Ahmad Nizam Abdullah for kind cooperation in the preparation of the coating specimens and plasma spraying.

### References

- [1]. R. S. Lima, A. Kucuk and C. C. Berndt. 2001, Integrity of nanostructured partially stabilized zirconia after plasma spray processing. *Materials Science and Engineering A*, Volume 313, Issues 1-2, pp. 75-82, 2001.
- [2]. Zhou, C., N. Wang and H. Xu. Comparison of thermal cycling behavior of plasma-sprayed nanostructured and traditional thermal barrier coatings, *Materials Science and Engineering: A*, Volumes 452-453, pp. 569-574, 2007.
- [3]. J.F. Li, H. Liao, X.Y. Wang, B. Normand, V. Ji, C.X. Ding, C. Coddet. Improvement in wear resistance of plasma sprayed yttria stabilized zirconia coating using nanostructured powder, *Tribology International* 37, pp, 77-84, 2004.
- [4]. Chen, H., Y. Zhang, C. Ding. Tribological properties of nanostructured zirconia coatings deposited by plasma spraying. *Wear* 253, pp. 885-893, 2002.
- [5]. Chen, H., C. Ding, P. Zhang, P. Lab, S. W. Lee. Wear of plasma-sprayed nanostructured zirconia coatings against stainless steel under distilled-water conditions. *Surface and Coatings Technology* 173, pp. 144-149, 2003.
- [6]. JIS B 0601-1982: *Japanese industrial standard. Definitions and designation of surface roughness*. Japanese Standards Association
- [7]. L.L. Shaw, R. Ren, D. Goberman, Measurements of the fracture energy of the coating/substrate interfacial region through radial-notched cylindrical specimens *Surface and Coatings Technology*, Volume 130, Issue 1, 1 pp. 74-79, 2000.
- [8]. O. Racek, C.C. Berndt. Mechanical property variations within thermal barrier coatings. *Surface & Coatings Technology* 202, pp. 362-369, 2007.
- [9]. M. Vardelle, A. Vardelle, P. Fauchais, M.I. Boulos. Fundamentals of Plasma-Particle Momentum and Heat Transfer. In. *Plasma Technology in Metallurgical Processing*, J. Fein-man (Ed.), Iron & Steel Society, pp. 49-63, Warrendale, USA., 1987.

## WEAR AND FRICTION CHARACTERISTICS OF WASTE VEGETABLE OIL CONTAMINATED LUBRICANTS

M. A. Kalam<sup>1</sup>, H. H. Masjuki<sup>2</sup> and Liaquat Ali Memon<sup>3</sup>

Department of Mechanical Engineering, University of Malaya, 50603 Kuala Lumpur

Corresponding Author: Email: [kalam@um.edu.my](mailto:kalam@um.edu.my), Tel: + 603-796786863, Fax: + 603-79675317

### Abstract

This paper presents the experimental results of normal lubricant, additive added lubricant and waste vegetable oil (WVO) contaminated lubricants to evaluate friction and wear characteristics. The test was conducted using a four-ball tribotester with standard test method IP-239. The balls used in four-ball tribotester were based on carbon-chromium steel ball bearings. The data presented to evaluate friction and wear characteristics are coefficient of friction ( $\mu$ ), wear scar diameter (WSD), flash temperature parameter (FTP), viscosity index (VI) and total acid number (TAN). Each test was conducted for five different loads such as from 50 kg to 90 kg (with 10 kg intervals) to observe the variation of above parameters. The lubricant was contaminated with WVO from 1% to 5%. The normal lubricant (as sample A) was used for comparison purposes. The test results show that WVO contaminated lubricants with suitable anti-wear additive has influences in reducing wear and friction coefficient. The objective of this investigation is to develop a new lubricant based on waste palm oil (such as WVO). The promising results have been presented with discussions.

**Keywords:** WVO, WSD and Four-ball tribotester

### 1. Introduction

There is a close relationship between development of lubricant (lubricant formulation), engine materials and fuel. The conventional mineral oil based lubricant was developed based on fossil fuel (such as gasoline and diesel fuels) which is not suitable for biodiesel fuelled engine as it degrades lube oil quality and increases engine wear rate as found in Masjuki et al. 1997[1]. This happens due to mixing fuel with lubricant through the piston-cylinder friction zone. In this investigation, waste palm oil (as WVO) contaminated lubricant has been developed as a biodegradable lubricant to be used for biodegradable fuelled engine such as biodiesel fuelled engines. Based on four ball tribotesting results, WVO contaminated lubricant with the presence of suitable anti-wear additive shows promising result as compared to conventional lubricant. This is mainly due to better thermal and oxidative properties of WVO consisting of long chain saturated fatty acids that leads to inferior cold flow behaviour [2]. The results of this investigation have given an indication for formulation of a new lubricant.

### 2. Experimental details

#### 2.1 Equipment

Four-ball tribotester machine was used with standard test method of IP-239. This machine is simple to use for testing friction and wear of lubricating oils. Three balls are located in a (Fig.1) cup below a fourth ball which is connected to a rotating shaft via a chuck. Different loads are applied to the balls by weights on load lever. The frictional torque exerted on the three lower balls can be measured by a calibrated arm,

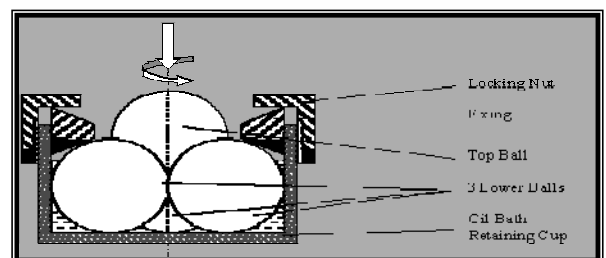


Fig. 1. Schematic diagram of the four-ball tribotester

which is connected to the spring of a friction recording device. The extension of the spring in resisting the frictional torque is transmitted through a link mechanism, to a pen which records its travel on a drum at 1 revolution in 60-75s.

## 2.2 Ball materials

The tested ball's material was carbon-chromium steel (SKF), 12.7mm in diameter with a surface roughness of 0.1µm C.L.A. The chemical composition of ball material was scanned by Energy Dispersion X-Ray Spectrometer (EDS) as shown in Table 1. Before starting a test, all the balls were cleaned using spirit alcohol and dried with dry air.

Before starting a test, the four-ball tribotester machine was operated without any load for a period of 15 min, all the approximate parts of the machine were clean by solvent, dry with a clean soft lint-free cloth or clean dry air.

**Table 1 Chemical composition (wt. %) of carbon-chromium steel ball material**

Element	C	Si	P	S	Total	100.00
wt. %	10.20	0.45	0.12	0.07		
Element	Cr	Mn	Fe	Ni		
wt. %	1.46	0.42	87.21	0.06		

## 2.3 Lubricant samples

Three samples were explicitly prepared such as (1) Sample A – normal lubricant as SAE40 grade. It can be stated that sample A is the reference lubricant, (2) Sample B- consists of sample A with 0.5% Amine phosphate additive, and (3) Sample C – consists of sample A with 0.5% Octylated/

**Table 2 Lubricant sample compositions**

Samples	Lubricant compositions
A	Normal lubricant as SAE 40 grade
B	Sample A with 0.5% Amine phosphate additive
C	Sample A with 0.5% Octylated/butylated diphenylamine additive plus 1% to 5% waste palm oil with base lubricant
D	Sample B with 1% to 5% waste palm oil with base lubricant
E	Sample C with 1% to 5% waste palm oil with base lubricant

butylated diphenylamine additive. It can be stated that sample B and sample C are prepared with two different types of anti-wear additives. The sample B and sample C can be referred to as base

lubricants with respect to contaminated lubricant by WVO. The sample B and sample C were contaminated with WVO from 1% to 5%. Details of lubricant compositions can be seen in Table 2. Details properties of anti-wear additives can be seen in Table 3.

**Table 3 Properties of anti-wear additives**

Chemical description	Amine phosphate	Octylated/butylated diphenylamine
Treat level/range (%)	0.1 – 1.0	0.3 – 1.0
Viscosity at 40°C (mm <sup>2</sup> /s)	220	280 (mm <sup>2</sup> /s)
Melting point	<10°C	<10°C
Density at 20°C (g/m <sup>3</sup> )	0.92	0.98
Phosphorus (%)	4.8	-
Nitrogen (%)	2.7	4.5
Flash point (°C)	135	185
Solubility limits at 5°C (wt. %)		
oil	Mineral 3	5
	Ester >5	5
	water <0.01	<0.01

## 2.4 Test procedure

At the beginning of the experiment, lubricant sample is placed on the erected plate where three balls are held position into a cup (at the end of the motor spindle) with the clamping ring and assembly secured by tightening the locknut. The fourth ball is then fitted on the upper balls chuck. Mounting disks are placed between the thrust bearing and the cup. The desired loads are then placed on the load lever to be tested at. The conducted test method is standard IP-239.

## 2.5 Friction evaluation

The coefficient of friction is calculated by multiplication of the mean friction torque and spring constant [3]. The friction torque on the lower balls may be expressed thus;

$$T = \frac{\mu \times 3W \times r}{\sqrt{6}} \Rightarrow \mu = \frac{T \sqrt{6}}{3W \times r} \dots\dots(1)$$

Where,  $\mu$  = coefficient of friction

T = frictional torque in kg/mm

W = applied load in kg

r = distance from the center of the contact surfaces on the lower balls to the axis of rotation, which is 3.67mm

## 2.6 Wear test

The test run was carried out at loads (50, 60, 70, 80 and 90 in kg) and at 1500 rev min<sup>-1</sup> with test duration of 60 minutes. The wear scar diameter (WSD) is measured and analyzed by “ducom software” with installed image acquisition system.

## 2.7 Flash temperature parameter

A single number is used to express the critical flash temperature above which a lubricant will fail under given conditions. For conditions existing in the four-ball test, the following formula is used [4].

$$FTP = \frac{W}{d^{1.4}} \dots\dots\dots (2)$$

Where, W = load in kg  
 d = mean wear scar diameter in mm

## 2.8 Kinematics Viscosity Analysis

The ISL Automatic HOUILLON Viscometer is used to measure the viscosity of the lubricating oil using ASTM Method D-455 with two controlled bath temperatures such as 40°C and 100°C. Before measuring the viscosity of the lube oil, the viscometer tubes are calibrated by standard sample lube oil. The lube oil is warmed to the desired temperature and allowed to flow through the calibrated region to be measured. The lube oil’s viscosity (in cSt) is the flow time (in second) multiplied by the apparatus constant.

## 3. Results and Discussion

All the samples preparation and test are conducted at Engine Tribology Laboratory, Department of Mechanical Engineering, University of Malaya. All the test results can be discussed as follow-

### 3.1 Coefficient of Friction (COF) Analysis

The coefficient of friction versus applied loads on four-ball testing is shown in Fig.2. The sample A is the reference lubricant as SAE40 grade. The sample B and sample C are the anti-wear additive added lubricants with sample A. The figure 2 shows how the different types of anti-wear additive affect on coefficient of friction. It is found that sample C increases COF from 0.08 to 0.24 for increasing loads from 50 kg to 90 kg.

However, the sample B shows lower COF than reference lubricant as lubricant A. It is clearly evident that the additive (0.5% Octylated/butylated diphenylamine based additive) in sample C has an adverse effect on COF with reference lubricant A. The lowest COF was found from sample B followed by sample A and sample C. The sample B consists of 0.5% Amine phosphate additive with sample A. Hence, Amine phosphate additive is effective in reducing friction and enabled to keep consistency throughout the load range.

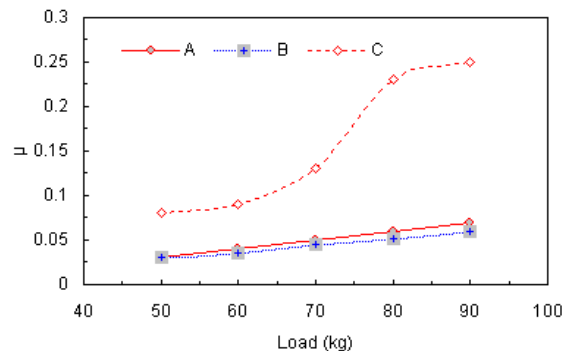


Fig.2. Coefficient of friction (μ) vs loads for sample A, B and C (Table 2).

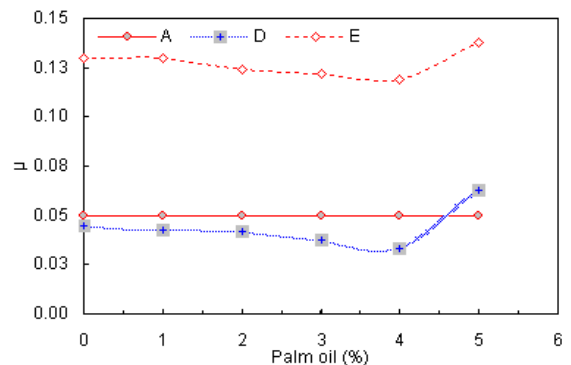


Fig. 3. Coefficient of friction (μ) vs percentage (%) of palm oil in samples D & E (Table 2) at constant 70 kg load.

Fig. 3 shows comparison of coefficient of friction (μ) for sample A, D and E at 70kg applied load. The medium load as 70 kg was chosen for comparison purposes. It can be stated that samples D and E are palm oil contaminated lubricant which are obtained from base lubricants B and C respectively (Table 2). In addition, sample A is always a reference lubricant as neither anti-wear additive nor palm oil have been added in it. The sample E which consists of octylated/butylated diphenylamine as anti-wear agent and palm oil shows adverse result. The friction coefficient for Sample E is found within 0.14 to 0.15 and sample A and D are found within 0.04 to 0.06

only. This indicates that, octylated/butylated diphenylamine is not a suitable anti-wear additive to reduce friction. Although its detailed chemical structure is unknown, changes in its physical properties such as viscosity can be observed [5]. Furthermore, the best performance is obtained when percentage combination of WVO is at maximum 4% of palm oil. However, above 4% of palm oil mixture drops friction coefficient.

### 3.2 Wear scar diameter (WSD) analysis

Fig. 4 shows WSD for samples A, B and C and Fig. 5 shows WSD for samples A, D and E. The sample A is the reference lubricant used in both the Fig.4 and Fig.5 for comparison purposes. The sample A did not contain either anti-wear additive or palm oil. Referring to Fig.4, it is found that sample C produces higher level WSD followed by sample A and sample B.

Sample B shows the best performance (a reduction of 20% of WSD as compared to sample A) which means that amine phosphate is effective in palm oil contaminated lubricant. It can be explained that the friction and wear resistance mechanism of anti-wear additive in palm oil contaminated lubricant causes from complex chemical transformation on the metal surface. The amine phosphate has the general structure represented (below) by: R = mostly aliphatic groups (2-ethylhexyl, hexyl and *n*-octyl); amines have *tert*-alkyl group with 10–24 carbon atoms [5].

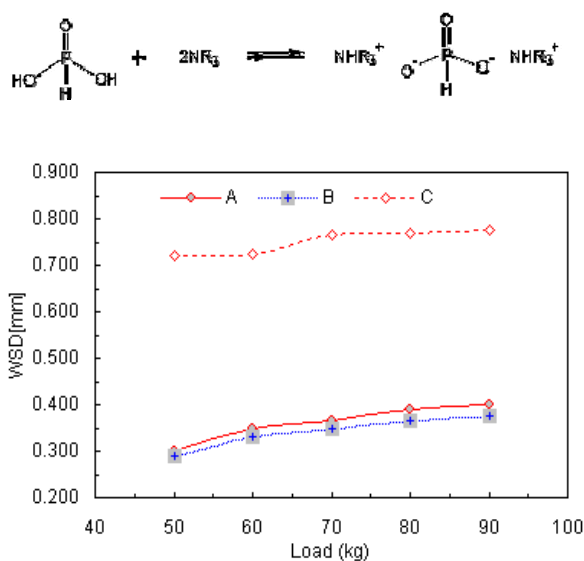


Fig.4. Wear scar diameter (WSD) vs loads for sample A, B and C (Table 2).

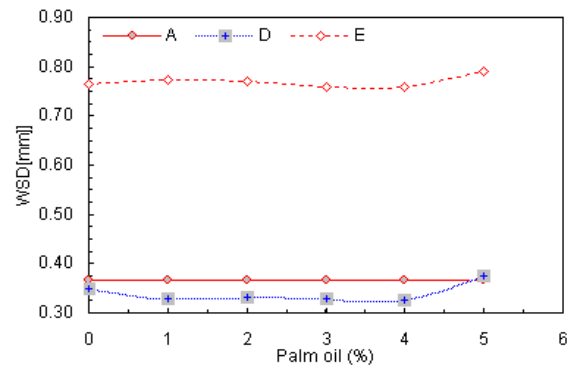


Fig.5. Wear scar diameter WSD) vs percentage (%) of palm oil in samples D & E (Table 2) at constant 70 kg load.

Fig.5 shows that sample D reduces WSD with maximum 4% palm oil contaminated lubricant with amine phosphate additive (from base lubricant sample B). However above 4% palm oil contaminated lubricant, the film thickness might be broken due to increasing palm oil percentage. The presence of up to 4% of palm oil makes the sample D more effective than other combination (as sample E). The breakdown of WVO (palm oil) molecule during tribo-chemical process results in the formation of fatty acids which can react with the phosphorus containing group from amine phosphate. These fatty phosphates function as effective friction modifiers and anti-wear agent in the presence of WVO. The long hydrocarbon chain of the fatty acid provide an excellent molecular barrier while the polar group coordinate with iron to form a protective film on the metal surface.

The sample C shows the WSD between 0.70 - 0.80 mm up to 4% palm oil combination which is 50% higher than sample B. This can be caused by the high friction in contact surfaces by using a composition containing octylated/butylated diphenylamine additive as anti-wear agent. It can be realized that the octylated/butylated diphenylamine additive works as anti-oxidant rather than anti-wear agent while added with palm oil contaminated lubricant. This additive and the palm oil neutralize each other at the high temperature that combinely adverse effect on the metal surface. Hence, surface wears increase. A similar phenomenon was found by Maleque et al.[6] and Adhvaryu et al [7].

### 3.3 Flash temperature parameter analysis

The maximum flash temperature parameter (FTP) can be defined as a number used to express critical temperature above which a lubricant film

thickness will be breakdown under given conditions. The value of FTP has been calculated using equation (2) which is obtained from four ball operating condition. From the equation it can be seen that FTP value depends on applied load and WSD.

According to Fig. 6 and Fig. 7, it can be said that amine phosphate based lubricants such as sample B (Fig.6) and sample D (Fig.7) show higher level of FTP number which means the lubricant stability of a particular condition. The sample C as well as sample E shows lower FTP value that causes breakdown of lubricant film thickness, hence WSD increases. However, above 4% palm oil contaminated lubricant, the FTP value drops as found in Fig.7.

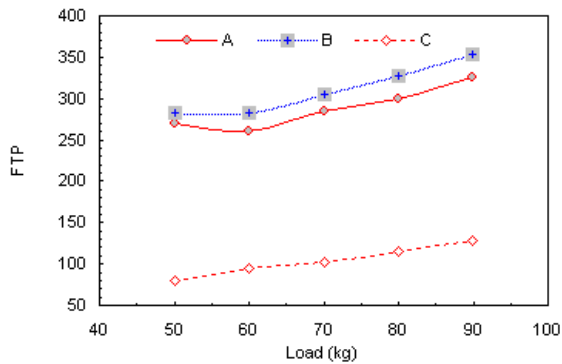


Fig.6. Flash temperature parameter (FTP) vs loads for sample A, B and C (Table 2)

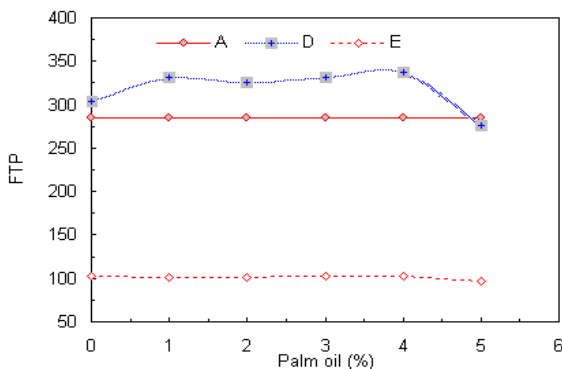


Fig. 7. Flash temperature parameter (FTP) vs. percentage (%) of palm oil in samples D & E (Table 2) at constant 70 kg load.

### 3.4 Total acid number (TAN) analysis

The total acid number (TAN) is a measure for the total amount of both weak and strong organic acids present in the lubricant and is expressed in mgKOH/g, i.e., the number of milligrams of potassium hydroxide required to neutralize one

gram of lubricating oil. The TAN test results are shown in Fig. 8 and Fig. 9.

According to Fig.7, the lowest Tan value is found from sample B (1.60 mgKOH/g) followed by sample A (1.70 mgKOH/g) and sample C (2.30 mgKOH/g). It can be found that sample E produces higher level of Tan followed by sample D and sample A. It is the evidence that the octylated/butylated diphenylamine additive is not suitable in both the normal lubricant (sample A) and palm oil contaminated lubricant (sample E). This is mainly due to the chemical properties of octylated/butylated diphenylamine additive that does not suit with sample A and sample E. In addition, the amine phosphate anti-wear additive shows higher Tan value (Fig. 9) as compared to normal lubricant (sample A) mainly due to the fatty acid and oxygen in palm oil. However, the Tan value can be increased due to several causes such as (i) effect of oxygen in palm oil, (ii) dropping the additives due to the effect of fatty acid in palm oil, and (iii) at higher temperature, the fatty acid molecules or other organic acids can be decomposed during operation.

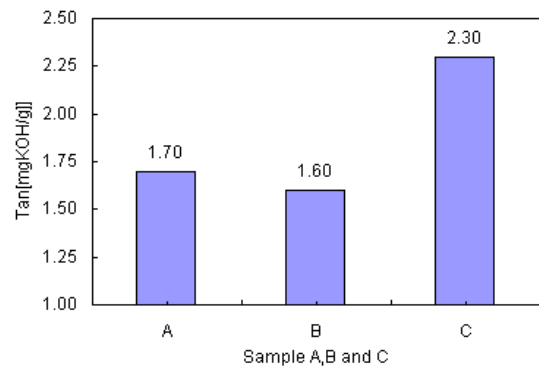


Fig.8. Total acid number (TAN) vs load for sample A, B and C (Table 2).

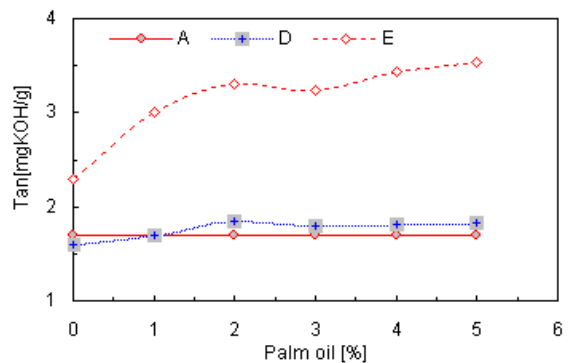
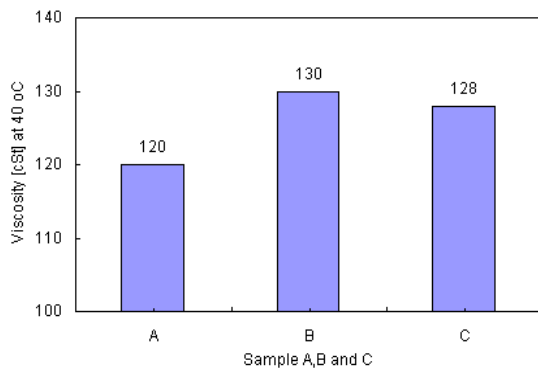


Fig.9. Total acid number (TAN) vs. percentage (%) of palm oil in samples D & E (Table 2) at constant 70 kg load.

### 3.5 Viscosity index (VI) analysis

Viscosity is the property used for identification of individual grades of lube oil and for monitoring the changes occurring in the lube oil while in service. Higher viscosity indicates that the lubricant is being deteriorated by either oxidation or contamination, while a decrease usually indicates dilution by lower viscosity oil or by fuel [6]. The Fig. 10 and Fig.11 show viscosity at 40 °C and Fig. 12 and Fig. 13 show viscosity at 100 °C. According to Fig.10 to Fig.13, it can be seen that amine phosphate increases viscosity (as sample B in Fig.10 and Fig.12). However, the same additive such as amine phosphate decreases viscosity with palm oil (Fig.11 and Fig.13) as



**Fig.10. Viscosity (at 40 °C) vs. loads for sample A, B and C (Table 2)**

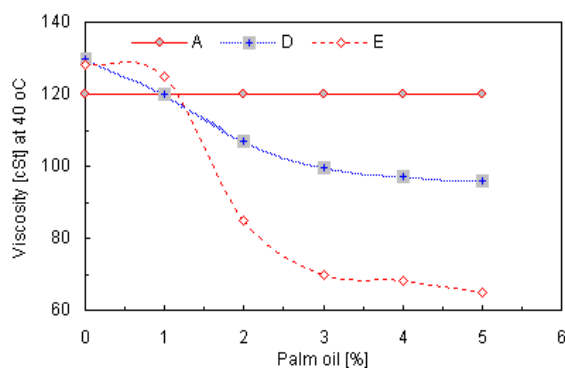


**Fig.11. Viscosity (at 40 °C) vs. percentage (%) of palm oil in samples D & E (Table 2) at constant 70 kg load.**

compared to original sample A, but this change is usually within the useful range in the both the temperature ranges such as at 40 °C and 100 °C.

The sample D shows increasing palm oil from 1% to 5% decreases viscosity from 120 cSt to 100 cSt which is good for machinery operations. Normally at 40 °C the lower limit of engine oil

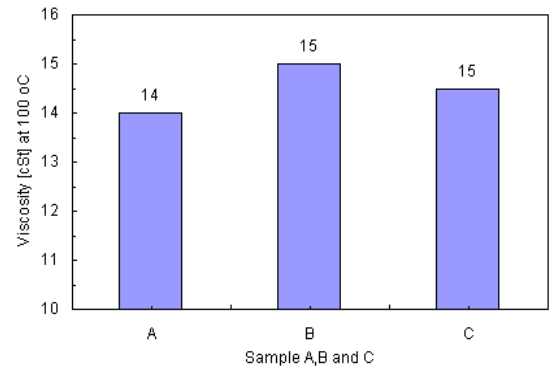


**Fig.12. Viscosity (at 100 °C) vs. loads for sample A, B and C (Table 2)**

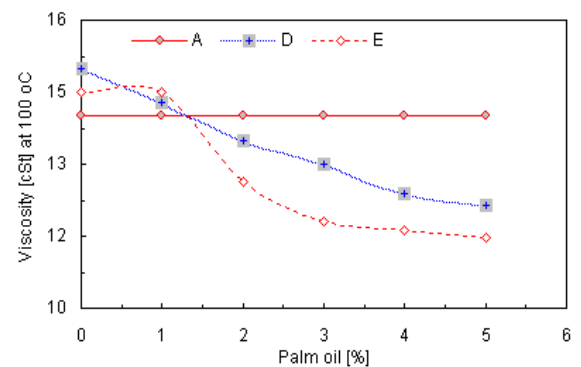


**Fig.13. Viscosity (at 100 °C) vs. percentage (%) of palm oil in samples D & E (Table 2) at constant 70 kg load**

should be 80 cSt and below this value indicates that the oil has decreased its quality. The applicable range of engine oil/lubricating oil at 40 °C and 100 °C are '80 cSt to 150 cSt' and '12 cSt to 20 cSt' respectively. However, the sample C as well as sample E shows the higher decreasing trend as compared to sample B and sample D. Hence, the sample C as well as E will increase components wear through degrading oil quality.

### 4. Conclusions

The following conclusions may be drawn from present study-

1. Amine phosphate as anti-wear additive shows better result with normal lubricant (SAE grade 40) such as reduces coefficient of friction (Fig.2), reduces WSD (Fig.4), increases FTP (Fig.6), reduces Tan value (Fig.8), and increases viscosity (Fig. 10 and Fig.12) as compared to octylated/butylated diphenylamine additive..
2. Combination of amine phosphate, normal lubricant and palm oil (upto 4%) show better

results such as reduces coefficient of friction (Fig.3), reduces WSD (Fig.5), increases FTP (Fig.7), reduces Tan value (Fig.8), and reduces viscosity to the better level (Fig. 11 and Fig.13) as compared to octylated/butylated diphenylamine additive.. Hence, it can be stated that waste palm oil can be used as lubricant substitute (maximum 4%) with normal lubricant and amine phosphate additive.

Remarks: Palm oil based lubricant still shows higher Tan value (Fig.9) which will be further investigated.

### Acknowledgment

The authors wish to thank Ministry of Science, Technology and Innovation of Malaysia for research grant and University of Malaya which made this study possible. The authors would like to thank Mr. Sulaiman bin Arifin (Lab Assistance) for technical help provided.

### References

- [1] Masjuki, H.H. and Maleque, M.A., Investigation of anti-wear characteristic of palm oil methyl ester using Four-Ball Tribometer Test, *Wear*, Pp. 179-186, 1997.
- [2] Zeman, A., Sprengel, A., Niedermeier, D. and Spath, M., Biodegradable Lubricants-Lubricants - Studies on Thermo-Oxidation of Metal - Working and Hydraulic Fluids by Differential Scanning Calorimetry (DSC), *Thermochemica Acta*, Vol. 268, Pp. 9-15, 1995.
- [3] [http://www.ducom.com/g\\_four.htm](http://www.ducom.com/g_four.htm) (12-24-2008).
- [4] IP-239 Standard. Extreme pressure properties: friction and wear test for lubrications, four-ball machine, 45<sup>th</sup> Annual Education Manual for analysis and testing, Vol. 1, Part 1, pp.239.116,1986.
- [5] Bowman, W.F. and Stachowiak, G.W., Determining the oxidation stability of lubricating oils using sealed capsule differential scanning calorimetry (SCDSC), *Tribology International*, Vol. 29;I, Pp. 21-34, 1996.
- [6] Maleque, M.A., Masjuki, H.H. and Haseeb, A.S.M.A, Effect of mechanical factors on tribological properties of palm oil methyl ester blended lubricant, *Wear*, Vol. 239;1, Pp. 117-125, 2000.
- [7] Adhvaryu, A., Erhan, S.Z. and Perez, J.M., Tribological Studies of Thermally and Chemically Modified Vegetable Oils for Use as Environmentally Friendly Lubricants, *Wear*, Vol. 257;3-4, Pp 359-367, 2004.

## TRENDS TO SUBSTITUTE DIESEL WITH TRIBOLOGICAL PROPERTIES ENHANCED BIODIESEL

M.I. Rafiqul , H. H. Masjuki, R. Saidur and M.H. Jayed

*Department of Mechanical Engineering, University of Malaya*

*50603 Kuala Lumpur, Malaysia*

*Email: rafiqum@yahoo.com*

### Abstract

*Biodiesel is the mixture of mono-alkyl ester of saturated and unsaturated long chain fatty acid produced from vegetable oil or animal fat or other sources of ordinary oil. It has been accepted as one of the best alternate fuel mainly for its environmental advantages. But the major problem is, it oxidizes rapidly which increases the engine tribology. It also corrodes the engine oil by polymerization due to the presence of oxygen and iodine in it. In this paper we have discussed about the researches that has been done to take bio diesel at such a level so that it can be a good alternate for conventional fuel like diesel, petrol, natural gas etc. For this purpose it has been found that in most cases various additives have been tried. But still the objective has not been fulfilled completely because of further research. The way to make biodiesel the most effective alternate for conventional fuel is the use of more promoted additives such as high temperature and pressure uphold anti oxidant and corrosion inhibitor additives. This paper discusses the properties of the biodiesel and effects of various additives on it and the effective way to improve the properties of biodiesel.*

**Keywords:** Tribology, Corrode, Polymerization, Promoted, Corrosion, Inhibitor

### 1. Introduction

The major energy demand is fulfilled from the conventional energy resources like coal, petroleum and natural gas (NG). Petroleum-based fuels are limited reserves concentrated in certain regions of the world. These sources are in the verge of getting extinct. The scarcity of known petroleum reserves will make renewable energy resources more attractive [1].

The world energy demand continues to increase. The most feasible way to meet this growing demand is by utilizing alternative fuels. One such fuel that exhibits great potential is bio-fuel, in particular, biodiesel [2]. Bio-fuels are generally considered as offering many priorities, including sustainability, reduction of greenhouse gas emissions, regional development, social structure and agriculture and security of supply [3]. In developed countries there is a growing

trend towards employing modern technologies and efficient bio-energy conversion using a range of bio-fuels, which are becoming cost-wise competitive with fossil fuels [4]. The scarcity of conventional fossil fuels, growing emissions of combustion generated pollutants and their increasing costs will make biomass sources more attractive [5].

On the other hand, biomass use, in which many people already have an interest, has the properties of being a biomass source and a carbon neutral source [6]. Experts suggest that current oil and gas reserves would suffice to last only a few more decades. To exceed the rising energy demand and reducing petroleum reserves, fuels such as biodiesel and bio ethanol are in the forefront of the alternative technologies. Accordingly, the viable alternative for compression-ignition engines (CIEs) is biodiesel.

It is well known that transport is almost totally dependent on fossil,

particularly, petroleum-based fuels such as gasoline, diesel fuel, liquefied petroleum gas (LPG) and NG. An alternative fuel to petro diesel must be technically feasible, economically competitive, environmentally acceptable and easily available. This current alternative diesel fuel can be termed as biodiesel. Biodiesel use may improve emissions levels of some pollutants and deteriorate other. However, for quantifying the effect of biodiesel it is important to take into account several other factors such as raw material, driving cycle, vehicle technology etc. Usage of biodiesel will allow a balance to be sought between agriculture, economic development and the environment [7].

Different studies have been carried out using different oils as raw material, different alcohols (methanol, ethanol, butanol) as well as different catalysts, homogeneous ones such as sodium hydroxide, potassium hydroxide, sulfuric acid and supercritical fluids, and heterogeneous ones such as lipases to make biodiesel as try for replacing ordinary diesel [8].

Diesel fuel can also be replaced by biodiesel made from vegetable oils. Biodiesel is now mainly being produced from palm, soybean and rapeseed oils. Soybean oil is of primary interest as biodiesel source in the United States, while many European countries are concerned with rapeseed oil, and countries with tropical climate prefer to utilize coconut oil or palm oil. However, any vegetable oil—corn, cottonseed, peanut, sunflower, safflower, coconut or palm—could be used to produce biodiesel [9]. Furthermore, other sources of biodiesel studied include animal fats and used or waste cooking oils. Researchers are also developing algae that produce oils, which can be converted to biodiesel [10].

Biodiesel is the pure, or 100%, biodiesel fuel. It is referred to as B100 or “neat” fuel. A biodiesel blend is pure biodiesel blended with petro diesel. Biodiesel blends are referred to as B<sub>xx</sub>. The xx indicates the amount of biodiesel blend (i.e., a B80 blend is 80% biodiesel and 20% petro diesel). In this paper, the performance of Biodiesel-diesel blend with property enhancing additives in various amount compare to pure diesel fuel without any additives has been discussed based on various studies that had been done previously. In these studies mostly

it has been seen that the performance of bio diesel-diesel blends with elevated additives have shown better results than ordinary diesel.

## 2. Worldwide Bio Diesel Scenarios

Renewable resources are more evenly distributed than fossil and nuclear resources, and energy flows from renewable resources are more than three orders of magnitude higher than current global energy use. Today's energy system is unsustainable because of equity issues as well as environmental, economic, and geopolitical concerns that have implications far into the future[1].

According to International Energy Agency (IEA), scenarios developed for the USA and the EU indicate that near-term targets of up to 6% displacement of petroleum fuels with bio diesel appear feasible using conventional bio diesel, given available cropland. A 5% displacement of gasoline in the EU requires about 5% of available cropland to produce ethanol based bio diesel while in the USA 8% is required. A 5% displacement of diesel requires 13% of USA cropland, 15% in the EU [11]

The EU have also adopted a proposal for a directive on the promotion of the use of bio-fuels with measures ensuring that bio-fuels account for at least 2% of the market for gasoline and diesel sold as transport fuel by the end of 2005, increasing in stages to a minimum of 5.75% by the end of 2010[2].

In some European countries, biodiesel oil is sold commercially. However, in other countries biodiesel is not available commercially, because of its higher cost than petroleum diesel. Biodiesel is primarily used mainly for practical purpose. As an example, some US demonstration programs are using biodiesel in more than 200 vehicles, including buses, trucks, construction/maintenance equipment, and motor boats, etc. In France, to investigate the effect of rape seed methyl ester on lubricating oil performance, there are 2000 vehicles including buses and trucks running on rape seed methyl ester. Some countries have started reservation of biodiesel for emergency uses or reduce dependency on imported fuels. In Asia, Malaysia is

producing palm oil diesel 3000 Mt/yr that is used in transit fleet, bus and cars [12].

Favorable fuels of the last category could be bio-fuels made from agricultural products, which not only may offer benefits in terms of exhaust emissions, but they will also reduce Europe's, and the world's in general, dependence on oil imports and help farmers [1]. Figure 1 shows the price comparison of different fuels.

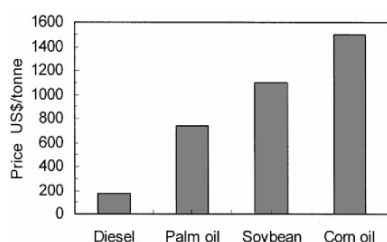


Fig. 1. Price comparison of different fuels

### 3. Oxidation of Bio Diesel

Oxidation of fatty compounds has been discussed extensively in the literature [13-16]. While the oxidation mechanism discussed in this literature is the widely accepted version, other researchers propose that species other than hydro peroxides, the species seen as being formed in the initial oxidation step, are active in auto oxidation [16].

Oxidation of fatty materials is promoted by factors such as elevated temperature, presence of light or extraneous materials such as metals or initiators. The nature of the radicals also influences the products observed and double bond geometry can also play a role. Antioxidants function by delaying oxidation but not preventing it.

The primary oxidation products of double bonds are allylic hydro peroxides. In these species, the original double bond(s) may have shifted or undergone cis / trans isomerization. Hydro-peroxides are unstable and easily form a variety of secondary oxidation products. Reactions of hydro peroxides include rearrangement to products of similar molecular weight, fission to give shorter-chain compounds (Aldehydes and Acids) and dimerization to give higher molecular weight materials.

The oxygen molecule,  $O_2$ , with which the olefinic fatty acid chains react, exists in two forms. Thus two oxidation mechanisms, auto-oxidation and photo-oxidation are possible. The common ground state of oxygen is the triplet

form  $^3O_2$ , which is a di-radical,  $\cdot O-O$ . The other oxygen form is the excited singlet form  $O_2$ , which is more reactive than the triplet form by 22.5 kcal / mol. The amounts and nature of the hydro peroxides formed by these two forms of oxygen vary.

Photo-oxidation is more rapid than auto-oxidation by several orders of magnitude. For oleate, photo-oxidation is about 30,000 times more rapid and for linoleate and linolenate this value is 1500 and 900 [14]. Literature values for relative auto-oxidation rates of oleate, linoleate and linolenate are 1, 27 and 77, respectively [14]. and 1, 41, and 98, respectively [13], with that of 20:4 being 195. The relative oxidation rate of triacylglycerols is lower, that of trilinolenin being 50. Thus the relative rates of photo-oxidation between oleate, linoleate, and linolenate are considerably smaller compared to auto oxidation.

The auto oxidation process usually exhibits an induction time during which the overall reaction is slow, followed by a more rapid stage. The purpose of antioxidants is to either prolong the onset of the initiation reaction or to enhance termination, reducing the length of propagation. However, the rates of oxidation in natural mixtures such as vegetable oils can differ from those in studies on pure compounds due to the presence of pro- and antioxidants.

The complex variety of secondary degradation products is reflective of the complicated decomposition process of hydro-peroxides. These secondary products can be categorized as monomeric (products with the same chain length as the original material but with different functional groups), oligomeric (products of higher molecular weight) and short chain. Various types of reactions can occur during the decomposition process including dehydration, cyclization, rearrangement, radical substitution, chain cleavage, dimerization, etc. In many cases, a combination of these reactions occurs to form the final "secondary" oxidation product.

The reactions occurring during the formation of secondary products are influenced by factors such as temperature and presence of light or air or extraneous materials, which also affect the initial oxidation step of hydro peroxide formation. The various secondary oxidation products are formed in different amounts and depend on the substrate (oleate, linoleate or linolenate). Monomeric secondary oxidation species that can arise include keto compounds, epoxy

compounds, di and tri hydroxy compounds, hydroperoxy epidioxides and dihydro peroxides. Oligomeric materials, usually obtained from linoleate or linolenate, include dimers linked via peroxy or ether groups as well as C–C linked dimers and dimers and oligomers containing conjugated diene-triene, dihydroperoxide or hydroperoxy epidioxide units. Volatiles formed include various shorter-chain saturated and unsaturated aldehydes as well as keto compounds and shorter-chain fatty acids. The location of the functional groups in the chain is mainly determined by the location of the original double bonds and thus the resulting hydroperoxides. More details are given in the literature [13–15].

### 3.1. Antioxidants

Several approaches exist to either prevent oxidation as far as possible or decelerate its rate. One is obviously to prevent contact of the fatty material with air. Another is to prevent contact with pro-oxidants or to avoid elevated temperatures or presence of light. These solutions are not always viable, so that antioxidants are of significant interest.

The use of antioxidants only delays the onset of oxidation, i.e., extends the so-called induction period until the antioxidant is exhausted and oxidation commences. Thus, fatty materials should not be exposed to oxidation-promoting factors as far as possible even when using antioxidants. Antioxidants used with biodiesel affect auto oxidation but not photo-oxidation. However, there is a mechanistic connection (radicals formed by photo-oxidation can be effective in auto oxidation) between photo- and auto oxidation. Photo-oxidation is affected by quenchers of singlet oxygen, such as  $\beta$ -carotene.

Antioxidants occur naturally, for example vitamin E (tocopherols and tocotrienols; four species of each,  $\alpha$ ,  $\beta$ ,  $\gamma$ ,  $\delta$ , exist), or are deliberately added synthetic materials such as butylated hydroxytoluene (BHT), butylated hydroxyanisole (BHA), tert-butylhydroquinone (TBHQ) or propyl gallate (PG). The level of natural antioxidants in vegetable oils is affected by the refining process. Recently reported pyrimidinols, which contain a strongly electron-donating dialkylamino group, are among the strongest synthetic antioxidants known, although pyridinols may be even more effective.

Antioxidants such as phenols and amines either have a hydrogen atom that can be “donated” to interrupt the chain reaction, whereby, for example, phenols become quinones, or they can react with a radical in an additive fashion.

Synthetic antioxidants, which are generally used at levels of 100–200 PPM, possess somewhat differing solubility and effectiveness. For example, propylgallate is probably the least soluble of the antioxidants mentioned. The effectiveness of an antioxidant can depend on a variety of factors, including the fatty acid profile of the oil or fat, the amount of naturally occurring antioxidants, and storage or other conditions. Systems with more than one antioxidant, resulting in primary and secondary antioxidants, are possible. Synergistic effects between antioxidants can influence their effectiveness.

## 4. Comparative Study of Engine Performance

An extended experimental study was conducted to evaluate and compare the use of various Diesel fuel supplements at blend ratios of 10/90 and 20/80, in a standard, fully instrumented, four stroke, direct injection (DI), Ricardo/Cussons ‘Hydra’ Diesel engine located at the authors’ laboratory. More specifically, a high variety of vegetable oils or bio-diesels of various origins are tested as supplements, i.e. cottonseed oil, soybean oil, sunflower oil and their corresponding methyl esters, as well as rapeseed oil methyl ester, palm oil methyl ester, corn oil and olive kernel oil. The series of tests are conducted using each of the above fuel blends, with the engine working at a speed of 2000 rpm and at a medium and high load. In each test, volumetric fuel consumption, exhaust smokiness and exhaust regulated gas emissions such as nitrogen oxides ( $\text{NO}_x$ ), carbon monoxide (CO) and total unburned hydrocarbons (HC) are measured. From the first measurement, specific fuel consumption and brake thermal efficiency are computed. The differences in the measured performance and exhaust emission parameters from the baseline operation of the engine, i.e. when working with neat Diesel fuel, are determined and compared. This comparison is extended between the use of the vegetable oil blends

and the bio-diesel blends. Theoretical aspects of Diesel engine combustion, combined with the widely differing physical and chemical properties of these Diesel fuel supplements against the normal Diesel fuel, are used to aid the correct interpretation of the observed engine behavior[1].

Fig. 2a and 2b shows, for the medium and the high load, respectively, the brake specific fuel consumption (b.s.f.c.) expressed in g/kWh (grams per kilowatt hour), for the neat Diesel fuel, the bio-diesel blends and the

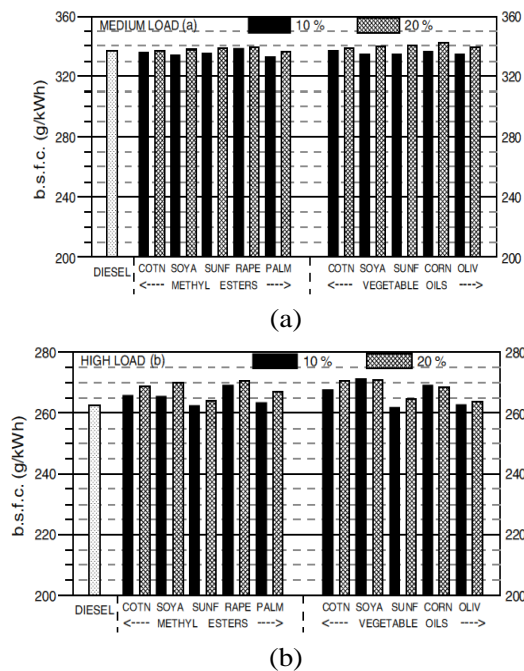


**Fig.2. a & b Brake specific fuel consumption (b.s.f.c.) for the neat Diesel fuel, the bio-diesel blends and the vegetable oil blends of various origins, for the medium load (a) and the high load (b).**

vegetable oil blends of various origins. The fuel blend mass flow rate is calculated from the respective measured volume flow rate value and the blend density, which is computed by considering the blending ratio and the densities of the fuels involved. Since the comparison is made at the same load (brake mean effective pressure) and speed, which is translated into the same engine power, then these values effectively are directly proportional to the fuel mass flow rate; it is to be noted, however, that the air mass flow rate remains constant under the same operating conditions[11].

It is observed that for the high load case (Fig. 2b), the brake specific fuel consumption

for all the bio-diesel blends of various origins is a little higher than that for the corresponding Diesel fuel case, with the increasing the percentage of the bio-diesel in the blend. This also holds true for all the vegetable oil blends of various origins. As discussed at the end of the previous subsection, this is the more likely behavior due to the lower calorific values of the bio-diesels or the vegetable oils compared to that of neat Diesel fuel. On the contrary, this picture changes a little as far as the medium load case is concerned (Fig. 2a), where one can observe, in a rather consistent way, a minimum of the specific fuel consumption at any 10% fuel blend with either the bio-diesel or the vegetable oil of any origin. A possible explanation of this, as discussed at the end of the previous subsection, is that the injection system acquires an optimum for this fuel blend ratio at the conditions corresponding to this medium load[1].

To study the comparative engine performance another computer-controlled dynamometer-engine test bed was used to measure engine brake power and SFC at half throttle condition with a speed range of 1000–4000 rpm. The emission test was done with a dynamometer fixed load of 50Nm and constant engine speed of 2250 rpm. A total of three fuels, such as 100% diesel fuel (B0); 20% palm diesel and 80% B0 (B20); and B20 with X% additive (B20X), were selected for this investigation. The B20X is the additive-added biodiesel, where X is the parentage (in this investigation X  $\frac{1}{4}$  1% of B20) of additive in B20 fuel. Anti-wear characteristics in terms of coefficient of friction, wear scar diameter (WSD) and flash temperature parameter (FTP) of fuel's contaminated lubricants were measured using a tribo meter test [11].

It was found that B20X fuel shows better overall performance such as improved brake power, reduced exhaust emissions and shows better lube oil quality as compared to other tested fuels. This is mainly due to the effect of fuel additive in the blended fuel of B20. The specific objective of this investigation is to develop the performance of B20 fuel by using an in-house-formulated fuel additive [17].

The results of brake power output from diesel engine for every test fuel are shown in Fig 3. It can be seen that fuel B20X

produces higher brake power over the entire speed range in comparison to other fuels. It is found that fuel B20X produces an average of 11.82kW brake power over the entire speed range followed by B20 (11.38kW) and B0 (11.50kW). It is calculated that fuel B20X produces 2.93% higher brake power than fuel B20, which is the effect of 1% additive in fuel B20. The maximum brake power obtained at 2500rpm is 12.28kW [17].

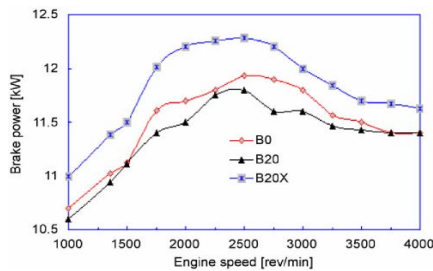


Fig. 3 Brake power output vs. engine speed.

From B20X fuel followed by 11.93kW (B0) and 11.8kW (B20). This can be attributed to the effect of fuel additive in B20 blend which influences the conversion of thermal energy to work or increases the fuel conversion efficiency by improving the fuel ignition and combustion quality (complete combustion)[4]

Fig. 4 shows specific fuel consumption (SFC) for B0, B20 and B20X fuels. It can be seen that the behavior of fuels B20 and B20X is similar to B0 fuel until the engine speed of 2250 rpm. After that, fuel consumption of B20 increases. Fuel B20X shows similar SFC as B0 fuel until the engine speed of 3500 rpm. It can be explained that 1% additive in fuel B20 produces fuel conversion similar to B0 fuel and up to 3500 rpm, and then produces higher fuel conversion as compared to B0 fuel at engine speed higher than 3500rpm. The lowest SFC is obtained from B20X fuel followed by B0 and B20 fuels. The average SFC values all over the speed range are 405, 426.69 and 505.38  $\text{g kW}^{-1} \text{h}^{-1}$  for B20X, B0 and B20 fuels, respectively[4].

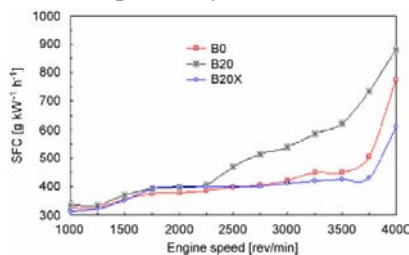


Fig. 4. Specific fuel consumption vs. engine speed

## 5. Tribology properties of Bio Diesel

Sliding contact between metallic components of any mechanical system is always accompanied by wear, which results in the generation of minute particles of metal. In diesel engines, the components that are normally subjected to the wear and tear process are piston, piston ring, cylinder liner, bearing, crankshaft, cam, tappet and valves. In a lubrication system, wear particles remain in suspension in the oil. By analyzing and examining the variations in the concentration of the metallic particle in the lubricant oil after certain running duration, sufficient information about wear rate, source of element and engine condition can be predicted. Wear metals debris such as Fe, Cu, Al and Pb reduced with increasing POD into blends. Additive compounds (like Zn, Ca) are used as detergents in typical commercial lube oil. These compounds provide an alkaline reserve to neutralize acidic by-products of combustion. Detergents react with oxidation products to reduce the formation of insoluble compounds and provide some measure of corrosion protection. Increase of palm diesel with addition of corrosion inhibitor increases the brake of a POD blends that. The reason of increasing brake power with increasing POD in blends is the effect influences conversion of heat energy to work or increases fuel conversion efficiency through the complete combustion. On an average, fuel B produced 10–15% higher brake power than OD. This is the effect of additive that enhances POD in producing higher power [17].

### 5.1. Wear & tear in engine components:

Fig. 5 shows the friction torque that is developed by various lubricants sample. It can be seen that the lowest level of friction torque was developed by B0X contaminated fuels. The maximum friction torque was produced by pure lubricant (B0) as 53.05 kg m. Low friction torque means good lubricity as well as lower coefficient of friction as is shown in Fig. 10. Hence, it can be said that antioxidant and anti-wear-based additive addition with B20 is effective as additive with lubricant [17].

Fig. 6 shows the variation of friction coefficient for all the fuel's contaminated lubricants. The lowest level of coefficient of

friction is obtained from B20X fuel's contaminated lubricants. The lower coefficient friction means developing low

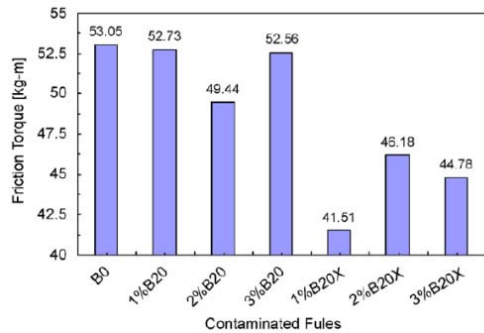


**Fig.5 Friction torque for various contaminated Fuel's lubricants at constant load of 50 Nm**

friction torque by lubricants within the frictional surfaces. The maximum coefficient of friction was produced by B0 and 3% B20 fuels' contaminated lubricants. The lowest coefficient of friction was achieved by 1% B20X contaminated lubricants as well as by 2% B20X and 3% B20X. Hence, it can be ensured that additive in B20 fuel is effective in reducing the coefficient of friction[4].

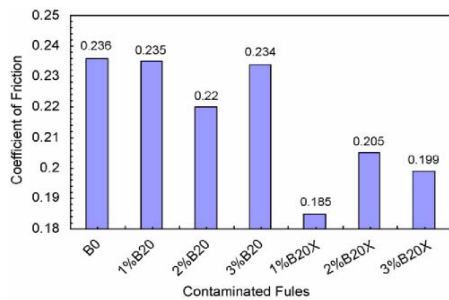


**Fig.6 Coefficient of friction for various contaminated fuel's lubricants at constant load of 50 Nm.**

Fig. 7 shows WSD diameter of used ball for all the lubricant samples with contaminated fuels. It is found that the lubricant sample B0 (Table 5) produces the highest WSD (3.7481 mm) as compared to other lubricant samples. All the B20 contaminated lubricants such as 1% B20, 2% B20 and 3% B20 produce WSD 3.5253, 3.452 and 3.5147mm, respectively.

The lowest WSD (3.419 1 mm) is obtained from 2% B20X, and it can be said that all the additive-based fuel's contaminated lubricants produce comparatively lower WSD than B20 as well as B0 fuel's contaminated lubricants, which is the effect of 1% additive in B20 [4].

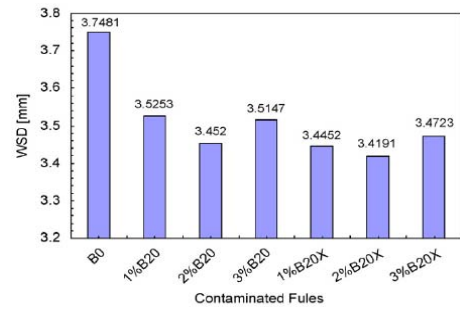


**Fig.7 Wear scar diameter (WSD) of the used ball with various contaminated fuels at constant load of 50 Nm**

## 6. Carbon Deposit in Automotive Components

Fig. 8.shows, for the medium and high load, respectively, the smoke (soot) density expressed in milligrams per cubic meter of exhaust gas for the neat Diesel fuel, the bio-diesel blends and the vegetable oil blends of various origins, with the organization of the bar diagram as referred to above. One can observe that the soot emitted by all the bio-diesel blends of various origins is significantly lower than that by the corresponding neat Diesel fuel case, with the reduction being higher the higher the percentage of the bio-diesel in the blend. This is attributed to the combustion being mixing controlled for these blends, as is also the case for the neat Diesel fuel, which is, however, now assisted by the presence of the fuel bound oxygen, even in locally rich zones. On the contrary, the soot emitted by all the vegetable oil blends of various origins is higher than that by the corresponding Diesel fuel case, with the increase being higher the higher the percentage of the vegetable oil in the blend. This is attributed to the combustion being rather evaporation controlled, so that the potential beneficial advantage of the fuel

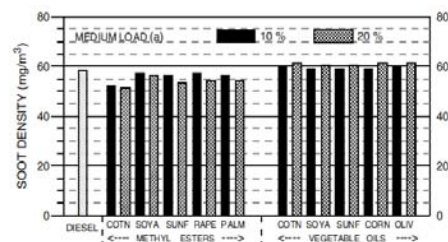


**Fig. 8.Emitted soot (Smoke) density for the neat Diesel fuel, the bio diesel and the vegetable oil blends of various origins, for the medium load and high load.**

bound oxygen comes into effect very late in the cycle and is, thus, of little help, with the hole situation aggravated further by the heavy fuel molecules[1].

Fig. 9a and 9b shows, for the medium and high load, respectively, the carbon monoxide (CO) exhaust emissions expressed in PPM (parts per million, by volume) for the neat Diesel fuel, the bio-diesel blends and the vegetable oil blends of various origins. One can observe that the CO emitted by all bio-diesel blends of various origins is lower than that by the corresponding neat Diesel fuel case, with the reduction being higher the higher the percentage of the bio-diesel in the blend. On the contrary, the CO emitted by all the vegetable oil blends of various origins is higher than that by the corresponding Diesel fuel case, with the increase being higher the higher the percentage of the vegetable oil in

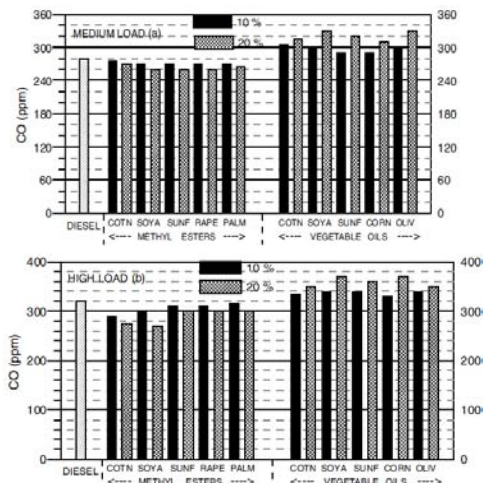


**Fig. 9a & b. Emitted carbon monoxide (CO) for the neat Diesel fuel, the bio-diesel blends and the vegetable Oil blends of various origins, for the medium load (a) and the high load (b).**

the blend. Conclusively, the emitted CO follows the same behavior as the emitted soot by the engine, a fact collectively attributed to the same physical and chemical mechanisms affecting almost in the same way, at least qualitatively, the net formation of these emissions. In any case, it should be reminded that the CO emitted levels in Diesel engines exhaust are small in absolute terms, so that they are of no real concern[1].

Fig. 10.a and 10b shows, for the medium and the high load, respectively, the total unburned hydrocarbons (HC) exhaust emissions expressed in PPM (parts per million, by volume) for the neat Diesel fuel,

the bio-diesel blends and the vegetable oil blends of various origins. One can observe for the blends of vegetable oils an increase of the emitted HC against the neat Diesel fuel case, as also reported in most cases. Concerning the blends of bio-diesels, a decrease of the emitted HC against the neat diesel fuel case is reported and an increase was reported when the injection timing was high. Actually, in the present study, where the injection timing is high, an increase is observed for the medium load case (see Fig. 10a). The situation is changed, however, a little for the high load case (Fig. 10b) where there is no definite trend (increasing or decreasing) with the bio-diesel blends of various origins[1].

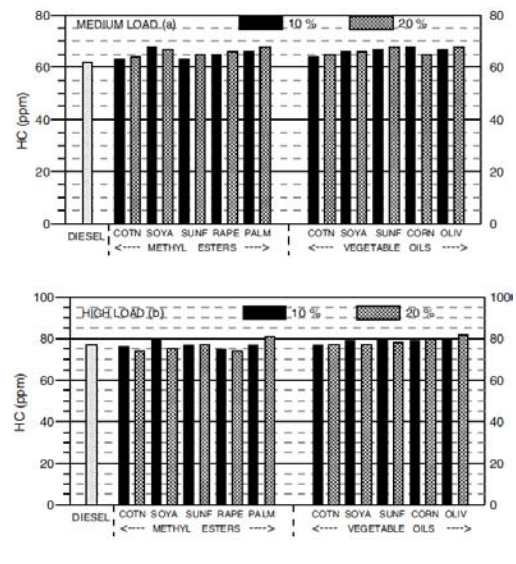


**Fig.10a and b. Emitted total unburned hydrocarbons (HC) for the neat Diesel fuel, the bio-diesel blends and the vegetable oil blends of various origins, for the medium load (a) and the high load (b)**

Carbon deposit is for CO formation and emission of unburned hydrocarbons. CO is formed during the combustion process with rich air-fuel mixtures regions and when there is insufficient oxygen to fully burn all the carbon in the fuel to CO<sub>2</sub>. However, a diesel engine normally uses more oxygen (excessive air) to burn fuel, which has little effect on CO emissions. Since the operating conditions are exclusively lean, the CO concentration value for all the fuels is less than 1% as shown in Fig. 11. It is found that among all the fuels, fuel B20X produces the lowest level of CO

emissions, which is 0.1%, followed by B20 (0.2%) and B0 (0.35%). It can be explained that 1% additive in biodiesel-blended fuel produces complete combustion as compared to B0 fuel [17].

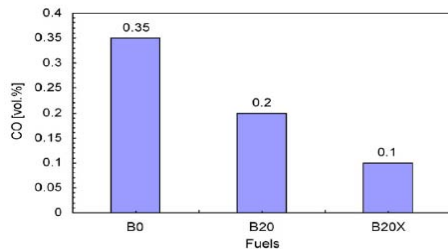


Fig.11. CO at constant load of 50 Nm and engine speed of 2250 rpm

Fig. 12 shows HC emissions for all the fuels. It is found that fuel B20X produces lowest HC emission (29 PPM) followed by B20 (34ppm) and B0 (41 PPM). The difference between B20 and B20X is 5 PPM, revealing that fuel B20X produces better combustion than B20 fuel.

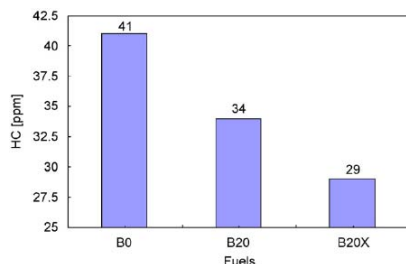


Fig.12. HC emission at constant load of 50 Nm and engine speed of 2250rpm

## 7. Polymerization and Corrosion in Engine oil

Fig. 13 shows Flash Temperature Parameter (FTP) for all the fuel's contaminated lubricants. From the figure, it can be seen that the maximum and minimum FTP were obtained from 2% B20X and B0 contaminated lubricants, respectively. The maximum FTP value means that good lubricating performance occurred, indicating less possibility of lubricant film breakdown. This phenomenon is also observed by other workers [11, 12]. This seems to indicate that additive in fuel is potential anti-wear additive for lubricating oil. From 1% to 3% of B20X contaminated lubricants show better FTP as compared to B20 and B0 contaminated lubricants [4].

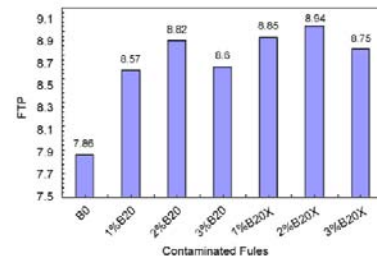


Fig.13. Flash temperature parameter (FTP) of used lubricants vs. contaminated fuels at constant load of 50 Nm.

## 8. Summary & Conclusion

The potential way of utilization of oil Biodiesel in various industrial, automobile and other sectors has been discussed. Various sources of vegetable oils can not only be used as source of edible oil but also can be enhanced into excellent renewable energy. Vegetable oils and animal fats all over the world are the most productive bio-diesel raw materials. Elevated with performance enhancement additives Biodiesel can solve the future power demand and can be the complete replacement of Diesel and other sources of energy. In present research the additives like antioxidants and anti polymerization and anti corrosion additives that are used cannot sustain high temperature and pressure. Their properties change. That's why these additives don't work properly. If we make more research and can use some high quality additives like high temperature and pressure resistance additives then bio diesel will be the best and one and only solution of future energy problem. Moreover, its waste streams can be used to produce vast amounts of bio-gas and other values added products. This facts proves that vegetable oils are the energy crops that yields the highest energy balance of all energy crops leaving all other competitors far behind. With this encouraging achievement, vegetable oil industries will circuitously intensify the economic and revenue growth of many countries. In near future bio-diesel made from vegetable oils and other byproducts could be one of the major contributors of renewable energy in the world at the same time.

## References:

- [1] Demirbas, A., 2006a. Global biofuel strategies. *Energy, Education, Science and Technology* 17, 27–63.

- [2] Fernando, S., Hall, C., Jha, S., 2006. NO<sub>x</sub> reduction from biodiesel fuels. *Energy Fuels* 20, 376–382.
- [3] Reijnders, L., 2006. Conditions for the sustainability of biomass based fuel use. *Energy Policy* 34, 863–876.
- [4] Puhan, S., Vedaraman, N., Rambrahman, B.V., Nagarajan, G., 2005. Mahua (*Madhuca indica*) seed oil: a source of renewable energy in India. *Journal of Scientific and Industrial Research* 64, 890-896.
- [5] Sensoz, S., Angin, D., Yorgun, S., 2000. Influence of particle size on the pyrolysis of rapeseed (*Brassica napus* L.): fuel properties of bio-oil. *Biomass and Bioenergy* 19, 271–279.
- [6] Dowaki, K., Ohta, T., Kasahara, Y., Kameyama, M., Sakawaki, K., Mori, S., 2007. An economic and energy analysis on bio-hydrogen fuel using a gasification process. *Renewable Energy* 32, 80–94.
- [7] Meher, L.C., Vidya Sagar, D., Naik, S.N., 2006. Technical aspects of biodiesel production by transesterification—a review. *Renewable and Sustainable Energy Reviews* 10, 248-268.
- [8] Marchetti, J.M., Miguel, V.U., Errazu, A.F., 2007. Possible methods for biodiesel production. *Renewable and Sustainable Energy Reviews* 11, 1300–1311
- [9] Demirbas, A., 2006b. Biodiesel production via non-catalytic SCF method and biodiesel fuel characteristics. *Energy Conversion and Management* 47, 2271-2282.
- [10] Nagel, N., Lemke, P., 1990. Production of methyl fuel from microalgae. *Applied Biochemistry Biotechnology* 24, 355–361.
- [11] Rakopoulos, C.D., Antonopoulos, K.A., Rakopoulos, D.C., Hountalas, D.T., Giakoumis, E.G., 2006. Comparative performance and emissions study of a direct injection Diesel engine using blends of Diesel fuel with vegetable oils or biodiesels of various origins. *Energy Conversion and Management* 47(18-19): p. 3272-3287.
- [12] John, M.H., 1988. Wear debris associated with engine operation. *Wear*; 90:29–36.
- [13] Frankel, E.N., 2005. *Lipid Oxidation, second edition*, The Oily Press, PJ Barnes & Associates, Bridgewater, England.
- [14] Gunstone, F.D., 2004. Oxidation through reaction with oxygen, in: *The Chemistry of Fats and Oils by Gunstone, F.D.*, Blackwell Publishing, CRC Press, Oxford, UK, pp 150–168.
- [15] Kenar, J.A., Knothe, G., Chemical properties of lipids, in: *The Lipid Handbook*, (in press).
- [16] Porter, N.A., Caldwell, S.E., Mills, K.A., 1995. Mechanisms of free radical oxidation of unsaturated lipids, *Lipids* 30, 277–290.
- [17] Kalam, M.A. and Masjuki, H.H., 2008. Testing palm biodiesel and NPAA additives to control NO<sub>x</sub> and CO while improving efficiency in diesel engines. *Biomass and Bioenergy*, 32(12), p. 1116-1122.

## EFFECT OF 12-HYDROXYSTEARIC ACID ON THE TRIBOLOGICAL PROPERTIES OF ENVIRONMENTAL FRIENDLY LUBRICANTS

M. Farooq<sup>1</sup>, A. Ramli<sup>2</sup>, M. Sudin<sup>3</sup>, M. Nawshad<sup>4</sup>

<sup>1,2,4</sup> Chemical Engineering Department, Universiti Teknologi PETRONAS, Bandar Seri Iskandar, 31750Tronoh, Perak, Malaysia

<sup>3</sup> Mechanical Engineering Department, Universiti Teknologi PETRONAS, Bandar Seri Iskandar, 31750Tronoh, Perak, Malaysia

Corresponding Author: [farooq\\_tribo@yahoo.com](mailto:farooq_tribo@yahoo.com)

### Abstract

*Vegetable oils are biodegradable, renewable, non-toxic and show excellent lubricating performance due to the presence of long chain fatty acids in their composition. Because of the worldwide interest in the environmental issues and harmful effects caused by mineral oil based lubricants, environmentalists and engineers have made attempts to explore the possibilities of using vegetable oils as environmentally friendly lubricants for wide range of applications. In this work the tribological properties of selected vegetable oils, namely castor oil and sesame oil in the presence of 12-hydroxystearic acid as anti-wear additive were investigated using four-ball tribometer. The viscosity, acid value, peroxide value and iodine value of these vegetable oils were determined experimentally. Results show that addition of 12-hydroxystearic acid to the selected vegetable oils especially castor oil considerably improved their anti-wear performance during the rubbing process. The improved anti-wear performance of the vegetable oils in the presence of additive may be attributed to the formation of protective layer as a result of tribochemical reaction on the metal surface.*

**Keywords:** vegetable oils, wear scar diameter, four-ball tribometer, 12-hydroxystearic acid,

### 1. Introduction

There has been an increasing demand for eco-friendly “green” lubricants and additives nowadays due to concerns about environmental issues and loss of mineral oil based lubricants to the environment. In many countries there have been quite a lot of developments on the environmentally acceptable lubricants. There are well defined guidelines and legislations for environmentally friendly lubricants. For example according to the Blue Angel Guideline of Germany the biodegradability of base stock must be 80% and additive non toxic. Similarly, Austrian water protection regulation requires the chain saw lubricants to be at least 90% biodegradable, possess low water solubility and contain no halogen or nitrile additives [1]. Mineral oil based lubricants contain many kinds of additives such as antioxidant agent, antiwear agents, detergents, dispersants, anti-forms, extreme pressure agents, friction modifiers, and

viscosity improvers. Some of these additives are toxic and harmful to the environment [2,3]. Due to the environmental pollution and problems various government and non government organizations strongly recommend to replace mineral oil based lubricants by environmentally friendly lubricants as soon as possible. Environmentally friendly lubricants are readily biodegradable nontoxic and have a minimum impact on the environment. Biodegradable lubricants are suitable for various kinds of applications such as outboard, two cycle engine oils, chain saw oils, wire rope lubricants, hydraulic oils for forest and agricultural equipment, etc. [4]. Vegetable oils, due to their high biodegradability, low toxicity, excellent lubricity and renewability are attractive and promising candidates to replace mineral oil based lubricants. They also acquire most of the properties required for lubricants such as high viscosity index, low volatility, and are also good

solvents for fluid additives [5].

Vegetable oils contain long fatty acid chains in their compositions. The long chain fatty acids and presence of polar groups in the vegetable oil structures make them amphiphilic in nature and therefore allow them to be used as base stock for lubricants [6]. They have better anti-corrosion properties because of their better affinity to metal surfaces. The triacylglycerol molecules orient themselves in such a way that the polar end is directed towards the metal surface making a close packed monomolecular or multimolecular layer on the surface and thus inhibited metal-to-metal contact reducing corrosion during the sliding [7,8].

In summary, vegetable oils displays many desirable characteristics that give them edge over petroleum based lubricating oils and make them attractive as base oil for lubricants for a wide range of applications. The tribological properties of vegetable oils can further be enhanced by using suitable additives.

In this paper we are going to evaluate the tribological properties of vegetable oil [castor oil] in the presence of 12-hydroxystearic acid as anti-wear additive using four-ball machine.

## 2. Experimental Methods and Materials

### 2.1. Base stock and chemicals

Vegetable oils [castor oil and sesame oil] were purchased from the local market and were used without any further treatment as base stock. All the chemicals used in the experiments were of Merck A.R. grade.

### 2.2. Viscosity measurement

Viscosity of the selected vegetable oils [castor oil, sesame oil] was measured using viscometer having viscometer constant of 0.091cSt/sec at 30°C temperature.

### 2.3. Acid value measurement

Acid value of the selected vegetable oils [castor oil, sesame oil] was determined by using the American Oil Chemist Society (AOCS) standard method (Ca 5a-40) [9]. According to this method about 2g of the given oil sample was mixed with 25cm<sup>3</sup> ethanol followed by two drops of phenolphthalein indicator in a titration flask and then titrated against 0.01N aqueous solution of potassium hydroxide [KOH] until

pinkish colour appeared. Then from the titration data acid value was calculated.

### 2.4. Iodine value measurement

Iodine value of the given vegetable oil samples [castor oil, sesame oil] was determined by AOCS standard method (Cd 1-25) [10]. According to this method oil solution was made by dissolving 20g of the given oil sample in one dm<sup>3</sup> of chloroform. About 10cm<sup>3</sup> of this solution was taken and mixed thoroughly with about 25cm<sup>3</sup> of iodine monochloride solution [0.2M iodine monochloride solution in acetic acid] in a 250cm<sup>3</sup> titration flask and was kept stoppered in dark for one hour with gentle stirring. After one hour 10cm<sup>3</sup> of 2.5M potassium iodide [KI] aqueous solution was added to this reaction mixture followed by 50cm<sup>3</sup> of distilled water and titrated against 0.1M sodium thiosulfate Na<sub>2</sub>S<sub>2</sub>O<sub>3</sub>.H<sub>2</sub>O aqueous solution till light brown colour was appeared. To this reaction mixture a few drops of starch as indicator were added and again titrated against 0.1M sodium thiosulfate Na<sub>2</sub>S<sub>2</sub>O<sub>3</sub>.H<sub>2</sub>O aqueous solution until the bluish colour was disappeared. Similar experiment was run without containing oil sample under the same experimental conditions. From the titration data iodine value was calculated.

### 2.4 Peroxide value measurement

Peroxide value was also determined by AOCS standard method (Cd 8b-90) [11] for the given vegetable oil samples. About 2.5g of the selected vegetable oil sample was mixed with 20cm<sup>3</sup> of acetic acid and chloroform solution [3:2] followed by addition of 1cm<sup>3</sup> standard aqueous solution of potassium iodide [KI] and 35cm<sup>3</sup> distilled water with constant stirring. Few drops of starch indicator were added to this reaction mixture and then titrated against 0.01N standard aqueous solution of Na<sub>2</sub>S<sub>2</sub>O<sub>3</sub>.5H<sub>2</sub>O until the yellow color was disappeared. Similar experiment was also performed under the same conditions without the oil sample. The peroxide value was calculated from the titration data.

### 2.5 Measurement of wear

Four-ball machine [ASTM, D2266] was used to evaluate the anti-wear properties of the selected vegetable oils [castor oil, sesame oil] under applied load of 63.74N. Anti-wear performance of the given oil sample can be estimated from the size of wear scar diameter obtained from the

lower three stationary balls of the tribometer during the experiment. The steel balls and appropriate parts of the four-ball machine were washed properly with toluene before starting each experiment and were dried in the oven at about 50°C. These washed balls were then fitted in the four-ball machine where the top ball held in a special chuck at the lower end of the vertical spindle of a electric motor moving with constant speed, is rotating in the cavity of three identical balls in contact and clamped in a steel cup, containing the test fluid.. The four ball machine was then run for specific time duration under desired load and temperature. After completion of experiment, these balls from the four-ball tribometer were collected and washed in an ultrasonic bath for about two minutes and dried. The wear scar diameter on each of the three lower balls was measured with optical microscope and recorded in millimeter.

### 3. Results and Discussions

The results of the tribological evaluation of the selected vegetable oils based lubricants are discussed in the following section.

#### 3.1 Additive free oil sample

The anti-wear performance of the selected vegetable oils was assessed by measuring the wear scar diameter on the three lower stationary balls of the four-ball tribometer as shown in the Fig 2. The figure shows that castor oil has good anti-wear performance as compared to sesame oil. Vegetable oils are generally triglycerides of fatty acids which make them desirable fluids for lubrication. Castor oil is roughly 87% triglyceride of ricinoleic acid  $[\text{CH}_3(\text{CH}_2)_5\text{CH}(\text{OH})\text{CH}_2\text{CH}=\text{CH}(\text{CH}_2)_7\text{COO}]_3(\text{OC})_3\text{H}_5$  ] which is unique because there is a double bond at the C<sub>9</sub> and hydroxyl group at the C<sub>11</sub> as shown in Fig 1. It is the hydroxyl group of the ricinoleic acid which makes castor oil highly polar fluid and is used as base fluid for many applications like lubrication. Due to high polarity castor oil shows greater affinity to adsorb on the metal surface to form a thick protective film reducing both wear and friction as compared with sesame oil where the fatty acids do not have hydroxyl groups in their structure.

Moreover, it is well known that oil with high acid value, low iodine value, high viscosity and high peroxide value show good anti-wear

properties. Castor oil under investigation meets all these requirements showing better performance as compared with other vegetable oils.

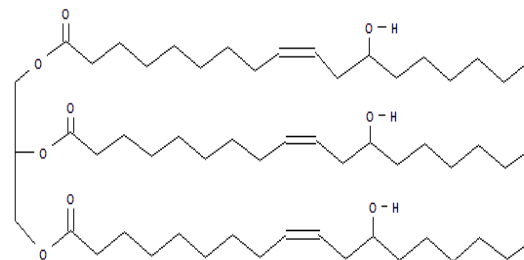


Fig.1. Structure of the major component (90%) of castor oil

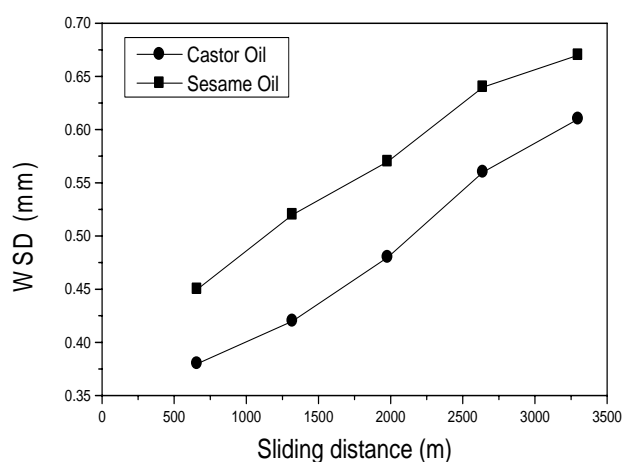


Fig.2. Variation of WSD of the selected vegetable oils as a function of sliding distance

Table 1 some important parameters of the tested vegetable oils

No	Castor Oil	Sesame Oil
Viscosity/cSt sec <sup>-1</sup>	60	43.35
Acid Value/mg KOH g <sup>-1</sup>	1.12	1.03
Iodine Value	87	112
Peroxide value/meq kg <sup>-1</sup>	7.2	6

#### 3.2 Effect of additive on anti-wear properties of oil sample

12-hydroxystearic acid was used as anti-wear additive for the given vegetable oils [castor oil, sesame oil] and then the tribological properties were assessed by four-ball tribometer under specific experimental conditions as shown in the Fig 3. It is clear from the figure that 12-hydroxystearic acid improved the anti-wear performance of the selected vegetable oils to considerable amount. Moreover, castor oil blended with 12-hydroxystearic acid showed excellent anti-wear performance as compared

with the sesame oil and additive free castor oil. 12-hydroxycarboxylic acid contains carboxyl group as well as hydroxyl group in its molecule. Due to the presence of these functional groups, 12-hydroxystearic acid possesses high polarity showing greater adsorption affinity for the steel surfaces. It has been found that with hydroxycarboxylic acids chemically polymerized molecules are produced on the steel surface which play an important role in friction and wear reduction on the metal surface during sliding [12]. Moreover, in the case of 12-hydroxystearic acid carboxyl and hydroxyl groups are apart from each other in the molecule which resulted in greater affinity to adsorb on the metal surface at both the functional groups producing a thick layer as a result of tribochemical reaction on the metal surfaces.

12-hydroxystearic acid showed excellent performance in castor oil as compared to the sesame oil under similar experimental conditions. This may be attributed to the chemical composition of the castor oil which is different from the other vegetable oils. Castor oil is a triglyceride in which approximately ninety percent of fatty acid chains are ricinoleic acids. Oleic and linoleic acids are other significant components. Ricinoleic acid contains hydroxyl functional group in its molecule. This functional group causes ricinoleic acid (and castor oil) to be unusually polar. This polar mass of the castor oil provide good competition ground for the 12-hydroxystearic acid and therefore shows greater affinity to adsorb at both the functional groups producing a thick and strong protective film on the surface as compared to the sesame oil.

Furthermore, the chain length of additive molecules also plays an important role in the anti-wear performance of various kinds of lubricants. Hydroxycarboxylic acids have a long

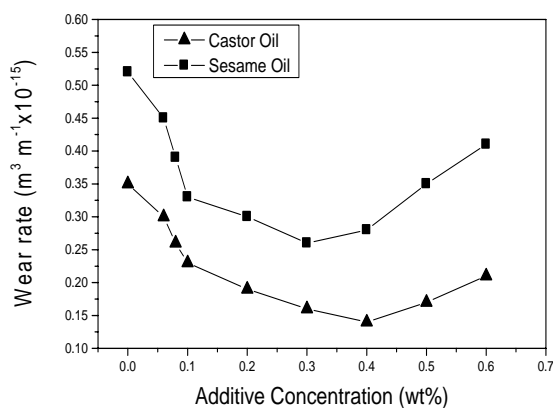


Fig.3. Variation of WSD of selected vegetable oils as a function of additive concentration

straight alkyl chain and therefore show excellent anti-wear characteristics. It is supposed that these acid molecules align themselves as a straight chain resulting in a close packing on the surface, providing a strong and thick protective layer on the metal surface as compared with short chain fatty acids [13, 14].

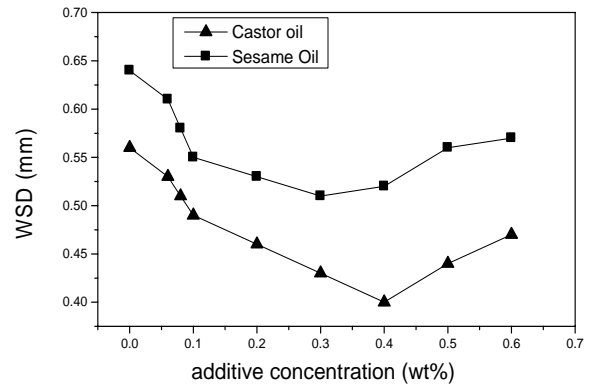


Fig.4. Variation of wear rate as a function of additive concentration

Fig 4 shows the variation of wear rate with respect to additive concentration. It is clear from the figure that 12-hydroxystearic acid causes decrease in the wear rate. However, in the case of castor oil minimum wear rate was observed at 0.4wt% whereas for the sesame oil decrease in the wear rate was observed in the range of 0.2 to 0.4wt% under the same conditions.

#### 4. Conclusions

Castor oil showed good lubricating properties as compared with the sesame oil under similar experimental conditions. Addition of 12-hydroxystearic acid improved the anti-wear performance of castor oil as compared with the sesame oil and additive free castor oil. The excellent performance of the 12-hydroxystearic acid in the castor oil might be attributed to the formation of protective layer on the steel surface consisting of polymers produced by the tribochemically generated intermolecular esterification of 12-hydroxystearic acid on the metal surface.

#### References

- [1]. X. Zeng, H. Wu, H. Yi, T. Ren, Tribological behavior of three novel triazine derivatives in rapeseed oil, *Wear.*, 262; 5-6, 718-726, 2007
- [2]. B.K. Sharma, A. Adhvaryu, S.Z. Erhan,

- Friction and wear behavior of thioether hydroxy vegetable oil, *Tribology International*, 42, 353-358,2009
- [3]. A. Suzuki, R. Ulfiati, M. Masuko, Evaluation of antioxidants in the rapeseed oils for railway application, *Tribology International*, Article in press (www.elsevier.com/locate/tribont)
- [4]. W.J. Bartz, lubricants and the environment, *Tribology International*, 31; 1-3, 35-47, 2007
- [5]. P.S. Lathi, B. Mattiasson, Green approach for the preparation of biodegradable lubricant base stock from epoxidized vegetable oil, *Applied Catalysis B: Environmental*, 69; 3-4, 207-212, 2007
- [6]. A. Adhvayu, S.Z. Erhan, J.M. Perez, Tribological studies of thermally and chemically modified vegetable oils for use as environmentally friendly lubricants, *Wear*, 257; 3-4, 359-367, 2004
- [7]. B.K. Sharma, A. Adhvaryu, S.Z. Erhan, Friction and wear behavior of thioether hydroxy vegetable oil, *Tribology International*, 42, 353-358,2009
- [8]. A. Kleinova, P. Fodran, L. Brncalova, J. Cvengros, Substituted esters of stearic acid as potential lubricants, *Biomass and Bioenergy*, 32, 366-371, 2008
- [9]. AOCS Official Method Ca 5a-40, "Free Fatty Acids," Official Methods and Recommendation Practice of the American Oil Chemists' Society (AOCS), Champaign, Illinois, 1997
- [10]. AOCS Official Method Cd 1-25, "Iodine Value," Official Methods and Recommendation Practice of the American Oil Chemists' Society (AOCS), Champaign, Illinois, 1997
- [11]. AOCS Official Method Cd 8b-40, "Peroxide Value," Official Methods and Recommendation Practice of the American Oil Chemists' Society (AOCS), Champaign, Illinois, 1997
- [12]. M. Masuko, T. Ohmori, H. Okabe, Anti-wear properties of hydroxycarboxylic acids with straight alkyl chains, *Tribology International*, 21; 4, 199-203, 1988
- [13]. S. Jahanmir, Chain length effects in boundary lubrication, *Wear*, 102; 4, 331-349, 1985
- [14]. F.P. Bowden, J.N. Gregory, D. Tabor, Lubrication of metal surfaces by fatty acids, *Nature*, 156; 97-101, 1945
- [15]. R.P.S. Bhisht, G.A. Sivasankaran, V.K. Bhatia, additive properties of jojoba oil for lubricating oil formulations, *Wear*, 161,193-197, 1993.

## ADHESION AND WEAR BEHAVIOR OF NANOSTRUCTURED TITANIUM OXIDE THIN FILMS

M.M. Hasan<sup>1\*</sup>, A.S.M.A. Haseeb<sup>1</sup>, R. Saidur<sup>1</sup>, H.H. Masjuki<sup>1</sup>, M. Hamdi<sup>2</sup>

<sup>1</sup>Department of Mechanical Engineering, Faculty of Engineering,  
University of Malaya, 50603 Kuala Lumpur, Malaysia

<sup>2</sup>Department of Engineering Design and Manufacture, Faculty of Engineering,  
University of Malaya, 50603 Kuala Lumpur, Malaysia

\*Corresponding Author: Email:[mmhasan92@yahoo.com](mailto:mmhasan92@yahoo.com); Tel/Fax: +60379674448

### Abstract

*This study aims to investigate structural, mechanical and tribological properties of titanium oxide films deposited on glass substrates by radio frequency (RF) magnetron sputtering. All the as-grown titania films possess the anatase structure having a grain size of about 44 nm irrespective of the variation of substrate temperatures. AFM images show a nodular morphology with an increase of surface roughness. From micro-scratch tests, the optical micrographs of the scratch tracks show that the complete delamination of TiO<sub>2</sub> films deposited at higher temperatures appear at a higher value of adhesion critical loads. The highest adhesion critical load between titanium oxide films and glass was found to be 2.24 N for the film prepared at 300 °C. It represents an enhanced adhesion strength for films deposited at higher temperatures. Scratch hardness was also found to increase from 5.5 to 8.4 GPa with increasing substrate temperature. From micro-wear test, it is found that the wear resistance of TiO<sub>2</sub> films deposited at higher substrate temperatures exhibits higher wear resistance.*

**Keywords:** Structural properties, Adhesion strength, Scratch hardness, Tribological properties

### 1. Introduction

TiO<sub>2</sub> is one of the most widely studied ceramic materials used as films. These films are frequently employed for many optical devices in optics industry [1], dye-sensitized solar cells [2], heat mirrors [3] and environmental applications [4] for their remarkable optical, photocatalytic and hydrophilic properties. TiO<sub>2</sub> films also possess noble antibacterial, disinfection, antifogging and self-cleaning properties [5]. Now-a-days, TiO<sub>2</sub> films have a wide range of applications on glass substrates such as heat mirror films on building and automotive glasses, self-cleaning glass, air cleaning lamp, wiperless windshield etc. For these applications, thin TiO<sub>2</sub> films with nanometer thickness are mostly employed. As they are exposed to adverse environments, scratch and wear resistance play a significant role for their mechanical stability and durability. A variety of conventional deposition methods have been used to prepare TiO<sub>2</sub> films, such as electron-beam evaporation [6], ion-beam assisted deposition [7], DC or RF magnetron

sputtering [2, 3], sol-gel methods [8], chemical vapor deposition [5] and plasma enhanced chemical vapor deposition [9] etc.

Sputter deposition technique is popular to produce adherent and uniform film over wide areas with better stoichiometric control. A number of studies on the deposition of TiO<sub>2</sub> films by sputtering appear in the literature recently [2, 3, 10-12]. Most of the studies investigated structural, morphological and optical properties of TiO<sub>2</sub> films. Few reports are available in the literature on the adhesion properties, wear and scratch resistance of TiO<sub>2</sub> films [13-18]. These studies attempted to evaluate adhesion strength and/ or wear resistance of TiO<sub>2</sub> films deposited mostly on metal substrates prepared by a variety of deposition techniques other than magnetron sputtering. Few reports are found to study tribological behavior of TiO<sub>2</sub> films deposited on metallic substrates using ball-on-plate or pin-on-disk tests [13-15]. These studies evaluated mechanical or/and tribological properties for titania films with micron-scale film thicknesses

using micro and macro-scale measurements. However, majority of the transparent functional titanium oxide films on glass substrate have thickness in the nanometer range. Evaluation of mechanical properties of such films requires measurement technique with control capability at the nanometer level. Investigations dealing with the mechanical properties of titanium oxide at the nanometer level are scarce in the literature. Kuo et al. [18] reported adhesion strength of TiO<sub>2</sub> films with a nano-scale thickness of 240 nm deposited on silicon substrates using RF magnetron sputtering. In that work, a conventional scratch testing machine with an indenter tip radius of 200 μm was employed to evaluate adhesion critical load of nano-scale films.

Hence, in order to predict the durability of nanometric titanium oxide films on glass substrate and a coating/substrate system of great practical interest, it is important to have adequate data on their mechanical properties. In the present work, nano-TiO<sub>2</sub> thin films have been deposited on glass substrates by RF reactive magnetron sputtering at a constant sputtering pressure of 3 Pa. The main objective of this study is to evaluate mechanical properties such as scratch adhesion and wear resistance for TiO<sub>2</sub> thin films deposited on glass substrates by NanoTest platform having a depth and load resolution better than 0.2 nm and 1 mN, respectively. The effects of substrate temperatures on the mechanical properties have also been evaluated.

## 2. Experimental Details

Anatase TiO<sub>2</sub> films were prepared on microscope glass slides as substrates by radio-frequency (RF) reactive magnetron sputtering of Ti target of 4 N purity. First the target was pre-sputtered in an argon atmosphere in order to remove the oxide layer. Sputter deposition was performed in a mixture of 46 sccm of Ar (99.999%) and 10 sccm of O<sub>2</sub> (99.999%) atmosphere supplied as working and reactive gases, respectively, through an independent mass-flow controller. The sputtering chamber was evacuated down to  $5 \times 10^{-4}$  Pa by the turbo-molecular pump and the working pressure was kept at about 3 Pa. During deposition, the RF power was maintained at 250 W and the substrates were kept at room temperature, 200 and 300 °C respectively. Prior to deposition, the glass substrates were sequentially cleaned in an

ultrasonic bath with acetone and ethanol. Finally, they were rinsed with distilled water and dried.

The crystalline quality of the TiO<sub>2</sub> films were investigated by X-ray diffraction (XRD) measurements (Model-D 5000, Siemens) in  $\theta$ -2 $\theta$  geometry using Cu K<sub>α</sub> radiations ( $\lambda=0.15406$  nm). The grain size of the films was calculated by using the Scherrer equation:

$$d = \frac{0.89\lambda}{B \cos \theta} \quad (1)$$

where  $d$  is the grain size,  $\lambda$  the wavelength of X-ray,  $B$  the full-width at half-maximum of diffraction peak (FWHM), and  $\theta$  is the diffraction angle. The thickness of the as-deposited film on unheated substrate was measured by a field emission scanning electron microscope (FESEM). For surface morphology, atomic force microscope (AFM) images were recorded using Nanoscope IIIa scanning probe in a tapping mode.

The NanoTest platform by Micro Materials Ltd., UK, was used for the micro-scratch and wear testing. The system has a depth and load resolution better than 0.2 nm and 1 mN, respectively. A 25 μm radius spherical diamond indenter probe (Rockwell sharp diamond) was used for the tests. The micro-scratch test was performed with a constant indenter velocity of 5 μm s<sup>-1</sup>. An initial load of 2 mN was applied during the first 100 μm of the scratch, and the load was then increased to 2500 mN over a distance of 1900 μm at a fixed rate of 7 mNs<sup>-1</sup>. Optical micrographs for the scratch tracks were captured by an optical microscope OLYMPUS BX61, Japan. The scratch hardness, which is a measure of the resistance of the material to normal penetration, is defined as [19]:

$$SH = \frac{8.N}{\pi.d^2} \quad (2)$$

where SH is the scratch hardness, N is the applied normal force and  $d$  is the corresponding scratch width. In this investigation, scratch hardness of the studied films is measured at three positions on the scratch tracks before the coating failure and the average value was taken into consideration.

The procedure for wear tests involved a set of five topography scan and four wear scan at a constant velocity of 1 μm s<sup>-1</sup> along the same surface on the films unidirectionally. In each

topography scan including the first scan, the indenter moves at a constant load of 2mN. In each wear scan, an initial load of 2 mN was applied during the first 200  $\mu\text{m}$ , and then a constant load of 500 mN was abruptly applied for the further scan of 800  $\mu\text{m}$ . Each wear scan is followed by a topography scan.

### 3. Results and Discussion

In our previous work, the thicknesses measured by optical spectrophotometry for the as-deposited films at room temperature, 200 and 300  $^{\circ}\text{C}$  were found to be 315, 335 and 345 nm respectively [20]. A cross-sectional image of the as-deposited  $\text{TiO}_2$  films on unheated substrate is shown in Fig. 1. It is found that the thickness of the film is approximately 330 nm which is in

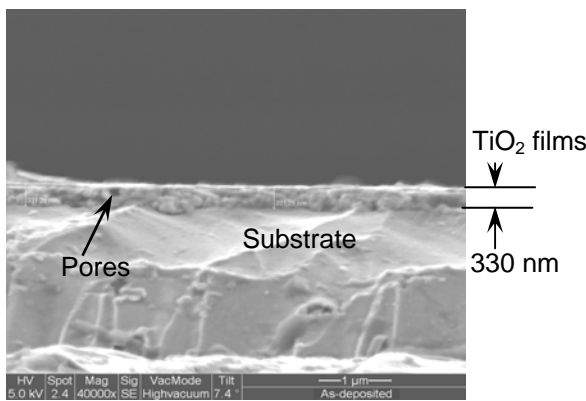


Fig. 1. SEM cross-sectional image of the  $\text{TiO}_2$  film deposited at room temperature.

good agreement with the optical thickness. The cross-sectional view shows that the film possesses granular structure. It also shows dense and compact nature for the as-deposited  $\text{TiO}_2$  film prepared at room temperature. It may be

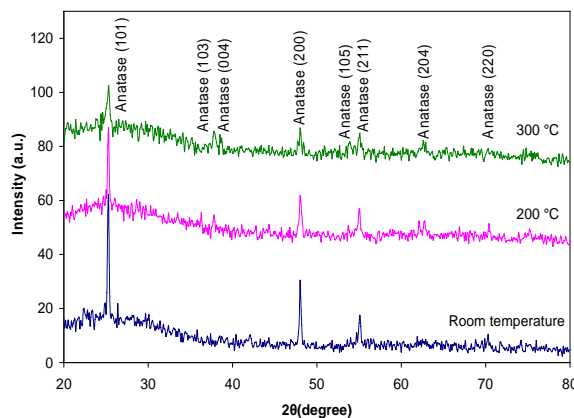


Fig. 2. X-ray diffraction patterns of  $\text{TiO}_2$  films deposited at room temperature, 200 $^{\circ}\text{C}$  and 300 $^{\circ}\text{C}$ .

mentioned that Eufinger et al. [21] obtained a columnar structure in their dc magnetron sputtered  $\text{TiO}_2$  films at a power of 60 W. A few voids are also found in the cross section (arrow) to exhibit its porous structure. The diffraction patterns of  $\text{TiO}_2$  films deposited at different substrate temperatures are shown in Fig. 2. From Fig. 2, as-deposited  $\text{TiO}_2$  film prepared at room temperature is found to be crystalline and possesses anatase structure as it shows few strong peaks of anatase (101), (200) and (211). Although at a high pressure the depositing species have lower energy, there are suggestions that high density negative oxygen ions are movable at high pressure which impart high energy to the growing film [10]. This may be the reason for the growth of crystalline anatase phase in the present study even at room temperature.

Some additional weak peaks along the anatase planes (103), (004), (105), (204) and (220) appear for the samples of heated substrates. It is also observed that the peak intensities of the anatase planes (101), (200) and (211) decrease significantly with increasing substrate temperature. It may be inferred that crystallinity is found to decrease with increasing substrate temperature. Tomaszewski et al. [22] reported that sodium ion from glass substrate diffused into their  $\text{TiO}_2$  films during annealing treatment which suppressed anatase crystallization. Alkali ion diffusion from glass slides to titania films might also occur in the

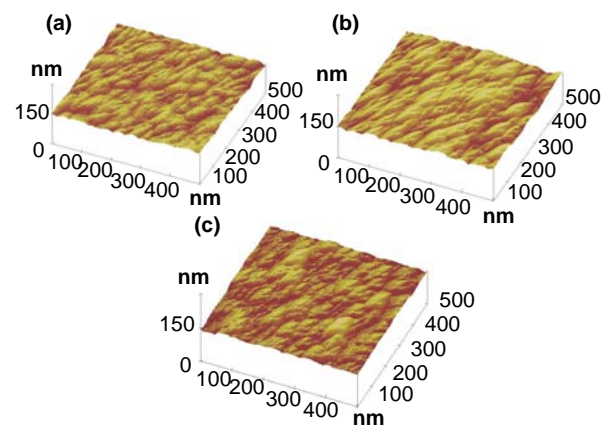


Fig. 3. AFM images of  $\text{TiO}_2$  films deposited at: (a) Room temperature, (b) 200  $^{\circ}\text{C}$  and (c) 300  $^{\circ}\text{C}$ .

present study to decrease the crystallinity. In the present work, the crystallite sizes calculated by Scherrer equation for  $\text{TiO}_2$  films prepared at different substrate temperatures are seen to have a grain size of  $\sim 44$  nm. Substrate temperature

does not seem to have any significant effect on the grain size. It is observed that the range of grain size of the deposited films on microscope slides obtained in the present study is close to that obtained by Eufinger et al. [21].

The surface morphology of TiO<sub>2</sub> films as recorded by AFM in the tapping mode is shown in Fig. 3. The anatase TiO<sub>2</sub> films are all found to be as compact and dense. AFM images exhibit a nodular morphology. Substrate temperature does not appear to have a significant effect on the morphology of the film. From AFM surface roughness analysis, the root mean square (rms) surface roughness of TiO<sub>2</sub> films deposited at room temperature, 200 °C and 300 °C are found to be 4.75, 5.23 and 6.26 nm, respectively. It indicates an increase of rms roughness with increasing substrate temperature. Hou et al. [23] observed a lower rms roughness (2.38 nm) for their AC magnetron sputtered TiO<sub>2</sub> films having comparable thickness as in the present study.

The adhesion critical load of the studied TiO<sub>2</sub> films was determined by the micro-scratch tests combined with the observation of the scratch tracks under the optical microscope. Three different micro-scratch tests were performed for each TiO<sub>2</sub> films deposited at different substrate temperatures and all the tests give consistent results. Optical micrographs of the scratch scars on TiO<sub>2</sub> films are shown in Fig. 4. It is observed that each scratch track gets wider uniformly with progressively increasing load. At a certain point (shown by arrows) a wide damaged area appears representing a complete delamination of the films which can be defined as the critical load for

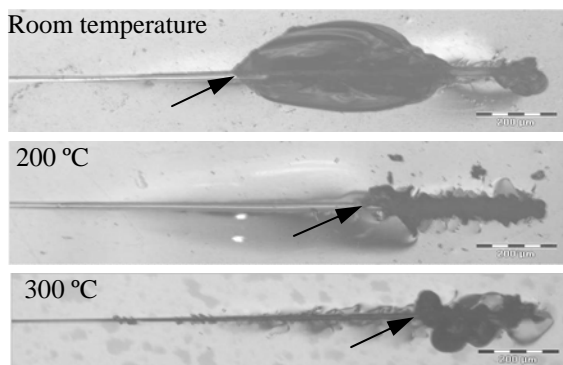


**Fig. 4. Optical micrographs on TiO<sub>2</sub> films deposited at different substrate temperatures.**

adhesion. Two types of failure are mainly encountered in scratch tests, namely, cohesive failure of the coating or substrate and interfacial failure of the coating-substrate interface [19].

The cohesive failure of a coating is mainly accompanied by partial conical cracks and some debris at the side of the scratch tracks [24]. The complete delamination of films is due to the interfacial failure at the coating-substrate interface. From Fig. 4, it is observed that no cohesive failure mode appears for the film deposited on unheated substrate, but for the films prepared at higher substrate temperatures exhibit an earlier damage with small cracks and some debris. It may be attributed to the higher surface roughness. Higher residual stress resulting from mismatch of coefficients of thermal expansion of the substrate and films deposited at higher temperatures might also contribute to this. The critical loads of TiO<sub>2</sub> films deposited at room temperature, 200 and 300 °C were estimated by the scratch tests and found to be 1.5, 2 and 2.24 N, respectively. It is thus seen that higher substrate temperatures lead to improved adhesion of TiO<sub>2</sub> films on glass substrates. There are suggestions that cohesive bonding in anatase structure and interdiffusion of film/substrate interface can cause enhanced film adhesion [15]. The increase of adhesion critical load may be due to interdiffusion of atoms in the film/substrate interface and densification of the films at higher substrate temperatures.

A number of researchers reported on the adhesion critical load for titanium oxide films. Chen et al. [16] reported an increase of adhesion critical loads from 1.5 to 19.25 N using a scratch tester with 200 μm tip radius diamond indenter. They investigated sol-gel prepared TiO<sub>2</sub> films (6.7-10 μm thick) on stainless steel at different annealing temperatures, 400 to 600 °C. Kuo et al. [18] evaluated critical loads for 240 nm thick RF sputtered TiO<sub>2</sub> films on silicon substrates varying substrate temperature from 200 to 500 °C. They estimated the critical load using a diamond indenter of tip radius 200 μm and it was found to be about 7 N without any significant effects of substrate temperatures. In this study, a spherical diamond indenter of tip radius 25 μm was drawn with progressively increasing load during micro-scratch tests. Due to the smaller radius of the indenter tip, a force was applied on a smaller contact area of films. Although a low force was applied, it produces a high contact pressure and severe plastic flow with a very few asperities. This mechanism is most likely responsible for the coating failures at lower values of critical loads in the present investigation. As a result, it can be inferred that

the lower values of critical loads obtained in this work may be attributed to the combined effects of film thickness, indenter tip radius, substrate materials and coating-substrate interfaces.

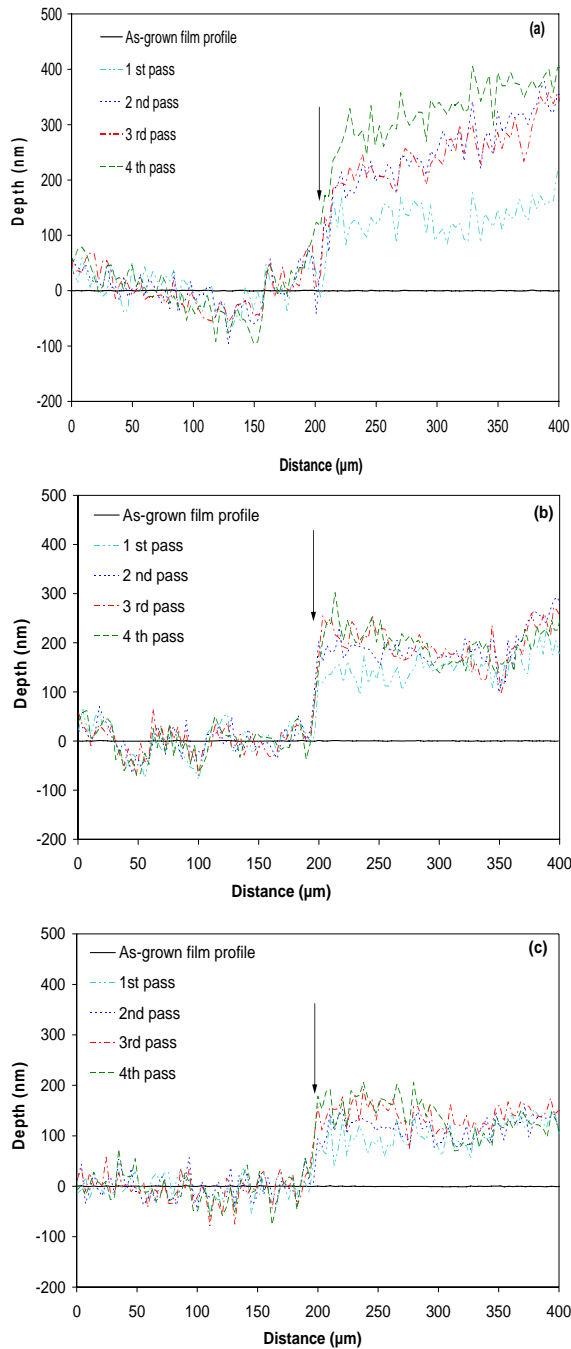


**Fig. 5. Wear tests for TiO<sub>2</sub> films deposited at (a) room temperature, (b) 200 °C and (c) 300 °C.**

The scratch hardness is a measure of coating cohesion. The values of scratch hardness calculated using equation (2) are found to be 5.5, 6.7 and 8.4 GPa for TiO<sub>2</sub> films prepared at room temperature, 200 and 300 °C respectively. Because of the nano-scale thickness of the films, it is likely that the substrate also contributes to

the measurements of both critical load and scratch hardness. It is observed that scratch hardness is found to increase with the increase of substrate temperatures. Joworski et al. [17] reported a scratch hardness of 3.6 GPa for their anatase titania films where the scratch test were done using a 200 μm indenter tip under a higher load of 30 N. In addition, Lackner et al. [13] reported an increase of surface hardness from 4.25 to 11.16 GPa determined by nanoindentation with the decrease of oxygen flow rate. The scratch hardness values found in the present study is nearly comparable to the surface hardness values found in that study.

In tribological tests, a spherical diamond indenter of radius 25 μm of NanoTest high load head equipment is drawn unidirectionally along the same surface using a load of 500 mN at a sliding speed of 1 μm/sec for a wear track distance of 800 μm. Fig. 5 shows the profilometry of four successive wear passes including the as-grown film surface. From the figure, it is observed that upon the application of load, the penetration depth suddenly increases. The penetration becomes progressively deeper as the number of passes on the same wear track increases. Data extracted from Fig. 5 is tabulated in Table 1. It is seen that films deposited at

**Table 1 Penetration depth for TiO<sub>2</sub> films deposited at different temperatures during wear test.**

Substrate temperature (°C)	Penetration depth (nm)			
	1 <sup>st</sup> Pass	2 <sup>nd</sup> Pass	3 <sup>rd</sup> Pass	4 <sup>th</sup> Pass
25	100	170	200	250
200	80	150	175	210
300	50	120	140	180

higher substrate temperature exhibits lower penetration. Thus higher deposition temperature results in titanium oxide film with improved resistance to penetration. This result correlates well with the increase of scratch hardness for higher substrate temperatures as discussed

**Table 2 Average wear track width of TiO<sub>2</sub> films deposited at different substrate temperatures.**

Sample	Substrate temperature (°C)	Mean wear track width (μm)
1	Room temperature	18.8
2	200 °C	14.2
3	300 °C	9.6

earlier. The wear track width was measured at three different positions along the wear tracks of

the studied films. The mean width of the wear tracks of TiO<sub>2</sub> films deposited at different substrate temperatures are given in Table 2. It is observed that the width of the wear track is found to decrease with increasing substrate temperature which is consistent with the penetration data. Thus it can be inferred that wear resistance is found to improve with higher substrate temperatures. The improvement in the tribological properties may be interpreted as the effects of enhanced adhesion strength and densification at higher substrate temperatures as well. Several reports [13-15] suggested the improvement of wear resistance with the increase of crystallinity, adhesion critical loads and surface hardness in their micro/macro scale wear measurements. In the present work, the enhancement of wear resistance may be attributed to the improvement of critical loads and hardness for films deposited at higher substrate temperatures.

#### 4. Conclusion

The anatase phase titanium dioxide films with grain size of about 44 nm have been produced by RF reactive sputtering method on unheated and heated glass substrates. AFM images of as-deposited TiO<sub>2</sub> films at different substrate temperatures show a uniform, compact and nodular morphology. The mechanical and tribological properties of TiO<sub>2</sub> films were investigated by micro-scratch and wear tests respectively. The adhesion critical load, scratch hardness and wear resistance are seen to have strong dependence on the substrate temperature. The critical loads of adhesion of TiO<sub>2</sub> films deposited at room temperature, 200 and 300 °C are found to be 1.5, 2 and 2.24 N respectively. The values of scratch hardness are also found to be 5.5, 6.7 and 8.4 GPa for the films prepared at room temperature, 200 and 300 °C respectively. In wear tests, the final penetration is found to decrease for films prepared at higher substrate temperature. Titanium oxide films at higher substrate temperatures show better resistance to penetration. From the optical micrographs of the wear scars, similar trend for the width of wear scars are also observable. The combined decrease of penetration and wear track width results in an enhanced wear resistance for the TiO<sub>2</sub> films deposited at higher temperatures. This improvement of wear properties for the films deposited at higher temperature is likely to

be attributed to the improved adhesion critical loads and scratch hardness.

#### Acknowledgements

The authors gratefully acknowledge the financial support given for this work by the Ministry of Science, Technology and Innovation Malaysia (MOSTI) under the ScienceFund by Grant No: 13-02-03-3033 and the Institute of Research Management and Consultancy, University of Malaya (UM) by PPP Fund Project No. : PS 051/2007B.

#### References

- [1] H.K. Pulker, *Coatings on Glass*, Elsevier, Amsterdam, Netherlands, 1999.
- [2] Y.M. Sung and H.J. Kim, Sputter deposition and surface treatment of TiO<sub>2</sub> films for dye-sensitized solar cells using reactive RF plasma, *Thin Solid Films*, Vol. 515, pp. 4996-4999, 2007.
- [3] M. Okada, M. Tazawa, P. Jin, Y. Yamada, K. Yoshimura, Fabrication of photocatalytic heat-mirror with TiO<sub>2</sub>/TiN/ TiO<sub>2</sub> stacked layers, *Vacuum*, Vol. 80, pp. 732-735, 2006.
- [4] A. Fujishima, T.N. Rao, D.A. Tryk, Titanium dioxide photocatalysis, *Journal of Photochemistry and photobiology C: Photochemistry Reviews*, Vol. 1;1, pp. 1-21, 2000.
- [5] H. Sun, C. Wang, S. Pang, X. Li, Y. Tao, H. Tang, M. Liu, Photocatalytic TiO<sub>2</sub> films prepared by chemical vapor deposition at atmosphere pressure, *Journal of Non-Crystalline Solids*, Vol. 354, pp. 1440-1443, 2008.
- [6] M.H. Habibi, N. Talebian, J.H. Choi, The effect of annealing on photocatalytic properties of nanostructured titanium dioxide thin films, *Dyes and Pigments*, Vol. 73, pp. 103-110, 2007.
- [7] C. Yang, H. Fan, Y. Xi, J. Chen, Z. Li, Effects of depositing temperatures on structure and optical properties of TiO<sub>2</sub> film deposited by ion beam assisted electron beam evaporation, *Applied Surface Science*, Vol. 254, pp. 2685-2689, 2008.
- [8] Z. Wang, U. Helmersson, P.O. Käll, Optical properties of anatase TiO<sub>2</sub> thin films prepared by aqueous sol-gel process at low temperature, *Thin Solid Films*, Vol. 405, pp. 50-54, 2002.

- [9] W. Yang and C.A. Wolden, Plasma-enhanced chemical vapor deposition of TiO<sub>2</sub> thin films for dielectric applications, *Thin Solid Films*, Vol. 515, pp. 1708-1713, 2006.
- [10] A. Karuppasamy and A. Subrahmanyam, Studies on the room temperature growth of nanoanatase phase TiO<sub>2</sub> thin films by pulsed dc magnetron with oxygen as sputter gas, *Journal of Applied Physics*, Vol. 101, pp. 1-7(064318), 2007.
- [11] Q. Ye, P.Y. Liu, Z.F. Tang, L. Zhai, Hydrophilic properties of nano-TiO<sub>2</sub> thin films deposited by RF magnetron sputtering, *Vacuum*, Vol. 81, pp. 627-631, 2007.
- [12] Y. Zhang, X. Ma, P. Chen, D. Yang, Effects of the substrate temperature on the crystallization of TiO<sub>2</sub> films prepared by DC reactive magnetron sputtering, *Journal of Crystal Growth*, Vol. 300, pp. 551-554, 2007.
- [13] J.M. Lackner, W. Waldhauser, R. Ebner, B. Major, T. Schöberl, Pulsed laser deposition of titaniumoxide coatings at room temperature—structural, mechanical and tribological properties, *Surface and Coatings Technology*, Vol. 180-181, pp. 585-590, 2004.
- [14] Y.X. Leng, J.Y. Chen, P. Yang, H. Sun, N. Huang, Structure and properties of passivating titanium oxide films fabricated by DC plasma oxidation, *Surface and Coatings Technology*, Vol. 166, pp. 176-182, 2003.
- [15] C.J. Chung, P.Y. Hsieh, C.H. Hsiao, H.I. Lin, A. Leyland, A. Matthews, J.L. He, Multifunctional arc ion plated TiO<sub>2</sub> photocatalytic coatings with improved wear and corrosion protection, *Surface and Coatings Technology*, Vol. 203, pp. 1689-1693, 2009.
- [16] Y. Chen, D.D. Dionysiou, Effect of calcination temperature on the photocatalytic activity and adhesion of TiO<sub>2</sub> films prepared by the P-25 powder-modified sol-gel method, *Journal of Molecular Catalysis A: Chemical*, Vol. 244, pp. 73-82, 2006.
- [17] R. Jaworski, L. Pawlowski, F. Roudet, S. Kozerski, F. Petit, Characterization of mechanical properties of suspension plasma sprayed TiO<sub>2</sub> coatings using scratch test, *Surface and Coatings Technology*, Vol. 202, pp. 2644-2653, 2008.
- [18] D.H. Kuo, K.H. Tzeng, Growth and properties of titania and aluminum titanate thin films obtained by r.f. magnetron sputtering, *Thin Solid Films*, Vol. 420-421, pp. 497-502, 2002.
- [19] J. Malsbender, J.M.J. den Toonder, A.R. Balkenende, G. de With, Measuring mechanical properties of coatings: a methodology applied to nano-particle-filled sol-gel coatings on glass, *Materials science and Engineering R*, Vol. 36, pp. 47-103, 2002.
- [20] M.M. Hasan, H.H. Masjuki, A.S.M.A. Haseeb, R. Saidur, M. Hamdi, RF reactive sputter deposition of TiO<sub>2</sub> films at different temperatures: structural, optical and mechanical properties, *Proceedings of the 1<sup>st</sup> AUN/SEED-Net Regional Workshop in the Interdisciplinary Area of Natural Resources/Materials*, Phnom Penh, Cambodia, August 2008, pp. 132-139.
- [21] K. Eufinger, D. Poelman, H. Poelman, R.D. Gryse, J.B. Marin, Effect of microstructure and crystallinity on the photocatalytic activity of TiO<sub>2</sub> thin films deposited by dc magnetron sputtering, *Journal of Physics D: Applied Physics*, Vol. 40, pp. 5232-5238, 2007.
- [22] H. Tomaszewski, K. Eufinger, H. Poelman, D. Poelman, R.D. Gryse, P.F. Smet, G.B. Marin, . Effect of substrate sodium content on crystallization and photocatalytic activity of TiO<sub>2</sub> films prepared by dc magnetron sputtering, *International Journal of Photoenergy*, Vol. 1, pp. 1-5(95213), 2007.
- [23] Y.Q. Hou, D.M. Zhuang, G. Zhang, M. Zhao, M.S. Wu, Influence of annealing temperature on the properties of titanium oxide thin film, *Applied Surface Science*, Vol. 218, pp. 98-106, 2003.
- [24] B.D. Beake and N. Ranganathan, An investigation of the nanoindentation and nano/micro-tribological behaviour of monolayer, bilayer and trilayer coatings on cemented carbide, *Materials Science and Engineering A*, Vol. 423, pp. 46-51, 2006.

# IONIC TRANSPORT STUDY OF POLYMETHYLMETHACRYLATE BASED SALICYLIC ACID DOPED PROTON CONDUCTING GEL POLYMER ELECTROLYTES

M.I.N. Isa<sup>1</sup> and A.K.Arof<sup>2</sup>

<sup>1</sup>Department of Physical Sciences, Faculty of Science and Technology  
University Malaysia Terengganu, 21030 Kuala Terengganu, Terengganu, Malaysia

<sup>2</sup>Department of Physics, Faculty of Science, University of Malaya  
50670 Kuala Lumpur, Malaysia.

Corresponding Author: Email: [ikmar\\_isa@umt.edu.my](mailto:ikmar_isa@umt.edu.my)

## Abstract

*In this work, the ionic transport of DBP/DMF plasticized salicylic acid doped PMMA based gel electrolyte has been studied. The number of mobile ions, mobility of mobile ion and diffusion coefficient of mobile ions obtained from calculation using the Rice and Roth Model. It was found that the conductivity of the GPE was influenced by the number of mobile ions, mobility of mobile ion and diffusion coefficient of mobile ions. The GPE also found to be a proton conductor based from the compare value of anionic and cationic mobility and diffusion coefficient.*

**Keywords:** ionic transport, PMMA, gel electrolytes, number of mobile ions

## 1. Introduction

Much attention has been directed to proton conducting polymeric electrolytes because of their possible applications in advanced electrochemical devices such as batteries, capacitors, sensors, electrochromic displays, photoelectrochemical solar cells and fuel cells [1]. A lot of efforts have been done to enhance the transport properties of polymer electrolytes (PE) in order to make them feasible for power applications.

Polymer electrolytes can be grouped into several classes, namely solid polymer electrolytes (SPEs), liquid polymer electrolytes (LPEs) and gel polymer electrolytes (GPEs). Gel polymer electrolytes have the advantages of space and mass, structural stability and low volatility.

In this work, the ionic transport of DBP/DMF plasticized salicylic acid doped PMMA based gel electrolyte has been study. The number of mobile ions, mobility of mobile ion and diffusion coefficient of mobile ions obtained from calculation using the Rice and Roth Model (1972). It was found that the

conductivity of the GPE was influenced by the number of mobile ions, mobility of mobile ion and diffusion coefficient of mobile ions. The GPE also found to be a proton conductor based from the compare value of anionic and cationic mobility and diffusion coefficient.

## 2. Experimental

### 2.1 Sample preparation

The solvents (EC-PC) were mixed at room temperature. Salicylic acid (SA) was then added and dissolved. The dual plasticizers were then added. Later the polymer poly (methyl methacrylate) (PMMA) was added and the whole mixture was heated to 70<sup>0</sup>C to promote gel formation. Finally the mixture was cast into petri dishes for the gel to form properly in a silica gel containing dessicator. The sample composition was 35 wt% EC, 30 wt% PC, 5 wt% SA, 4wt% DBP, 1wt% DMF and 25 wt% PMMA for DBP-rich dual plasticizer and 35 wt% EC, 30 wt% PC, 5 wt% SA, 1wt% DBP, 4wt% DMF and 25 wt% PMMA for DMF-rich dual plasticizer.

## 2.2 Electrochemical Impedance Spectroscopy (EIS) study

The sample was sandwiched between two stainless steel electrodes under spring pressure. Impedance spectroscopy was measured using a computer-interfaced HIOKI 3531-01 LCR bridge with frequency ranging from 42 Hz to 1 MHz. The impedance of the sample was measured at every frequency, at room and elevated temperatures. The electrical conductivity was obtained by inserting the bulk resistance value, thickness and area into equation below.

$$\sigma = \frac{t}{R_b A}$$

Here  $t$  is thickness of the gel and  $A$  is the area of contact between the gel and the electrolyte. The bulk resistance  $R_b$  was obtained from the complex impedance plot,  $-Z_i$  vs.  $Z_r$ . The conductivity increase as temperature increases. The regression value is almost unity and the plot can be considered Arrhenian. From the slope of  $\log \sigma$  versus  $1000/T$  the conductivity activation energy,  $E_A$  was calculated as  $(0.30 \pm 0.06)$  eV and  $(0.30 \pm 0.08)$  eV for DMF rich dual plasticizer and DBP rich dual plasticizer respectively.

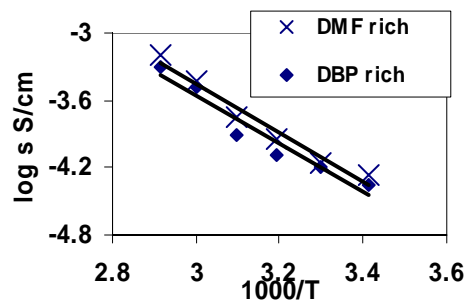


Fig.2. Conductivity as a function of temperature

Using the Nernst-Einstein equation,  $n$  equals  $3.17 \times 10^{20} \text{ cm}^{-3}$ . The Rice and Roth model expresses the conductivity as:

$$\sigma = \frac{3e^2}{2kTM} n E_A \tau [\exp(-E_A / kT)]$$

The exponential term tends to unity. Hence  $\tau$  calculated from the Rice and Roth conductivity is of the order  $10^{-14}$  s. Using the value of  $\tau$  and the activation energy from the  $\log \sigma$  versus  $10^3/T$  plot, the number density of mobile ions,  $n$ , mobility of mobile ions,  $\mu$  and diffusion coefficient of the mobile ions,  $D$ , were calculated. Table 1 and Table 2 list the estimated values of  $n$ ,  $\mu$  and  $D$  for the dual plasticized gel electrolyte of the present work.

Table 1: Transport parameter of sample PMMA-EC-PC-SA-4wt% DMF-1wt% DBP gel.

T (K)	$\sigma$ (S cm <sup>-1</sup> )	$\Delta\sigma$ (S cm <sup>-1</sup> )	n (cm <sup>-3</sup> )	$\mu$ (cm <sup>2</sup> V <sup>-1</sup> s <sup>-1</sup> )	D (cm <sup>2</sup> s <sup>-1</sup> )
293	5.50E-05	4.04E-06	(5.70±1.25)E+19	(6.03±1.39)E-06	(1.52±0.36)E-07
303	6.81E-05	5.01E-06	(7.30±1.60)E+19	(5.83±1.35)E-06	(1.52±0.36)E-07
313	1.14E-04	8.40E-06	(1.26±0.28)E+20	(5.65±1.30)E-06	(1.52±0.36)E-07
323	1.77E-04	1.34E-05	(2.02±0.44)E+20	(5.47±1.27)E-06	(1.52±0.36)E-07
333	2.09E-04	1.60E-05	(2.46±0.95)E+20	(5.31±1.24)E-06	(1.52±0.36)E-07
343	2.88E-04	2.30E-05	(3.49±0.17)E+20	(5.15±1.21)E-06	(1.52±0.36)E-07

Table 2: Transport parameter of sample PMMA-EC-PC-SA-1wt% DMF-4wt% DBP gel.

T (K)	$\sigma$ (S cm <sup>-1</sup> )	$\Delta\sigma$ (S cm <sup>-1</sup> )	n (cm <sup>-3</sup> )	$\mu$ (cm <sup>2</sup> V <sup>-1</sup> s <sup>-1</sup> )	D (cm <sup>2</sup> s <sup>-1</sup> )
293	4.50E-05	5.38E-06	(6.39±2.07)E+19	(4.40±1.52)E-06	(1.11±0.42)E-07
303	6.47E-05	7.82E-06	(9.50±3.09)E+19	(4.26±1.48)E-06	(1.11±0.42)E-07
313	8.16E-05	1.00E-05	(1.24±0.40)E+20	(4.12±1.43)E-06	(1.11±0.42)E-07
323	1.24E-04	2.22E-05	(1.94±0.63)E+20	(3.99±1.39)E-06	(1.11±0.42)E-07
333	1.91E-04	2.96E-05	(3.08±0.18)E+20	(3.87±1.45)E-06	(1.11±0.42)E-07
343	2.51E-04	4.40E-05	(4.17±0.29)E+20	(3.76±1.47)E-06	(1.11±0.42)E-07

From Table 1 and 2, the increase in conductivity with temperature is observed to be influenced by the number density of mobile ions and the mobility, since the diffusion coefficient of the

ions remains constant throughout the temperature range in the present investigation.  $n$  increases with temperature while  $\mu$  decreases with temperature. The decrease in mobility with

temperature is attributed to the blocking effect due to 'ion overcrowding', thereby making the ions less mobile. Hence, temperature helps to dissociate the acid into ions thereby leading to an increase in conductivity.

To obtain the ionic transference number of the material, transference number measurement will be carried out using the dc polarization technique. The sample was sandwiched between two stainless steel blocking electrodes and the current through the circuit was monitored with time until it saturates.

Knowing  $t_{ion}$  from the temporal plots of normalized polarization current graphs,  $\mu_+$  can be obtained from equation:

$$t_{ion} = \frac{\mu_+}{\mu_+ + \mu_-} = \frac{\mu_+}{\mu}$$

$\mu_+$  can be calculated since  $\mu$  is obtained from the equation  $\sigma = nq\mu$ . By substituting  $\mu_+$  into the equation

$$\sigma = nq\mu_+ + nq\mu_-$$

$\mu_-$ , i.e. mobility of the anion can be obtained.  $\sigma$  is the conductivity at room temperature.

From the equation

$$t_{ion} = \frac{D_+}{D_+ + D_-} = \frac{D_+}{D}$$

**Table 4: cationic and anionic mobility and diffusion coefficient**

Sample	4 wt% DMF +1 wt% DBP	1 wt% DMF +4 wt% DBP
T(K)	293	293
$\sigma$ (Scm <sup>-1</sup> )	5.50E-05	4.50E-05
$n$ (cm <sup>-3</sup> )	5.70E+19	6.39E+19
$\mu$ (cm <sup>2</sup> V <sup>-1</sup> s <sup>-1</sup> )	6.03E-06	4.40E-06
$D$ (cm <sup>2</sup> s <sup>-1</sup> )	1.52E-07	1.11E-07
$t_{ion}$	9.43E-01	8.89E-01
$\mu_+$	5.69E-06	3.91E-06
$\mu_-$	3.44E-07	4.89E-07
$D_+$	1.44E-07	9.89E-08
$D_-$	8.69E-09	1.23E-08

$D_+$  can be calculated.  $D$  is obtained from the Nernst-Einstein equation. By substituting  $D_+$  into

$$D_+ + D_- = \frac{\sigma kT}{nq^2}$$

$D_-$ , i.e. the diffusion coefficient for the anion can be calculated where  $n$  is obtained from Rice and Roth model.

Table 4 presents the cationic and anionic mobility and diffusion coefficient for sample PMMA-EC-PC-SA-4wt% DMF- 1wt% DBP and PMMA-EC-PC-SA-1wt% DMF-4wt% DBP gels at room temperature respectively. It can be seen from Table 4, the value of  $\mu_+$  is higher than  $\mu_-$  and  $D_+$  is higher than  $D_-$ . So, it can be concluded that the material is more cationic than anionic conductor and as a result it can be said that the sample is a proton conductor.

### 3. Conclusion

The conductivity is controlled by the number density of mobile ions,  $n$  and their mobility,  $\mu$ , and diffusion coefficient,  $D$ . The mobility of the protonic gel is of the order 10<sup>-6</sup> cm<sup>2</sup>V<sup>-1</sup>s<sup>-1</sup> and the diffusion coefficient is of the order 10<sup>-8</sup> to 10<sup>-7</sup> cm<sup>2</sup>s<sup>-1</sup>. The sample also have higher value of  $\mu_+$  and  $D_+$  than  $\mu_-$  and  $D_-$  which shows that the materials are proton conductors.

### References

- [1] Wieczorek, W., Florjan'czyk, Z. and Stevens, J.R., Proton conducting polymer gels based on a polyacrylamide matrix, *Electrochimica Acta*, 40, 1995, pp. 2327-2330.
- [2] Rice, M.J., and Roth, W.L., Ionic transport in super ionic conductors: a theoretical model, *J. of Solid State Chemistry*, 4, 1972, pp. 294-310.
- [3] Ericson, H., Svanberg, C., Brodin, A., Grillone, A.M., Panero, S., Scrosati, B., Jacobsson P., Poly(methyl methacrylate)-based protonic gel electrolytes: a spectroscopic study, *Electrochimica Acta*, 45, 2000, 1409–1414.

## NEURO-FUZZY GENETIC ALGORITHM

M. Jalali V.<sup>1</sup>, L.S. Lee<sup>2</sup>

<sup>1,2</sup> *Laboratory of Applied and Computational Statistic, Institute for Mathematical Research,*

<sup>2</sup> *Department of Mathematical, Faculty of Science*

*University Putra Malaysia, 43400 UPM Serdang, Selangor, MALAYSIA.*

<sup>1</sup>[jalali@inspem.upm.edu.my](mailto:jalali@inspem.upm.edu.my) ; Tel: +6 017-6660803

### Abstract

*Premature convergence is a classical problem in finding optimal solution in Genetic Algorithms (GAs). The population diversity is a way of avoiding the premature convergence in a GA. If the population diversity is low, the GA will converge very quickly. On the other hand, if the population diversity is high, the GA will takes a lot of time to converge and this may caused wastage in computational resources. This paper proposes a new variant of GA: neuro-fuzzy genetic algorithm with sexual selection. The motivation of this algorithm is to maintain the population diversity throughout the search procedure. To promote diversity, the proposed algorithm combines the concept of gender and age of individuals and the fuzzy logic during the selection of parents. The goal of this technique is to maintain suitable diversity in the population and to prevent GA from converge prematurely to local optimal. Computational experiments are conducted to compare the performance of this new technique with some commonly used mechanisms found in a standard GA from literature for solving the well known Generalised Rosenbrock's Function.*

**Keywords:** *genetic algorithm, neuro-fuzzy, sexual selection*

### 1. Introduction

Genetic Algorithms (GAs) were first coined by John Holland [1] in 1960s. A GA is a numerical optimization procedure that is based on evolutionary principles such as selection, recombination and mutation. GA uses a population of chromosomes, each representing a solution to the problem that has to be solved. In a traditional GA, chromosomes reproduce asexually where any two chromosomes may be parents during crossover. Gender division and sexual selection here inspire a model of gendered GA in which crossover takes place only between chromosomes of opposite sex. The sex of chromosomes is not only accountable for preserving diversity in population and maintaining a victorious genetic pool by means of selection, crossover and mutation, but also are accountable for the optimization of the different tasks which are very important for survival.

In this study, an obvious characteristic between the two gender groups, with the possibility of embedding different tasks for each one is considered such as the determination of which partners are suitable for mating and

crossover. We believe the relations between age, effectiveness and fitness as in biological systems will effect the selection procedure. A bi-linear allocation lifetime approach is used to label the chromosomes based on their fitness value [2]. The obtained chromosomes labels are used to characterize the diversity of the population. The population is then divided into two groups: male and female, so that they are selected in an alternate way. In each generation the layout of selection for male and female are different.

In short, the aim of this paper is to keep the diversity of population by female preference. The selection of the female chromosome is done through a set of fuzzy rules and a newly developed genetic-neuro-fuzzy algorithm.

Numerous works have been performed using mate choice in GA, with encouraging results. Ronald [3] shows how the use of a seduction function based upon a visual measure, such as unitation in the case of the royal road problem [4], where it has been shown that selection of the second parent can improve GA performance. Work in [5] discussed the various ways of sexual selection that can be used in evolutionary computation, and indicate that speciation

behaviours may occur when sexual selection is used [6]. Good genes models of sexual selection rely on the idea that fitness is genetic, which contrasts stridently with the non-additive form of genetic quality associated with compatible gene models of sexual selection, which is not generally considered heritable ([6], [7]).

Theoretical developments have played a critical part in understanding the role of genetic ability in sexual selection by providing new hypotheses and predictions for empiricists to test. Several works in this issue explore new theoretical avenues with respect to genetic ability ([6], [8]).

## 2. Fuzzy Rules Systems

Fuzzy systems are encountered in numerous areas of application. Fuzzy rules for example, viewed as a generic mechanism of grainy knowledge representation, are positioned in the center of knowledge-based systems. In this paper we use a linguistic variable 'age' for chromosomes. Figure 1 describes the linguistic variable age where **Infant**, **Adult** and **Old** are the linguistic values. The membership functions for the linguistic terms are called semantic rules.

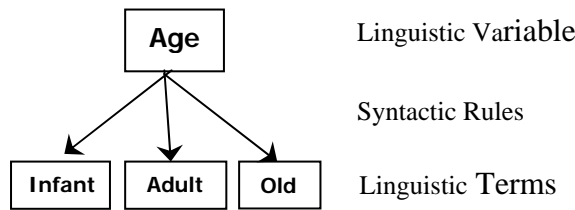


Fig. 1. Three linguistic variables for age.

To find the membership function, we use the fitness value of each chromosome and the minimum, maximum and average fitness values of the population in each generation. Each chromosome has its own label determined by the age function.

$$\text{Let } \varphi = \frac{f_i - f_{\min}}{f_{\text{avr}} - f_{\min}}, \quad \phi = \frac{f_i - f_{\text{avr}}}{f_{\max} - f_{\text{avr}}} \text{ and}$$

$$\tau = f_{\text{avr}} - f_i$$

where

$f_i$  is fitness value of chromosome  $i$  ;

$f_{\text{avr}}$  is average fitness value;

$f_{\min}$  is minimum fitness value; and

$f_{\max}$  is maximum fitness value of population.

The age function can be written as

$$\text{age}(c_i) = \begin{cases} \frac{L + \alpha\varphi}{n}; & \tau \geq 0 \\ \frac{\beta + \alpha\phi}{n}; & \tau < 0 \end{cases} \quad (1)$$

or

$$\text{age}(c_i) = \begin{cases} \frac{U - (L + \alpha\varphi)}{n}; & \tau \geq 0 \\ \frac{U - (\beta + \alpha\phi)}{n}; & \tau < 0 \end{cases} \quad (2)$$

where

$c_i$  is chromosome  $i$  ;

$n$  is population size;

$$\alpha = \frac{U - L}{2} \text{ and } \beta = \frac{U + L}{2};$$

$L$  and  $U$  are minimum and maximum age respectively.

Equation (1) is suited for maximization problems which relate to higher fitness values while equation (2) is more suitable for minimization problems which relate to lower fitness values. The fuzzification interface defines for each chromosome the possibilities of the three linguistic values. These values determine the applicability degree for each rule premise. The computation takes into account all chromosomes in each generation, and relies on the triangular membership functions shown in Figure 2 with  $L = 2$  and  $U = 10$ .

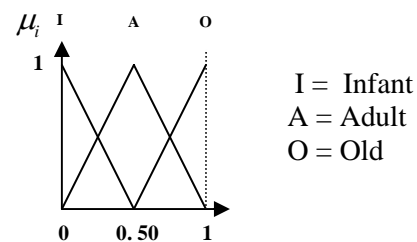


Fig. 2. The membership function for male and female chromosomes.

On the other hand we can consider linguistic rules and membership function for each rule as follow:

$$\text{age} = \begin{cases} \text{Infant} & \mu_1 = -2x + 1 & 0 \leq x \leq 0.50 \\ \text{Adult} & \mu_2 \begin{cases} 2x & 0 \leq x \leq 0.50 \\ -2x + 2 & 0.50 < x \leq 1 \end{cases} \\ \text{Old} & \mu_3 = 2x - 1 & 0.50 \leq x \leq 1 \end{cases} \quad (3)$$

A bi-linear allocation lifetime approach proposed in [2] is used to label the chromosomes

based on their fitness value which will then be used to characterize the diversity of the population.

$$D(c_i) = \begin{cases} L + \alpha\varphi; & \tau \geq 0 \\ \beta + \alpha\phi; & \tau < 0 \end{cases} \quad (4)$$

Let  $\psi$  be the label of half of the population, then the population can be divided into three levels, **Low**, **Medium** and **High** diversity as follows:

$$\text{Population Diversity} = \begin{cases} \text{High} & 0 \leq \psi \leq 2L+t \\ \text{Medium} & 0 \leq \psi \leq 4L+2t \\ \text{Low} & 2L+t \leq \psi \leq 4L+2t \end{cases} \quad (5)$$

where  $t = \left\lceil \frac{\lambda(L+U)}{n} \right\rceil$  is a parameter that has correlation with the domain of labels in the population and  $\lambda = \left\lceil \frac{n}{10} \right\rceil$  ( $\lceil x \rceil$  means nearest integer number to  $x$ , for example  $\lceil 2.3 \rceil = 2$  and  $\lceil 2.8 \rceil = 3$ ). This computation is performed in every generation and relies on the triangular membership functions shown in Figure 3.

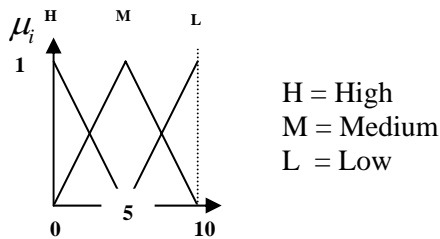


Fig.3. The membership function for diversity.

We can consider linguistic rules and membership function for each rule as follow:

$$D = \begin{cases} \text{High} & \eta_1 = -\frac{1}{5}x + 1 & 0 \leq x \leq 5 \\ \text{Medium} & \eta_2 = \begin{cases} \frac{1}{5}x & 0 \leq x \leq 5 \\ \frac{1}{4}x - \frac{1}{4} & 5 < x \leq 10 \end{cases} \\ \text{Low} & \eta_3 = \frac{1}{5}x - 1 & 5 \leq x \leq 10 \end{cases} \quad (6)$$

### 3. ANFIS: Adaptive Neuro-Fuzzy Inference System

The Sugeno fuzzy model [9] was proposed for a systematic approach to generate fuzzy rules from a given input-output data set. A typical Sugeno fuzzy model given in Figure 4 shows the ANFIS architecture that corresponds to the first order Sugeno fuzzy model. For simplicity, we assume that the ANFIS has two inputs  $x_1$  and  $x_2$  but only one output  $y$ .

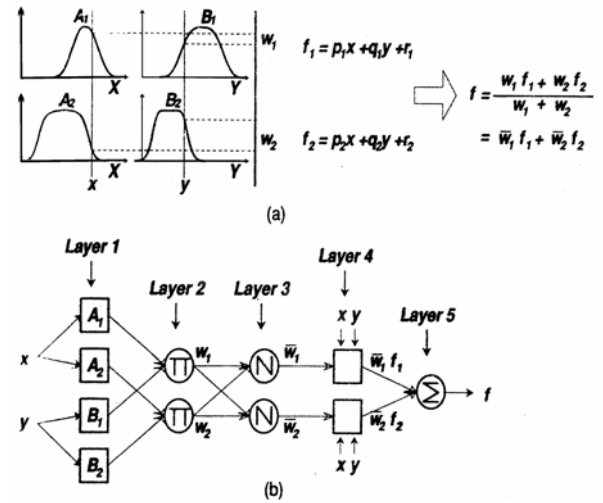


Fig. 4. Adaptive Neuro-Fuzzy Inference Systems [9]

### 4. Adaptive Neuro-Fuzzy Inference Systems Genetic Algorithm (ANFISGA)

This method is based on Neuro-Fuzzy Inference System and GA. In ANFISGA there are two inputs:  $x_1$  = male's age and  $x_2$  = population diversity and one output:  $y$  = female's age,  $F_{age}$ .

In ANFISGA we have five layers. **Layer 1** is the input layer. Neurons in this layer simply pass external crisp signal to **Layer 2**. Layer 2 is the fuzzification layer. Neurons in this layer perform fuzzification. **Layer 3** is the rule layer. Each neuron in this layer corresponds to signal Sugeno-type fuzzy rule. **Layer 4** is the normalization layer. Each neuron in this layer receives inputs from all neurons in the rule layer, and calculates the normalized firing strength of given rule. **Layer 5** is the defuzzification layer. Each neuron in this layer is connected to the respective normalization neuron, and also receives initial inputs,  $\alpha$  and  $\beta$ .

The main difference between ANFISGA and ANFIS is the adaptation. The ANFIS relies

on the weights,  $w_i$  during adaptation. But in the ANFISGA, the weights are all constant. For adaptation, we use sexual selection based on female choice and population diversity. Figure 5

shows the ANFISGA architecture that corresponds to the first order Sugeno fuzzy model with genetic algorithm. The rules for ANFISGA are given in Table 1.

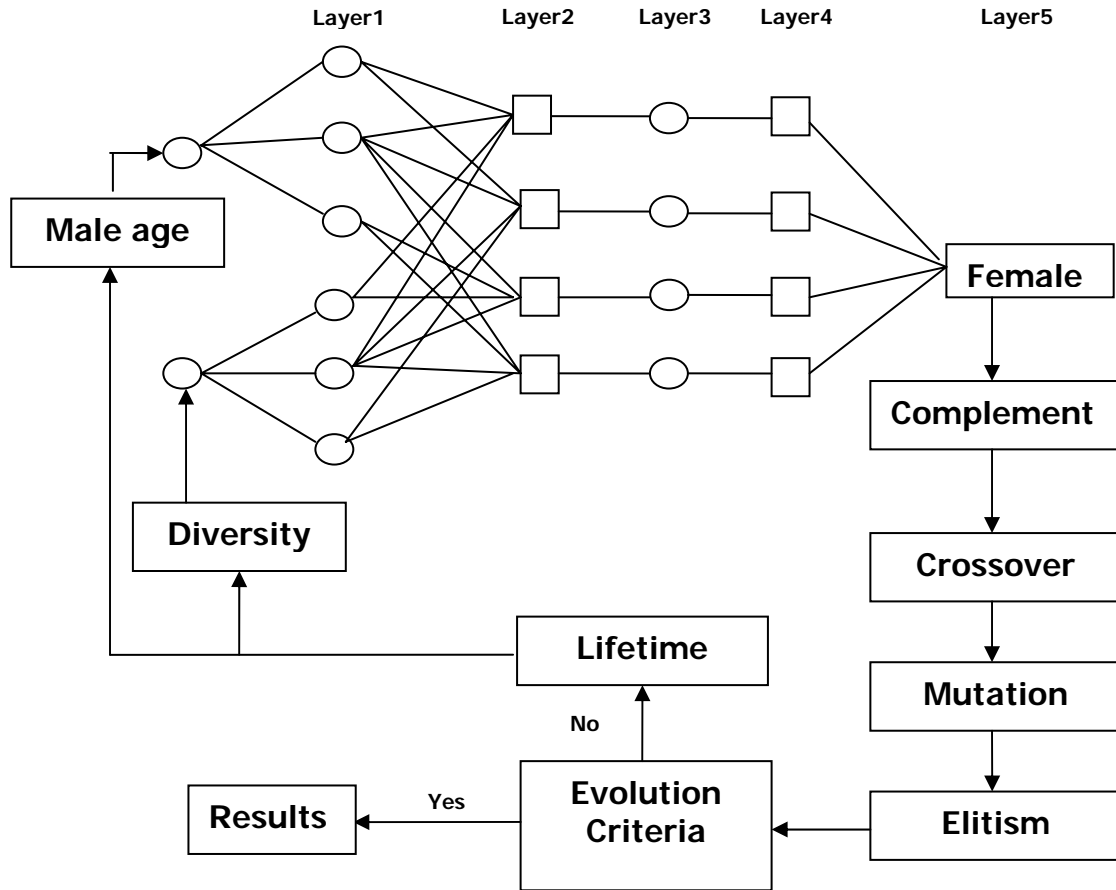


Figure 5: Adaptive Neuro-Fuzzy Inference Systems Genetic Algorithm (ANFISGA)

Table 1: Rules for ANFISGA

Layer 3	Layer 5
$W_1 = w_1\mu_1 + w_2\mu_2 + w_3\eta_1 + w_4\eta_2$	$D_1 = \bar{W}_1 + \beta/2$
$W_2 = w_1\mu_1 + w_2\mu_2 + w_3\eta_2 + w_4\eta_3$	$D_2 = \bar{W}_2 + \beta/3$
$W_3 = w_1\mu_2 + w_2\mu_3 + w_3\eta_1 + w_4\eta_2$	$D_3 = \bar{W}_3 + \alpha/2$
$W_4 = w_1\mu_2 + w_2\mu_3 + w_3\eta_2 + w_4\eta_4$	$D_4 = \bar{W}_4 + \alpha/3$

where  $w_i = i$  ( $i = 1, 2, 3, 4$ ),  $\bar{W}_i = \frac{W_i}{\sum |w_i|}$ ,  $\alpha$

and  $\beta$  are defined in equation (1),  $\mu_i$  is given in equation (3),  $\eta_i$  is taken from equation (6) and the output of ANFISGA is  $D_i = F_{age}$  which refers to the lower bound of the  $F_{age}$  during the selection of the female chromosome.

After the finding of the  $F_{age}$  we may not find a chromosome that has a value at least equal to  $F_{age}$ , then we select a chromosome having the nearest fitness value to  $F_{age}$ , or may be we can find more than one chromosome which satisfies having  $F_{age}$  condition, therefore we choose a chromosome having the highest fitness value of them. This technique called complement method.

## 5. Computational Experiments

The experiments are conducted to compare the performance of our proposed ANFISGA to other GAs found in [12] (see Table 2) for solving the well known Generalised Rosenbrock's Function introduced in [10]:

**Generalized Rosenbrock's Function ( $f_{Ros}$ ):**

$$f_{Ros}(x) = \sum_{i=1}^{n-1} [100(x_{i+1} - x_i^2)^2 + (x_i - 1)^2]$$

where  $-5.12 \leq x_i \leq 5.12$ .

**Table 2: Real Coded Genetic Algorithms (RGA) [12]**

Algorithms	Mutation	Crossover
RGA1	Random	Simple
RGA2	Non-uniform	Simple
RGA3	Random	Uniform. $\alpha = 0.35$
RGA4	Non-uniform	Uniform. $\alpha = 0.35$
RGA5- $\alpha$	Non-uniform	BLX ( $\alpha : 0.,15.,3.,5$ )
RGA6	Non-uniform	Discrete
RGA7	Non-uniform	Linear
RGA8	Non-uniform	Extended Intermediate
RGA9	Non-uniform	Extended Line
ANFISGA	$p_m \in [0.001, 0.2]$	$p_c = 0.70$

The function is a continuous and unimodal function, with the optimum located in a steep parabolic valley with a flat bottom. This feature will probably cause slow progress in many algorithms since they must continually change their search direction to reach the optimum.

We also included a binary coded GA (BGA) with 30 genes per variable, multiple crossovers with two points and proportional selection probability into the experiments.

Each algorithm is tested for 30 times with a maximum of 5000 generations per each run. The

results of the test function are listed in Table 3. The entries reported the average over 30 runs of the best fitness value found at the end of each run.

**6. Conclusions**

The principle conclusions derived from the results of experiments carried out are the following:

- (a) The procedure presented is the most successful one for controlling diversity as compared with other methods proposed in the GA literature that have been considered for the experiments.
- (b) The adaptation capability of this procedure allows suitable parent to be used for producing a robust operation for test function with different difficulties.

Therefore we may conclude that the female choice by ANFISGA is a suitable way for improving the performance of GAs in keeping the diversity of the population.

**Acknowledgement**

The authors would like to thank Ministry of Higher Education (MOHE) and Universiti Putra Malaysia (UPM) for support through Fundamental Research Grant Scheme (FRGS) (02-10-07-320FR).

**Table 3: Comparison of GAs with ANFISGA**

Algorithms	Average	Algorithms	Average
BGA	1.9045e+00	RGA5-0.3	4.8854e-01
RGA1	6.0669e+00	RGA5-0.5	1.7329e+00
RGA2	4.7343e-01	RGA7	5.1499e-01
RGA3	6.3745e+00	RGA8	5.3325e-01
RGA4	8.9244e-01	RGA9	3.8014e-02
RGA5-0.0	9.1602e-01	RGA9	3.8014e-02
RGA5-0.15	7.0929e-01	ANFISGA	2.3240e-03

**References**

- [1] J.H. Holland, *Adaptation in Natural and Artificial Systems*, University of Michigan Press, 1975.
- [2] J. Arabas, Z. Michalewicz, and J. Mulawka, GAVaPS - A Genetic Algorithm with Varying Population Size, *In proceedings of the Evolutionary Computation Conference*, IEEE press, 73-78, 1994.
- [3] E. Ronald, *When Selection Meets Seduction*, In Larry I. Eshelman, (Ed.), *proceedings of the sixth International Conference on Genetic Algorithm*, San Francisco, CA, Morgan Kaufmann, 1995.
- [4] M. Mitchell, S. Forrest, and J.H. Holland, *The Royal Road for Genetic Algorithm*, *Fitness Landscapes and GA performance*,

- In Towards a Practice of Autonomous Systems: proceedings of the First European Conference on Artificial Life*, Cambridge, MA, MIT Press, 1991.
- [5] G.F. Miller, Exploiting Mate Choice in Evolutionary Computation: Sexual Selection as a Process of Search Optimization, and Diversification, *In T. C. Fogarty, (Ed.) proceedings of the AISB Workshop on Evolutionary Computing*, Springer Verlag, 1994.
- [6] T.E. Pitcher and H.L. Mays Jr., An Introduction to Genetic Quality in the Context of Sexual Selection, *Genetica*, Springer Netherlands, 134:1-4, 2008.
- [7] B. Neff and T. Pitcher, Mate Choice for Non-additive Genetic Benefits: a Resolution to the Lek Paradox, *Journal of Theoretical Biology*, (in press) 2008.
- [8] H. Kosko and K. Heubel, Condition-dependence, Genotype-by-environment Interactions and the Lek Paradox, *Genetica* 132: 209–216, 2008.
- [10] T. Takagi, and M. Sugeno, Fuzzy Identification of Systems and its Application to Modelling and Control, *IEEE Transactions on Systems, Man and Cybernetics*, SMC-15(1): 116–132, 1985.
- [11] K.A. De Jong, *An Analysis of the Behaviour of a Class of Genetic Adaptive Systems*, Doctoral Dissertation, University of Michigan, 1975.
- [12] J.E. Baker, Reducing Bias and Inefficiency in the Selection Algorithm, *In proceedings of the 2<sup>nd</sup> International Conference on Genetic Algorithms*, LEA Cambridge, MA, 14-21, 1987.
- [13] F. Herrera, E. Herrera-Viedma, M. Lozano, and J. Verdegay, Fuzzy Tools to improve Genetic Algorithm, *Second European Congress on Intelligent Techniques and soft computing*, EUFLT'94, 1532-1539, 1994.

## PARASITIC ENERGY SAVINGS IN ENGINES USING NANOLUBRICANTS

R. Saidur<sup>1\*</sup>, M. Husnawan<sup>1,2</sup>, Lai Y. K<sup>1</sup>

<sup>1</sup>Department of Mechanical Engineering

University of Malaya, 50603 Kuala Lumpur, Malaysia

<sup>2</sup>Department of Mechanical Engineering, Syiah Kuala University

Jl. S. Abd. Rauf, No.7, Darussalam – Banda Aceh, Indonesia

\*Corresponding Author: [saidur@um.edu.my](mailto:saidur@um.edu.my)

### Abstract

*The engine friction is one of the causes of power losses found in the operation of a vehicle. This friction is caused by the relative motion of moving components in an engine. As significant portion of an engine's generated power is used at low loads, a reduction in an engine friction would provide significant amount of fuel savings. The study focused on the possible usage of nano-technology in enhancing lubricant properties to achieve a lower friction coefficient. The study also estimated the friction of energy lost due to friction in an engine. In this study, it has been found that even with the modest estimation, a net fuel savings of 4% can be achieved with the application of nano-additives in lubricants.*

**Key words:** Nano-lubricants, Engine friction, Energy saving.

### 1.0 Introduction

Worldwide, there are approximately 806 million cars and light trucks as of 2007 [1]. These vehicles consume an estimated 940 billion litres of gasoline and diesel annually and releasing huge amounts of carbon dioxide and many other pollutants to the atmosphere [1]. With nearly one motor vehicle for every 8 human being on this planet, every number associated with a motor vehicle on the global scale; consumption, pollution, road related deaths and many others is inevitably enormous. This fact holds true for energy savings related to a motor vehicle. Even one percent savings worldwide, if it is implementable, could provide huge savings in fuel consumption and also in reducing emissions [1]. Nanotechnology is a broad term to describe technologies involving the control of a matter up to near molecular or atomic levels. When structures are shrunk up to these levels, physical properties of even ordinary materials start to change. This is mostly due to the dramatic increase in surface area to volume ratio of structures at that size [1].

In this study, it has been focused on the possible energy savings achievable by applying nanotechnology in reducing rubbing friction in an automotive engine. Mathematical analysis and calculations have been performed to estimate possible energy savings from using

nanotechnology enhanced lubricants in an automotive engine. Firstly, the amount of energy lost due to rubbing friction has been estimated, followed by an analysis on the possible friction reduction from applying nanotechnology to lubricants. The net energy that can be saved from the application of this technology has been calculated. Figure 1 demonstrates the direction of this research.

It may be mentioned that huge researches have been carried on different aspect of nanotechnology in the available literatures. Major focus of these works were on the materials characteristics, properties, thermal conductivities of nanofluids, heat transfer enhancement mechanism of nanofluids, transport properties of nanofluids, and many other application of nanotechnology in different areas [2, 3]. However, there is no work on the quantification of energy savings associated with the application of nano-lubricants to reduce friction in an engine. The aim of this work is to estimate energy savings with the application of nanotechnology.

### 2.0 Estimation of Engine Friction Losses

#### 2.1 Theory of engine lubrication

In an automotive engine, the available power to the transmission (the brake power) is

significantly lower than the power generated in the cylinders (the indicated power). The indicated power is the net power generated through the expansion and compression strokes only. From this generated power, a portion is used to pump in air through the intake stroke and pump out air during the exhaust stroke, a portion is used to overcome resistance to the relative motion of all moving parts in an engine, and to drive accessories. After subtracting these losses from the indicated power, the remaining power is known as the brake power [4].

These losses in an engine could be determined experimentally by few methods. One particular method highly related to this study is the motored engine breakdown test. This method describe tests where the engine is disassembled or broken down in stages and at each disassemble stage, the power required to motor the engine is measured. Motoring the engine in this context means cranking the engine with an external electric motor where the power required to crank the engine can be measured accurately. This method will give us an insight about how much power is lost to each engine component. The drawback of this measurement technique is that the friction from each component measured might not be representative to the friction faced by the engine in a real operating environment. This is because when the engine is motored, the engine is not subjected to all the heat, stresses and conditions faced by a firing engine. This might result in measurement deviations from an actual engine operation. There are various parts in an engine where relative motion between two solid surfaces occurs. Among the main parts where relative motion occurs are the piston rings against the cylinder walls, the pins connecting the piston rod and the piston and to the crankshaft, valve train (including the camshafts and the push rods), and also various seals through out the engine assembly [4].

It is necessary to have some sort of lubrication in many of these components for the following reasons: to reduce resistance to motion, to prevent seizure, to reduce wear rate of sliding surfaces, and to carry away heat generated by the friction. In general, a low viscosity lubricating fluid is desirable to allow cold starting and minimal losses from viscous losses, but a high enough viscosity is required during the usual running of the engine (where temperature is high) to avoid the lubricant from being forced out of tight spaces [5].

Friction between two mutually contacting sliding surfaces with a lubricating fluid in between can generally be categorized into three ways: Boundary (solid) lubrication, mixed lubrication and hydrodynamic (viscous) lubrication. The category which a friction system belongs to is determined by a dimensionless parameter  $ZN/P$  where  $Z$  is the dynamic viscosity of the fluid,  $N$  is the relative sliding velocity of the surfaces and  $P$  is the pressure between the surfaces [6]. A plot of the coefficient of a friction (the ratio between the lateral or shear force and the normal force) against this dimensionless parameter is known as the Stribeck diagram as shown in Figure 2. Boundary lubrication occurs when the value of  $ZN/P$  is sufficiently low, corresponding to low relative velocity between the surfaces and/or high nominal pressure between the surfaces. Boundary lubrication conditions are suggested to occur when there is significant solid to solid contact where the lubricants have been squeezed into the valleys, leaving certain points of the solid surface touching one another directly. Hence for boundary lubrication systems, the characteristics of the solid surfaces are generally more important in determining the friction coefficient compared to the properties of the lubricant. At higher speeds and lower pressures, the lubrication system becomes a hydrodynamic lubrication system where the friction coefficient increases with the increase in the dimensionless parameter  $ZN/P$ . This is when there is a steady film of lubricant at all points throughout the surface and there is little or no solid to solid contact. With this, the friction coefficient would be primarily due to the viscous forces of the lubricant, resulting in the slope that can be seen in the Figure 2 [7]. For most of the lubricated surfaces in engine components, the lubricant operates in the said hydrodynamic regime [5]. This fact would be an important factor in the estimation of energy savings later on.

## 2.2 Frictional losses in an engine

The amount of friction in moving parts in an engine depends on many factors. Among the factors which are highly significant are: the engine design, the nature of the lubricant used, and the size of the engine [5, 6].

Generally, larger engines have higher friction than smaller engines, but they tend to have lower friction per engine displacement volume. This is due to the fact that friction is

highly dependent on the contact surface area, and as the volume of an engine increases, its respective surface areas increases with an index of 2/3 of the volume. This ultimately means that the contact surface area of an engine with a fixed design does not increase as quickly as its displacement volume.

For an engine with a given displacement, its friction would also vary with the design. Similar to the argument above, a six cylinder piston would have higher friction than a four cylinder piston. An engine with a high stroke/bore ratio where the mean piston speed of an engine will be higher than a short stroke engine would also tend to have higher friction. An engine with Vee configuration which would have two sets of camshafts would have more friction contributed by the valve train than an inline engine. Similarly, an engine with multiple camshafts would have more friction from the valve train than an engine with a single camshaft.

Lubricants with higher viscosity would also tend to increase the friction in an engine. Since viscous friction is the dominating friction in an engine, the friction in an engine is highly dependent on speed [6]. The common practice in quantifying the amount of friction is by stating it in terms of a mean effective pressure. Mean effective pressure is the amount of work done per engine cycle (not revolution) divided by the displacement volume of an engine. This would enable us to compare the performance of engines irrespective of their sizes. The mean effective pressure can be expressed as [4]:

$$imep = bmep + pmep + fmep + amep \dots\dots(1)$$

In this expression, the indicated mean effective pressure (which is proportional to the net energy produced through the expansion and compression stroke) is the sum of the brake mean effective pressure and all the mean effective pressure losses which occur in an engine. This includes pumping losses, losses to accessories of the engine and losses to the rubbing friction of the engine [4] It has to be calculated how the indicated mean effective pressure can be reduced using the assumptions that nano-lubricants would be able to reduce friction, keeping other factors unaffected. It would then be relatively easy to calculate the fuel savings from this new lubricant. The problem with this calculation is that it is needed to know exactly by how much this new lubricant would decrease the friction in an engine. Since

the friction in an engine consist of many rubbing components, it is difficult to simply put a lump sum to the reduction in friction for the engine as a whole.

Another problem in estimating energy savings from the reduction of friction is that the engine does not run at one specific speed and load. The load and speed varies by many folds and with this, the contribution of rubbing friction to the overall energy usage would vary by a very significant amount too. Table 1 shows the variation of the rubbing friction mean effective pressure with brake mean effective pressure for a 3.2 litre four cylinder SI engine at 1600RPM. The indicated mean effective pressure is the sum of all three mean effective pressures [4]. It can be seen that even though the frictional mean effective pressure increases as load on an engine increases (at a fixed rotational speed), the ratio of friction mean effective pressure to the indicated mean effective pressure drops dramatically. It is expected that at a fixed load, the friction mean effective pressure would increase as the rotational speed increases and hence the portion of indicated mean effective pressure lost to rubbing friction would increase.

Figure 3 shows the variation of friction losses over a range of speed and load. It can be seen that depending on the speed and load, the amount of fuel lost due to friction varies considerably. This variation is more significant in diesel engines where the amount of fuel used to overcome friction can vary from more than 60% to less than 10%. A similar pattern exists for gasoline engines, but the percentage of fuel lost due to friction is rarely above 40% [8].

### 2.3 Estimation of Average Friction Losses

Using the data from Table 1, it can be estimated the average portion of energy lost due to friction in an engine for a particular load and speed. For example, when a vehicle is idling at traffic light, the engine is at a no load situation. At this condition, the ratio of power lost to friction is very high. When a vehicle is cruising at a fixed speed, the speed of the engine would be at mid range for both speed and load, which means that the ratio of power lost to friction would be mediocre. Under a very fast acceleration, or when climbing up a steep slope, the engine would be running very fast and near maximum load which in turn means that the ratio of power lost to friction is considerably lower. Hence, the average ratio of power lost to friction would

vary considerably according to driver, driving location and driving conditions, making an average number difficult to determine unless there is a comprehensive statistical data.

From the data and examples, it is probably safe to estimate the fraction of indicated mean effective pressure lost due to rubbing friction at about 0.20. From this point on, calculations would be based on this assumption where overall, 20 percent of power generated in an engine is lost due to rubbing friction.

### 3.0 Studies Done on Friction Reduction by Nano-Additives in Lubricants

#### 3.1 Fullerene additive in mineral oil

In an experiment conducted by Lee et al; [9], a spinning disc-on-disc tester was used to evaluate the lubricating performance of mineral oil with varying amount of fullerene as an additive. Results showed that the friction coefficient decreases with increasing percentage of fullerene added. Authors found that the friction coefficient of mineral oil with 0.1 and 0.5 volume percent of fullerene is significantly lower than the pure mineral oil as can be seen in the Figure 4.

In this experimental work, the discs were rotated at a fixed speed of 1000 rpm, with normal forces between 50N and 1000N acting between the discs. With these parameters, a Stribeck diagram as shown in Figure 5.

Most lubricated surfaces in engines are in the hydrodynamic region [6]. This fact would allow one to simplify the calculations on friction reduction. The Stribeck diagram in Figure 5 shows that in the hydrodynamic region, the friction coefficient of mineral oil added with 0.1 volume percent fullerene is about 0.005 while the friction coefficient for the raw mineral oil is 0.02.

This shows that for this experiment, in the hydrodynamic lubrication region the reduction of friction coefficient for a mineral oil with 0.1 volume percent of fullerene is 75 percent.

#### 3.2 Onion like fullerene additive

In a separate research, onion-like fullerenes (OLFs) were added to a commercial lubrication oil with grade 15 W/40. These additives were dispersed in the base oil with an ultrasonic vibrator. The size of OLFs added was measured

to be 20 – 30 nm. The friction coefficient of these lubricant samples were then measured using a four ball type tribometer at the rate of 2003 RPM for 30 minutes under varying loads. In this study, it is seen that friction coefficient for a lubricant can be lowered by the addition of nano-particles (in this case OLFs) from 0.12 for the pure lubricant to as low as 0.07. This shows a potential reduction of 42% reduction given the right amount of OLF added. This study also shows wear reduction on the metal surfaces when OLFs were added to the lubricant. Figure 6 demonstrates the friction results from this study [10].

#### 3.3 Nano-diamond additive

In a separate research, nano-diamonds were used as an additive in a Mobil commercial lubricant. The average size of these nano-diamonds is 20 nm. The amount of nano-diamond added was 0.5 mg/liter. The lubricant was then tested with mild steel contact pairs and aluminium contact pairs. Among the measurements carried out was the initial friction force, the dynamic friction coefficient and the surface roughness of the contact surface after a wear test. Table 2 summarizes these results. It can be seen that for the mild steel samples, the friction coefficient and initial friction force decreased with the usage of the nano-enhanced lubricant, while for the aluminium sample, both the friction coefficient and initial friction force increased with the usage of the nano-enhanced lubricants. However, the surface wear of the mild steel samples degraded with the usage of the nano-enhanced lubricants [11].

#### 3.4 CuO, TiO<sub>2</sub> and diamond nano-particles as additives

In a research conducted in year 2006, CuO, TiO<sub>2</sub> and diamond nano-particles were added into two standard lubricating oils. One of the lubricating oil has anti wear and friction reduction additives already added to it by the manufacturer (this oil will henceforth be known as SF oil). The other lubricating oil has similar viscosity grade with the SF oil but it does not have anti wear and friction reducing additives to it (this oil will henceforth be known as base oil). Both of these lubricating oil were added with 0.1 weight percent CuO, TiO<sub>2</sub> or nano-diamonds. There are a total of 8 samples including both the pure lubricating oil sample. The dynamic friction

coefficients of these samples were then measured at varying temperatures. Figure 7 shows the results from this study. It can be seen that these nano-additives generally lower the friction coefficient for both lubricating oil. This is especially true with the nano-CuO additives. The Figure 7 shows an 18 percent friction reduction for the SF oil sample with CuO nanoparticles and an 8 percent friction reduction for the base lubricant. This study also shows a significant improvement in wear resistance for the lubricant enhanced with nano-CuO [12].

#### 4.0 Estimation of Energy Savings by Nano-Lubricants

Based on earlier studies available in the literatures, it has been found that the magnitude of friction reduction by having nano-additives in lubricants depend largely on the measurement conditions. In a vehicle's engine, the speed and load experienced by the engine varies significantly during the operation. This would in turn mean that the amount of friction reduction by having nano-additives would vary accordingly. Table 3 summarizes the findings of different nano-lubricants to reduce friction coefficient. Throughout these studies, it has been observed the improvement in friction reduction.

The amount of fuel that could be saved by using nano-additives in the lubricants could be expressed by the following formula:

$$Q_{\text{saved}} = Q_{\text{initial}} \times f_{\text{friction}} \times f_{\text{enhancement}} \dots (2)$$

where;

$Q_{\text{saved}}$  is the amount of fuel saved by using nano-additive in the lubricant

$Q_{\text{initial}}$  is the amount of fuel used in an ordinary lubricant

$f_{\text{friction}}$  is the average fraction of energy generated by an engine lost to rubbing friction

$f_{\text{enhancement}}$  is the average fraction of friction reduction provided by the nano-additive

It has been observed in various studies on the friction reduction by using nano-additives. These studies showed varying degrees of friction reduction, depending on the load, speed and temperature. In order to simplify the estimation, an average friction loss of 0.25 is assumed for this analysis. Based on previous work, it can be assumed that about 75% of average friction losses can be reduced.

With these assumptions, the fraction of fuel that can be saved as:

$$\frac{Q_{\text{saved}}}{Q_{\text{initial}}} = f_{\text{friction}} \times f_{\text{enhancement}} = 0.04 = 4\%$$

Using the data in Table 4 energy savings has been projected for a period of 12 years (2009-2020) and shown in the same table. It has been estimated that cumulative amount of 11,943 ktOE energy can be saved even with this 4% energy savings. It may be mentioned that this savings has been shown only for Malaysian transportation sector. If global transportation sectors are combined, huge amount of energy can be saved. Moreover, significant amount of emission can be reduced by not burning the amount that can be saved with the application of nano-lubricants.

#### 5.0 Conclusion

The fraction of energy lost due to friction in an engine varies from approximately 10% to 40%, depending on the load, speed and characteristics of the engine. Studies have shown that up to 75% of the friction can be reduced with the addition of nano-particles in the lubricants. This friction reduction is often accompanied by a reduction in wear of the contacting surfaces as well. Assuming that on an average about 25% of an engine's power goes in overcoming friction and that the usage of nano-additives in lubricants can provide an average value of 75% of the power can be reduced. This will consequently saving about 4% of total fuel used in an engine. If the savings for total transportation sector is accumulated, about 11,943 ktOE can be saved along with protecting environment from different pollutants. Nanotechnology is an emerging technology that has been applied in many energy related areas to reduce energy use, to improve heat transfer and so on. However, it has to bear in mind that there are challenges such as cost, health; environmental risks and so on must be tackled.

#### References

- [1] Anon, 2008, Automobile industry introduction, online, retrieved 5<sup>th</sup> December 2008, from <http://www.plunkettresearch.com/Industry/AutomobilesTrucks/AutomobileTrends/tabid/89/Default.aspx>.
- [2] Tarasov S., Kolubaev A., Belyaev S., Lerner M., Tepper F., 2002, Study of

- friction reduction by nanocopper additives to motor oil, *Wear* 252, 63–69
- [3] Sheng-shan Bi, Lin Shi, Li-li Zhang, 2008, Application of nanoparticles in domestic refrigerators, *Applied Thermal Engineering* 28, 1834–1843
- [4] Heywood, J. B., 1988, Internal combustion engine fundamentals, International edition, *McGraw-Hill*, Singapore.
- [5] Garrett, T.K., Newton, K. and Steeds, W. 2001, *The motor vehicle*, 13<sup>th</sup> edition, Reed educational and professional publishing, Jordon Hill, Oxford.
- [6] Challen, B. and Baranescu, R. (eds) 1999, *Diesel engine reference book*, 2<sup>nd</sup> edition, Reed educational and professional publishing, Jordon Hill, Oxford
- [7] Müser, M.H. 2006, Theory and simulation of friction and lubrication, *Lecture notes in physics*, vol. 704, Springer Verlag, Berlin.
- [8] Hoshi, M. 1984, Reducing friction losses in automobile engine. *Tribology international*. 17(4): 184 – 189
- [9] Lee, J., Cho, S., Hwang, Y., Lee, C. and Kim, S.H. 2007, Enhancement of lubrication properties of nano-oil by controlling the amount of fullerene nanoparticle additives. *Tribology letter* (2007). 28: 203 – 208.
- [10] Yao, Y., Wang, X., Guo, J., Yang, X. and Xu, B. 2008, Tribological properties of onion-like fullerenes as lubricant additives. *Materials letter* (2008). 68: 2524 – 2527.
- [11] Chou, C.C. and Lee, S.H. 2008, Rheological behaviour and tribological performance of a nanodiamond-dispersed lubricant. *Journal of materials processing technology* (2008). 201: 542 – 547
- [12] Wu, Y.Y, Tsui, W.C. and Liu, T.C. 2007, Experimental analysis of tribological properties of lubricating oils with nanoparticle additives. *Wear* (2007). 262: 819 – 825.
- [13] National Energy Balance, (2008). *Ministry of Energy, Communications and Multimedia*, Kuala Lumpur, Malaysia.

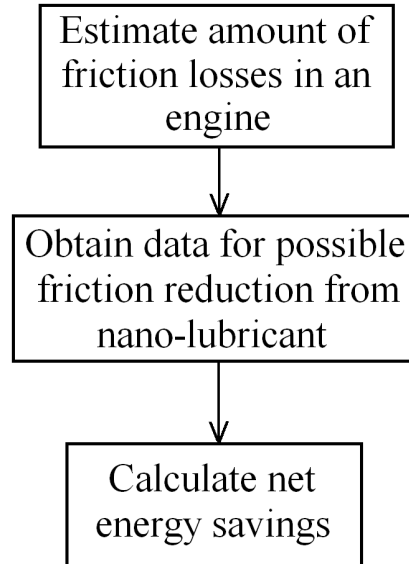


Fig.1. Direction of present research

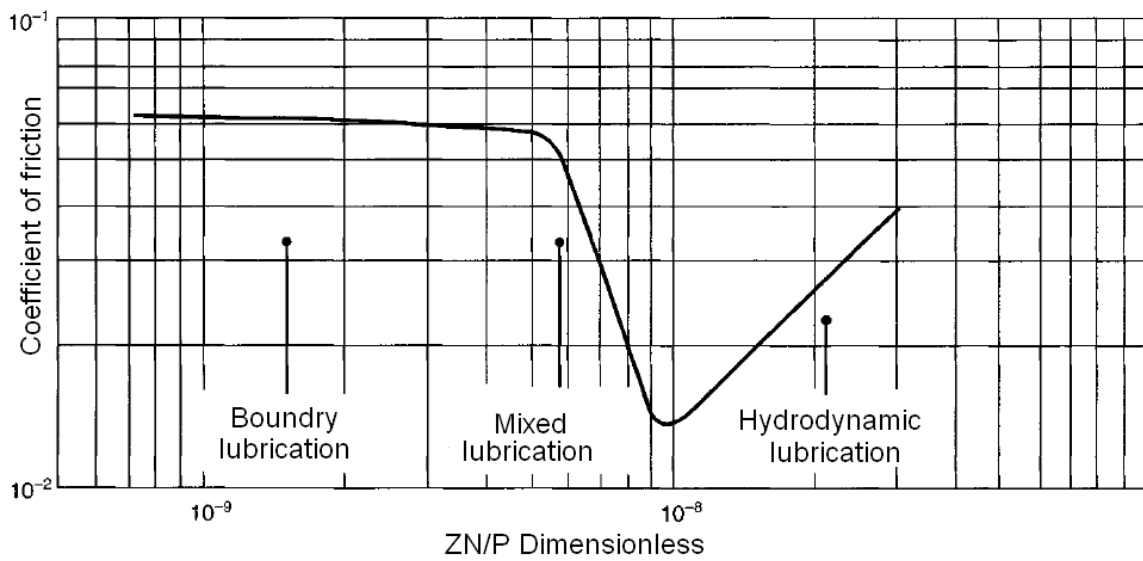
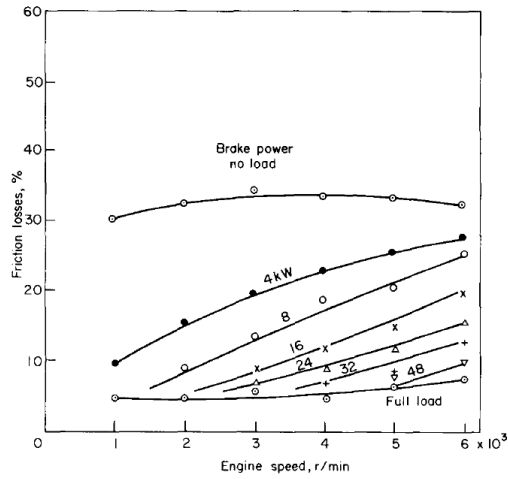
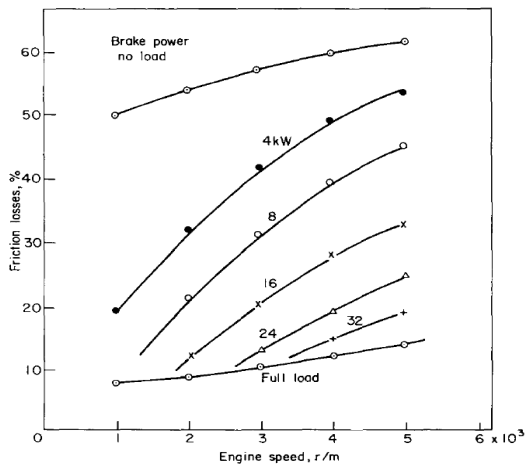


Fig.2. Stribeck diagram example [7]



(a)



(b)

Fig.3. Variation of fractional friction loss with speed and load (a) gasoline engine (b) diesel engine [8]

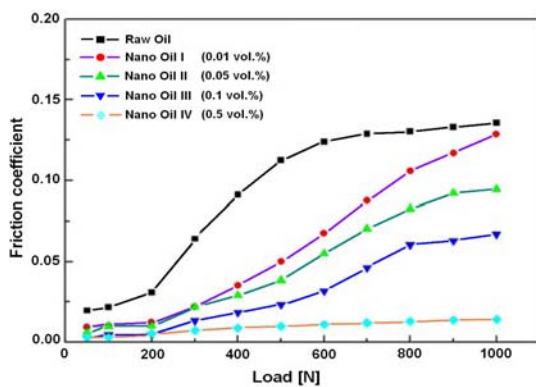


Fig.4. Variation of friction coefficient with load for different oil samples [9]

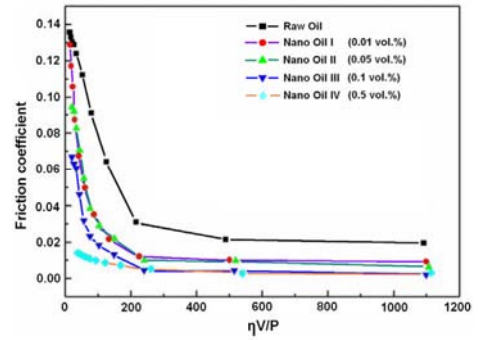


Fig.5. Stribeck diagram of oil samples with different amounts of fullerene additive [9]

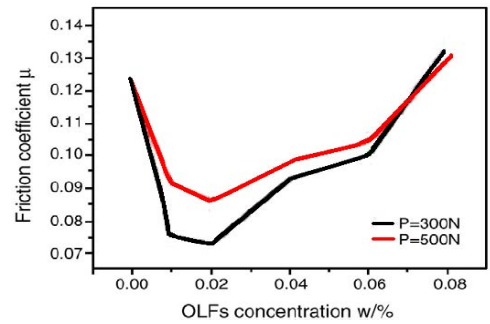
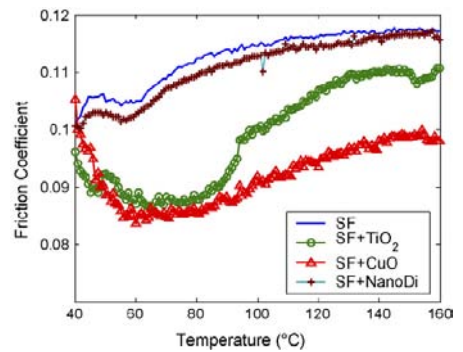
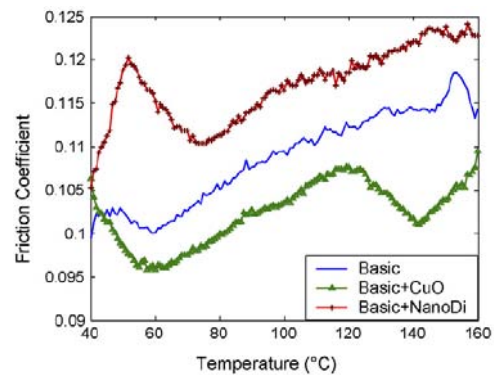


Fig.6. Variation of friction coefficient with onion-like fullerene concentration [10]



(a)



(b)

Fig.7. Variation of friction coefficient with temperature for different oil samples [12]

**Table 1 Variation of mean effective pressures with load [4]**

Brake MEP	Mean effective pressure (kPa)		Friction MEP/ Indicated MEP
	Friction MEP	Pumping MEP	
25	100	80	0.488
220	105	60	0.273
450	110	50	0.180
770	145	30	0.153
950	170	25	0.148

**Table 2 Result for experiments conducted with nano-diamond enhanced lubricant [11]**

Sample material	Percentage change in measured quantity compared to pure lubricant		
	Initial friction force	Friction coefficient	Surface roughness
AISI1025 Mild steel	-7.20	-11	+27
AISI1045 Mild steel	-7.50	-13	+23
6061 Aluminium alloy	+7.64	+6.1	-15

**Table 3 Summary of nano-lubricant findings [9, 11, 12]**

Additive type	Coefficient of friction reduction (%)	Enhancement in anti-wear properties	Comments
Fullerene additive	75	Yes	Friction reduction taken at hydrodynamic lubrication region
Onion-like Fullerene (OLFs)	42	Yes	Maximum friction reduction obtained in study
Nano-diamond	13	No	Friction reduction with AISI1045 mild steel
CuO nanoparticle	18	Yes	Maximum friction reduction obtained in study

**Table 4 Energy savings with the application of different nano-additives**

Additive type	Reduction in engine energy used (%)
Fullerene additive	15
Onion-like Fullerene (OLFs)	8.4
Nano-diamond	2.6
CuO nanoparticle	3.6

**Table 5 Energy consumption pattern of transportation sector based on fuel types**

Year	Total transportation energy used	*Energy savings (ktoe) for			
		2.60%	3.60%	8.40%	15%
2009	20,374	530	733	1,711	3,056
2010	21,193	551	763	1,780	3,179
2011	22,013	572	792	1,849	3,302
2012	22,832	594	822	1,918	3,425
2013	23,652	615	851	1,987	3,548
2014	24,471	636	881	2,056	3,671
2015	25,291	658	910	2,124	3,794
2016	26,110	679	940	2,193	3,917
2017	26,930	700	969	2,262	4,039
2018	27,749	721	999	2,331	4,162
2019	28,569	743	1028	2,400	4,285
2020	29,388	764	1058	2,469	4,408
Total		7,763	10,748	25,080	44,785

**Source:** National Energy Balance [13], \*Author's calculation

## DESIGNING MATERIALS AGAINST WEAR FOR ORTHOPEDIC BIOENGINEERING SYSTEMS

**Zainul Huda**

Department of Mechanical Engineering  
University of Malaya  
Kuala Lumpur  
Malaysia

Tel: 03-79674593; Email: [drzainulhuda@hotmail.com](mailto:drzainulhuda@hotmail.com)

### Abstract

*Wear resistance is the most important property of a bearing material. This review paper highlights application of tribological principle to design materials for application in orthopedic bioengineering systems with particular reference to Artificial Total Hip Replacement. It has been established that substantially different alloys should be used for minimizing wear in bearing surfaces. Frictional forces at these rubbing counter-faces must be minimized to prevent loosening of the femoral stem and acetabular socket assembly from their positions secured by the fixation agent. A comparative analysis of various wear-resistant biomaterials resulted in the lowest production of wear particles in a total hip where a ceramic socket articulates against the ceramic ball; it produces only 0.004 cubic millimeters of ceramic wear particles. Surface modification, through the application of coatings, offers the potential to reduce the wear rate without compromising the bulk mechanical behavior of the implant material. These hard coatings were found to include diamond-like carbon, amorphous diamond, and titanium nitride.*

**Keyword:** Wear, tribology, orthopedic bioengineering system, artificial total hip replacement

### 1. Introduction

Wear is recognized as one of the major causes of failures in automotive, engineering, and biomaterials [1-4]. It is, therefore, extremely important to design materials and systems against wear for engineering and biological applications (e.g. orthopedic bioengineering system). Many factors may be considered for improving the wear resistance of materials. Designing components so that loads are small and surfaces are smooth, and continual lubrication help to prevent wear [5]. As wear is a surface or near surface phenomenon it has long been realized that the wear resistance of a component can also be improved by providing a surface of different composition from the bulk material.

Resistance to wear is the most important property of a bearing material [6, 7]. Normal tribological considerations in the engineering of bearing surfaces preclude using two exactly similar metals, or more correctly, alloys. Depending on the lubrication regime, one of the

major factors that determine the tendency towards high friction and high wear rates is the affinity that the two surfaces have for each other [8-10]. Two identical metals, in contact and under pressure, will have greater affinity; the force of attraction requires greater forces to produce sliding movement (that is, higher friction) and there is a greater tendency to generate wear particles [11, 12]. This problem can be overcome by using different alloys as bearing surfaces for orthopedic bioengineering applications; and is discussed in the subsequent section.

### 2. Application of Tribological Principle to Orthopedic Bioengineering

Having established in the preceding introductory section that two identical metals have greater tendency to generate wear particles, we now apply tribological principle to solve the problem. First principles in tribology state that substantially different alloys should be used for

minimizing wear; this statement is justified since before the 1960s often one surface was chosen as a relatively soft material bearing against a much harder one. This led to the development of families of alloys designed specifically to be bearing surfaces, for example, a range of bronzes was developed [13]. However, this solution was not available to the orthopaedic bioengineer, because of the problems of corrosion that would occur when dissimilar metals were in contact within the fluids of the human body. The only alternative was to use similar metals, but to select the hardest and the most corrosion resistant of them. The usual choice was a cobalt–chromium–nickel alloy [14]. It was at this point that the biological arguments started to arise. Cobalt, chromium and nickel were not deemed to be the most appropriate. Although they could be considered to be essential minor trace elements with specific biological functions, they could also induce adverse effects, locally or systemically, especially in view of their potential proinflammatory and prohypersensitivity character [15]. Although clinical follow up showed that many hip replacements worked extremely well and without any problems whatsoever (indeed many surgeons considered them to be superior to the Charnley prosthesis), the number of patients who experienced significant tissue reactions meant that the devices fell into disrepute.

### 3. Material Requirements for Artificial Total Hip Replacement

The artificial total hip replacement is a typical interesting situation in which wear and corrosion are important considerations in materials selection. The human hip joint (see Fig 1) occurs at the junction between the pelvis and the upper leg (thigh) bone, or femur. A relatively large range of rotary motion is permitted at the hip by a ball-and-socket type of joint; the top of the femur terminates in a ball-shaped head that fits into a cup-like cavity within the pelvis.

As illustrated in Fig 1, hip is a ball-and-socket joint uniting two separate bones – the thighbone, or femur, and the pelvis. The pelvis features two cup-shaped depressions called sockets or acetabulum. One is on either side of the body. The thighbone is the longest bone in the body and connects into the pelvis at the hip joint. The head of the thighbone is shaped like a

ball and fits tightly into the socket, forming the ball-and-socket joint of the hip.

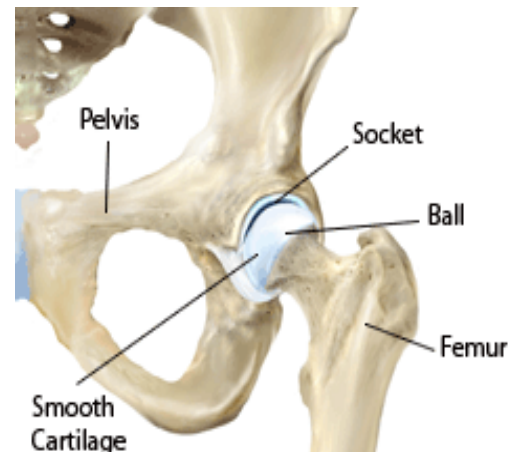


Fig 1: Hip anatomy

Wear plays an important role in ball-and-socket joint in the human hip. In the hip, femur provides the 'ball' whereas the pelvis, or hip bone, provides the socket [15]. Figure 2 shows a ball-and-socket joint; which allows a circular movement in the human hip joint. Since the ball-and-socket articulating surfaces rub against one another, wear of these surfaces can be minimized by the employment of very hard and wear-resistant materials (e.g. Co-Ni-Cr-Mo alloys, high-purity polycrystalline aluminum oxide, etc). Excessive and uneven wear can lead to deterioration of articulating surfaces and cause the prostheses to malfunction. In addition, particulate debris will be generated as the articulating surfaces wear against one another; which may cause damage to bone tissues [16].



Fig 2: A ball-and-socket joint in the human hip.

Frictional forces at these rubbing counter-faces must be minimized to prevent loosening of the femoral stem and acetabular socket assembly from their positions secured by the fixation agent.

#### 4. Material Selection for Artificial Total Hip Replacement

Early prosthetic hip designs called for both the femoral stem and ball (see Figs 1-2) to be made of same material --- a stainless steel; however, stainless steel is susceptible to pitting corrosion and has low fatigue strength. Hence, current applications involve improved materials as well as construction of the stem and ball from different materials (combination of materials). In a *total hip joint* there are these possible combinations of bearing materials for joint surfaces: (1) Polyethylene sockets may be coupled with metallic or ceramic balls [17], (2) Metallic sockets may be coupled with metallic balls, and (3) Ceramic sockets may couple with ceramic balls.

The femoral stem and ball are normally made of a cold-worked 316L stainless steel, a hot-forged Co-Ni-Cr-Mo alloy, or a hot-forged titanium alloy. Various Co-Cr-Mo and Co-Ni-Cr-Mo alloys have been used for artificial hip prostheses; one of them is MP35N whose chemical composition is given in Table 1.

**Table 1: Composition of MP35N alloy used in artificial hip prostheses**

Element	Co	Ni	Cr	Mo
wt %	35	35	20	10

The MP35N alloy has been found to be especially suitable for application in artificial hip prostheses due to its excellent resistance to wear, corrosion and fatigue. Of those metal alloys that are implanted for prostheses hip joint, probably the most biocompatible is the titanium alloy Ti-6Al-4V; its composition is 90 wt% Ti, 6 wt% Al, and 4 wt % V. The properties of this alloy along with other Co-Ni-Cr-Mo alloys are given in Table 2.

**Table 2: Mechanical and Corrosion Characteristics of Alloys used in Prosthetic Hip**

Alloy	Elastic Modulus (GPa)	Yield strength (MPa)	Tensile Strength (MPa)	Elongation at fracture (%)	Fatigue strength (MPa)	Corrosion Rate (0.001 in./yr)
316L stainless steel	196	700	875	12	383	0.001-0.002
MP35N	230	1000	1200	13	500	0.0012-0.002
Ti-6Al-4V	120	950	1075	13	580	0.007-0.04

It is evident from Table 2 that 316L stainless steel, Co-Ni-Cr-Mo alloy, and titanium alloy have excellent mechanical properties and corrosion-resistance; however their wear resistance behavior is only fair. Recent improvements for femoral stem and ball device include using a ceramic material --- high-purity polycrystalline aluminum oxide; which is harder and more wear-resistant. However, the fracture toughness of alumina is relatively low and its fatigue characteristics are poor. Hence, femoral stem, being subjected to significant stress levels, should be still fabricated by the alloys mentioned in Table 2.

Figure 3 shows a comparative column chart for wear rates for various combinations of bearing material surfaces for total hips. It

is evident from Fig 3 that different bearing surface combinations produce different amount of wear particles (measured as cubic millimeters per year). The worst "shedder" of wear particles

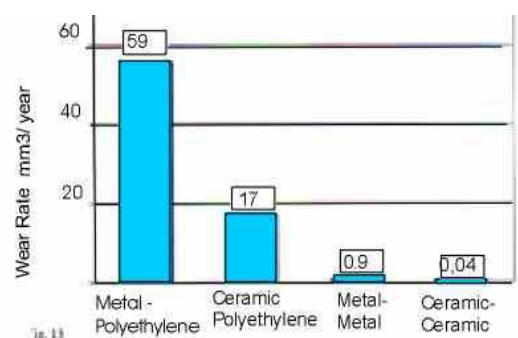


**Fig 3: Wear rate in combinations of bearing material surfaces for total hips**

is a total hip where the socket made from conventional ultra-high molecular weight polyethylene (UHMWPE) articulates against a metallic ball component. Such combination produces (when tested in hip simulator) 56 cubic millimeters of UHMWPE wear particles. The lowest production of wear particles has a total hip where a ceramic socket articulates against the ceramic ball; it produces only 0.004 cubic millimeters of ceramic wear particles [17].

Wear particle-induced aseptic loosening of hip replacement prostheses remains a major cause of revision surgeries for the commonly used metal/ultra-high molecular weight polyethylene (UHMWPE) [18], and metal/metal articulating pair configurations [19]. In addition to osteolytic loosening, metal/metal articulations are plagued by concerns of electrochemical corrosion and carcinogenesis, owing to the dissemination of wear particles to other parts of the body [19, 20]. Surface modification, through the application of coatings, offers the potential to reduce the wear rate without compromising the bulk mechanical behavior of the implant material. A variety of hard coatings have been investigated in the past for metallic bearing surfaces (for a comprehensive review, see Ref. [21]); examples include diamond-like carbon [22-26], amorphous diamond [27], and titanium nitride [26].

## 5. Summary and Recommendations

Tribological principle has been applied to design materials for application in orthopedic bioengineering systems. It has been established that substantially different alloys should be used for minimizing wear in bearing surfaces. Wear was found to play an important role in ball-and-socket joint in the human hip. Wear of these surfaces can be minimized by the employment of very hard and wear-resistant materials (e.g. Co-Ni-Cr-Mo alloys, high-purity polycrystalline aluminum oxide, etc). A comparative analysis of various wear-resistant biomaterials resulted in the lowest production of wear particles in a total hip where a ceramic socket articulates against the ceramic ball; it produces only 0.004 cubic millimeters of ceramic wear particles. Surface modification, through the application of coatings, offers the potential to reduce the wear rate without compromising the bulk mechanical behavior of the implant material. A variety of hard coatings have been investigated for metallic bearing surfaces; examples include diamond-like

carbon, amorphous diamond, and titanium nitride.

## References

- [1] Huda, Z., Shi, K.W. and Bulpett, R.; Failure Analysis of a Steel Motor-Cycle-Stand; *Journal of Failure Analysis and Prevention*, Aug 2009, **ASM International**, USA
- [2] Roe, M.; Torrance, A.A.; *The surface failure and wear of graphite seals; Tribology International*, Vol. 41(11), 2008, pp 1102-1008
- [3] Zhou, G., Li, X., Yaowu Shi, Y., Chang, B; *Wear mechanism of clutch separating ring in a heavy load vehicle, Engineering Failure Analysis*, Vol. 13(4), 2006, pp 606-614.
- [4] Pavoov, P.P, Gearing, P.G., Muratoglu, O., Cohen, R.E, and Anuj Bellare, A.; Wear reduction of orthopaedic bearing surfaces using polyelectrolyte multilayer nanocoatings, *Biomaterials*, Vol. 27(8), 2006, pp 1527-1533
- [5] Askeland , D.R. and Phule, P.P.; *The Science and Engineering of Materials*, Thomson Books, USA
- [6] Goudarzi, M.M., Jahromi, S.A.J., and Nazarboland, A.; Investigation of characteristics of tin-based white metals as a bearing material; *Materials and Design*, Vol. 30(6), 2009, pp 2283-2288
- [7] Lapper K, James M, Chashechkina J, Rigney D.A., Sliding behavior of selected aluminum alloys. *Wear*; Vol. 203–204, 1997, pp: 46–56
- [8] Rigney DA; *Fundamentals of friction and wear of materials*. Metals Park, OH: American Society for Metals; p. 43–69, 1981
- [9] Zeren A, Feyzullahoylu E, Zeren M.; A study on tribological behavior of tin based bearing material in dry sliding, *Materials and Design*, Vol. 28, 2007, pp 318–23.
- [10] Pratt G.C.; *Materials for plain bearings*; *Int Metall Rev*, Vol. 8, 1973, pp 62–68
- [11] Kingsbury R., *Metals Handbook*, 9th Ed., Vol. 3. Metals Park, OH: ASM International; pp 802–822, 1980
- [12] Booser E, Khorasani M; *Applied tribology bearing design and lubrication*; John Wiley, New York, 2001

- [13] Barry BTK, Thwaites CJ.; Tin and its alloys and compounds; Ellis Wood, UK, 1983
- [14] Massalski T.B., Binary alloy phase diagrams. Metals Park, OH: American Society for Metals, USA, 1982
- [15] Williams, D.F. (Editor); Biocompatibility of Orthopedic Implants, Vol. 1, Franklin Book Company, PA, USA, 1982
- [16] Gibbons, D.F. (1982); Materials for Orthopedic Joint Prostheses, Ch 4, p 116; In Williams, D.F. (Editor); Biocompatibility of Orthopedic Implants, Vol. 1, Franklin Book Company, PA, USA
- [17] Heisel H. et al.: J Bone Joint Surg-Am 2003; 85-A: pp 1366- 79
- [18] Kurtz, S.M., Muratoglu, O.K., Evans, M., and Edidin, A.A.; Advances in the processing, sterilization, and cross-linking of ultra-high molecular weight polyethylene for total joint arthroplasty, *Biomaterials* Vol. **20**, 1999, pp 1659–1688
- [19] Savarino, L., Granchi, D., Ciapetti, G., Cenni, E., Pantoli, A.N., and Rotini, R. *et al.*, *J Biomed Mater Res (Appl Biomater)* Vol. **63**, 2002, pp 467–474
- [20] Ingham, E. and Fisher, J. (2000); Biological reactions to wear debris in total joint replacement, *Proc Inst Mech Eng Part H—J Eng Med* Vol. **214** (H1): pp. 21–37
- [21] Dearnley, P.A., A review of metallic, ceramic and surface-treated metals used for bearing surfaces in human joint replacements, *Proc Inst Mech Eng Part H—J Eng Med* **213** (H), 1999, pp 107–135
- [22] Hauert, R.; A review of modified DLC coatings for biological applications, *Diamond Relat Mater* Vol. **12**, 2003, pp 583–589
- [23] Platon, F., Fournier, P., and Rouxel, S.; Tribological behavior of DLC coatings compared to different materials used in hip joint prostheses, *Wear*, **250**, 2001, pp 227–236
- [24] Saikko, V., Ahlroos, T., Calonijs, O., and Keranen, J; Wear simulation of total hip prostheses with polyethylene against CoCr, alumina and diamond-like carbon, *Biomaterials* Vol. **22**, 2001, pp 1507–1514.
- [25] Kiuru, M., Alakoski, E., Tiainen, V., Lappalainen, R., and Anttila, A.; Tantalum as a buffer layer in diamond-like carbon coated artificial hip joints, *J Biomed Mater Res Part B: Appl Biomater* **66B**, 2003, pp 425–428.
- [26] Onate, J.I., Comin, M., Bracerias, I., Garcia, A., Viviente, J.L., and Brizuela, M. *et al.*, Wear reduction effect on ultra-high-molecular-weight polyethylene by application of hard coatings and ion implantation on cobalt chromium alloy, as measured in a knee wear simulation machine, *Surf Coat Technol*, Vol. 142–144: 2001, pp 1056–1062.
- [27] Lappalainen, R., Selenius, M., Anttila, A., Kontinen, Y.T., and Santavirta, S.S., Reduction of wear in total hip replacement prostheses by amorphous diamond coatings, *J Biomed Mater Res Part B: Appl Biomater* Vol. **66B**, 2003, pp 410–413

## WEAR STUDY OF COATED/ UNCOATED HIGH SPEED STEEL ON NI-RESIST CAST IRON USING THE COMBINATION OF IONIC LIQUID AND VEGETABLE OIL-BASED LUBRICANT

M. Husnawan<sup>1\*</sup>, M.A. Sattar<sup>2</sup>, M.G. Saifullah<sup>2</sup>, H.H. Masjuki<sup>2</sup>, T.M.I. Mahlia<sup>2</sup>

<sup>1</sup>Department of Mechanical Engineering, Syiah Kuala University  
Jl. S. Abd. Rauf, No.7- Darussalam, Banda Aceh, Indonesia

<sup>2</sup>Department of Mechanical Engineering, University of Malaya  
50603 Kuala Lumpur, Malaysia

Corresponding Author: email: [m.husnawan@gmail.com](mailto:m.husnawan@gmail.com)

### Abstract

*Mechanical operations such as in the internal combustion engine require robust conditions especially gas engines where it can achieve high combustion temperatures. Materials for pistons rings and cylinder liners are carefully selected to withstand high combustion temperatures and severe wear and friction operation. Surface treatments by applying coats of chromium and DLC to the base material introduce protection to wear, fatigue and corrosion. In this experimental study, high speed steel is simulated as the piston rings and Ni-resist cast iron as the cylinder liner. A tribology study on the effects of bio-lubricant based palm oil combined with 1,3-diethyl imidazolium diethylphosphate on uncoated/coated high speed steel on Ni-resist Cast Iron was carried out using the Reciprocatory Friction Monitoring Machine. The experimental conditions were as follows; normal loads from 10N to 100N, sliding speed was 2000 rpm, with test duration of 30 minutes, approximately 240 meters of sliding distance, room temperature of 30°C and the test temperature of 150°C. The wear and friction curves were plotted and discussed. Used oil samples were checked for ferrous metal debris using the PQ/PQ90A dual-coil magnetometer.*

**Keywords:** Palm Oil, Ionic Liquid, High Speed Steel, Ni-resist Cast Iron, Tribology,

### 1. Introduction

Mineral oils have been dominated the lubricant market since its introduction. But due to growing worldwide interest in environmental issues, the trend is biodegradable lubricant so vegetable oil is a promising candidate. Vegetable oils have been used as substitute for mineral based oil due to their natural biodegradability, non-toxicity and excellent lubricity [1]. But when viewed from a different perspective, vegetable oils still have major limitations such as high and fluctuating prices, thermal and oxidation instability, and low temperature problem [2]. These limitations are sometimes improved with additives. But the mixing of additives is only justified if the additives are biodegradable and non-toxic when considering producing a biodegradable

lubricant. Currently additives on the market such as ZDDP, TCP and some other additives contains several active elements such as S, P, N or some other heavy metal elements [3-5]. So in a fundamental study for investigating biodegradable lubricants it is best to not to introduce additive mixing for it is hard to find biodegradable and non-toxic additives on the current local market. Nonetheless, the current local scene for biodegradable lubricants is still under researched and a simple study using vegetable oil such as palm oil should be sufficient and steps to improve it can be taken from this study. Moreover, this study also emphasis on the use of ionic liquid since this type of liquid shown rapid progress in terms of usage and found become suitable as lubricant. Currently, most of the ionic liquid lubricants have been studied which consist of midazolam

alkyl cation and hexafluorophosphate or tetrafluoroborate root anions [6-8]. Although such ionic liquids show good anti-wear and lubricating properties, their application has been extremely limited due to the corrosion issue to metal pairs, which was caused by the hydrolysis of the anions to form phosphoric acid or boric acid in the presence of water and release of hydrogen fluoride. As one of the most used additives of lubricating oil [6], phosphate can be used to make an ionic liquid possessing both excellent lubrication/anti-wear characteristics and no corrosion issue to metallic friction pairs if phosphate could be modified by being coordinated with some cations that cannot be easily hydrolyzed. Inspired by this idea, a series of ionic liquids consisting of vegetable oil-based lubricant and alkyimidazolium cation were synthesized, and the tribological properties of these ionic liquids as lubricants were studied as well.

## 2. Experimental Details

### 2.1 Test Apparatus

Wear tests were carried out on a wear and friction monitoring machine using a pin on plate configuration as shown in Fig. 1.

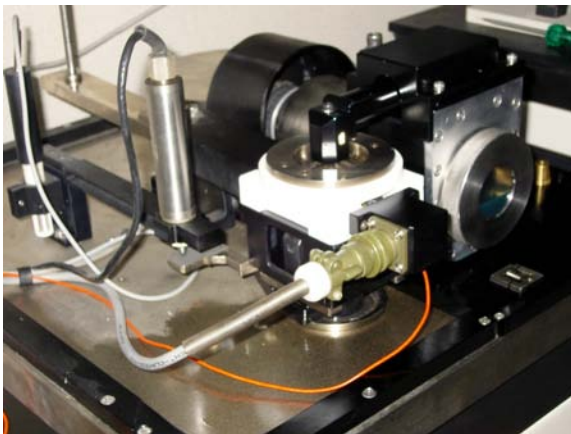


Fig. 1 Wear machine configuration

The pin material used is based from ASTM A600 high speed tool steel (HSS). The plate material used is ASTM A439 Ni-resist austenitic ductile cast iron. On-line measurements were made in the course of each test, including oil bath temperature, instantaneous friction force, coefficient of friction and wear from the sliding pair. Results are measured via a PC linked to the machine and displayed by the software.

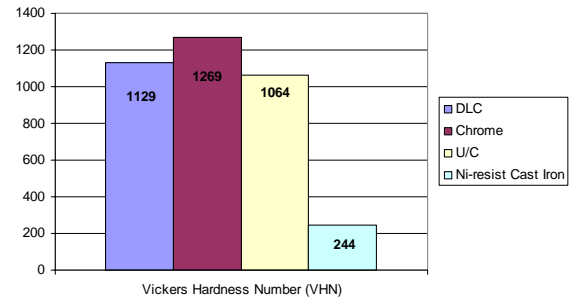


Fig. 2 Vickers Hardness Number for all material samples at 10kgf

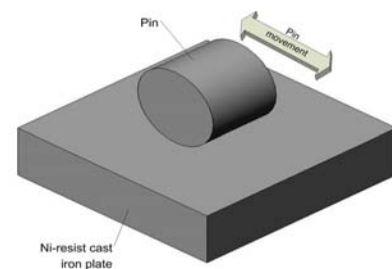


Fig. 3 Schematic diagram of the pin on disk apparatus.

### 2.2 Test method

The test conditions are as follows; load, 10 – 100N; temperature, 150°C; sliding velocity, 0.13m/s; frequency, 33.3 Hz; stroke length, 2mm; test duration, 30 minutes. This all adds to approximately 240 meters of sliding distance. Before and after each test, specimens are weighted to determined weight and mass loss. Upon completion of each test, specimens were cleaned and prepared for scanning electron microscopy (SEM). Used oil samples of each test were collected for checking ferrous metal debris using PQ/PQ90A dual-coil magnetometer.

### 2.3 Lubricant

In this investigation a type of ionic liquid namely alkyimidazolium diethyl phosphates ionic has been synthesized by Great Wall Oil Company and Palm Polyol was produced by Advance Oleochemical Technologies Development-MPOB were mixed stoichiometrically as lubricant base oil. There are no additional additive was used in this study in order to get fully information on wear behaviour of this base oil and its effect on coated/uncoated material.

The molecular structure of ionic liquid and key properties of base oil sample is showed in Fig.4 and Table.1 respectively.

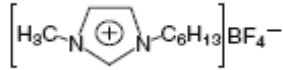


Fig.4 Molecular structures of Alkylimidazolium Diethyl Phosphates ionic liquids

Table.1 Key properties of oil sample

Properties	Ionic Liquid	50%w Ionic Liquid + 50%w Palm Polyol
Kinematic Viscosity (mm <sup>2</sup> /s)		
40 °C	137.8	188.4
100 °C	16.6	70.25
Viscosity index	129	120
Density(kg/m <sup>3</sup> )	1148	1244
Appearance	Light Brown	Yellowish

### 3. Results and discussions

#### 3.1 Effects of load on wear rate and COF

Wear measurements were carried out using a linearly variable differential transformer (LVDT). Wear rates, calculated from the LVDT measurements, are shown in Fig. 5, as a function of the loads used in the tests.

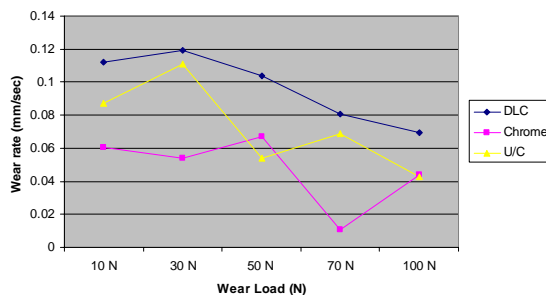


Fig 5. Wear rate (mm/sec) vs. load (N) for all samples

Fig. 5 shows higher wear rates in when using small loads (10N and 30N) compared to higher loads (etc 70, 100N). The only explanation to come up with is that with higher loads there is more pressure on the lubricant which leads to less viscous shear losses in the lubricant film. Viscous shearing will help to build up sufficiently thick film to separate the two surfaces but this will also increase friction coefficient as shown in Fig. 5 as it will require more force to overcome the viscous shearing of the lubricant. Overall DLC shows higher wear rate compared to other samples. Chrome coated HSS shows smallest wear rate which is near to uncoated HSS pin. Wear resistance might also

be related to microhardness of coatings. As shown in Fig. 2, chrome coating exhibited higher hardness which also shows lower wear rate in Fig.5 meaning possessing better wear resistance. However, the better wear resistance of uncoated HSS compared to DLC cannot be explained in this way. It may be explained by the DLC coating debris from the pin may have help in increasing the wear rate unintentionally.

Friction coefficient is highest for DLC coated pin maybe because of the coating chipping from the base material of HSS which adds excessive debris in the lubricant. And chrome coating show lowest COF maybe because of the oxides formed on soft coatings (copper, iron, aluminum, nickel, zinc, chromium). These oxides may improve the lubricity of soft coatings [9]. In environments containing oxygen such as air, a thin (about 1 to 10nm thick) oxide layer is formed very quickly on most metal surfaces. Oxides layers are sheared more easily than the metal and sometimes they form a very hard layer. Even if the oxide wear layer particles are hard, their abrasive effect is not necessarily important because of their small dimensions compared to the roughness of the surfaces of their embedment into the soft coatings. Sometimes the oxide particles agglomerate to layers strong enough to carry the load.

Also during the tests, experiments at 100N showed a stabilized condition compared to lower loads which had more vibration and shaking. A stabilized condition could also lead to less wear rate and lower coefficient of friction. The only explanation is that 100N is the optimum and sufficient force to be used on this kind of experiment running on this machine.

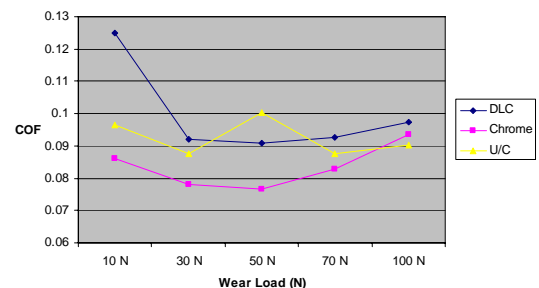


Fig.6 Coefficient of friction (COF) vs. load (N) for all samples

#### 3.2 Worn surface characteristics

The appearance of the surface damage on the pins and plates is shown in Fig.7. Surface

examinations of the worn specimens were done by SEM. These are taken after running test with 100N load, 2000 rpm, 100 °C and 30 minutes of running time. Fig. 7(a) shows mild abrasion on the surface of chrome coated pins while the plates in Fig 7(d) shows very little scars on the surface. The surface of the DLC pin shown in Fig. 7(b) clearly indicates some moderate wear on the surface and could come to the conclusion where there is some of the DLC coating has been chipped off. But the surface of the cast iron plate shows no signs of heavy scarring. Fig. 7(c) shows heavy wear abrasion on the uncoated HSS pin when sliding on Ni-resist cast iron plates. By visual inspection, chrome coating provides the least wear when sliding on Ni-resist cast iron plates.

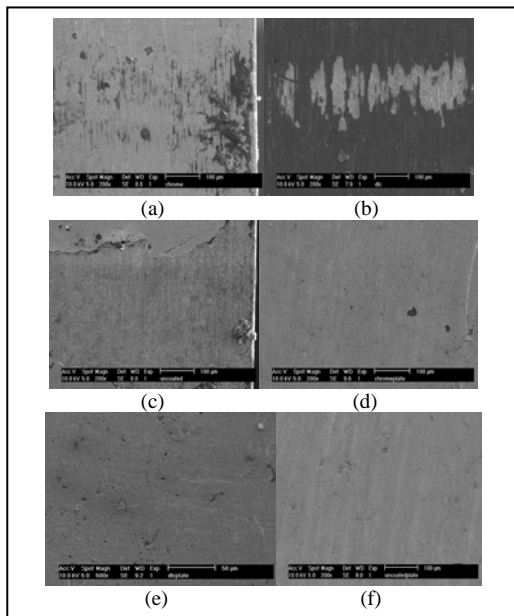


Fig. 7 Surface examinations of the worn specimens

Another explanation of why chrome coating shows less wear than DLC coating is the kind of lubricant used. Palm-polyol is a bit acidic as it is vegetable based oil compared to other mineral oils. The chemical reaction of palm-polyol may interact well with the chrome coating compared to DLC coating when the surfaces slide which provides less corrosive wear. Corrosive wear occurs in situations where the environment surrounding a sliding surface interacts chemically with it.

### 3.3 Total weight loss

As expected with higher load there will be higher total weight loss for all samples. On the contrary for 100N, it seems the total weight loss

of pin and plate has considerably decreased. This can be explained by the less vibration due to more stabilized condition when using load at 100N similar as the trend in wear rate before this. Total weight loss of specimens is shown in Fig. 8.

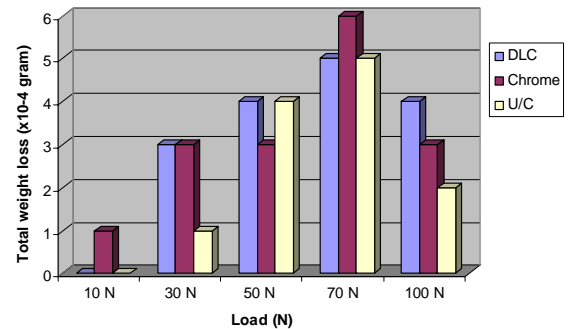


Fig.8 Total weight loss for all specimens (pins and plates)

### 3.4 Used lubricant oil analysis

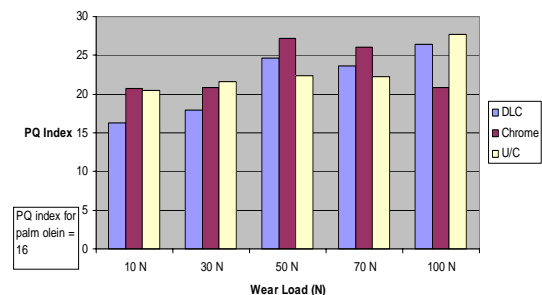


Fig. 9 PQ index result for all used oil samples.

Samples of used oil were taken from each test and checked for ferrous metal debris using the PQ/PQ90A dual-coil magnetometer. Results are shown in Fig. 9. The higher the PQ index number implies that are a higher quantity of metal debris in the oil sample. Apparently, at higher loads, more debris is found in the used oil samples compared to lower loads. At 50N, chrome coat shows higher PQ index number compared to others. This is also the same for 70N. But chrome coating HSS shows lowest PQ index number when running at the highest load (100N) compared to the other samples. DLC oil samples show low PQ index number at low loads but slowly rises when the load is increased. More wear implies more debris in the oil. But uncoated shows highest PQ index number when run at 100N. This result shows uncoated HSS still isn't enough to withstand wear and friction at very high loads.

#### 4. Conclusions

Some conclusions have been made to gain better understanding of the tribological behavior of sliding DLC and chrome coatings of high speed steel on Ni-resist cast iron while lubricated with palm-polyol. The following conclusions drawn are:

1. Chrome coating exhibit excellent wear resistance compared to DLC coating and uncoated HSS when using palm-polyol blended ionic liquid as the lubricant.
2. Wear rate of chrome coating was better than DLC coating HSS and uncoated HSS and this was the same for coefficient of friction of the test specimens.
3. Usually, wear rate is influenced by the microhardness of specimen except when in cases where excessive wear debris is taken into consideration of increasing the wear rate.
4. SEM of worn surfaces revealed few scratches on the Ni-resist cast iron plates compared to mild abrasive wear on the pins.
5. With higher load, the higher the PQ index number is. As higher load causes higher wear which leads to more wear debris in the used oil.
6. Palm-polyol blended ionic liquid shows good potential of lubricating purposes for the specimen used in this test as mild wear is reported from the experiments. Importantly palm-polyol is renewable and biodegradable compared to other lubricants.
7. Palm-polyol as well as ionic liquid is a promising candidate for biodegradable lubricants though its shows small complications on DLC coatings in certain conditions.

#### References

- [1] Boris Krzan, Jose Vizintin. Tribology properties of environmentally adopted universal tractor transmission oil based on vegetable oil, *Tribology International* 36, 2003, 827-833
- [2] U.S. Choi, B.G. Ahn, O.K. Kwon, Y.J. Chun. Tribology behavior of some antiwear additives in vegetable oils, *Tribology International* 30, 1997, 667-683
- [3] P. Sarin, D.K. Tuli, V. Martin, M.M. Rai, A.K. Bhatnagar. Development of N, P and S-containing multifunctional additives for lubricants, *Lubrication Engineering* 53, 1997, 21-26
- [4] W. Yong, X. Qunji, Friction and Wear characteristics of P-containing antiwear and extreme pressure additives in sliding of steel against aluminium alloy, *Wear* 188, 1995, 27-32.
- [5] Mu, Z.G., Zhou, F., Zhang, S.X., Liang, Y., Liu, W.: Effect of the functional groups in ionic liquid molecules on the friction and wear behavior of aluminum alloy in lubricated aluminum-steel contact. *Tribol. Int.* 2005, 38, 725-731.
- [6] Kamimura, H., Kubob, T., Minami, I., Mori, S.: Effect and mechanism of additives for ionic liquids as new lubricants. *Tribol.Int.* 2007, 40, 620-625.
- [7] Liu, X.Q., Zhou, F., Liang, Y.M.: Effect and mechanism of additives for ionic liquids as new lubricants. *Wear*, 2006, 261, 1174-1179
- [8] Carrion, F.J., Sanes, J., Bermudez, M.D.: Effect of ionic liquid on the structure and tribological properties of polycarbonate-zinc oxide nanodispersion. *Mater. Lett.* 2007, 61, 4531-4535
- [9] A.M. Barnes, K.D. Bartle, V.R.A. Thibon, A review of zinc dialkyldithiophosphates (ZDDPs): characterization and role in the lubricating oil, *Tribology International* 34, 2001, 389-395

## INVESTIGATION OF THE SWIRL EFFECT ON CAMPRO 1.6L ENGINE USING GT-SUITE

\***A.K.M. Mohiuddin and Ataur Rahman**

Department of Mechanical Engineering, Faculty of Engineering  
International Islamic University Malaysia

\*Corresponding Author: e-mail: [mohiuddin@iiu.edu.my](mailto:mohiuddin@iiu.edu.my)

### Abstract

*CAMPRO engine is a basic Double Overhead Camshaft (DOHC) which has a capacity of 1597 cc and installed with a total of 16 valves developed by Malaysian car manufacturer PROTON. The name CAMPRO is derived from its key design feature of the CAM PROFILE. Despite the low fuel consumption and good torque distribution, the engine still requires a lot of improvement to be made. That is why the CPS (Cam Profile Switching) is incorporated in the newer model of the CAMPRO as a solution to the previous CAMPRO problems. Improvement also can be done on the engine fuel consumption. The objective of this paper is to find the effect of swirl on the engine and compare it to the normal turbulence mixing process. The swirl effect analysis is done by using the GT-SUITE which has a standard swirl flow embedded in the software. The effect is simulated on the GT-SUITE and it is found that the swirl affects the engine in reducing the fuel consumption and increasing the volumetric efficiency.*

### 1. Introduction

The main objective of this work is to investigate the effect of swirl on Proton's CAMPRO Engine Model 1.6 L with a view to increase the engines capability to burn in a lean mixture during combustion and minimize its fuel consumption while comparing it with the normal turbulence at standard condition. The CAMPRO Engine is the first ever engine developed by Proton in collaboration with Lotus.

The CAMPRO engine is a basic Double Overhead Camshaft (DOHC) 4-cylinder engine which has a capacity of 1597 cc. It operated with of 4 valves on each cylinder and has a total of 16 valves altogether. The bore and stroke dimensions of each cylinder is 76 mm and 88 mm respectively. It is claimed to produce 110 bhp (82 kW) @ 6500 RPM of horsepower and 148 Nm of torque[1].

PROTON had currently come out with a new version of the CAMPRO engine which is the Cam Profile Switching (CPS) and Variable Intake Manifold (VIM) technologies. The CAMPRO CPS works similar with any other variable valve timing technology such as in Honda's VTEC and Toyota's VVTi. The VIM technology has dual length intake runner in the intake system.

The main objective of this work is to perform an extensive investigation of the swirl effect on CAMPRO engine using GT-Power – a solver of GT-Suite. GT-SUITE is an integrated set of computer-aided engineering (CAE) tools developed by Gamma Technologies, Inc. to address engine and power train design [2]. These tools are contained in a single executable form which is essential to its use in "Integrated Simulations". GT-SUITE comprised of six solvers (GT-Power, GT-Drive, GT-Vtrain, GT-Cool, GT-Fuel, and GT-Crank), a model-building interface (GT-ISE), a powerful post-processing package (GT-POST), and a collection of supporting tools [3]. The solvers of GT SUITE are:

1. GT POWER – Engine simulation for performance and acoustics analysis.
2. GT DRIVE – Vehicle performance and cycle analysis for fuel economy and emissions and driveline components dynamics.
3. GT VALVE TRAIN – Valve train kinematics, dynamics and tribology, camshaft vibrations, cam design.
4. GT FUEL – Injection system pressure and flow dynamics, hydraulic system analysis.
5. GT COOL – Engine heat management and cooling system analysis.

6. GT CRANK – crankshaft dynamics and torsional vibrations, engine balance, block vibrations, mounts, bearing oil films
7. GT POST – viewing the results of the simulation and customizing plots.

GT-ISE provides the user with the graphical user interface (GUI) that is used to build models as well as the means to run all GT-SUITE applications. Swirl is the rotational flow of charge within the cylinder about its axis [4]. Swirl is usually defined as organized rotation of the charge about the cylinder axis. Swirl is created by bringing the intake flow into the cylinder with an initial angular momentum. While some decay in swirl due to friction occurs during the engine cycle. Intake generated swirl usually persists through the compression, combustion, and expansion process. An engine with bowl-in-piston combustion chambers, the rotation motion set up during intake is substantially modified during compression. Swirl is used in diesels and some stratified-charge engine concepts to promote more rapid mixing between the inducted air charge and the injected fuel. Swirl is also used to speed up the combustion processing in spark-ignition engines. In two-stroke engines it is used to improve scavenging. In some designs of pre-chamber engines, organized rotation about the pre-chamber axis is also called swirl. In the engine where swirl within the pre-combustion chamber is important, the flow into the pre-chamber during the compression process creates the rotating flow.

There are two general ways of producing swirl during the induction process. Firstly, the flow is discharged into the cylinder tangentially towards the cylinder wall, where it is deflected sideways and downward in a swirling motion. In the other one, the swirl is largely generated within the inlet port: the flow is forced to rotate about the valve axis before it enters the cylinder. The former type of motion is achieved by forcing the flow distribution around the circumference of the inlet valve to be non-uniform, so that the inlet flow has a substantial net angular momentum about the cylinder axis. The directed port and the deflector wall port are two common ways of achieving this result. The directed port brings the flow toward the valve opening in the desired tangential direction. Its passage is straight, which due to other cylinder head requirements restricts the flow area and results in a relatively low discharge coefficient. The deflector wall port uses the port inner side

wall to force the flow preferentially through the outer periphery of the valve opening, in a tangential direction. Since only one wall is used to obtain a directional effect, the port areas are less restrictive.

## 2. Simulation using GT-SUITE

A GT-Model is created to model the CAMPRO engine. The model data were referred from PROTON Power train department database [1]. Due to insufficient information, some data were taken from default value [2]. Fig. 1 shows the model of the CAMPRO in GT Power.

The design processes of the engine is as follows:

1. The inlet and outlet boundary conditions is described by setting the EndEnvironment object.
2. The intake and exhaust runner is created using pipe object.
3. The FStateInit template object is referred to the init object. It is the initial conditions for the pipe object at the start of the simulation.
4. Intake and exhaust ports are created using the pipe object. The created objects are cloned to create the other ports.
5. The cylinder is created using the EngCylinder object. The cylinder geometry is set in the Cylinder Geometry Object under the name of geom.
6. Cylinder wall attributes are defined in the twal object under EngCylTWal template.
7. Cylinder heat transfer attributes are defined in the htr object under EngCylHeatTr template.
8. Cylinder combustion attributes are defined in the comb object under EngCylCombsIWie template.
9. Cylinder Flow attributes are defined in the swl object under EngCylFlow template to create the swirling flow. Notice that the EngCylHeatTr's Heat Transfer Model is set to "Flow"
10. Fuel injection attributes are defined in the si-inject object under InjAFSeqConn template.
11. The cranktrain is created using the cranktrain object under the EngineCrankTrain template.
12. The friction attributes are defined. The friction object in the cranktrain main tab is named friction.
13. The parts are connected by creating links between each of them.

14. Then the components are cloned to produce a 4 cylinder model.

15. After the model is built, the simulation is run.

16. GT-Post is opened for result analysis.

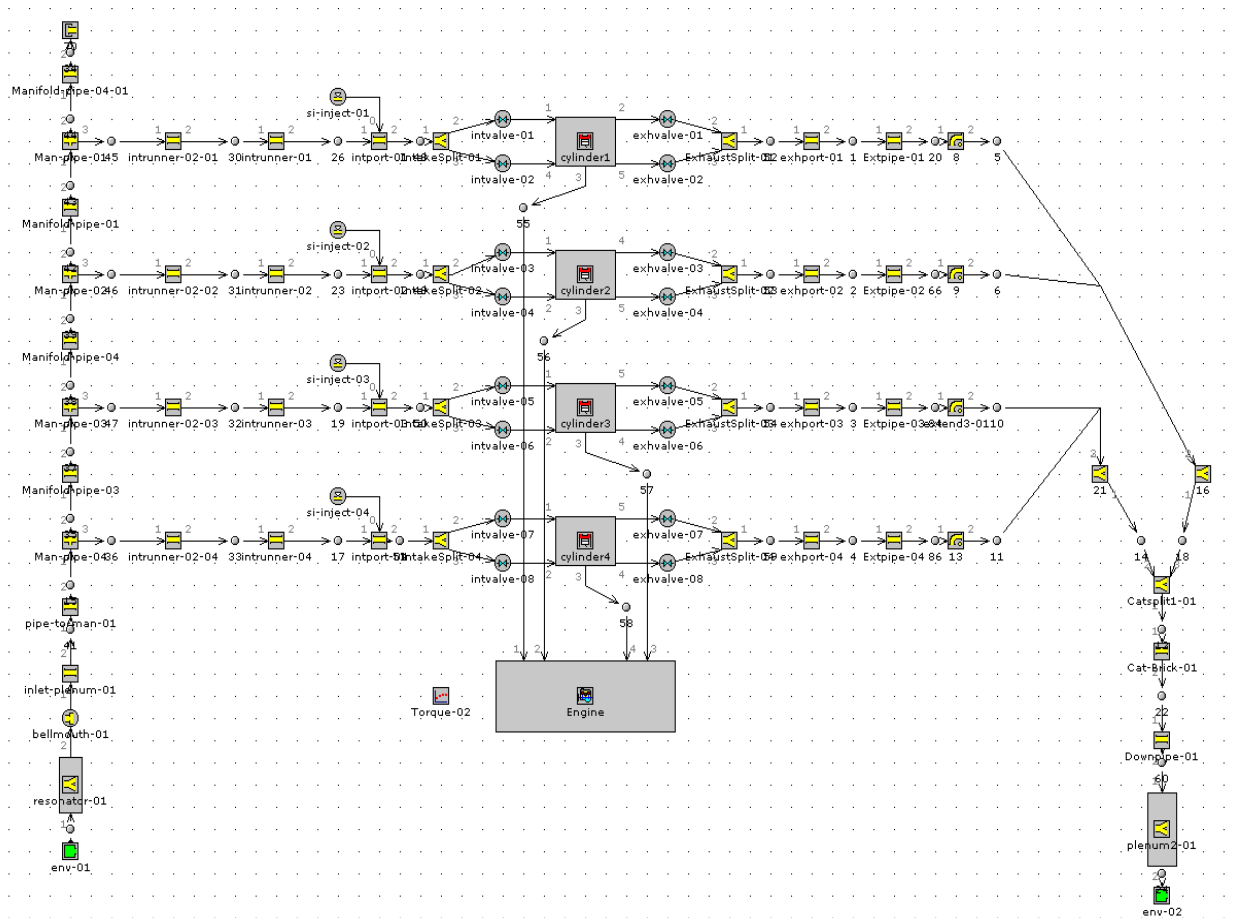


Fig.1. CAMPRO model in GT Power

### 3. Swirl Adapter

The swirl adapter is theoretically placed inside the intake port of the CamPro Engine Model. The Adapter angle is set to  $45^\circ$  to force the charge to bounce off the wall of the port to create swirl. Notice that the adapter can be turned to see the effective angle to direct the charge. Since the inside of the CAMPRO intake port is round and is considered as directed intake port the charge should not have any problem in swirling.

The fabrication of the swirl adapter will be done in the experimental investigation. The design of the adapter is shown in Fig. 2 and the adapter placement is shown in Fig. 3.

### 4. Discussion and Analysis

The simulation data obtained from GT-SUITE are compiled and analyzed. The data are obtained for both the Swirl CAMPRO Model and the Normal CAMPRO Model. Most of the data are gained from the cylinder 2. Fig. 4 shows that the swirl is generated in the initial part of the engine speed. It starts off with  $7.017 \times 10^{-14}$  and gradually decreases. When the speed reaches 1500 RPM the swirl is completely gone since at higher speed the swirl process is not significant. While in Fig. 5 as expected there is no swirl generation as the mixing process totally depended on normal turbulence only.

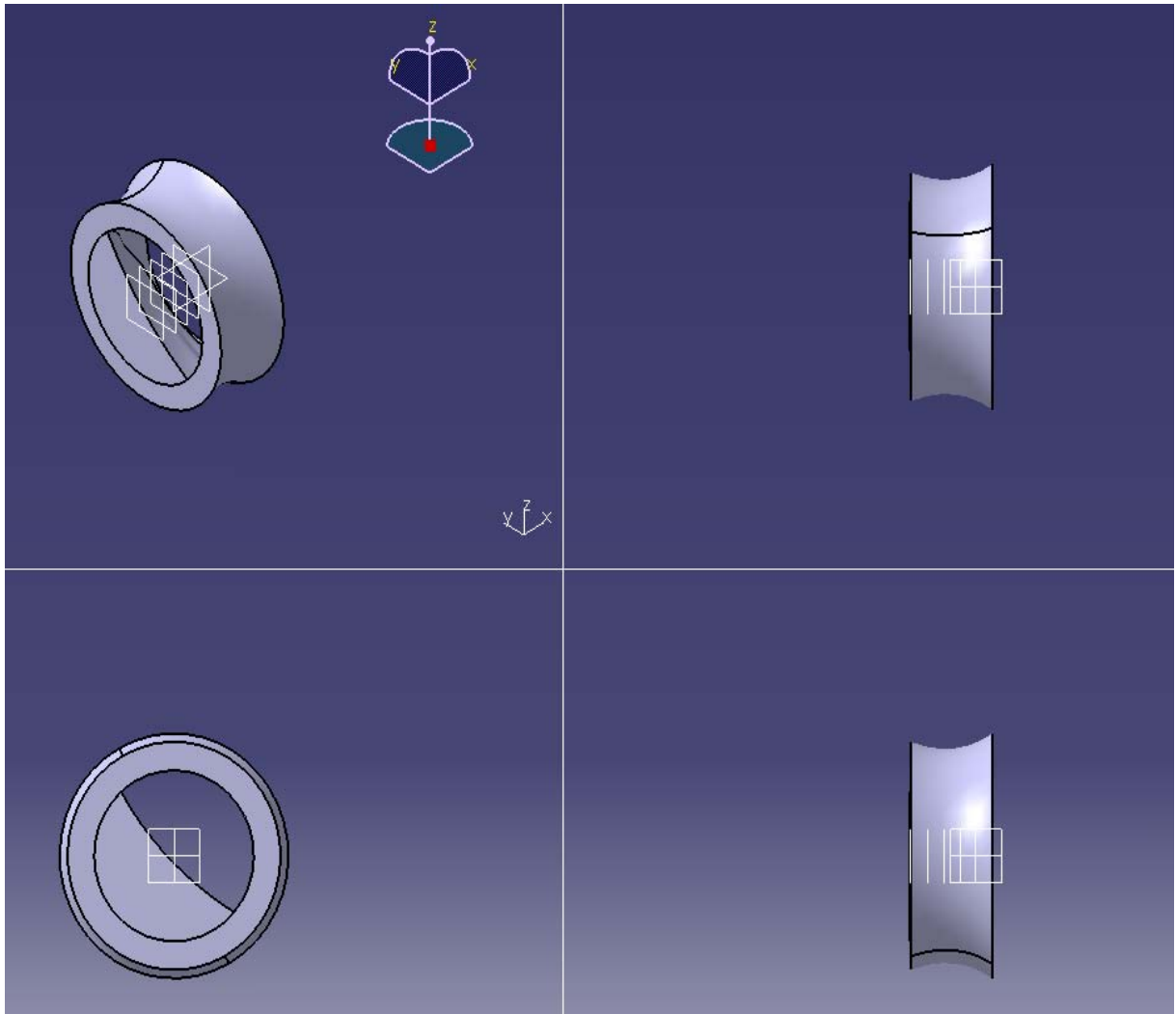


**Fig. 2. Swirl Adapter**

Fig. 6 shows the comparison of volumetric efficiency with the swirl and the normal CAMPRO model. The volumetric efficiency of the swirl engine has increased due to the increase of mass flow into the intake port as the swirl effect is taking place. Volumetric efficiency is the effectiveness of an engine intake or induction system [5]. An engine may reach up to 100% volumetric efficiency with a good intake system. A typical engine's volumetric efficiency may vary from 80% to 90%. An engine with higher efficiency indicates that the engine is effectively consumed most of the air supplied by the intake system [6]. The specific fuel consumption shows the effectiveness of an engine using the fuel supplied to produce work [7]. From the figures 7 and 8, it can be deduced that the specific fuel consumption of the swirl is lower than the normal CAMPRO model. The Swirl effect shows that it has lower fuel consumption i.e.,

more fuel economy than the Normal CAMPRO. Even in higher RPM the figures show that the swirl model saves more fuel than the normal model.

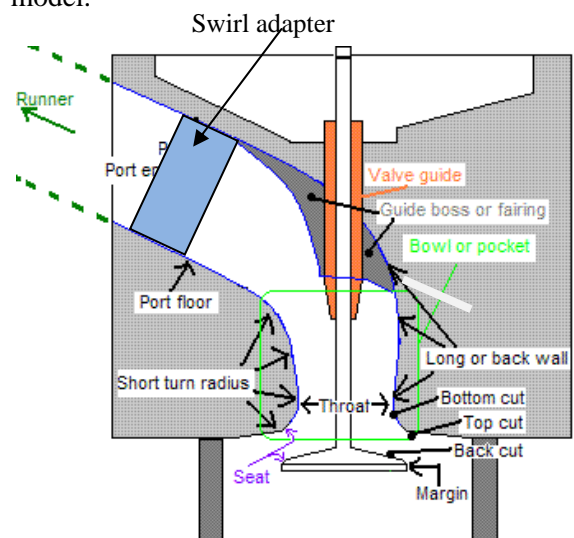


**Fig. 3. Swirl Adapter Placement**

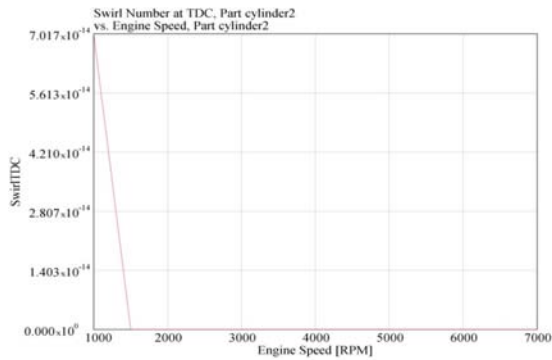


Fig. 4. Swirl Campro: Swirl versus Engine Speed

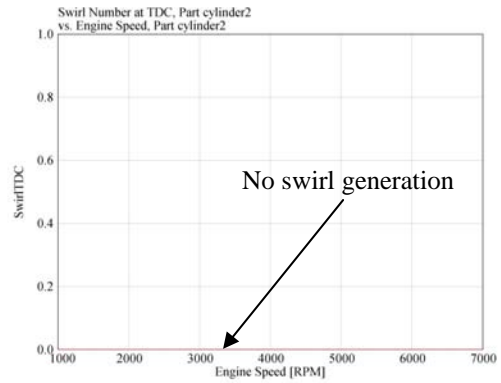


Fig. 5. Normal Campro: Swirl versus Engine speed

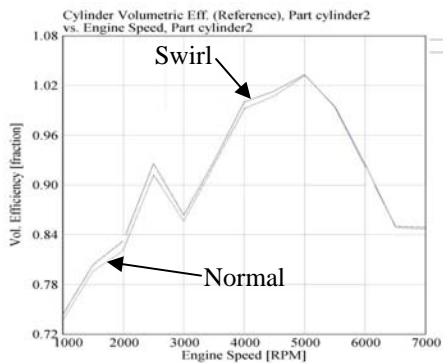


Fig. 6. Comparison of volumetric efficiency

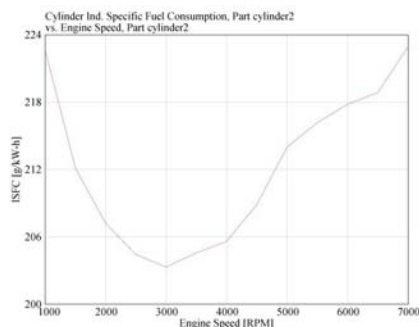


Fig. 7. CamPro: Indicated Specific Fuel Consumption versus Engine Speed

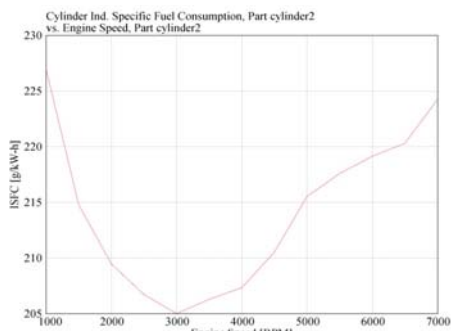


Fig. 8. Normal CamPro: Indicated Specific Fuel Consumption versus Engine Speed

## 5. Conclusion

Investigation of the swirl effect on Model CAMPRO Engine is performed and the result is compared with the normal engine. The effect of swirl in comparison to turbulence shows an increase of the volumetric efficiency. It also shows a decrease of the specific fuel consumption.

## References

- [1] <http://www.proton.com/innovation/rnd/campro.php>, (2005)
- [2] Gamma Technologies, GT-Suite, <http://www.gtisoft.com>, (2004).
- [3] GT-suite V6.1 User's Manual, Gamma Technologies, (2004).
- [4] Heinz, H., Advanced Engine Technology, Arnold, (1995).
- [5] Ganesan, V., Internal Combustion Engines Second Edition. Mc Graw-Hill., (2004).
- [6] Ohata, A., and Ishida, Y., "Dynamic Inlet Pressure and Volumetric Efficiency of Four Cycle Four Cylinder Engine" SAE paper 820407, SAE Trans., vol. 91, (1982).
- [7] Kyung-H L , Kisung K.(2001), "Influence of Initial Combustion In SI Engine on Following Combustion Stage and Cycle-By-Cycle Variations in Combustion Process". International Journal of Automotive Technology, Vol. 2, No. 1, pp. 25-31.

Paper Number: NTC-2009-030

# MACHINE CONDITION MONITORING TECHNIQUE IS USED TO DETECT THE FAILURE OF ROLLING ELEMENT BEARING FOR ISMECA MACHINES IN PRODUCTION LINE

**Andy S.W. Tan**

STMicroelectronics Sdn. Bhd.  
Tanjung Agas, Muar, Johor Darul Takzim,  
84007, Malaysia.  
E-mel: tansongwee\_20052000@yahoo.com

## Abstract

*The performance of the machines pick & place depend on movement of each elements of this machine. Each elements of the machine provide a smooth movement also depend on the rolling-element bearings condition. To ensure that the performance of pick & place machines move smoothly, bearings in this machine need to be monitor/need to be change time to time when this machines is expose to daily operation. Machine condition monitoring technique need to be done every 6 months. Machine condition monitoring techniques for roller element bearings are designed to detect the characteristic fault frequencies. The fault location are inner race, outer race, ball, or cage damage. The four characteristic fault frequencies is necessary, that commonly had been neglected by industrial. This research introduces the notion of categorizing bearing faults as either single-point defects or generalized roughness. These classes separate bearing faults according to the fault signatures that are produced rather than by the physical location of the fault. Specifically, single-point defects produce four predictable characteristic fault frequencies while faults categorized as generalized roughness produce unpredictable broadband change due to machine vibration. Experiment results are provided from bearing failed. These results illustrate the vibration and current of bearing failure in situ via shaft current.*

**Keywords :** pick & place machines, rolling-element bearings, machine vibration

## 1. Introduction

The first recorded use of rolling elements to overcome sliding friction was by Egyptian construction workers, to move heavy stone slabs, probably before 200 B.C. and possibly by the Assyrians in about 650 B.C. It is believed that some early chariot wheels used crude roller bearing made from round sticks. Around A.D. 1500 Leonardo da Vinci is considered to have invented and partially developed modern ball and roll bearings. A few ball and roller-type bearings were constructed in France in the eighteenth century. The builder of a roller-bearing carriage claimed, in 1710, that his roller bearings permitted one horse to do work otherwise hardly possible for two horses. But it was not until after the invention of the Bessemer steel process in 1856 that a suitable material for

rolling-element bearings was economically available. During the remainder of the nineteenth century, ball bearings were rapidly developed in Europe for use in bicycles.

The simplest possible bearings are unlubricated plain or sliding bearings-like the wooden cart wheels mounted directly on wooden axles in ancient times. Lower friction and longer life were obtained by adding a lubricant, such as animal or vegetable oil. In modern machinery using sliding bearings, steel shafts are supported by the surfaces of bearings made of a wear-compatible material, such as bronze or TFE. Oil or grease is used in common low-speed applications-lawn mower wheels, garden carts, children's tricycles-but the lubricant does not completely separate the surface. On the other hand, sliding bearings used with engine crankshafts receive hydrodynamic

lubrication during normal operation; that is, the oil film completely separates the surfaces.

Rolling-element bearings are either ball bearings or roller bearings. In general, ball bearings are capable of higher speeds, and roller bearings can carry greater loads. Most rolling-element bearing can be classed in one of three categories: (1) radial for carrying loads that are primarily radial; (2) thrust, or axial-contact for carrying loads that are primarily axial; and (3) angular-contact for carrying combined axial and radial loads.

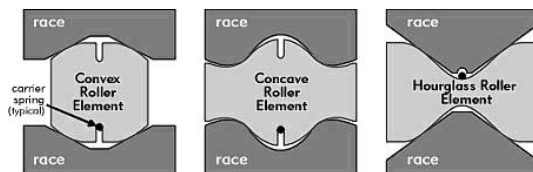


**Fig.1. Front view for rolling element bearing**

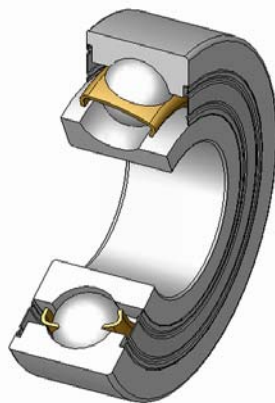


**Fig.2. Angular-contact rolling element bearing.**

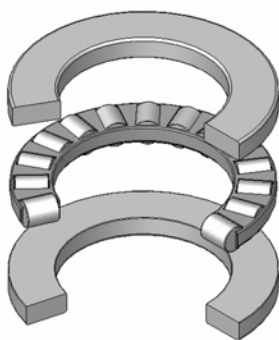


**Fig.3. Thrust rolling element bearing.**

## 2. Wear caused by vibration.

When a bearing is not running, there is no lubricant film between the rolling elements and the raceways. The absence of lubricant film gives metal to metal contact and the vibrations produce small relative movements of rolling

elements and rings. As a result of these movements, small particles break away from the surfaces and this leads to the formation of depressions in the raceways. This damage is known as false brinelling, sometimes also

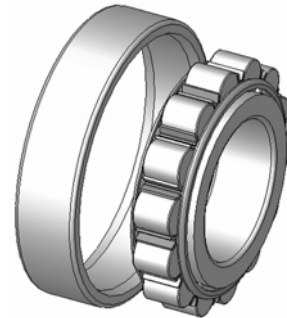


**Fig.4. Radial rolling element bearing.**

referred to as washboarding. Balls produce sphered cavities while rollers produce fluting. In many cases, it is possible to discern red rust at the bottom of the depressions. This is caused by oxidation of the detached particles, which have a large area in relation to their volume, as a result of their exposure to air. There is never any visible damage to the rolling elements. The greater the energy of vibration, the more severe the damage. The period of time and the magnitude of the bearing internal clearance also influence developments, but the frequency of the vibrations does not appear to have any significant effect. Roller bearings have proved to be more susceptible to this type of damage than ball bearings. This is considered to be because the balls can roll in every direction. Rollers, on the other hand, only roll in one direction; movement in the remaining directions takes the form of sliding. Cylindrical roller bearings are the most susceptible. The fluting resulting from vibrations sometimes closely resembles the fluting produced by the passage of electric current. However, in the latter case the bottom of the depression is dark in colour, not bright or corroded. The damage caused by electric current is also distinguishable by the fact that the rolling elements are marked as well as the raceways. Bearings with vibration damage are usually found in machines that are not in operation and are situated close to machinery producing vibrations. Examples that can be cited are transformer fans, stand-by generators and ships' auxiliary machinery. Bearings in machines transported by rail, road or sea may be subject to vibration damage too. Graph in fig.8 shows the problem roller element bearing.



Fig.5. Types of bearing have been exposed to long term operation in manufacturing process.

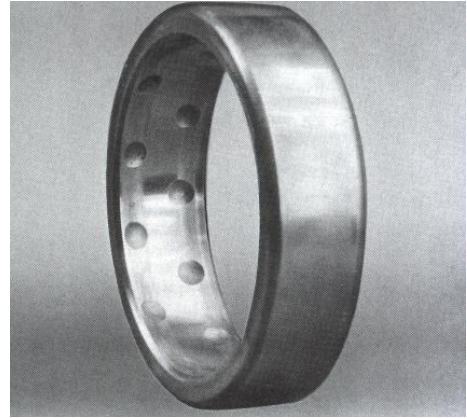


Fig. 6. The outer ring of a self aligning ball bearing damaged by vibration. The bearing has not rotated at all.

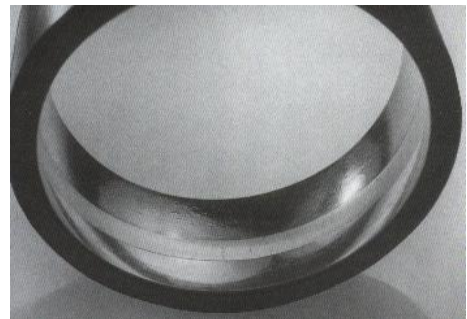
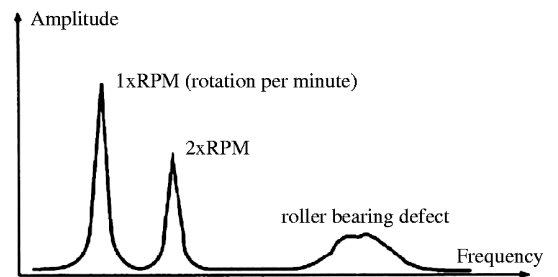


Fig. 7. The outer of a spherical roller bearing that has not been adequately lubricated. The raceways have a mirror finish.



Source: Mirshawaka (1991)

Fig.8. Graph shows the problem roller element bearing.

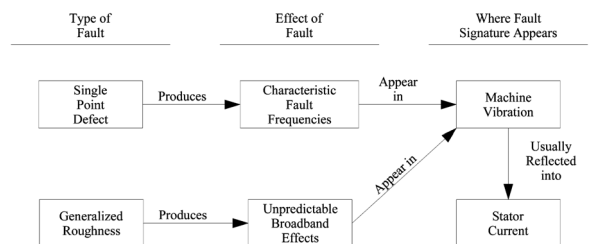
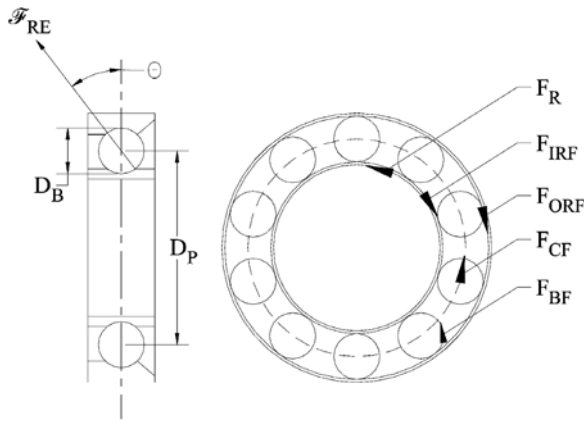


Fig. 9. Flowchart showing the effects of the two categories of faults and where their fault signatures appear.



**Fig. 10. Dimensions and frequencies related to the characteristics fault frequencies.**

### 2.1 Categorizing Bearing Faults

A single-point defect is defined here as a single, localized defect on an otherwise relatively undamaged bearing surface. A common example is a pit or spall. A single-point defect produces one of the four characteristic fault frequencies depending on which surface of the bearing contains the fault. These predictable frequency components typically appear in the machine vibration and are often reflected into the stator current. In spite of the name, a bearing can possess multiple single-point defects.

Generalized roughness is a type of fault where the condition of a bearing surface has degraded considerably over a large area and become rough, irregular, or deformed. This damage may or may not be visible to the unaided eye. Nevertheless, there is no localized defect to be identified as *the* fault; rather, large areas of the bearing surface(s) have deteriorated. A common example is the overall surface roughness produced by a contamination or loss of lubricant. The effects produced by this type of fault are difficult to predict, and there are no characteristic fault frequencies for the current or vibration associated with this type of fault. Generalized roughness faults are common in industry, while they are often neglected in the research literature. However, when a generalized roughness fault reaches an advanced stage and the bearing is near failure, the fault can typically be detected via the rudimentary techniques commonly employed in industry (e.g., ISO 10816 [1]). Since many of the newer, more sophisticated condition monitoring techniques focus only on single-point defects, this could explain the discrepancy between the large number of state-of-the-art techniques in the

research literature and their lack of use in industry. Ideally, a condition monitoring scheme should be able to identify both types of faults while still in incipient stages of development. The flowchart in Fig. 9 illustrates the effects of these two categories of faults and where their fault signatures appear. From this figure, it is evident that both types of faults directly affect the machine vibration, albeit in different ways. These effects are often reflected into the stator current, although there they are typically much more subtle.

### 2.2 Single-Point Defects

A single-point defect will cause certain characteristic fault frequencies to appear in the machine vibration. The frequencies at which these components occur are predictable and depend on which surface of the bearing contains the fault; therefore, there is one characteristic fault frequency associated with each of the four parts of the bearing [2]. The majority of the bearing-related condition monitoring schemes focus on these four characteristic fault frequencies. These frequencies are:  $F_{IRF}$ : inner race fault frequency,  $F_{ORF}$ : outer race fault frequency,  $F_{CF}$ : cage fault frequency, and  $F_{BF}$ : ball fault frequency. A thorough derivation of these frequencies is presented in [3]. The four characteristic fault frequencies are defined in (1)–(4) and illustrated in Fig. 10 where  $N_B$  is the number of balls,  $D_B$  is the ball diameter, and  $D_P$  is the ball pitch diameter. The angle  $\theta$  is the ball contact angle; this is the angle between the centerline of the bearing and  $F_{RE}$ , which indicates the direction of the force that the rolling elements exert on the outer race.

$$F_{CF} = \frac{1}{2} F_R \left( 1 - \frac{D_B \cos \theta}{D_P} \right) \quad \dots (1)$$

$$F_{ORF} = \frac{N_B}{2} F_R \left( 1 - \frac{D_B \cos \theta}{D_P} \right) \quad \dots (2)$$

$$F_{IRF} = \frac{N_B}{2} F_R \left( 1 + \frac{D_B \cos \theta}{D_P} \right) \quad \dots (3)$$

$$F_{BF} = \frac{D_P}{2D_B} F_R \left( 1 - \frac{D_B^2 \cos^2 \theta}{D_P^2} \right) \quad \dots (4)$$

The characteristic fault frequencies are the result of the absolute motion (vibration) of the machine. The stator current is not affected by the absolute motion of the machine, but rather by a

relative motion between the stator and rotor (i.e., changes in the air gap). In the instance of a bearing fault, the characteristic fault frequencies are essentially modulated by the electrical supply frequency and are predicted by (5) [4]. In this equation, is the resulting fault frequency component in the stator current, is the electrical supply frequency, is one of the four characteristic fault frequencies defined by (1)–(4), and is an integer. Experimentation suggests that the presence of a characteristic fault frequency in the machine vibration does not guarantee its presence in the stator current

$$F_{\text{BNG}} = \left| F_E \pm m^* F_V \right| \dots\dots (5)$$

### 2.3 Generalized Roughness

The purpose of this research is to recognize the importance and illustrate the effects of this second category of bearing faults, generalized (i.e., not localized) roughness. This type of failure is observed in a significant number of cases of failed bearings from various industrial applications. There are a wide variety of causes that can lead to this type of fault. Some of the more common fault sources observed by the authors include contamination of the lubricant, lack or loss of lubricant, shaft currents, and misalignment. While these fault sources may also produce single-point defects, it is common for them to produce unhealthy bearings that do not contain single-point defects (i.e., they contain generalized roughness faults). If one of these bearings is removed from service prior to catastrophic failure (typically because of increased machine vibration), a technician can easily recognize that a problem exists within the bearing because it either spins roughly or with difficulty. However, upon a visual examination (nonmicroscopic), there is no single-point defect, and the actual damage to the bearing (e.g., surface roughness, deformed rolling elements, warped raceway, etc.) may or may not be visible to the unaided eye. Since there is no single-point defect, there is nothing to excite any of the characteristic fault frequencies. This research experimentally generates bearing faults that fall under the category of generalized roughness via an externally applied shaft current [5]. In this method, bearings are placed in a test motor, and a shaft current is injected through the bearing to induce faults in situ. This paper investigates data from ten bearings failed by this method. Among these ten bearings, the fault characteristics

include microscopic pitting on all surfaces and microscopic scratches on the rolling elements and cage. None of these ten bearings contain single-point defects. An important point to emphasize from this data is that the specific way in which these bearings fail is unpredictable; therefore, the effect the fault has on the machine vibration and stator current is also unpredictable. As Fig. 9 suggests, these effects are broadband changes in the machine vibration and stator current spectra. To illustrate this principle, consider Fig. 15. This figure shows the machine vibration and stator current for one bearing. The solid line represents the bearing when it was first installed while the dashed line represents the same bearing once it reached a point near failure. The 60-Hz component is removed from the stator current before sampling. Fig. 15 (top) indicates a significant increase over all frequencies making this fault easily detectable in the machine vibration. However, Fig. 15 (bottom) illustrates that the change in stator current is more selective. For this bearing, the only parts of the stator current spectrum affected by the bearing fault are the sidebands (of width 25 Hz) around 60 and 180 Hz. Results for a different bearing are illustrated in Fig. 16 (top) where a similar broadband increase in machine vibration is observed. However, the changes in stator current of Fig. 16 (bottom) are in contrast to that of the previous bearing. For Fig. 16 (bottom), the only change in stator current is an increase in the noise floor above approximately 200 Hz.

In other bearings from these trials, the effects that the faults were observed to have on the stator current included an increase in all components, an increase in the noise floor only, and an increase in all low frequency components (i.e., below 300 Hz). The effects of the generalized roughness faults on the machine vibration in these figures support the claim of broadband changes accompanied by the absence of the characteristic fault frequencies. While the data in these two figures represent the extremes (i.e., a new, healthy bearing and the same bearing near failure), the data acquired at intermediate stages of fault development are consistent with these results. That is, as the fault increases in severity the magnitude of the broadband changes in machine vibration increase accordingly. The figure legends have been updated for Figs. 15 and 16. In an attempt to illustrate how the shaft current physically affects the test bearing, consider Fig. 11. This is a photograph of the inner race of a bearing that

was failed using the shaft current experimental setup taken with a standard digital camera. From this figure, it is seen that the rolling elements have left a rough track down the center of the inner raceway. The arrow is pointing to the top of this track. Above the tip of the arrow is the smooth, polished surface of the inner raceway that has not come into contact with the rolling elements (the darker area). Below the tip of the arrow is a coarse, rough track in the middle of the inner race where the rolling elements have passed and conducted the shaft current. Fig. 12 contains a photograph of the boundary between where the rolling elements caused the rough track on the inner race and the untouched portion of the inner race surface. This photograph is a 5 magnification of the area at the tip of the arrow in Fig. 11. The left side of Fig. 12 is the rough, pitted surface traversed by the rolling elements. The right side is the smooth area untouched by the rolling elements. The vertical lines on the right side are machining marks from the cutting tool that manufactured this bearing. In all photographs taken through the microscope, the black arc and black line are generated by the photography equipment. The black line is for reference and is 400  $\mu\text{m}$  in length for all photographs taken at 5 magnification. This observation further supports the concept of a generalize roughness category for bearing failures. The photograph in Fig. 13 was taken at an arbitrary point in the middle of the inner race of a bearing. The top portion of the photograph was taken at 5 magnifications. Notice the general roughness of the surface and the pitting. This roughness was common to all raceways on all bearings failed by this method, albeit in differing degrees of severity for the various surfaces and the various bearings tested. The bottom portion of this photograph is a magnification of approximately 10 of the pits from the top photograph. This magnified photograph illustrates the depth of the pits, which were found on all raceways of all bearings failed by this method (again is various degrees of severity). Fig. 14 is a photograph of the surface of one of the rolling elements from another failed bearing. The scratches and surface roughness seen here were consistently found on the rolling elements from all bearings failed using this method. This supports the notion of generalized-roughness damage to the rolling elements as well as the raceways.

Below the tip of the arrow is a coarse, rough track where the rolling elements have passed

conducting the shaft current. Above is the smooth, polished surface where the rolling elements have not contacted the raceway.



**Fig.11. Inner race of a bearing failed by the shaft current experimental setup.**

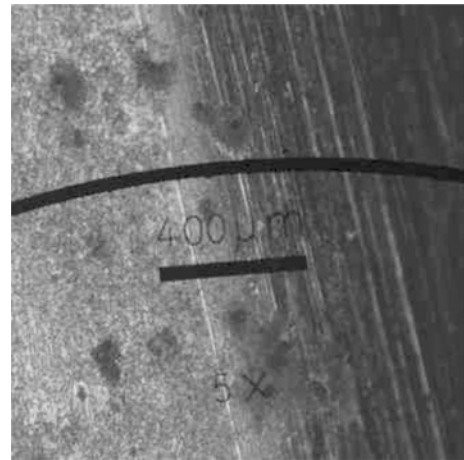


**Fig. 12. Photograph taken at 5x magnification of the boundary between the rough area and undamaged area on the bearing depicted in Fig. 11. This area was photographed at the tip of the arrow in Fig. 11.**

These scratches were common to all rolling elements in all bearings failed by this method.

#### 2.4 Wear Caused by Inadequate Lubrication

If there is not sufficient lubricant, or if the lubricant has lost its lubricating properties, it is not possible for an oil film with sufficient

carrying capacity to form. Metal to metal contact occurs between rolling elements and raceways.

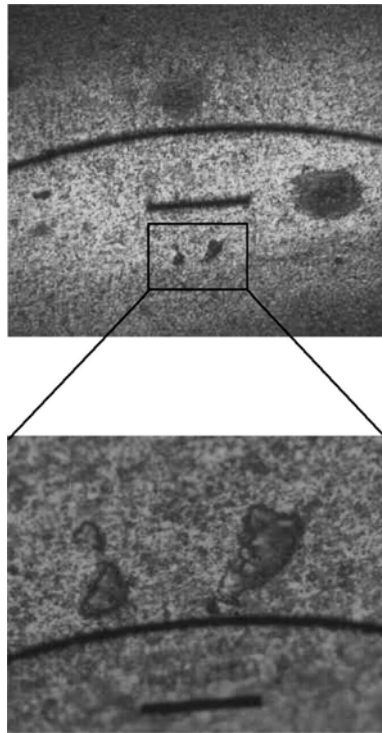


**Fig. 13.** Photograph of an arbitrary point on the inner race of a bearing failed by the shaft current method. The top photograph was taken at 5x and the bottom photograph is a ~10x magnification of the two pits above. This roughness and pitting was common to all raceways of all bearings failed by this method.

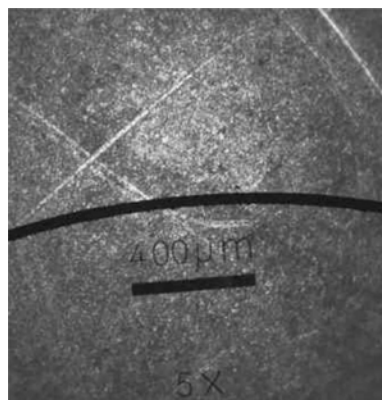


**Fig. 14.** Photograph of a rolling element failed by the shaft current method.

In its initial phase, the resultant wear has roughly the same effect as lapping. The peaks of the microscopic asperities, that remain after the production processes, are torn off and, at the same time, a certain rolling-out effect is obtained. This gives the surfaces concerned a

varying degree of mirror-like finish. At this stage surface distress can also arise. If the lubricant is completely used up, the temperature will rise rapidly. The hardened material then softens and the surfaces take on blue to brown hues. The temperature may even become so high as to cause the bearing to seize.

### 2.5 Graphs for Vibration and Current of a Bearing failed *in situ* via Shaft Current

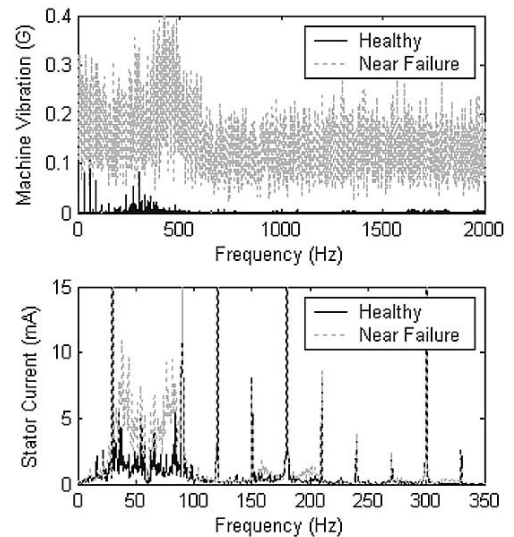


**Fig.15.** Vibration and current of a bearing failed *in situ* via shaft current. Solid line is the bearing when healthy and new; dotted line is same bearing near failure. Top: machine vibration indicates a significant increase at all frequencies. Bottom: stator current displays increase in sidebands (~25 Hz at 60 and 180 Hz).

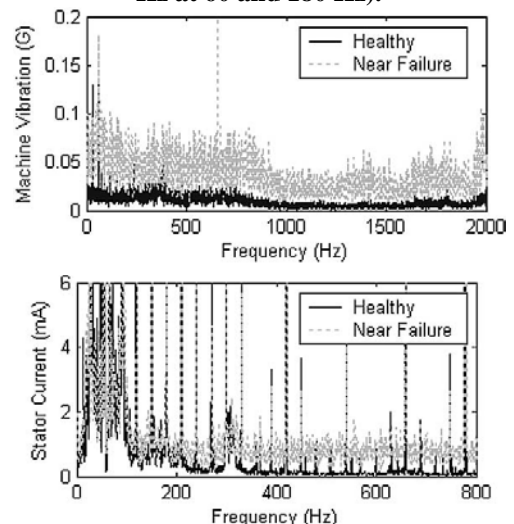


**Fig. 16.** Vibration and current of a different bearing failed *in situ* via shaft current. Top: machine vibration again indicates a significant increase at all frequencies. Bottom: stator current displays increase in only the noise floor above ~200 Hz. All other peaks remained unchanged.

### **3. Conclusion**

This paper has introduced the notion of categorizing bearing faults as either single-point defects or generalized roughness. This is important because it divides these faults according to the type of fault signatures they produce rather than the physical location of the fault. The benefit of this categorization is two fold. First, it ensures that the faults categorized as generalized roughness are not overlooked. The majority of bearing condition monitoring schemes in the literature focus on detection of single-point defects. While this is an important class of faults, a comprehensive and robust scheme must be able to detect both generalized roughness and single-point defect bearing faults. Second, grouping faults according to the type of fault signature they produce provides a clearer understanding of how these faults should be detected. This should provide improved insight into how bearing condition monitoring schemes should be designed and applied.

Experimental results obtained from this research suggest generalized roughness faults produce unpredictable (and often broadband) changes in the machine vibration and stator current. This is in contrast to the predictable frequency components produced by single-point defects. This research investigates generalized roughness faults produced in situ by an externally applied shaft current. While shaft current is only one way this type of fault can be produced, it is a common source for bearing failures in industry. Microscopic inspection

reveals pitting and roughness on all bearing surfaces. This further supports the assertion of a nonlocalized or generalized roughness type of fault.

### **References**

- [1] Mechanical Vibration—Evaluation of Machine Vibration by Measurements on Non-Rotating Parts—Part 1: General Guidelines International Organization for Standardization, ISO 10816-1:1995(E), 1995.
- [2] R. A. Collacott, *Vibration Monitoring and Diagnosis*. New York: Wiley, 1979, pp. 109–111.
- [3] B. Li, M. Y. Chow, Y. Tipsuwan, and J. C. Hung, “Neural-network based motor rolling bearing fault diagnosis,” *IEEE Trans. Ind. Electron.*, vol. 47, pp. 1060–1068, Oct. 2000.
- [4] R. R. Schoen, T. G. Habetler, F. Kamran, and R. G. Bartheld, “Motor bearing damage detection using stator current monitoring,” *IEEE Trans. Ind. Applicat.*, vol. 31, pp. 1274–1279, Nov./Dec. 1995.
- [5] J. R. Stack, T. G. Habetler, and R. G. Harley, “Experimentally generating faults in rolling element bearings via shaft current,” in *Proc. IEEE Int. Symp. Diagnostics for Electric Machines, Power Electronics and Drives (SDEMPED)*, 2003, pp. 188–192.
- [6] C. J. Robert and M. M. Kurt, *Fundamentals of Machine Component Design*. John Wiley & Sons, 1991, pp. 518-519.

## TRIBOLOGY IN BIOLOGY: BIOMIMETIC STUDIES ACROSS DIMENSIONS AND ACROSS FIELDS

I.C. Gebeshuber<sup>1,2,3,4</sup>, B.Y. Majlis<sup>1</sup> and H. Stachelberger<sup>2,5</sup>

<sup>1</sup>Institute of Microengineering and Nanoelectronics (IMEN), Universiti Kebangsaan Malaysia, 43600 UKM, Bangi, Selangor, Malaysia

<sup>2</sup>TU BIONIK Center of Excellence for Biomimetics, Vienna University of Technology Getreidemarkt 9/134, 1060 Wien, Austria

<sup>3</sup>Institut fuer Allgemeine Physik Vienna University of Technology Wiedner Hauptstrasse 8-10/134, 1040 Wien, Austria

<sup>4</sup>AC<sup>2</sup>T Austrian Center of Competence for Tribology, Viktor Kaplan-Straße 2 2700 Wiener Neustadt, Austria,

<sup>5</sup>Institute of Chemical Engineering & University Service-Center for Transmission Electron Microscopy Getreidemarkt 9/166, 1060 Wien, Austria

Corresponding Author: email: ille.gebeshuber@ukm.my; Tel/Fax: 012 392 9233/03 8925 0439

### Abstract

*Biomimetics is a field that has the potential to drive major technical advances. It might substantially support successful mastering of current tribological challenges, i.e., friction, adhesion and wear in machines and devices from the meter to the nanometer scale. Science currently goes through a major change, with biology gaining increasing importance. A new Leitwissenschaft that can be called „Biological Engineering“ is evolving. Tribology is omnipresent in biology. Various examples for biological tribosystems across dimensions are introduced to the reader, exemplifying the hierarchical nature of biomaterials, and concepts such as integration instead of additive construction, optimization of the whole instead of maximization of a single component feature, multi-functionality instead of mono-functionality and development via trial-and-error processes. The current state of biomimetics in tribology is reviewed, and possible biomimetic scenarios to overcome current tribological challenges are envisaged (switchable adhesives, micromechanic devices, novel lubricants and adhesives).*

**Keywords:** biological physics, biological tribosystems, biological tribosystems on the micrometer scale, biomaterials, biomimetic concepts, biomimetics, crack redirection, interdisciplinarity, multi-functionality, switchable adhesive molecules, technoscience, tribology in biology

### 1. Introduction

Biomimetics is a growing field that has the potential to drive major technical advances (see Figure 1). It might substantially support successful mastering of current tribological challenges, i.e., friction, adhesion and wear in machines and devices from the meter to the nanometer scale.

In biomimetics, materials, processes and systems in nature are analysed, the underlying principles are extracted and subsequently applied to science and technology [4][7][3]. This approach can result in innovative new technological constructions, processes and developments. Biomimetics can aid tribologists to manage the specific requirements in systems or product design, especially to create products

and processes that are sustainable and perform well (e.g. to overcome stiction), to integrate new functions, to reduce production costs, to save energy, to cut material costs, to redefine and eliminate “waste”, to heighten existing product categories, to define new product categories and industries, to drive revenue and to build unique brands [4][5][6][7]. Recurrent principles in biological materials and systems are hierarchy and multi-functionality [8][9].

Science currently goes through a large change: in biology more and more causation and natural laws are being uncovered [10]. Biology has changed from being very descriptive to a science that can be acknowledged and understood (in terms of concepts) by tribologists. The amount of causal laws in this new biology (indicated by the ratio of causal

versus correlational knowledge, or the ratio of explanatory versus descriptive knowledge) is steadily growing and a new field that can be called “biological engineering” is emerging. The languages of the various fields of science increasingly get compatible (see Figure 2), and the amount of collaborations and joint research projects between tribologists and biologists have increased tremendously over the last years.

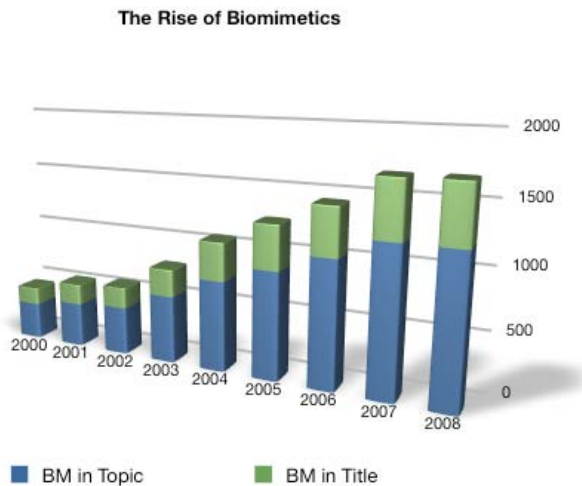


**Fig. 1. The number of scientific publications with “biomim\*” as topic or in the title.**  
 Source: ISI Web of Knowledge, Thomson Reuters. [http:// www.webofknowledge.com](http://www.webofknowledge.com)

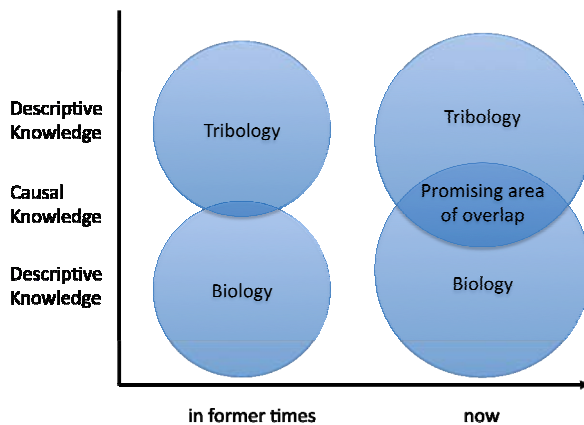


**Fig. 2. The increasing amount of causal laws in biology generates promising areas of overlap with mechanical engineering.**

Tribology is omnipresent in biology [11]. Examples for biological tribosystems across dimensions are the crack redirection in the horse hoof [12][13], biological tribosystems on the micrometer scale [4][6][14][15][16][17][18], plant wax structures preventing herbivores to adhere to plants [19][20][21] and single switchable adhesive molecules that enable the

rolling adhesion of red blood cells on the endothelium [22][23][24].

Recurrent concepts in all these examples are such integration instead of additive construction, optimization of the whole instead of maximization of a single component feature, multi-functionality instead of mono-functionality and development via trial-and-error processes. Such concepts can easily be transferred to technology, and can be applied by engineers with no knowledge of biology at all [3][7][10].

Biotribological systems can inspire novel tribological approaches [25]. First devices based on bioinspired materials are a technique for cell separation inspired by adhesion of white blood cells [26][27], devices inspired by the hierarchical dry adhesive in the Gecko’s foot [28][29], such as wall-climbing robots; and artificial hierarchical as well as novel adhesives [30].

## 2. Materials and Methods

### 2.1. Biomimicry Innovation Method

The Biomimicry Innovation Method is applied to identify biological systems, processes and materials that can inspire novel technological approaches concerning tribological issues. Biomimicry is an innovation method that seeks sustainable solutions by emulating nature’s time-tested patterns and strategies. The goal is to create products, processes, and policies - new ways of living - that are well adapted to life on earth over the long haul.

The Biomimicry Innovation Method (© Biomimicry Guild, Helena, MT, USA 2008, <http://www.biomimicryguild.com/>) involves specifically trained biologists as well as engineers, natural scientists, architects and/or designers from universities or companies. The Biomimicry Innovation Method is for example used in the rainforest (high species variety, high innovation potential) to learn from and emulate natural models).

The steps in the biomimicry process are as follows:

- Identify function,
- biologize the question,
- find nature’s best practices and
- generate product ideas.

Identify Function: The biologists distil challenges posed by engineers/natural

scientists/architects and/or designers to their functional essence.

**Biologize the Question:** In the next step, these functions are translated into biological questions such as “How does nature manage lubrication?” or “How does nature bond parts together?” The basic question is “What would nature do here?”

**Find Nature’s Best Practices:** Scientific data bases as well as the surrounding rainforest are used to obtain a compendium of how plants, animals and ecosystems solve the specific challenge.

**Generate Process/Product Ideas:** From these best practices (90% of which are usually new to clients), the biologists generate ideas for cost-effective, innovative, life-friendly and sustainable products and processes.

## 2.2. Tribological Challenges investigated

Tribology is a huge field, so only selected current tribological challenges can be dealt with in this manuscript. Areas that are treated here comprise the need for optimally designed rigid micromechanical parts (for 3D-MEMS), pumps for small amounts of liquid (for lab-on-a-chip applications), novel dry and wet adhesives and lubricants (for various applications) and functional material with crack redirection properties (for mechanical protection of viable parts in machinery).

## 3. Results

### 3.1. Optimally designed rigid micromechanical parts

Identified functions:

1. Hinges and interlocking devices
2. Click-stop mechanism
3. Springs
4. Parts connected in a chain with adjustable length
5. Movable rigid parts
6. Unfoldable structures
7. Energy dissipation
8. Stability (reinforcement)
9. Pressure resistant containers
10. Fixation

Relating biologized questions:

1. How does Nature mechanically connect hard single cells?

2. How does Nature unfold structures and then irreversibly fix them?
3. How does Nature reversibly store mechanical energy?
4. How does Nature provide stability to chains in turbulent environments?
5. How does Nature optimize moveable parts?
6. How does Nature generate 3D structures from rigid parts?
7. How does Nature dissipate mechanical energy?
8. How does Nature deal with high pressures?
9. How does Nature mechanically fix structures?

Nature’s best practices

1. Diatom chains with mechanical connections between the single cells. Diatoms are unicellular microalgae with a cell wall consisting of a siliceous skeleton enveloped by a thin organic case [31]. The cell walls of each diatom form a pillbox-like shell consisting of two parts that fit within each other. These microorganisms vary greatly in shape, ranging from box-shaped to cylindrical; they can be symmetrical as well as asymmetrical and exhibit an amazing diversity of nanostructured frameworks. These biogenic hydrated silica structures have elaborate shapes, interlocking devices, and, in some cases, hinged structures. The silica shells of the diatoms experience various forces from the environment and also from the cell itself when it grows and divides, and the form of these micromechanical parts has been evolutionarily optimized during the last 150 million years or more (see Figure 3).
2. The diatom species *Corethron pennatum* and *Corethron criophilum* are excellent examples for unfolding structures [34][33][34].
3. The diatom species *Rutilaria grevilleana* and *Rutilaria philippinarum* have structures that might be interpreted as springs [5][35]. However, more detailed investigation is needed to confirm this.
4. *Ellerbeckia arenaria* is a diatom which lives in waterfalls. *E. arenaria* cells form string like colonies which can be several millimeters long and can reversibly be elongated by one third of their original length [16].
5. The diatoms *Melosira sp.* [15], *Solium exsculptum* (Figure 3) and *Ellerbeckia*

*arenaria* [15] are interesting best practices for optimization of moveable parts in Nature. The diatom species *Solium exsculptum* lived 45 million years ago. Scanning Electron Microscopy images of this Eocene fossil from a deposit at Mors, Denmark reveal that the connections between sibling cells are still in good condition (Figure 3).

6. *Corethron pennatum* and *Corethron criophilum*. The process of new cell formation in these species is highly complex, and involves elaborate mechanisms [32][33].
7. The diatoms *Solium exsculptum* [25][36] and the diatoms *Melosira* sp. [5][34] and *Ellerbeckia arenaria* [37].
8. The green alga *Euglena gracilis* is a single-celled algal species that performs tasks as diverse as sensing the environment and reacting to it, converting and storing energy and metabolizing nutrients, living as a plant or an animal, depending on the environmental constraints. The striated pellicle covering the whole cell is a distinct exoskeletal feature of the *Euglena* species. The pellicle is a proteinaceous structure that provides mechanical stability to the cell, yet it is flexible. Its single strips are connected via interlocking ridges that can slide against each other and are lubricated via biogenic lubricants excreted from pellicle pores. Internal pressures up to several bar cannot break the exquisite pellicle arrangement in these algae (see [38] and references therein).
9. The mechanical click-stop mechanism in *Corethron* is an excellent best practice showing how Nature deals with the task to mechanically fix structures [32][33][34]. Generated product ideas comprise micromechanical optimization of 3D-MEMS structure, methods to obtain 3D structures from fabricated 2D structures, novel methods for energy storage in MEMS, development of (3D) MEMS with moveable parts, methods to obtain 3D structures from fabricated 2D structures, quality assurance of MEMS and novel methods to preventing stiction.

### 3.2. Pumps for small amounts of liquid

Identified function:

Pumps for small amount of liquids as they are needed in lab-on-a-chip devices and in microchemical reactors.

Biologized question:

How does Nature move fluids?

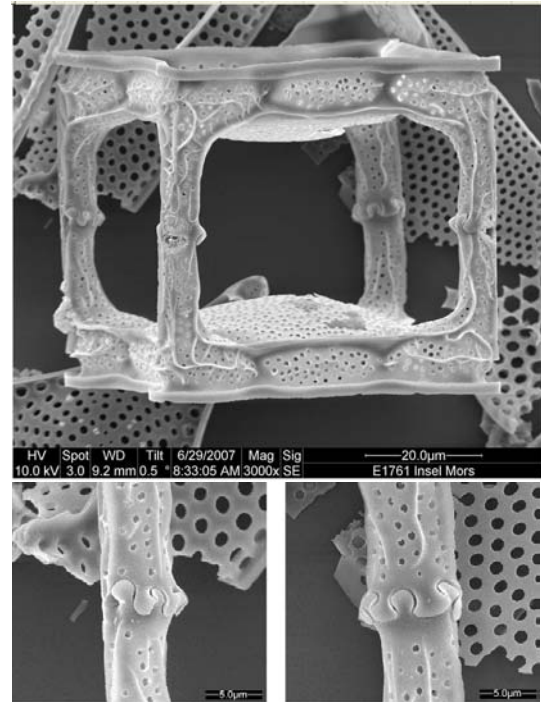


**Fig. 3. Biological example for optimally designed rigid micromechanical parts. The sample is from the Hustedt Collection in Bremerhaven, Germany, # E1761. © F. Hinz and R. M. Crawford, reproduced with permission.**

Nature's best practices:

*Rutilaria philippinarum* is a fossil colonial diatom thought to have lived in inshore marine waters (CRAWFORD pers. comm. 2008). In this species, the single diatoms connect by linking spines and by a complex siliceous structure termed the periplekton. These linking structures on the one hand keep the cells together, but on the other hand also keep distance between the cells. The shape of the spines allows expansion of the chain to a certain maximum distance and compression to a minimum distance, in which case there is still some fluid between the cells. The links allow movement of single cells in the chain against or from each other in a rather one-dimensional way [34]. Such elaborated linking mechanisms, inspired the question what would happen to such a diatom colony when subjected to water flow. Computer simulations performed by Srajer and

Gebeshuber suggest that a diatom colony subjected to water flow exhibits some kind of oscillatory movement. This movement might facilitate nutrient uptake of a diatom colony. The inspiring organisms for the computer simulation study are *Rutilaria grevilleana* and *Rutilaria philippinarum* [35]. Oscillatory movement increases the advective diffusion through the surface of the diatoms and therefore increases nutrient supply in a homogeneous nutrient solution [39].

Generated product ideas comprise the development of micropumps for lab-on-a-chip applications.

### 3.3. Novel dry and wet adhesives and lubricants

Identified functions:

Adhesion (wet, dry, reversible, switchable, selective), lubrication (wet, dry).

Biologized questions:

How does Nature prevent wear?

How does Nature reversibly adhere to structures?

Nature's best practices:

Articular cartilage, the bioactive surface on synovial joints (like the hip, the knee, the elbow, the fingers, the shoulder or the ankle) has a very small friction coefficient. Some groups report friction coefficients for normal synovial joints as low as 0.001 [40][41][42]. Identifying the mechanisms responsible for the low friction in synovial joints has been an area of ongoing research for decades. Furey lists more than 30 theories that have been proposed to explain the mechanisms of joint lubrication [43]. In summary, articular cartilage provides an efficient load-bearing surface for synovial joints that is capable of functioning for the lifetime of an individual.

Generated product ideas comprise improved lubrication strategies in cases where moveable hard parts have to be interconnected.

### 3.4. Functional material with crack redirecting properties

Identified functions:

Fracture control, crack redirection

Biologized question:

How does Nature tailor-shape wear particles and thereby protect viable parts?

Nature's best practices:

The horse hoof is a system that can tailored the shape of its wear particles. Hoof is an excellent example for a tough natural materials that increases the energy required for tearing by diverting cracks away from their preferred directions of propagation. Macroscopic wear particles from horse hoofs are more often than not of rectangular shape. A horse's hoof is difficult to split vertically. In the hoof, the keratin is arranged in an ordered three-dimensional array such that a crack initiated by a vertical cut will turn and split the material at right angles to the vertical direction [12][13].

Generated product ideas:

Studies of the mechanisms of synthesis of hoof material in the horse can be expected to provide hints for the industrial fabrication of such complex three-dimensional fibrous materials.

## 4. Conclusions

Current mechanical systems, synthetic adhesives and lubricants are not perfect, and the low friction coefficients in many natural systems are yet to be achieved in artificial systems. Technological innovations, completely new ideas, and unconventional approaches can all be learned from nature. These approaches have been tested and improved upon for millions of years; they are continuously being optimized with respect to their function and environment.

Tribology always have to do with applications and devices. For accelerated scientific and technological breakthroughs the "Three-gaps-theory" was proposed by Gebeshuber and co-workers in 2009 (Fig. 4, [10]): the inventor gap, the innovator gap and the investor gap have to be bridged. Since development always takes a path from the primitive over the complex to the simple, effective or efficient solutions can be envisaged, depending on the time frame provided and the acceleration wanted.

In nature, there is equilibrium between generalists and specialists; there are sources and drains, with natural flow between them. The whole system grows via evolution; there is no static natural system. In humans the necessities are shifted. To advance our system, more visions and a platform for "evangelists" are needed. Interdisciplinary working groups with

generalists as heads, coordinating the specialists, are needed.

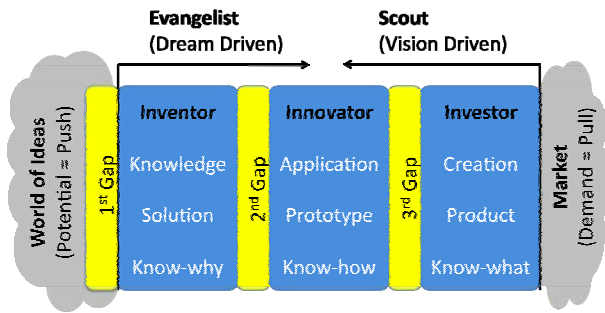


Fig. 4. The Three-Gaps-Theory as proposed by Gebeshuber et al. [10]

At the moment, we do not have such structures. Our scientific system fails because of a lack of competition, the “pull” is missing, we “push”, but industry does not want. Industry does not “pull”, because it needs products and no solutions. Economy needs a vision. Steve Jobs from Apple with the vision of making technology simple is a rare example for successful “pull”. Generally, current economy loses itself in details. Industry lacks visions, science cannot promote its knowledge, there is no platform.

To prevent being trapped in the inventor, innovator or investor gap, a cross dialogue is necessary, a pipeline from “know-why” to “know-how” to “know-what”, from the inventor who suggests a scientific or technological breakthrough to the innovator who builds the prototype to the investor who mass produces the product and brings the product to the consumer. Currently, and this is the main problem, at universities worldwide huge amounts of knowledge are piled up with little or no further usage. We know a lot, we can do relatively little. We need a joint language and a joint vision.

### Acknowledgements

Part of this work has been funded by the Austrian *Kplus*-Program via the Austrian Center of Competence for Tribology, AC<sup>2</sup>T research GmbH, Wiener Neustadt.

Part of this work has been financed by the biomimetics pilot projekt “BioScreen” of the Austrian Society for the Advancement of Plant Sciences.

### References

- [1] Bhushan B. “Biomimetics: lessons from nature-an overview”, *Phil. Trans. R. Soc. A* Vol. 367, pp. 1445-1486, 2009
- [2] Bar-Cohen Y. *Biomimetics: Biologically Inspired Technologies*, CRC Press, 2005
- [3] Gebeshuber I.C. and Drack M. “An attempt to reveal synergies between biology and engineering mechanics”, *J. Mech. Eng. Sci.* Vol. 222, pp. 1281-1287
- [4] Gebeshuber I.C., Pauschitz A. and Franek F. “Biotribological model systems for emerging nano-scale technologies”, in: *Proc. 2006 IEEE Conference on Emerging Technologies - Nanoelectronics*, pp. 396-400, 2006.
- [5] Gebeshuber I.C., Stachelberger H. and Majlis B.Y. “Exploring the innovational potential of biomimetics for novel 3D MEMS”, *Int. Conf. Mat. Adv. Technol. ICMAT 2009*, Singapore, July 27 - August 2, 2009.
- [6] Gebeshuber I.C., Stachelberger H. and Drack M. “Diatom tribology”, in: *Life Cycle Tribology*, Eds.: D. Dowson, M. Priest, G. Dalmaz and A.A. Lubrecht, Tribology and Interface Engineering Series, Vol. 48, Series Editor B.J. Briscoe, Elsevier, pp. 365-370, 2005.
- [7] Gebeshuber I.C., Majlis B.Y., Neutsch L., Aumayr F. and Gabor F. “Nanomedicine and Biomimetics: Life Sciences meet Engineering & Physics”, *Proc. 3rd Vienna Int. Conf. Micro- and Nanotech. Viennano09*, pp. 17-23, 2009.
- [8] Fratzl P. and Weinkamer R. “Nature’s Hierarchical Materials”, *Progr. Mat. Sci.* Vol. 52(8), pp. 1263-1334, 2007.
- [9] Vincent J.F.V. “Deconstructing the design of a biological material”, *J. Theor. Biol.* Vol. 236, pp. 73-78, 2005.
- [10] Gebeshuber I.C., Gruber P. and Drack M. “A gaze into the crystal ball - biomimetics in the year 2059”, *J. Mech. Eng. Sci.*, submitted
- [11] Gebeshuber I.C., Drack M. and Scherge M. “Tribology in biology”, *Tribology - Materials, Surfaces & Interfaces*, in press
- [12] Kasapi M.A. and Gosline J.M. “Design complexity and fracture control in the equine hoof wall”, *J. Exp. Biol.* Vol. 200, pp. 1639-1659, 1997.

- [13] Kasapi M.A. and Gosline J.M., "Micromechanics of the equine hoof wall: optimizing crack control and material stiffness through modulation of the properties of keratin", *J. Exp. Biol.* Vol. 202, pp. 377-391, 1999.
- [14] Crawford R.M. and Gebeshuber I.C. "Harmony of beauty and expediency", *Science First Hand* Vol. 5(10), pp. 30-36, 2006.
- [15] Gebeshuber I.C. and Crawford R.M. "Micromechanics in biogenic hydrated silica: hinges and interlocking devices in diatoms", *J. Eng. Tribol.* Vol. 220(J8), pp. 787-796, 2006.
- [16] Gebeshuber I.C., Stachelberger H. and Drack M. "Diatom bionanotribology - Biological surfaces in relative motion: their design, friction, adhesion, lubrication and wear", *J. Nanosci. Nanotechnol.* Vol. 5(1), pp. 79-87, 2005.
- [17] Gebeshuber I.C., Kindt J.H., Thompson J.B., Del Amo Y., Stachelberger H., Brzezinski M., Stucky G.D., Morse D.E. and Hansma P.K. "Atomic force microscopy study of living diatoms in ambient conditions", *J. Microsc.* Vol. 212(Pt3), pp. 292-299, 2003.
- [18] Gebeshuber I.C., Thompson J.B., Del Amo Y., Stachelberger H. and Kindt J.H. "In vivo nanoscale atomic force microscopy investigation of diatom adhesion properties", *Mat. Sci. Technol.* Vol. 18, pp. 763-766, 2002.
- [19] Gorb E.V. and Gorb S.N. "Attachment ability of the beetle *Chrysolina fastuosa* on various plant surfaces" *J. Entomologia Experimentalis et Applicata* Vol. 105(1), pp. 13-28, 2002
- [20] Gorb E., Haas K., Henrich A., Enders S., Barbakadze N. and Gorb S. "Composite structure of the crystalline epicuticular wax layer of the slippery zone in the pitchers of the carnivorous plant *Nepenthes alata* and its effect on insect attachment", *J. Exp. Biol.* Vol. 208, pp. 4651, 2005.
- [21] Koch K. Dommissie A., Barthlott W. and Gorb S. N. "The use of plant waxes as templates for micro- and nanopatterning of surfaces", *Acta Biomaterialia* Vol. 3(6), pp. 905-909, 2007.
- [22] Popel A.S. and Pittman R.N. "Mechanics and transport in microcirculation", In: J.D. Bronzino (Ed.), *The Biomedical Engineering Handbook: Second Edition*, CRC Press LLC, Boca Raton, chapter 31, pp. 31-1 - 31-12, 2000.
- [23] Patrick C.W., Sampath R. and McIntire L.V. "Fluid shear stress effects on cellular function", In: J.D. Bronzino (Ed.), *The Biomedical Engineering Handbook: Second Edition*, CRC Press LLC, Boca Raton, chapter 114, pp. 114-1 - 114-20, 2000.
- [24] Orsello C.E., Lauffenburger D.A. and Hammer D.A. "Molecular properties in cell adhesion: a physical and engineering perspective", *Trends Biotechnol.* Vol. 19, pp. 310-316, 2001
- [25] Gebeshuber I.C. "Biotribology inspires new technologies", *Nano Today* 2(5), pp. 30-37, 2007.
- [26] Li P.C.H. *Microfluidic lab-on-a-chip for chemical and biological analysis and discovery*, Chromatographic Science Vol. 94, Taylor & Francis / CRC Press, Boca Raton, Florida, 2005
- [27] Sakhalkar HS, Dalal MK, Salem AK, Ansari R, Fu J, Kiani MF, Kurjiaka DT, Hanes J, Shakesheff KM, Goetz DJ. "Leukocyte-inspired biodegradable particles that selectively and avidly adhere to inflamed endothelium *in vitro* and *in vivo*", *Proc. Natl. Acad. Sci. USA* Vol. 100, pp. 15895-15900, 2003.
- [28] Northen M.T. and Turner K.L. "A batch fabricated biomimetic dry adhesive", *Nanotechnology* Vol. 16(8), pp. 1159-1166, 2005.
- [29] Shah G.J. and Sitti M. "Modeling and design of biomimetic adhesives inspired by gecko foot-hairs". In: *IEEE International Conference on Robotics and Biomimetics (ROBIO)*, pp. 873-878, 2004.
- [30] Hansma P.K., Turner P.J. and Ruoff R.S. "Optimized adhesives for strong, lightweight, damage-resistant, nanocomposite materials: new insights from natural materials", *Nanotechnology* Vol. 18, 044026(3p), 2007.
- [31] Round F.E., Crawford R.M. and Mann D.G. "The diatoms: biology and morphology of the genera", Cambridge University Press, Cambridge, UK, 1990.
- [32] Crawford R.M. and Hinz, F. "The spines of the centric diatom *Corethron criophilum*: light microscopy of vegetative cell division", *Eur. J. Phycol.* Vol. 30, pp. 95-105, 1995.

- [33] Crawford R.M., Hinz F. and Honeywill C. "Three species of the diatom genus *Corethron* Castracane: structure, distribution and taxonomy", *Diatom Res.* Vol. 13, pp. 1–28, 1998.
- [34] Gebeshuber I.C. and Crawford R.M. "Micromechanics in biogenic hydrated silica: hinges and interlocking devices in diatoms", *J. Eng. Tribol.* Vol. 220(J8), pp. 787-796, 2006
- [35] Srajer J., Majlis B.Y. and Gebeshuber I.C. "Microfluidic simulation of a colonial diatom chain reveals oscillatory movement", *Acta Botanica Croatia*, in press
- [36] Gebeshuber I.C., Aumayr M., Hekele O., Sommer R., Goesselsberger C.G., Gruenberger C., Gruber P., Borowan E., Rosic A. and Aumayr F. "Bacilli, green algae, diatoms and red blood cells – how nanobiotechnological research inspires architecture", in: *Bio-Inspired Nanomaterials and Nanotechnology* (tentative title), edited by Yong Zhou, Nova Science Publishers 2009, in press
- [37] Schmid A-M.M. and Crawford R.M. "*Ellerbeckia arenaria* (Bacillariophyceae): formation of auxospores and initial cells", *Europ. J. Phycol.* Vol. 36, pp. 307-320, 2001.
- [38] Gruenberger C., Ritter R., Aumayr F., Stachelberger H. and Gebeshuber I.C. "Algal biophysics: *Euglena gracilis* investigated by atomic force microscopy", *Mat. Sci. Forum* Vol. 555, pp. 411-416, 2007.
- [39] Pahlow M., Riebesell U., Wolf-Gladrow D.A. "Impact of cell shape and chain formation on nutrient acquisition my marine diatoms", *Limnol. Oceanograph.* Vol. 42(8), pp. 1660-1672, 1997.
- [40] Linn F.C. "Lubrication of animal joints. I. The arthrotripsometer", *J. Bone Joint Surg. Am.* Vol. 49, pp. 1079-1098, 1967.
- [41] McCutchen C.W. "Mechanism of animal joints: sponge-hydrostatic and weeping bearings", *Nature* Vol. 184, pp. 1284-1285, 1959.
- [42] Unsworth A., Dowson D., Wright V. "The frictional behaviour of human synovial joints - Part 1. Natural joints", *Trans. Am. Soc. Mech. Eng. Seri. F: J. Lubrication Technol.* Vol. 97, pp. 369–376, 1975.
- [43] Furey M.J. "Joint Lubrication", in: J.D. Bronzino (Ed.), *Biomedical Engineering Handbook*, CRC Press, Boca Raton, chapter 21, pp. 21-1 - 21-26, 2000.